STRUCTURE AND BONDING 122

Series Editor D. M. P. Mingos
Volume Editor R. Winpenny

Single-Molecule Magnets and Related Phenomena

Springer

122
Structure and Bonding

Series Editor: D. M. P. Mingos

Contents

Struct Bond (2006) ■: 1–67
DOI 10.1007/430_022

Published online: 26 January 2006

Synthesis of 3*d* Metallic Single-Molecule Magnets

Guillem Aromí[1] (✉) · Euan K. Brechin[2]

[1]Departament de Química Inorgànica, Universitat de Barcelona, Diagonal 647, 08028 Barcelona, Spain
guillem.aromi@qi.ub.es

[2]School of Chemistry, The University of Edinburgh, West Mains Road, Edinburgh EH9 3JJ, UK
ebrechin@staffmail.ed.ac.uk

Abstract The phenomenon of single-molecule magnetism was established in the early 1990s with the cluster $[Mn_{12}O_{12}(AcO)_{16}(H_2O)_4]$. Since then, a large number of compounds displaying this behaviour have been synthesized. The vast majority of these consist of coordination clusters of 3*d* transition metals prepared by self assembly processes where the structure of the final product has not been predicted. The majority feature manganese ions, primarily in the Mn^{III} oxidation state, but over the years the search for novel examples of such compounds has been extended to other metals of the 3rd row, including iron, nickel, vanadium and cobalt. A host of new approaches and synthetic methodologies have been successfully explored and developed in order to prepare SMMs with new and improved properties. This review covers the synthesis and magnetic properties of SMMs consisting of homometallic coordination clusters of 3*d* transition metals made via serendipitous self-assembly – by far the largest source of such species – together with a brief overview of emerging methods.

Keywords Hysteresis · Molecular nanomagnets · Self-assembly · Single molecule magnets · Transition metal clusters

1 Introduction

The ability of certain molecular transition-metal clusters to be magnetized without need for long-range cooperative interactions was discovered in the early 1990s [1–3]. The phenomenon was first seen in a coordination complex made of 12 oxide and acetate bridged manganese ions (Fig. 1), with formula $[Mn_{12}O_{12}(O_2CMe)_{16}(H_2O)_4]$ (**1**) hereafter abbreviated as $Mn_{12}OAc$ [4]. The bulk magnetisation as induced by an external magnetic field is retained upon removal of the latter, thanks to the presence of an energy barrier (ΔE) to the thermal equilibration of all possible quantised orientations of the molecular magnetic moment (Fig. 2), giving rise to a hysteresis curve below a certain

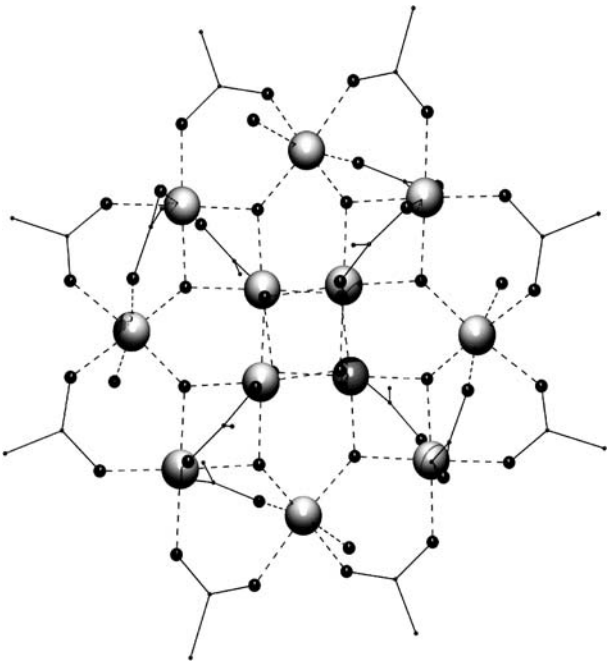

Fig. 1 PovRay representation of $[Mn_{12}O_{12}(O_2CMe)_{16}(H_2O)_4]$ (**1**). Hydrogen atoms are omitted for clarity. Code for atoms: *large grey*, Mn; *medium black*, O; *rest*, C

blocking temperature. Such orientations correspond to the various M_S components that result from the zero-field splitting (ZFS) of the spin ground state, S_T, of the cluster. In this manner, superparamagnetic-like behaviour was shown unambiguously in discrete molecules, and these have been now given the name single-molecule magnets (SMMs). This discovery has great significance since it suggests the possibility of employing molecules as the smallest possible particle for the storage of a bit of magnetic information.

The advent of single-molecule magnetism has stimulated a great deal of research in areas as diverse as physics, theoretical chemistry, spectroscopy, materials chemistry and synthetic coordination chemistry, as demonstrated by the several hundred papers published on the topic over the last 10 years. This effort has lead to the experimental observation of the long predicted phenomenon of quantum tunnelling of the magnetisation (QTM) [5], and to detailed descriptions of the dynamics of relaxation of the magnetic moment in such systems [6–8]. Understanding and mastery of such quantum processes are of primary importance if SMMs are to be used as information storage devices or as qubits in quantum computers [9]. A remarkable achievement is the thorough description of the magnetic and electronic structure of several SMMs through the use of sophisticated techniques such as high-field (HF) EPR [10–13], solid-state ^{55}Mn-NMR [14, 15], ^{1}H-NMR [16] and

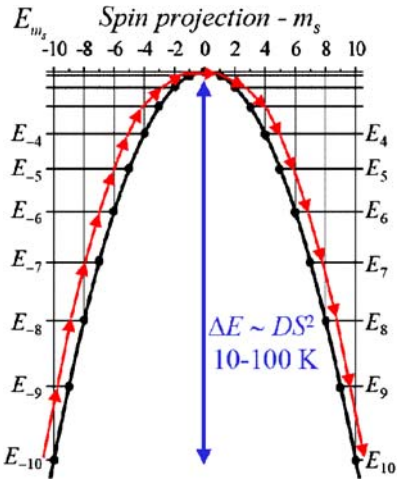

Fig. 2 Energy diagram showing the relative positions of the zero-field split M_S levels of an $S_T = 10$ system, and the barrier mediating between the $M_S = +10$ and the $M_S = -10$ states

^{13}C-NMR [17], inelastic neutron scattering (INS) [18, 19], and magnetic circular dichroism [20]. Invaluable knowledge about the properties of SMMs has also been obtained, thanks to the important effort made in this direction from the theoretical point of view in the form of density functional studies [21–23], employment of Monte Carlo methods [24] and *ab initio* calculations [25].

Much of the above progress has been made thanks to the work of synthetic chemists, who have provided the molecules of study for physicists, whose knowledge and work has, in turn, helped to highlight the next desirable synthetic targets. For example, it quickly became clear that in order to observe this behaviour from a molecular compound it is necessary to have a high spin ground state, S_T, and a large and negative ZFS of that ground state. The energy barrier ΔE is proportional to $S_T^2|D|$ (integer spin) or $(S_T^2 - 1/4)|D|$ (half-integer spin). However, despite the large number of SMMs prepared since the property was first discovered in $[Mn_{12}AcO]$ (**1**), the latter continues to show the highest blocking temperature *hitherto* observed. This temperature being very low (~ 3 K), it remains the main obstacle to some of the potential applications of SMMs. Nevertheless, important advances have been made in other aspects; for example, the ground state spin number has risen from $S_T = 10$ originally, to a record value of $S_T = 51/2 \pm 1$ on a Mn_{25} SMM [26]. Also, the family of compounds has been extended to various other metals besides manganese, including iron, vanadium, cobalt, nickel and, very recently, combinations of 3*d* with 4*d* [27], 5*d* [28] and 4*f* [29–31] paramagnetic ions. In this synthetic effort, different methodologies towards the molecular assembly of coordination compounds have been put to use. Of these, the

most prolific has been serendipitous self-assembly [32]. In this method, ligands capable of coordinating to one or more ions in a variety of modes are mixed with metal salts or compounds in a solvent where the precise outcome is rarely predicted. Conditions can be created, however, for the isolation of discrete polynuclear species that, in many instances, will display interesting magnetic properties. An alternative strategy, which has proven to be more challenging, can be termed "rational molecular design". In this approach, the components of the reaction system display lower flexibility, such that the geometry and properties of the products can often be forecasted. This suggests a "customized" preparation of SMMs. Some very interesting systems have been created in this manner, taking advantage of the linearity of the cyanide ligand in combination with the predictable geometry and electronic structure of specific transition metals [33, 34]. An alternative "rational" approach, the synthesis of complicated polytopic and polynucleating ligands, has allowed the preparation of many magnetically interesting clusters with fascinating pre-determined geometries [35–38]. However, this method has so far failed to produce any new SMM.

The task of preparing SMMs has met with a considerable degree of success over the decade since their discovery. It is surprising that no account exists that describes systematically the progress made in this area from the perspective of the synthetic chemistry. Only a few small reviews, gathering families of manganese [39, 40] or iron [41] SMMs, were published a few years ago, although the rate at which new SMMs are now being discovered quickly renders these accounts somewhat out of date. Likewise, recent papers have appeared compiling the progress made toward the synthesis of SMMs based on the predictable reactivity of the cyanide ligand with transition metals [42, 43]. The present paper is an attempt to exhaustively gather all the work done to date (up to May 2005) in the preparation of SMMs of 3*d* metals (the vast majority) using the serendipitous approach. A section briefly summarising all SMMs of a different class is also included at the end of this review. The majority of compounds reviewed here have had their SMM behaviour distinguished only by the presence of frequency-dependent out-of-phase ac susceptibility signals. While this is indeed an excellent indication of such behaviour, it is not definitive evidence, and ideally it should be coupled with the existence of temperature and sweep-rate dependent hysteresis loops. However, we recognise that many of these complexes would display hysteresis at temperatures below that obtainable with commercial SQUID magnetometers and that many workers do not have access to ultra-low temperature magnetometers. Thus, we include all of these clusters as SMMs bearing this very important caveat in mind.

The emphasis will be on the preparative and structural aspects, while the most relevant issues regarding the magnetic properties of the reviewed systems will be briefly discussed. No detailed descriptions of the exten-

sive physical or spectroscopic studies carried out on some of these compounds will be made. Reviews of this can already be found in the literature [5, 44–47].

2
SMMs of Manganese

Each of the complexes described in this section have been synthesised, at least initially, by the serendipitous assembly of manganese salts or pre-formed clusters of Mn with a combination of one or more flexible organic bridging ligands. These species represent the vast majority of SMMs reported to date. Mn cluster chemistry involves complicated processes in which the crystallographically characterised products are almost certainly not the only complexes present in solution at any one time and where the synthesis also involves the protonation/deprotonation, redox chemistry and structural rearrangement of many species simultaneously. Thus, mechanistic, kinetic and any other detailed studies of the reaction processes are almost impossible.

Compared to other 3*d* transition metals, clusters of manganese are often characterised by large spin ground states, and this, in conjunction with the presence of Jahn-Teller distorted Mn(III) ions (the source of the single-ion anisotropy) make manganese clusters ideal candidates for SMMs. However, there exists few "simple", readily available, soluble sources of Mn(III) and thus synthetic strategies toward making polymetallic complexes containing Mn(III) ions have generally involved either, the oxidation of Mn(II) species, the reduction of Mn(IV) or Mn(VII) species, and the use of small (or in some cases, large) pre-formed Mn(II/III/IV) containing species such as $[Mn_3O(O_2CR)_6L_3]^{0/+}$ or $[Mn_{12}O_{12}(O_2CMe)_{16}(H_2O)_4]$ in the presence of flexible organic bridging ligands such as carboxylates and alkoxides *via* self-assembly. This has been achieved both chemically and electrochemically, and here we give an overview of some of these procedures and the molecules they produce.

2.1
The $[Mn_{12}O_{12}(O_2CR)_{16}(H_2O)_x]^{n-}$ Family; The Prototype SMMs

The first, and most studied family of SMMs are the dodecanuclear complexes of general formula $[Mn_{12}O_{12}(O_2CR)_{16}(H_2O)_x]^{n-}$ ($n = 0,\ 1,\ 2$; $x = 3,\ 4$). Of the more than 100 different Mn clusters known to display SMM behaviour more than half the members belong to the $[Mn_{12}]$ family. This class of compounds retains the record for the largest energy barrier for the reorientation of the magnetisation and this, combined with the fact that $[Mn_{12}OAc]$ is the prototype SMM and is extremely easy to make, has led to numerous

papers describing its chemistry and physics, including the first examples of quantum tunnelling of the magnetisation [48, 49] and quantum phase interference [50].

$[Mn_{12}O_{12}(O_2CMe)_{16}(H_2O)_4]$ (**1**, Fig. 1) was first synthesized in 1980 [4]. It results from the oxidation of $Mn(OAc)_2 \cdot 4H_2O$ with MnO_4^- in an acetic acid/water mixture, quickly and in extremely high yield. Somewhat surprisingly, it took many more years to discover [1] that the molecule has a spin ground state of $S = 10$ resulting from the antiferromagnetic interaction between the eight outer Mn(III) ions and the four inner Mn(IV) ions. This coupled with a ZFS parameter of $D = -0.50\,cm^{-1}$ gave rise to the first molecule with an energy barrier to magnetisation reversal, and the birth of SMM chemistry. The origin of the cluster anisotropy arises from the near-parallel alignment of the Jahn-Teller (JT) axes on the eight Mn(III) ions. Indeed, the initially puzzling appearance of two separate out-of-phase ac susceptibility signals in some of the $[Mn_{12}]$ derivatives [51] has now been ascribed to the presence of separate isomers in which some of the JT axes are orientated differently [52]. The presence of JT-isomers means that there are slower and faster relaxing species within the same crystal that have different energy barriers to the reorientation of the magnetisation. This is a "problem" that has been recently overcome with the preparation of the bromoacetate analogue $[Mn_{12}O_{12}(O_2CCH_{2Br})_{16}(H_2O)_4]$ (**2**) which shows only one out-of-phase ac susceptibility signal and a "cleaner" hysteresis loop, thus simplifying the subsequent analysis [53].

Substitution of the carboxylate ligands surrounding the $[Mn_{12}]$ core can be achieved *via* ligand exchange on the original pre-formed cluster or by repetition of the original reaction in the presence of excess RCO_2H [2, 51]. For example reaction of $[Mn_{12}O_{12}(O_2CMe)_{16}(H_2O)_4]$ (**1**) with a large excess of the appropriate carboxylic acid (e.g. $PhCO_2H$) in CH_2Cl_2 often gives rise to the fully substituted analogue, in this case $[Mn_{12}O_{12}(O_2CPh)_{16}(H_2O)_4]$ (**3**). The reaction works by taking advantage of the relative p*Ka* values of the two carboxylic acids and the fact that acetic acid forms an azeotrope with toluene that can be easily removed. Thus the continual cycling – addition of substituting carboxylic acid/removal of toluene-acetic acid azeotrope – ensures complete substitution. An alternative, but less efficient route to $[Mn_{12}O_{12}(O_2CR)_{16}(H_2O)_4]$ complexes is the oxidation of the appropriate oxo-centred metal triangles $[Mn_3O(O_2CR)_6(py)_3]^{0/+}$ with MnO_4^- in MeCN or CH_2Cl_2 (*vide infra*). However, the yields obtained from this procedure can be 5–10 times smaller than that obtained *via* ligand substitution.

This substitution procedure has been successful not just with a wide variety of neutral and charged carboxylic acids (to produce model systems for the deposition of polycationic $[Mn_{12}]^{n+}$ units on oxide surfaces [54] or as precursors for the organisation of SMMs on silicon [55], or gold surfaces [56], for example), but also with other ligands that can bond in a similar manner. Thus, nitrate (e.g. $[Mn_{12}O_{12}(O_2CPh)_{12}(NO_3)_4(H_2O)_4]$, **4**) [57],

phosphinates (e.g. $[Mn_{12}O_{12}(O_2CMe)_8(O_2PPh_2)_8(H_2O)_4]$, **5**) [58], sulfonates (e.g. $[Mn_{12}O_{12}(O_2CMe)_8(O_3SPh)_8(H_2O)_4]$, **6**) [59], and dicarboxylates (e.g. $[Mn_{12}O_{12}(O_2CPh)_8(L1)_4(H_2O)_4]$ (**7**), where H_2L1 = 10-(4-acetylsulfanyl-methyl-phenyl)-anthracene-1, 8-dicarboxylic acid) [60] amongst others, have all been incorporated into the $[Mn_{12}]$ molecule. One of the primary objectives of this substitution was to allow access to different oxidation levels of the $[Mn_{12}]$ core, i.e. so that the Mn ions could be reduced or oxidized and the subsequent effect on the magnetism studied. Electrochemistry on various $[Mn_{12}]$ clusters revealed the presence of quasi-reversible one-electron oxidation and reduction processes. Thus, the ability to ligand exchange electron-withdrawing or electron-donating carboxylates onto the periphery of the molecule suggested that the isolation of reduced or oxidised versions was possible. The first one-electron reduced species, $(PPh_4)[Mn_{12}O_{12}(O_2CEt)_{16}(H_2O)_4]$ (**8**), was made from the reaction of PPh_4I with $[Mn_{12}O_{12}(O_2CEt)_{16}(H_2O)_3]$ (**9**) in CH_2Cl_2. A lone Mn(II) ion is localised on a formerly Mn(III) site to give a trapped valence $[Mn^{II}Mn^{III}{}_7Mn^{IV}{}_4]$ metallic core [51]. Magnetic studies revealed the complex to have a spin ground state of $S = 19/2$ with $D \sim -0.40\,cm^{-1}$. This complex also represented the first example of a half-integer spin SMM, the added interest here being that QTM was observed even though theory predicts that it should not [61].

The first two-electron reduced species, $(PPh_4)_2[Mn_{12}O_{12}(O_2CCHCl_2)_{16}(H_2O)_4]$ (**10**), was prepared in an analogous manner to the one electron reduced complex, except that this time two equivalents of PPh_4I were used in conjunction with the more electron-withdrawing dichloroacetate ligand [62]. The second Mn(II) in **10** is again located on a formerly Mn(III) position to give a trapped valence $[Mn^{II}{}_2Mn^{III}{}_6Mn^{IV}{}_4]$ metallic core. Magnetic studies of this complex revealed an $S = 10$ ground state with $D \sim -0.30\,cm^{-1}$. The reduction in the number of Mn(III) ions in the $[Mn_{12}]$ compounds leads to a concomitant decrease in the value of $|D|$. As has now been seen for many SMMs, the magnetic properties of the $[Mn_{12}]^{2-}$ cluster were found to be highly sensitive to subtle differences in environment [63], such as the presence of solvent molecules, the nature of the molecular packing and the overall crystal symmetry – an important caveat for workers in the field. To date, there are no published examples of a three-electron reduced complex, nor of any oxidised $[Mn_{12}]^{n+}$ cluster.

2.2
$[Mn_{84}O_{72}(OAc)_{78}(OMe)_{24}(OH)_6(MeOH)_{12}(H_2O)_{42}]$ (11); A Giant SMM

One of the most successful routes for SMM synthesis is the reaction between a pre-formed Mn cluster and (a) solvent, (b) reductant/oxidant, and/or (c) flexible organic bridging ligand. Commonly the metal complexes used are the triangular species [64] $[Mn_3O(O_2CR)_6(py)_3]^{0/+}$, but all Mn_x ($x \geq 2$) clus-

ters can, and should be, regarded as starting materials, even those already exhibiting SMM behaviour, like the series of $[Mn_{12}O_{12}(O_2CR)_{16}(H_2O)_4]$ compounds. The advantages of using pre-formed clusters are (i) they are convenient sources of Mn(III) ions; (ii) they can often be made in gram scale quantities very easily; (iii) they already contain multiple Mn ions; (iv) they may already contain multiple O^{2-}/OH^- ions; (v) they may already possess large spin ground states; (vi) they may already display large anisotropies; and (vii) they may already display SMM behaviour.

One of the most spectacular examples of this is the preparation of the largest known SMM, the cluster $[Mn_{84}O_{72}(O_2CMe)_{78}(OMe)_{24}(OH)_6(MeOH)_{12}$

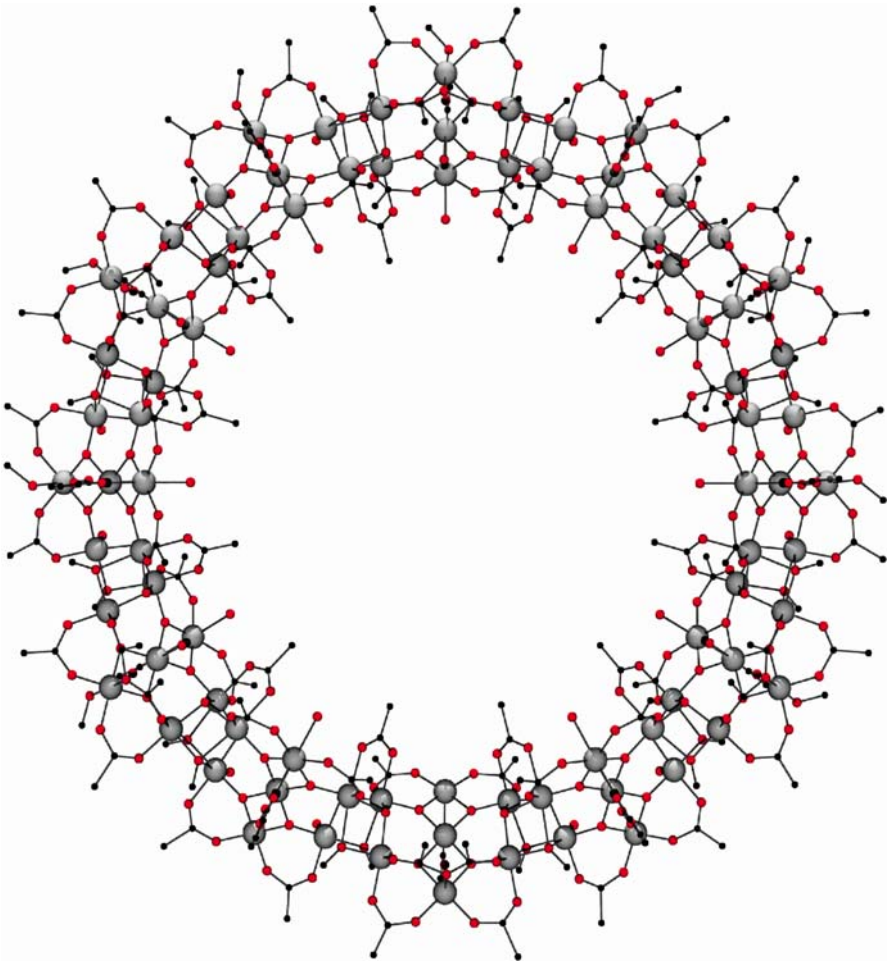

Fig. 3 PovRay representation of the molecular cluster $[Mn_{84}O_{72}(O_2CMe)_{78}(OMe)_{24}(OH)_6(MeOH)_{12}(H_2O)_{42}]$ (**11**). Hydrogen atoms are omitted for clarity. Code for atoms: *large grey*, Mn; *medium red*, O; *rest*, C

$(H_2O)_{42}]$ (**11**, $[Mn_{84}]$, Fig. 3) [65]. This complex forms from the reaction of $[Mn_{12}OAc]$ (**1**), MnO_4^-, and CH_3COOH with MeOH, in what can be effectively regarded as a reductive aggregation – dissolution of a high oxidation state ($[Mn^{IV}{}_4Mn^{III}{}_8]$; Mn^{VII}) species in an alcoholic solution that will reduce the Mn ions, but also provide additional bridging ligands (in this case MeO^-). The structure consists of a series of $[Mn_4]$ cubanes and $[Mn_3O]$ triangles linked together to form a giant "wheel" or "torus". Magnetic studies on $[Mn_{84}]$ indicate a relatively small spin ground state of $S = 6$, but low temperature micro-SQUID measurements confirm the presence of temperature and sweep rate dependent hysteresis loops. $[Mn_{84}]$ is by far the largest SMM made with a diameter of ~ 4.2 nm (the next largest is $[Mn_{30}]$ – *vide infra*) and can be regarded as the first meeting point of the top-down and bottom-up approaches to building nanoscale magnetic materials [65].

2.3 $[Mn_{30}O_{24}(OH)_8(O_2CCH_2{}^tBu)_{32}(H_2O)_2(MeNO_2)_4]$ (13); The Second Largest SMM

The use of alcohol as solvent in the synthesis of Mn SMMs is now an established and successful method (*vide infra*), but prior to the advent of the reductive aggregation concept, this was generally avoided when using preformed Mn clusters as starting materials, since it would inevitably lead to the reduction of the Mn centres and protonation of the oxo- and/or hydroxo groups that are generally responsible for holding these large Mn aggregates together. Thus, reactions of clusters of the type $[Mn_3O(O_2CR)_6(py)_3]^{0/+}$, $(TBA)[Mn_4O_2(O_2CR)_9(H_2O)]$, $(TBA)[Mn_8O_6Cl_6(O_2CPh)_7(H_2O)_2]$ or $[Mn_{12}O_{12}(O_2CR)_{16}(H_2O)_4]$ [39], with ligands such as H_3thme, Hhmp, Hhep and H_2pdm amongst others (Scheme 1) were carried out in non-protic solvents, typically MeCN and CH_2Cl_2. This produced a beautifully diverse array of SMMs.

The simplest way of applying this concept is by induction of structural rearrangement (and/or change in oxidation state) through reaction with solvent alone. For example, dissolution of $[Mn_{12}O_{12}(O_2CCH_2{}^tBu)_{16}(H_2O)_4]$ (**12**, a $[Mn^{IV}{}_4Mn^{III}{}_8]$ compound) [66] in a mixture of CH_2Cl_2 and $MeNO_2$ leads to the isolation of the second largest known SMM: $[Mn_{30}O_{24}(OH)_8(O_2CCH_2{}^tBu)_{32}(H_2O)_2(MeNO_2)_4]$ (**13**) containing a $[Mn^{IV}Mn^{III}{}_{26}Mn^{II}{}_3]$ metallic core [67]. The cluster bears little resemblance to its parent molecule, and consists of a central, near-linear $[Mn_4O_6]$ backbone to which are attached two $[Mn_{13}O_9(OH)_4]$ units. Magnetic studies reveal a spin ground state of $S = 5$ and $D = -0.51\ cm^{-1}$.

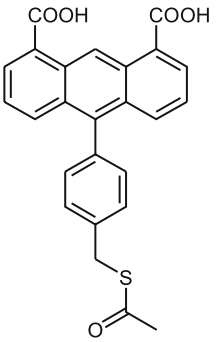

10-(4-acetylsulfanylmethyl-phenyl)-antracene-1,8-dicarboxylic acid (H_2L)

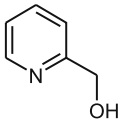

2-hydroxymethyl pyridine (Hhmp)

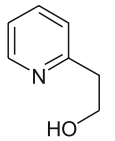

2-hydroxyethyl pyridine (Hhep)

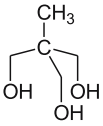

1,1,1-tris(hydroxymethyl)-ethane (H_3thme)

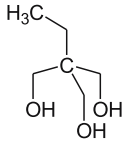

1,1,1-tris(hydroxymethyl)-propane (H_3tmp)

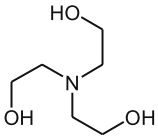

Triethanolamine (H_3tea)

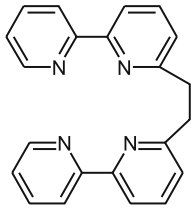

1,2-bis(2,2'-bipyridine-6-yl) ethane (bis-bpy)

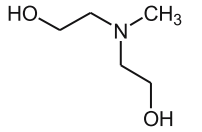

N-methyldiethanolamine (H_2mda)

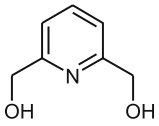

2,6-pyridinedimethanol (H_2pdm)

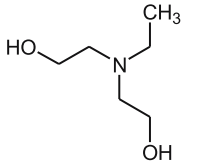

N-ethyldiethanolamine (H_2edea)

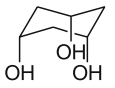

1,3,5-cyclohexantriol (H_3cht)

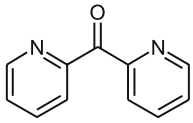

Dipyridylketone dpk

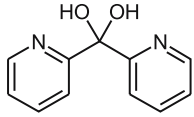

Dipyridyldiol (H_2pdol)

Scheme 1

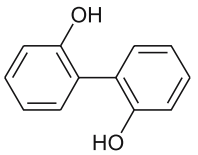

2,2'-Biphenol
(H_2biphen)

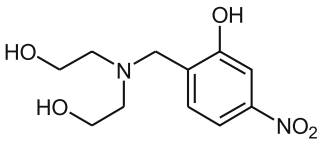

N-(2-hydroxy-5-nitrobenzyl)
iminodiethanol (H_3L2)

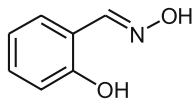

Salicylaldoxime
(H_3salox)

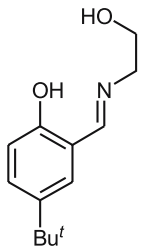

4-*tert*-butyl-salicylidene-2-
-ethanolamine (H_2sal)

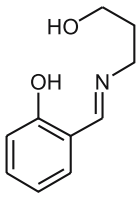

Salicylidene-2-
propanolamine (H_2sap)

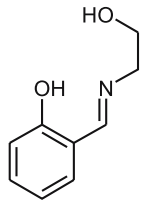

Salicylidene-2-
ethanolamine (H_2sae)

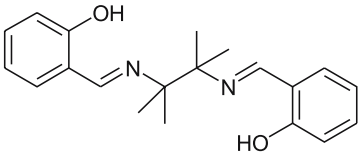

(1,1,2,2-tetramethylethylene)-bis-
(salicylideneamine) (H_2saltmen)

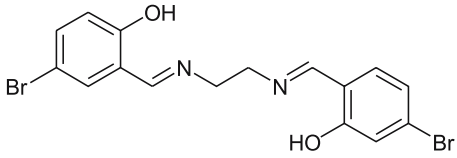

N,N'-ethylene-bis-(5-bromosalicylideneamine)
(H_2Brsalen)

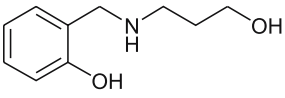

N-(2-hydroxybenzyl)-3-amino
1-propanol (H_2salpa)

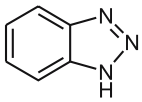

Benzotriazole
(Hbta)

Imidazole
(HIm)

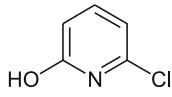

6-chloro-2-pyridinol
(Hchp)

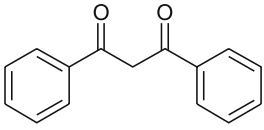

Dibenzoylmethane (Hdbm)

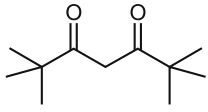

Dipivaloylmethane (Hdpm)

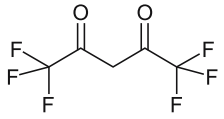

Hexafluoroacetylacetonate
(Hhfac)

Scheme 1 (continued)

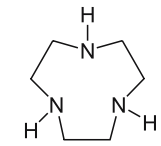
Triazacyclononane (tacn)

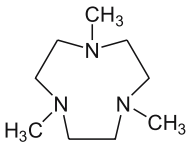
N,N',N''-trimethyl-triaza-cyclononane (Me_3tacn)

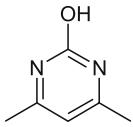
4,6-dimethylhdroxy-pyrimidine (Hdmhp)

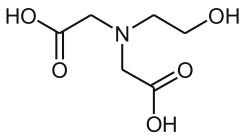
N-(1-Hydroxyethyl)amino diaceticacid (H_3heidi)

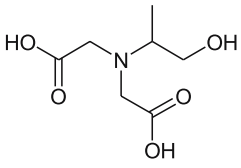
N-(1-Hydroxy-2-methylethyl) aminodiaceticacid (H_3metheidi)

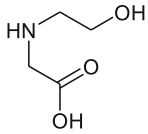
N-(1-Hydroxyethyl)amino aceticacid (Hheia)

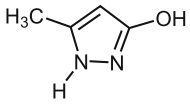
2-methylpyrazolinol (Hmpo)

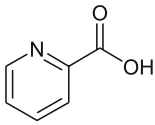
Picolinic acid (Hpic)

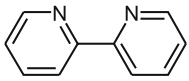
2,2'-bipyridine (bpy)

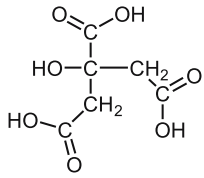
Citric Acid (H_4cit)

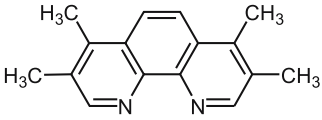
3,4,7,8-tetramethyl-1,10-phenantroline (tmphen)

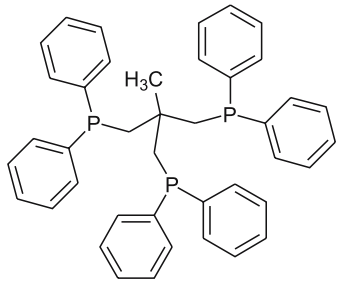
1,1,1-tris(diphenylphosphino-methyl) ethane (triphos)

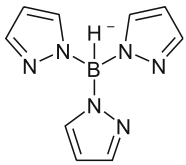
hydrotris(pyrazolyl) borate (Tp)

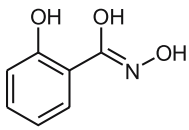
Salicylhydroxamic acid (H_3shi)

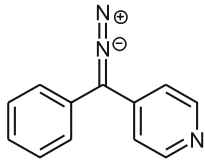
4-(α-diazobenzyl) pyridine (dabp)

Scheme 1 (continued)

2.4 $[Mn_{12}O_8Cl_4(O_2CPh)_8(hmp)_6]$ (14); A New Type of $[Mn_{12}]$ SMM

Rearrangement of a pre-formed cluster can also be achieved by the addition of a bridging co-ligand. For example, reaction of the octanuclear complex (TBA)$[Mn_8O_6(Cl)_6(O_2CPh)_7(H_2O)_2]$ with the ligand hmpH in MeCN produces the dodecanuclear complex $[Mn_{12}O_8Cl_4(O_2CPh)_8(hmp)_6]$ (**14**, $[Mn_{12}hmp]$, Fig. 4) [68] which comprises a $[Mn^{III}{}_{10}Mn^{II}{}_2O_6Cl_2]$ core made from three pairs of face-sharing cuboids. This complex has a ground state of $S = 7$ with $D = -0.60\ cm^{-1}$. Interestingly, the identical reaction with hepH produces its structural isomer $[Mn_{12}O_8Cl_4(O_2CPh)_8(hep)_6]$ (**15**). However, this complex has a diamagnetic ground state and is thus not an SMM.

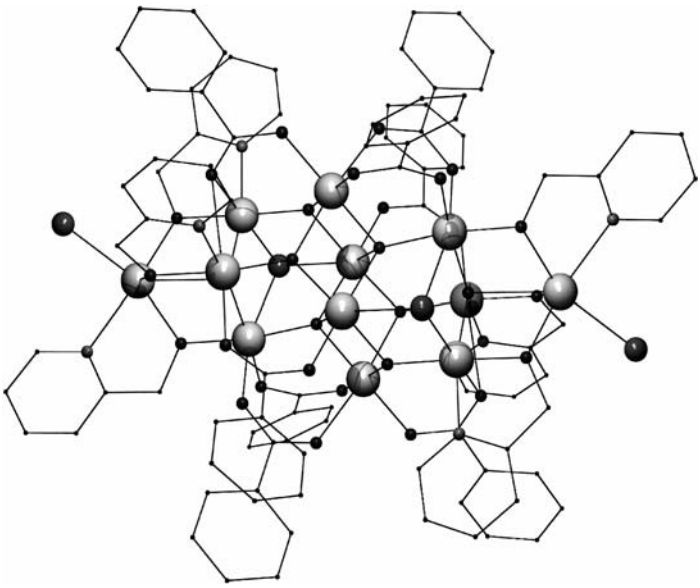

Fig. 4 PovRay representation of $[Mn_{12}O_8Cl_4(O_2CPh)_8(hmp)_6]$ (**14**). Hydrogen atoms are omitted for clarity. Code for atoms: *largest grey*, Mn; *second largest grey*, Cl; *medium black*, O; *medium grey*, N; *rest*, C

2.5 Use of $[Mn_3]$ Triangles as Starting Materials

Probably the most successful use of pre-formed Mn clusters as starting materials in SMM synthesis involves the triangular complexes of general formula: $[Mn_3O(O_2CR)_6(L)_3]^{0/+}$ (where L is a terminal ligand such as H_2O, MeCN or pyridine). These complexes are easily made in a short timescale and their reactivity is highly versatile. They are stable in solution, accessible to ligand

variation, i.e. the nature of the carboxylate can be changed at will as can the terminal ligand L, and they can be prepared with either three Mn(III) ions to give the charged complexes $[Mn_3O(O_2CR)_6(L)_3]X$ ($X^- = ClO_4^-$, NO_3^-, etc.) or with two Mn(III) ions and one Mn(II) ion to give the neutral complexes $[Mn_3O(O_2CR)_6(L)_3]$. For the charged complexes, the nature of the anion is an additional reaction variable. These variables allow for a systematic synthetic strategy which, if successful, can help to produce large families of related compounds. Indeed, the prototype SMMs $[Mn_{12}O_{12}(O_2CR)_{16}(H_2O)_x]$ can be made via the oxidation of the appropriate $[Mn_3O(O_2CR)_6(L)_3]^{0/+}$ complex with MnO_4^- in MeCN or CH_2Cl_2, albeit in rather poor yields.

Another good example of this approach is the reaction of the tripodal ligands H_3thme, H_3tmp and H_4peol (Scheme 1) with the neutral $[Mn_3]$ triangles. For example, reaction of $[Mn_3O(O_2CMe)_6(py)_3]$ with H_3thme in MeCN produces the enneanuclear complex $[Mn_9O_7(thme)(O_2CMe)_{11}(py)_3(H_2O)_2]$ (**16**, $[Mn_9thme]$, Fig. 5) [69, 70]. This complex has a core of six Mn(III) and two Mn(II) ions surrounding a central triangle of Mn(IV) ions – a structure with obvious parallels to $[Mn_{12}OAc]$. Indeed, the observed $S = 17/2$ ground state also arises from the antiferromagnetic interaction between the ferromagnetically coupled inner Mn(IV) ions and the peripheral Mn(III/II) ions. Low temperature micro-SQUID measurements of $[Mn_9thme]$ (**16**) provide a beautiful example of temperature and sweep rate dependent hysteresis loops in which the QTM steps are clearly seen (Fig. 6). Repetition of the reaction that produced $[Mn_9thme]$ (**16**) but using the benzoate triangle $[Mn_3O(O_2CPh)_6(py)_3]$ does not produce an analogous compound but the

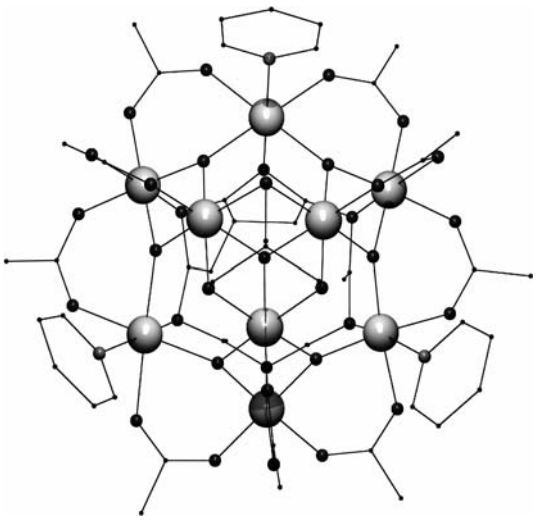

Fig. 5 PovRay representation of $[Mn_9O_7(thme)(O_2CMe)_{11}(py)_3(H_2O)_2]$ (**16**). Hydrogen atoms are omitted for clarity. Code for atoms as in Fig. 4

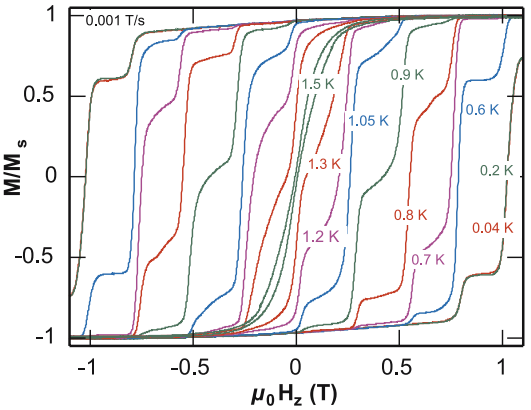

Fig. 6 Variable field isothermal magnetisation curves, recorded at different temperatures, for complex $[Mn_9O_7(thme)(O_2CMe)_{11}(py)_3(H_2O)_2]$ (**16**), emphasising large hysteresis loops caused by slow relaxation of the magnetisation and clearly showing steps as a result of enhanced relaxation due to quantum tunnelling

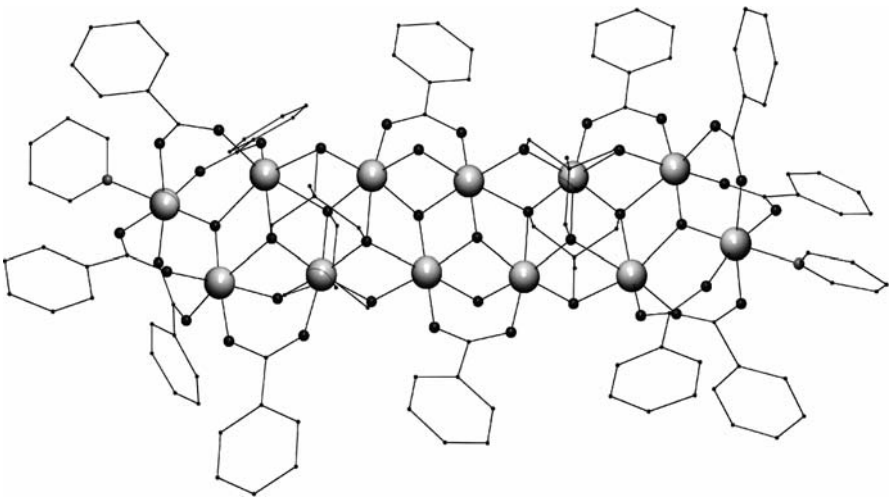

Fig. 7 PovRay representation of $[Mn_{12}O_4(OH)_2(O_2CPh)_{12}(thme)_4(py)_2]$ (**17**). Hydrogen atoms are omitted for clarity. Code for atoms as in Fig. 4

species $[Mn_{12}O_4(OH)_2(O_2CPh)_{12}(thme)_4(py)_2]$ (**17**, [Mn_{12}thme], Fig. 7) [71]. This complex consists of a series of ten edge-sharing triangular units, as directed by the tripodal organic ligands, which combine to form a long, thin, rod-like complex. The presence of so many triangular units and thus the presence of many competing exchange interactions, results in an intermediate spin ground state for the complex of $S = 7$. Repetition of the same reaction but utilising a number of different carboxylates leads to the formation of a large family of rod-like Mn species of differing nuclearities and spins [72].

Changing solvent from MeCN to MeOH, and use of the $[Mn^{III}_3]$ triangles, brings about a drastic change in the nature of the products obtained. For example, reaction of $[Mn_3O(O_2CMe)_6(HIm)_3](O_2CMe)$ with H_3tmp in MeOH affords the wheel-like complex $[Mn_{22}O_6(OMe)_{14}(O_2CMe)_{16}(tmp)_8(HIm)_2]$ (**18**, $[Mn_{22}tmp]$, Fig. 8) [73] $[Mn_{22}tmp]$ is a mixed valent $[Mn^{IV}_2Mn^{III}_{18}Mn^{II}_2]$ complex comprising a series of linked $[Mn_3O]$ triangles and partial $[Mn_4]$ cubanes, similar to that seen in $[Mn_{84}]$ (**11**). $[Mn_{22}tmp]$ has a spin ground state of $S = 10$ with $D = -0.10\,cm^{-1}$, and is a rare example of a "cyclic", high-spin Mn SMM.

Reaction of $[Mn_3O(O_2CMe)_6(py)_3](ClO_4)$ with the ligand Hhep in MeCN produces the complex $[Mn_{18}O_{14}(O_2CMe)_{18}(hep)_4(hepH)_2(H_2O)_2]$ (**19**, $[Mn_{18}hep]$, Fig. 9) [74] containing a complicated $[Mn^{III}_{16}Mn^{II}_2]$ metallic core made from a central, near-linear $[Mn_4O_6]$ unit either side of which is attached a $[Mn_7O_9]$ unit. The complex thus has some structural similarities to $[Mn_{12}hmp]$ (**14**). Magnetic studies reveal the complex to have a spin ground state of $S = 13$, with $D = -0.13\,cm^{-1}$. At the time of its publication this was both the largest spin and highest nuclearity SMM to show QTM.

Reaction of $[Mn_3O(O_2CCHPh_2)_6(py)_3](ClO_4)$ with H_3tea in MeCN yields the hexanuclear SMM $[Mn_6(teaH)_2(teaH_2)_2(O_2CCHPh_2)_8]$ (**20**, $[Mn_6tea]$,

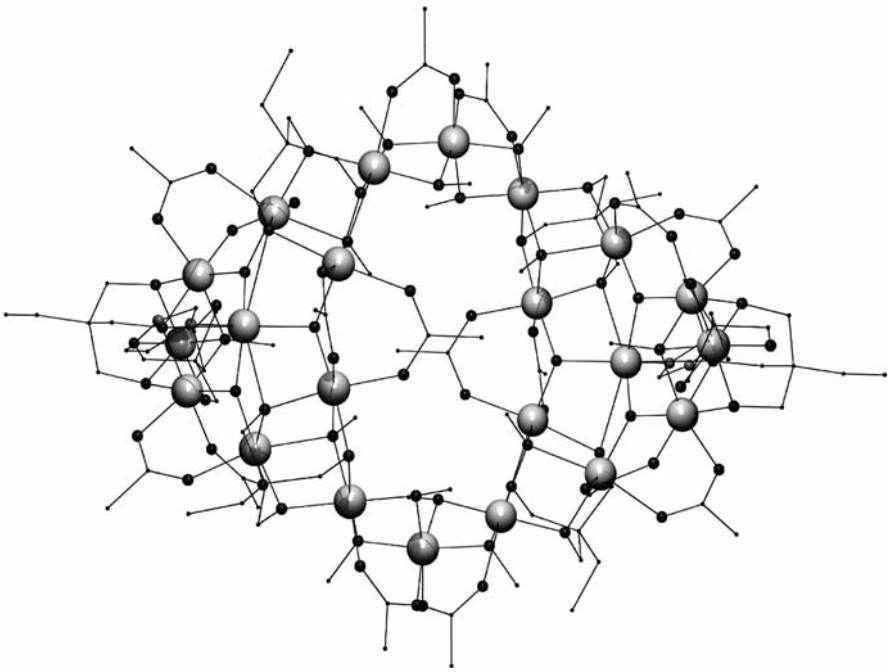

Fig. 8 PovRay representation of $[Mn_{22}O_6(OMe)_{14}(O_2CMe)_{16}(tmp)_8(HIm)_2]$ (**18**). Hydrogen atoms are omitted for clarity. Code for atoms as in Fig. 4

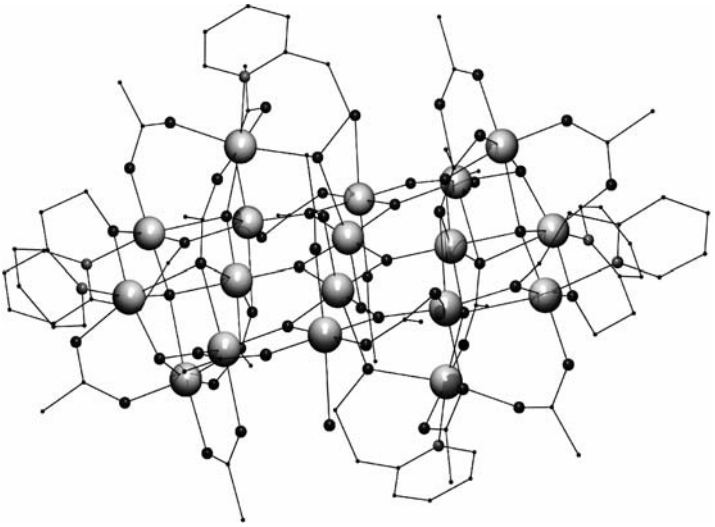

Fig. 9 PovRay representation of $[Mn_{18}O_{14}(O_2CMe)_{18}(hep)_4(hepH)_2(H_2O)_2]$ (**19**). Hydrogen atoms are omitted for clarity. Code for atoms as in Fig. 4

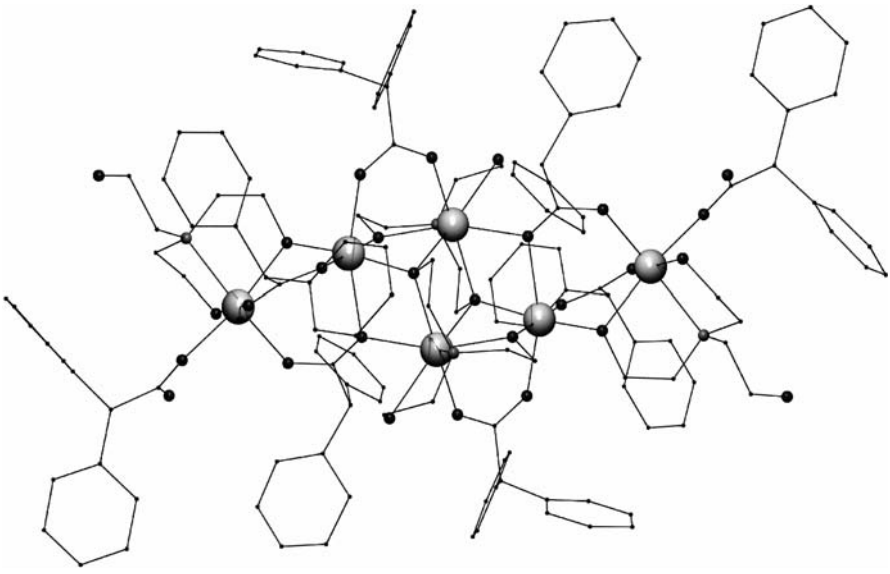

Fig. 10 PovRay representation of $[Mn_6(teaH)_2(teaH_2)_2(O_2CCHPh_2)_8]$ (**20**). Hydrogen atoms are omitted for clarity. Code for atoms as in Fig. 4

Fig. 10) [75]. The centrosymmetric complex contains a central planar $[Mn^{III}_2 Mn^{II}_2]$ rhombus and two peripheral Mn(II) ions. Magnetic studies reveal the complex to have a ground state of $S = 5$ with $D = -0.20\ cm^{-1}$.

2.6 A Family of Tetranuclear Mn SMMs

The central planar rhombus in $[Mn_6tea]$ (**20**) is similar to that found in the tetranuclear SMM $[Mn_4(O_2CMe)_2(pdmH)_6]^{2+}$ (**21**, $[Mn_4pdmH]$, Fig. 11), except that the Mn(II) and Mn(III) sites are interchanged. The latter complex is made *via* the reaction of $[Mn_3O(O_2CMe)_6(py)_3](ClO_4)$ with H_2pdm in either MeCN or CH_2Cl_2. The planar core consists of two "inner" Mn(III) ions and two "outer" Mn(II) ions that are ferromagnetically coupled to give an $S = 9$ ground state [76] with $D = -0.32\,cm^{-1}$. The $[Mn^{III}_2Mn^{II}_2]$ core has subsequently been observed in a number of tetranuclear SMMs, including $[Mn_4(hmp)_6(NO_3)_4]$ (**22**) [77], $[Mn_4(hmp)_6Br_2(H_2O)_2]Br_2$ (**23**) [78], $[Mn_4(hmp)_6(NO_3)_2(MeCN)_2](ClO_4)_2$ (**24**) [77], $[Mn_4(hmp)_4(acac)_2(MeO)_2](ClO_4)_2$ (**25**) [77] and $[Mn_4(O_2CPh)_4(mda)_2(mdaH)_2]$ (**26**) [79]. This is an important series of molecules because in order to understand the detailed physical properties displayed by SMMs, such as the mechanism of QTM, the origin of cluster anisotropy or the exact role of intermolecular interactions, it is imperative that families of related complexes displaying these properties are prepared. These $[Mn^{III}_2Mn^{II}_2]$ clusters now represent only the third well established "family" of SMMs after the $[Mn_{12}O_{12}(O_2CR)_{16}(H_2O)_x]^{n-}$ complexes and the $[Mn^{IV}Mn^{III}_3O_3X]$ cubanes (*vide infra*). Another tetranuclear SMM, although made with a completely different ligand, is the complex $[Mn_4O_2(MeO)(O_2CPh)_2(bis-bpy)_2(MeOH)](ClO_4)_2$ (**27**, $[Mn_4bis\text{-}bpy]$) [80], which is formed from the reaction of $[Mn_3O(O_2CMe)_6(py)_3](ClO_4)$ with bis-bpy in MeOH. The complex contains a ladder-like $[Mn_4O_4]$ core, but this time consisting of three Mn(III) ions and one Mn(II) ion. Magnetic studies suggest a ground state of $S = 7/2$ with $D = -0.77\,cm^{-1}$.

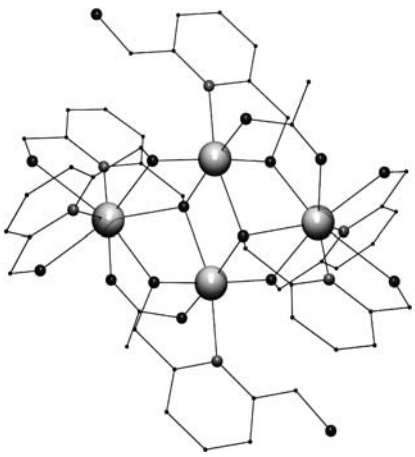

Fig. 11 PovRay representation of the complex cation $[Mn_4(O_2CMe)_2(pdmH)_6]^{2+}$ (**21**). Hydrogen atoms are omitted for clarity. Code for atoms as in Fig. 4

2.7 SMMs from Dinuclear Mn Complexes

Aside from the well used [Mn_3] triangles another useful starting material is the dinuclear complex [$Mn_2O_2(bpy)_4$](ClO_4)$_3$. As it contains high oxidation state Mn ions ([$Mn^{IV}Mn^{III}$]) and is easy to make in large quantities it is an ideal starting material [81]. In fact, there exist many such small Mn compounds in the literature that, as yet, are untried candidates for use in Mn cluster synthesis. For example, reaction of [$Mn_2O_2(bpy)_4$](ClO_4)$_3$ with H_3thme in MeCN produces the complex [$Mn_2(H_2thme)_2(bpy)_4$](ClO_4)$_2$ (**28**, [Mn_2thme], Fig. 12) [82]. Here the partial deprotonation of the ligands is accompanied by a reduction of one of the Mn ions. The two Mn(III) ions couple ferromagnetically through the alkoxide bridges to give a ground state of $S = 4$, with $D = -0.65\ cm^{-1}$, but the analysis of the magnetism is hindered by the weak exchange and resultant low-lying excited states. Single crystal micro-SQUID measurements do however show the existence of temperature and sweep rate dependent hysteresis loops at low temperature, suggesting [Mn_2thme] to be only the second example of a dinuclear Mn SMM after the complex [Mn_2saltmen] (*vide infra*).

Replacing H_3thme with another tripodal ligand, H_3cht, in the same reaction scheme produces the trinuclear SMM [$Mn_3(Hcht)_2(bpy)_4$](ClO_4)$_2$ (**29**, [Mn_3cht], Fig. 13) [83]. Again, the aggregation process is accompanied by reduction of one of the Mn ions and partial deprotonation of the ligand. The complex consists of a linear trinuclear array of Mn ions linked by alkoxides where the central metal is the sole Mn(III) ion, the other ions being in the oxidation state +2. Magnetic studies show the metal centres to be ferromagnetically coupled to give a ground state of $S = 7$, with $D = -0.10\ cm^{-1}$. [Mn_3cht] is the only trinuclear homometallic SMM reported to date and the first SMM to contain only one Mn(III) ion.

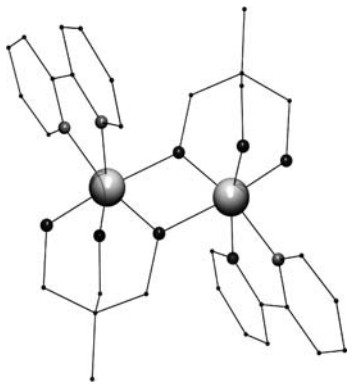

Fig. 12 PovRay representation of [$Mn_2(H_2thme)_2(bpy)_4$](ClO_4)$_2$ (**28**). Hydrogen atoms are omitted for clarity. Code for atoms as in Fig. 4

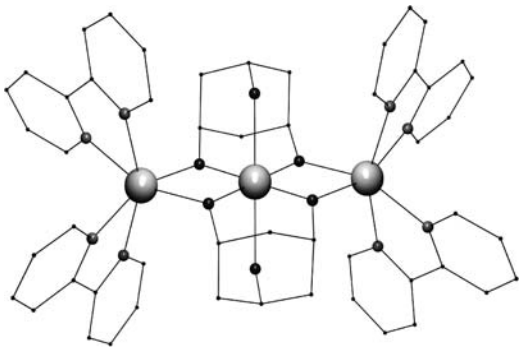

Fig. 13 PovRay representation of $[Mn_3(Hcht)_2(bpy)_4](ClO_4)_2$ (**29**). Hydrogen atoms are omitted for clarity. Code for atoms as in Fig. 4

2.8 Use of Ce(IV) as a Template

A recent, and elegant, extension to the methodology of using pre-formed Mn clusters as starting materials is the use of a templating agent to induce a structural and/or oxidation state change in clusters without the

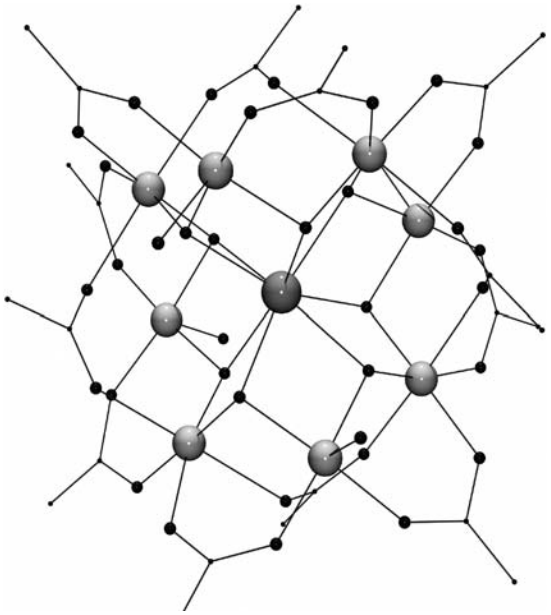

Fig. 14 PovRay representation of $[CeMn_8O_8(O_2CMe)_{12}(H_2O)_4]$ (**30**). Hydrogen atoms are omitted for clarity. Code for atoms: *largest grey*, Ce; *second largest grey*, Mn; *medium black*, O; *rest*, C

need for additional bridging ligands. For example, addition of the oxophilic Ce(IV) ion (in the form of $(NH_4)_2Ce(NO_3)_6$) to the Mn(III) linear polymer $\{[Mn(OH)(O_2CMe)_2]\cdot(MeCO_2H)\cdot(H_2O)\}_n$ in MeCN results in the formation of the "saddle-like" complex $[CeMn_8O_8(O_2CMe)_{12}(H_2O)_4]$ (**30**, $[Mn_8Ce]$, Fig. 14) [84]. The structure contains a central, diamagnetic, Ce(IV) ion around which the polymer is "wrapped", forming an outer $[Mn_8O_8]$ wheel or loop. This wheel is reminiscent of the outer $[Mn_8]$ wheel in $[Mn_{12}OAc]$ although in this case the Jahn-Teller axes are not all co-parallel. Magnetic studies show the Mn ions to be coupled ferromagnetically to give a ground state of $S = 16$, with $D = -0.10\,cm^{-1}$. This is the second largest spin ground state known for a Mn cluster, and one of the largest for any molecule.

2.9
A Series of SMMs from Simple One-Pot Reactions

The simplest synthetic route to Mn SMMs is the one-pot approach whereby a simple Mn(II) salt is combined with a bridging ligand (or combination of bridging ligands) and/or (a) a base – which has the dual purpose of deprotonating the ligand(s) and inducing the oxidation the manganese ions and/or

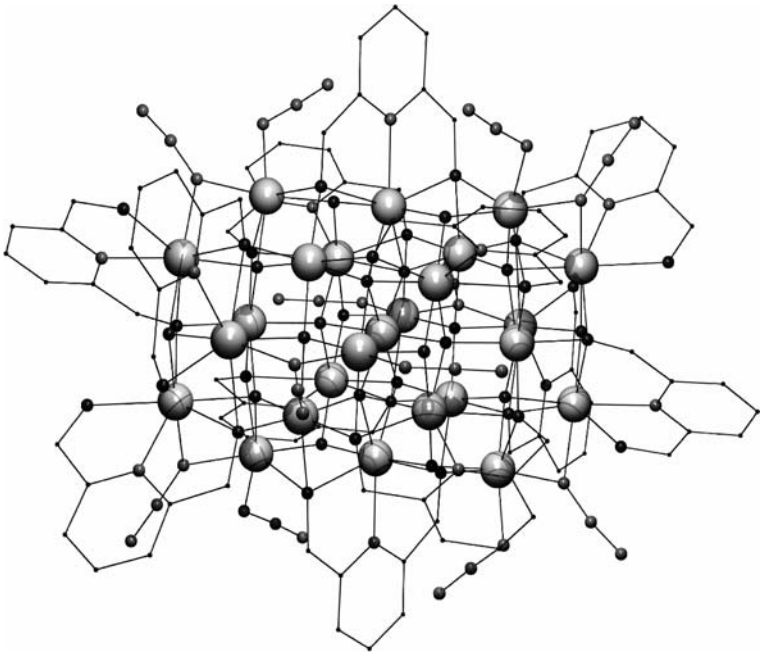

Fig. 15 PovRay representation of the complex cation of $[Mn_{25}O_{18}(OH)_2(N_3)_{12}(pdm)_6(pdmH)_6](Cl)_2$ (**31**). Hydrogen atoms are omitted for clarity. Code for atoms as in Fig. 4

(b) a solution of permanganate – in order to trigger a comproportionation reaction.

One of the most spectacular examples of this is the formation of the complex $[Mn_{25}O_{18}(OH)_2(N_3)_{12}(pdm)_6(pdmH)_6](Cl)_2$ (**31**, $[Mn_{25}]$, Fig. 15) via the reaction of $MnCl_2 \cdot 4H_2O$ with $pdmH_2$, NaN_3 and Me_4NOH in a mixture of MeOH and MeCN [26]. The complex describes a complicated barrel-like structure containing a core of five parallel layers of Mn ions held together through a combination of oxide, alkoxide and azide bridges. Magnetisation data taken below 4 K and in fields up to 7 Tesla were fit to give a ground state of $S = 51/2 \pm 1$, with $D = -0.022\,cm^{-1}$. This complex represents the largest mixed-valent $[Mn^{IV}Mn^{III}Mn^{II}]$ cluster known and the largest spin SMM to date. Indeed, it displays the largest spin ground state of any isolated molecule, surpassing the $S = 25$ of an $[Fe_{14}]$ cluster [85], and the $S = 39/2$ of a mixed-metal $[W_6Mn_9]$ cluster [86].

The largest Mn cluster made from the one-pot approach is the hexaicosanuclear compound $[Mn_{26}(pdol)_{12}(OMe)_{12}O_{16}(N_3)_6]$ (**32**, $[Mn_{26}pdol]$, Fig. 16) [87], which results from the reaction of $MnCl_2 \cdot 4H_2O$ with dpk, NaOH, and NaN_3 in MeOH. The structure contains a central core of 16 Mn(III) ions held together by a combination of oxide and methoxide ions, and surrounded by a "metallocryptand" comprised of ten Mn ions linked through the $pdol^{2-}$ ligands. The metallocrypt and has an adamantoid type structure comprising four Mn(II) and six Mn(III) ions. Ac susceptibility studies in the temperature range 1.9–10 K show the tails of frequency-dependent out-of-

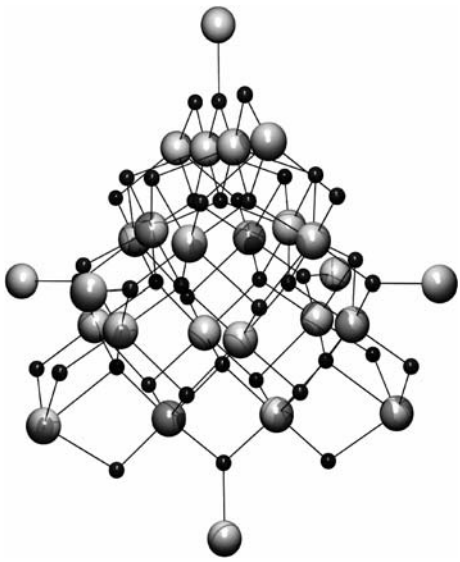

Fig. 16 PovRay representation of the core of the cluster $[Mn_{26}(pdol)_{12}(OMe)_{12}O_{16}(N_3)_6]$ (**32**). Code for atoms: *large grey*, Mn; *small black*, O

phase signals, but no peaks. No values for *S* and *D* have been reported thus far.

Reaction between $Mn(O_2CMe)_2 \cdot 4H_2O$, H_3tea and NEt_3 in MeCN results in the formation of the complex $[Mn_{16}(O_2CMe)_{16}(teaH)_{12}]$ (**33**, $[Mn_{16}$tea], Fig. 17) [75]. The structure comprises a loop of alternating Mn(III) and Mn(II) ions held together by $teaH^{2-}$ ligands, that describes a closed sinusoidal or saddle-like topology. Magnetisation measurements suggest a spin ground state of $S = 10$, with $D = -0.06\ cm^{-1}$. Given that ferromagnetic interactions between the metal centres would lead to a ground state of $S = 36$ and that antiferromagnetic interactions would give $S = 0$, this result is somewhat unusual. Therefore, both ferro- and antiferromagnetic interactions must be present and the competition between them results in the stabilisation of an intermediate spin value. $[Mn_{16}$tea] is the first example of a mixed valent Mn wheel and

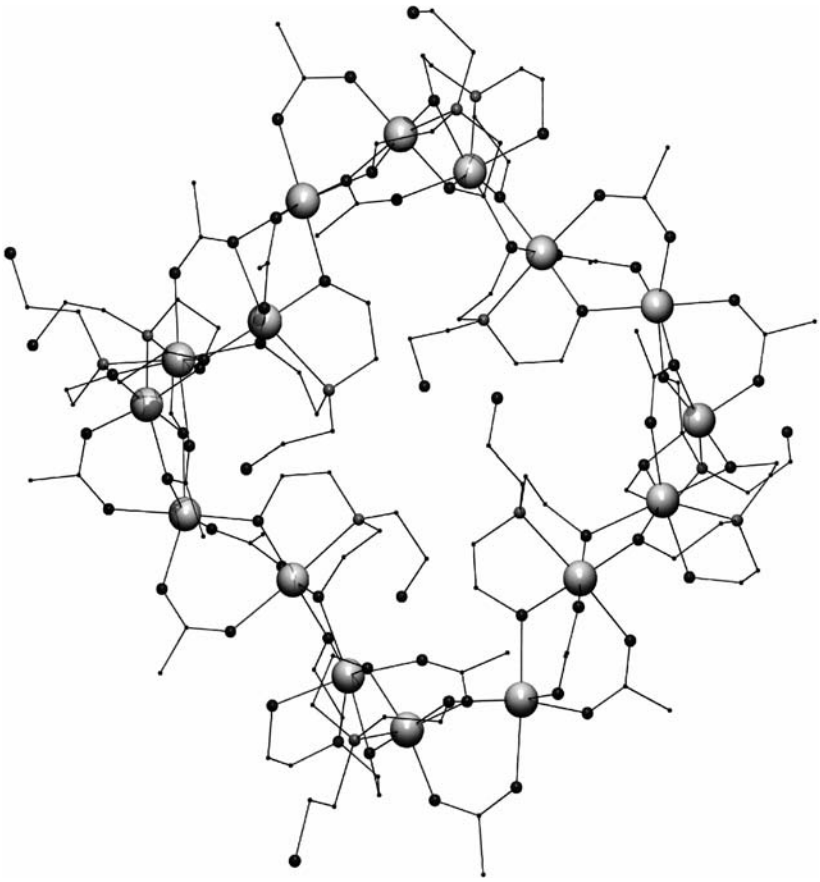

Fig. 17 PovRay representation of $[Mn_{16}(O_2CMe)_{16}(teaH)_{12}]$ (**33**). Hydrogen atoms are omitted for clarity. Code for atoms as in Fig. 4

the largest single-stranded Mn wheel reported to date. The second such wheel $[Mn_{12}(O_2CMe)_{14}(mda)_8]$ (**34**, $[Mn_{12}mda]$, Fig. 18) [79], made in a very similar fashion from the reaction of $Mn(O_2CMe)_2 \cdot 4H_2O$ with $mdaH_2$ and NEt_3 in MeCN, adopts a chair conformation. Again the Mn(III) and Mn(II) ions alternate around the loop, with competing ferro- and antiferromagnetic exchange interactions leading to an intermediate spin ground state of $S = 7$, with $D = -0.26\ cm^{-1}$. Here DFT calculations suggest that the ground state arises from weak ferromagnetic exchange between the two antiferromagnetically coupled $S = 7/2$ halves of the wheel.

Interestingly, the same complex and the *N*-ethyl-diethanolamine (H_2edea) analogue can also be made from the reaction of $[Mn_{12}O_{12}(O_2CMe)_{16}(H_2O)_4]$ (**1**) with H_2mda or H_2edea in CH_2Cl_2. Here, however, magnetisation measurements suggested spin ground states of $S = 8$ with with $D \approx -0.47\ cm^{-1}$ [88].

One of the simplest and most elegant one-pot syntheses is the reductive aggregation of MnO_4^-. Normally permanganate is used in comproportionation type reactions with another Mn salt, usually simple Mn(II) salts such as $MnCl_2$, $Mn(NO_3)_2$ or $Mn(O_2CMe)_2$, but recently it has been shown that the simple addition of a bridging ligand (e.g. a carboxylic acid) to an alcoholic solution of MnO_4^- results in the formation of beautiful clusters. The high oxidation state source is reduced by the solvent in the presence of excess ligand and as this process develops, the aggregation of the cluster occurs. For example, reaction of $TBAMnO_4$ with PhCOOH in MeOH produces the complex

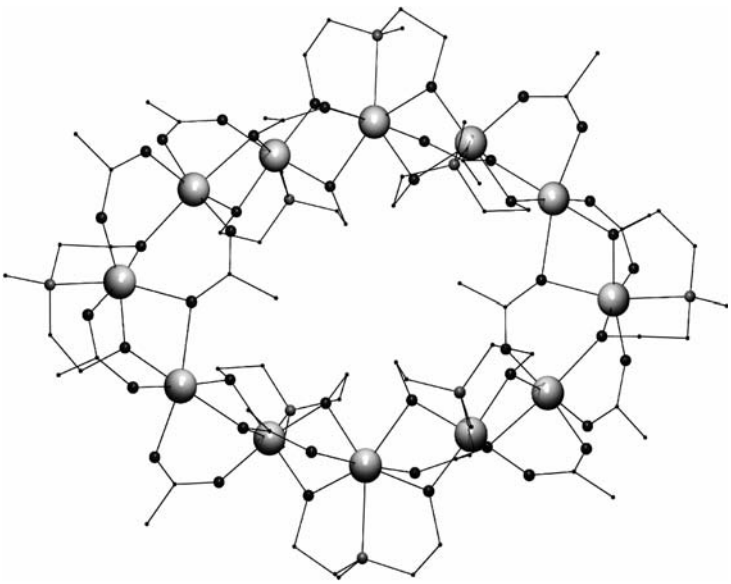

Fig. 18 PovRay representation of $[Mn_{12}(O_2CMe)_{14}(mda)_8]$ (**34**). Hydrogen atoms are omitted for clarity. Code for atoms as in Fig. 4

$(TBA)_2[Mn_{12}O_{12}(OMe)_2(O_2CPh)_{16}(H_2O)_2]$ (**35**, [Mn_{12}OMe], Fig. 19) [89]. The complex is a structural derivative of the $[Mn_{12}O_{12}(O_2CR)_{16}(H_2O)_4]$ family. It again has the same outer wheel of eight Mn(III) ions but this time the core is comprised of a central $[Mn^{IV}{}_4O_4(OMe)_2]^{6+}$ rhombus instead of a $[Mn^{IV}{}_4O_4]^{8+}$ cubane. The complex has a spin ground state of $S = 6$ with $D = -0.37\,cm^{-1}$. When the reaction is repeated using different carboxylic acids (phenylacetic acid, chloroacetic acid and bromoacetic acid) the obtained product is different: $[Mn_{16}O_{16}(OMe)_6(O_2CR)_{16}(MeOH)_6]$ ([Mn_{16}], R = $PhCH_2$ (**36**); R = $ClCH_2$ (**37**); R = $BrCH_2$ (**38**), Fig. 20) [90]. The structure is again very similar to [Mn_{12}], but now there is an outer non-planar wheel of ten Mn(III) ions encapsulating a $[Mn^{IV}{}_6O_6(OMe)_4]^{8+}$ core. The Mn(IV) ions are in a plane with the connecting oxides above and below that plane. Dc and ac magnetic susceptibility studies show the molecule to have a rather small spin ground state ($S \approx 2$), but no satisfactory fit of the magnetisation data could be obtained – probably because of the presence of many low-lying

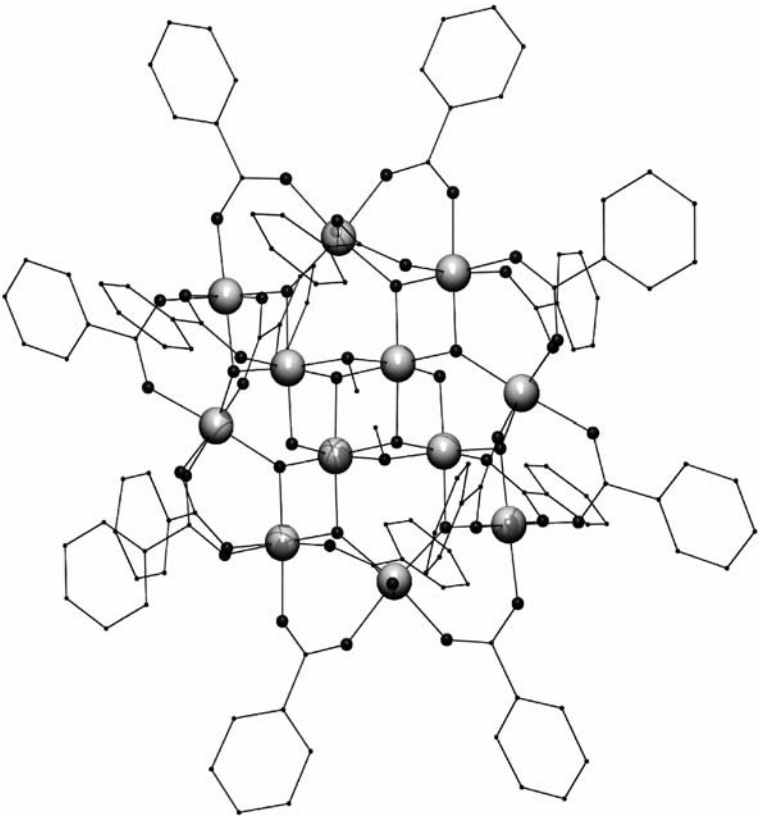

Fig. 19 PovRay representation of the complex anion of $(TBA)_2[Mn_{12}O_{12}(OMe)_2(O_2CPh)_{16}(H_2O)_2]$ (**35**). Hydrogen atoms are omitted for clarity. Code for atoms as in Fig. 4

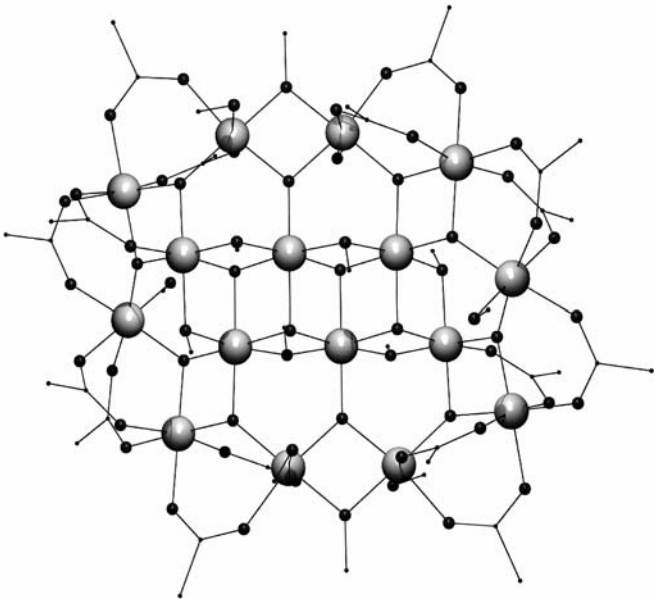

Fig. 20 PovRay representation of $[Mn_{16}O_{16}(OMe)_6(O_2CCBrH_2)_{16}(MeOH)_6]$ (**38**). Hydrogen and bromine atoms are omitted for clarity. Code for atoms as in Fig. 4

excited states. Despite the small ground state, sweep rate and temperature dependent hysteresis loops were observed below ~ 1.0 K suggesting that the complex must display appreciable ZFS within that ground state, most likely due to the near parallel alignment of the ten Jahn-Teller axes. Indeed, these molecules may well be the smallest spin SMMs known. The acetate analogue of these $[Mn_{16}]$ SMMs, $[Mn_{16}O_{16}(OMe)_6(O_2CMe)_{16}(MeOH)_3(H_2O)_3]$ (**39**) which was actually the first member of this family, was made somewhat differently from the reaction of $Mn(NO_3)_2 \cdot 6H_2O$, MeCOOH, and $TBAMnO_4$ in MeOH [91]. The magnetic properties reported for this complex appear somewhat different. Out-of-phase ac susceptibility signals were seen in the 3.9–4.6 K temperature range with the tail of a second peak appearing at ~ 2 K. This is in contrast to the other $[Mn_{16}]$ analogues where only the tail of the second peak is seen. Detailed studies of the acetate analogue (*S* and *D*) have yet to be reported.

Reaction of $MnBr_2 \cdot 4H_2O$ with biphenH_2 and NEt_3 in MeCN affords the complex $(Et_3NH)_2[Mn(CH_3CN)_4(H_2O)_2][Mn_{10}O_4(biphen)_4Br_{12}]$ ($[Mn_{10}$biphen], **40**, Fig. 21) [92]. The $[Mn^{III}{}_4Mn^{II}{}_6]$ decanuclear anion consists of an adamantine-like inner core connected to four peripheral Mn(II) ions. The overall topology resembles the metal chalcogenide clusters of general formula $[E_4M_{10}(E'R)_{16}]^{4-}$ whose structures are based on four fused adamantine units [93]. Magnetic studies show the decanuclear anion to have an $S = 12$ ground state with $D = -0.037\ cm^{-1}$.

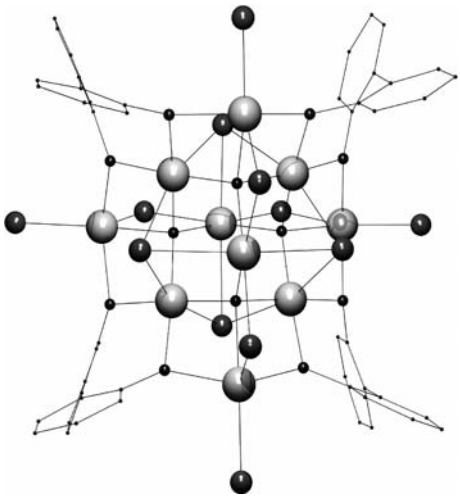

Fig. 21 PovRay representation of the decanuclear cluster anion of $(Et_3NH)_2[Mn(CH_3CN)_4(H_2O)_2][Mn_{10}O_4(biphen)_4Br_{12}]$ (**40**). Hydrogen atoms are omitted for clarity. *Largest grey*, Mn; *second largest grey*, Br; *medium black*, O; *rest*, C

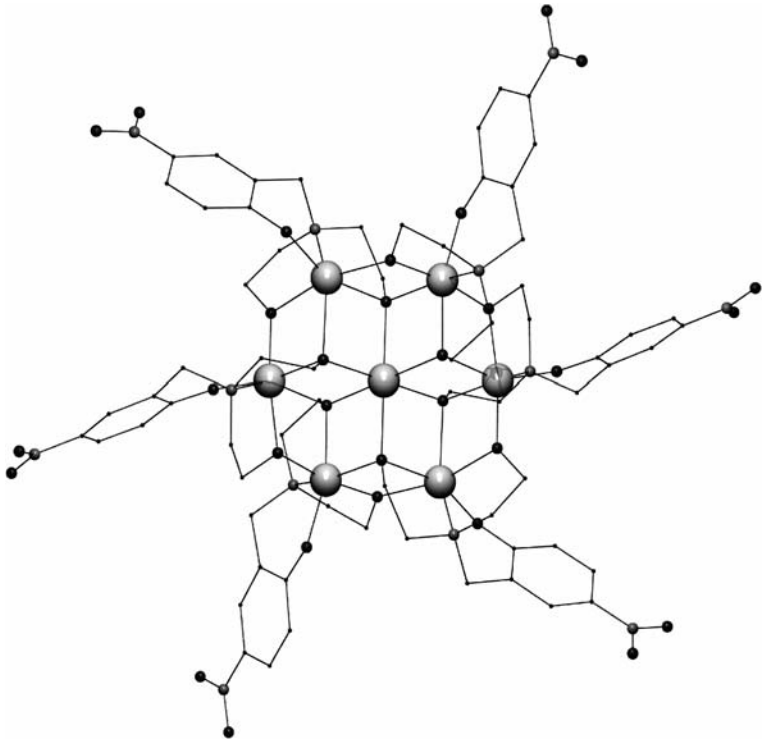

Fig. 22 PovRay representation of $[Mn_7(L2)_6]$ (**41**). Hydrogen atoms are omitted for clarity. Code for atoms as in Fig. 4

Reaction of the ligand *N*-(2-hydroxy-5-nitrobenzyl)iminodiethanol (H_3L2) with $MnCl_2 \cdot 4H_2O$ in MeOH gives the heptanuclear complex $[Mn^{III}_4Mn^{II}_3(L2)_6]$ ([Mn7], **41**, Fig. 22) [94]. The structure comprises a centred hexanuclear wheel in which the central ion and two peripheral ions are the Mn(II) ions. Magnetisation data collected in the ranges 1.8–5.0 K and 5–30 kG were fitted for $S = 21/2$ and $D = -0.20\ cm^{-1}$. This ground state can be rationalised by assuming an antiferromagnetic interaction between the central Mn ion and the six peripheral Mn(II) and Mn(III) ions. The metal topology of this species has been seen before in Mn and Fe cluster chemistry, but none of these other complexes have been reported as SMMs [95, 96].

2.10 A New Family of Hexanuclear SMMs

Reaction of $Mn(O_2CR)_2 \cdot 4H_2O$ (R = Me, Ph) with H_2salox and $TBAMnO_4$ in EtOH leads to the isolation of the hexanuclear complex $[Mn_6O_2(O_2CMe)_2(salox)_6(EtOH)_4]$ (**42**, [Mn_6salox], Fig. 23) and its benzoate analogue [97]. The core of the complex consists of two $[Mn^{III}_3O]$ triangles linked together by oximato oxygen atoms to give a near planar $[Mn_6O_2(OR)_2]^{12+}$ unit. Competing ferro- and antiferromagnetic interactions lead to the stabilisation of an $S = 4$ ground state, with $D = -1.22\ cm^{-1}$. The observed anisotropy is the largest displayed by any polynuclear Mn (> [Mn_2]) SMM and presumably arises from the parallel alignment of the Jahn-Teller axes. The same reaction can be performed successfully with a series of other carboxylate ligands, and thus this group of complexes already constitutes the beginning of a new family of SMMs.

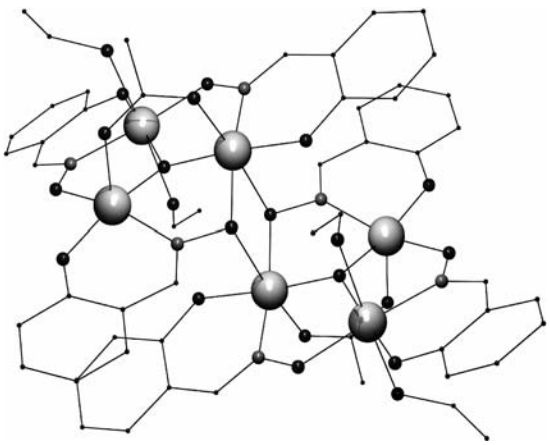

Fig. 23 PovRay representation of $[Mn_6O_2(O_2CMe)_2(salox)_6(EtOH)_4]$ (**42**). Hydrogen atoms are omitted for clarity. Code for atoms as in Fig. 4

2.11 Use of Schiff Bases as Ligands to Prepare SMMs

The application of Schiff base ligands is vast and spans diverse areas of coordination chemistry [98–101], but this rarely includes the preparation of SMMs [102]. The first such compound with Mn was prepared from the reaction of the ligand salicylidene-2-ethanolamine (H_2sal) with $MnCl_2 \cdot 4H_2O$ in EtOH, which produces the tetranuclear complex [$Mn_4Cl_4sal_4$] (**43**, [Mn_4sal], Fig. 24) [103]. The compound comprises a planar square of four Mn(III) ions linked together along each edge by one oxygen and one halide. The Mn ions are coupled ferromagnetically to give a spin ground state of $S = 8$, with $D = -0.10\ cm^{-1}$.

The smallest example of a Mn SMM, [Mn_2(saltmen)$_2$(ReO_4)$_2$] (**44**, [Mn_2salt], Fig. 25), also contains a Schiff base ligand, in addition to two Mn(III) ions and two diamagnetic Re(VII) ions. The complex is formed by the reaction of $Mn(O_2CMe)_2 \cdot 4H_2O$ with H_2saltmen and $NaReO_4$ in $MeOH/H_2O$ [104]. The complex can be described as a linear line of four metal ions with the two Mn(III) ions in the centre and the two Re(VII) ions on the periphery. The two Mn ions couple ferromagnetically to give a spin ground

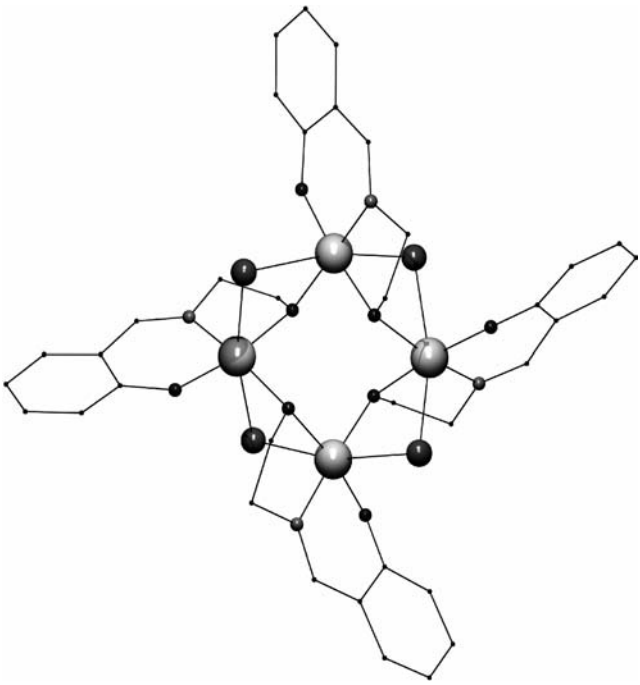

Fig. 24 PovRay representation of [$Mn_4Cl_4sal_4$] (**43**). Hydrogen atoms are omitted for clarity. Code for atoms as in Fig. 4

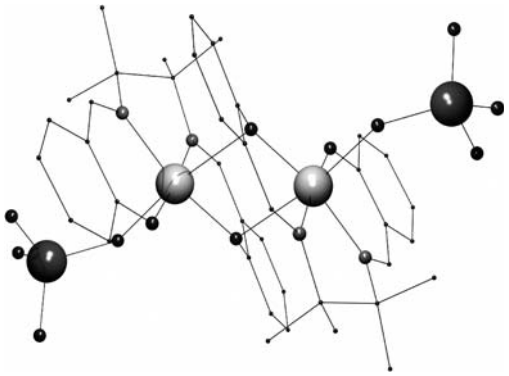

Fig. 25 PovRay representation of $[Mn_2(saltmen)_2(ReO_4)_2]$ (**44**). Hydrogen atoms are omitted for clarity. Code for atoms: *large dark grey*, Re; *large light grey*, Mn; *medium black*, O; *medium grey*, N; *rest*, C

state of $S = 4$, with $D = -1.2\ cm^{-1}$. Single crystal measurements at temperatures below 1 K show the sweep-rate and temperature dependent hysteresis loops indicative of SMM behaviour, though like the previous dinuclear SMM, [Mn_2thme], tunnelling at H = 0 appears to be very fast.

2.12 Use of MnF_3 as a Synthon in the Formation of SMMs

The only "simple", readily available source of Mn(III) is MnF_3. However MnF_3 is only sparingly soluble in common organic solvents and this has, so far, limited its use as a source of Mn(III). In addition F^- ions would be expected to promote rather weak exchange between metal centres (cf. hydroxide), although they happily function as terminal ligands. The first "problem" can be easily solved by one of two methods, as demonstrated by the formation of the only MnF_3-based SMM synthesised $[Mn_{26}O_{17}(OH)_8(OMe)_4F_{10}(Bta)_{22}(MeOH)_{14}(H_2O)_2]$ (**45**, [Mn_{26}F], Fig. 26) [105]. Originally the insolubility of the MnF_3 was overcome through the use of a "melt" type reaction whereby the MnF_3 and organic ligand (Hbta) were mixed together in a Schlenk tube under an inert atmosphere. The mixture was heated to the melting point of the organic ligand (in this case $\sim 100\,°C$), which acted as solvent, and the MnF_3 then dissolved as the reaction proceeded. The "melted" product could then be crystallised from alcohol to give the final product, **45**. It was later found that the same product could be obtained from a much simpler reaction scheme. Simply reacting MnF_3 with BtaH in boiling MeOH produces [Mn_{26}F] directly, in much larger yield. The compound is a complicated array of metal tetrahedra linked by a combination of oxides, hydroxides and methoxides, into a topology that loosely describes a half-wheel or ellipse. Magnetisation measurements were fit to give a spin

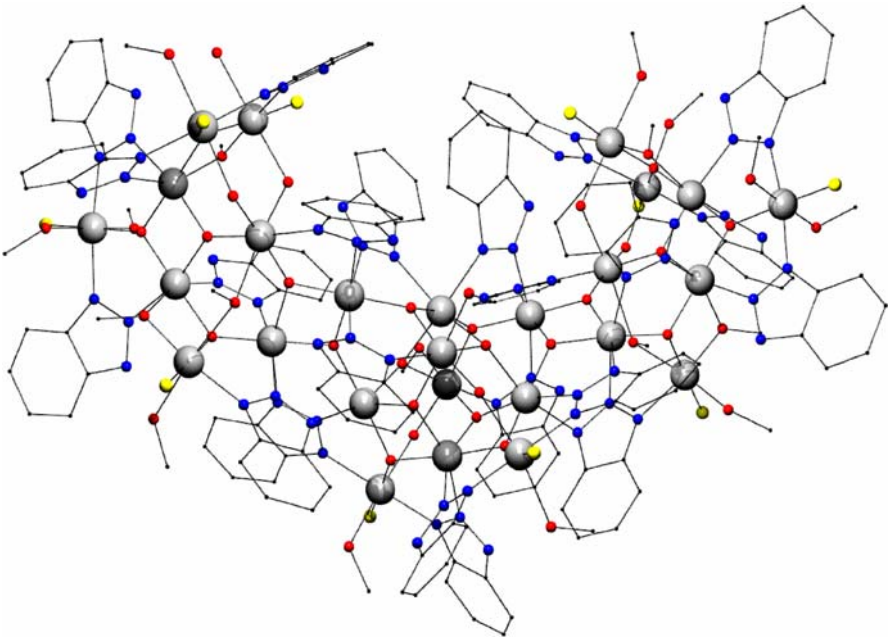

Fig. 26 PovRay representation of the molecular cluster $[Mn_{26}O_{17}(OH)_8(OMe)_4F_{10}(Bta)_{22}(MeOH)_{14}(H_2O)_2]$ (**45**). Hydrogen atoms are omitted for clarity. Code for atoms: *large grey*, Mn; *red*, O; *blue*, N; *yellow*, F; *rest*, C

ground state of $S = 4$, with $D = -0.90\ cm^{-1}$. As with many "large" SMMs, single crystal measurements show that the hysteresis loops do not display the step-like features associated with QTM, but instead appear smooth and typical for a cluster with a distribution of energy barriers. The steps may well be present but simply broadened or smeared out as a result of the inherent disorder associated with such a large structure, which results in a distribution of Mn environments.

2.13 The Family of Distorted Cubane $[Mn^{IV}Mn^{III}_3O_3X]^{6+}$ SMMs

This group of high-spin Mn clusters constitutes the second largest and second most studied family of SMMs. In general, these clusters contain a $[Mn^{IV}Mn^{III}{}_3(\mu_3-O)_3]^{7+}$ partial or distorted cubane whose "vacant" vertex is occupied by a η^1,μ_3-ligand "X" (where X = halide, N_3^-, etc.) to give an overall $[Mn^{IV}Mn^{III}{}_3(\mu_3-O)_3X]^{6+}$ core. The first member of this family was the complex $(HIm)_2[Mn_4O_3Cl_6(O_2CMe)_3(Im)]$ (**46**, Fig. 27) [106] and for many years the sole interest of this class of compounds remained their consideration as models for the water oxidation centre of photosystem II. They were later discovered as high-spin molecules that display slow relaxation of the magnetisa-

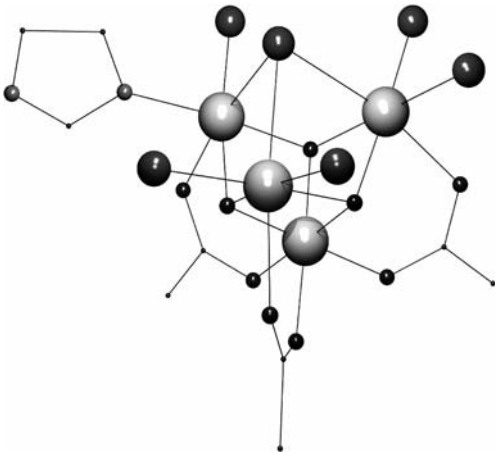

Fig. 27 PovRay representation of the anion of $(HIm)_2[Mn_4O_3Cl_6(O_2CMe)_3(Im)]$ (**46**). Hydrogen atoms are omitted for clarity. Code for atoms as in Fig. 4

tion. Antiferromagnetic exchange between the Mn(IV) ion ($S = 3/2$) and the three Mn(III) ions ($S = 2$) leads to the stabilisation of an $S = 9/2$ ground state. After the preparation of complex **46** followed several reports on the synthesis of various analogues containing the same overall topology, but with different combinations of $\mu_2 - RCO_2$ (R = Me, Et, Ph, etc.) and terminal ligands (Im, py, etc.). In most cases, the products were formed by carboxylate abstraction from polymeric "$Mn(O_2CMe)_3$" arrays or polynuclear oxo/carboxylate Mn complexes, by use of Me_3SiCl, triggering a disproportionation reaction that resulted in the formation of the high-valent cubanes and Mn(II) side products [107, 108]. In some cases, derivatives with other carboxylates were obtained by carboxylate metathesis [109]. An interesting addition to this family was the complex of formula $[Mn_4O_3Cl(O_2CMe)_3(dbm)_3]$ (**47**), prepared in a similar manner to that above but using a starting material containing the chelating ligand dbm^- [110]. Complex **47** was the first member of this family for which SMM properties were discovered [111].

An important breakthrough was the preparation of the analogue $[Mn_4O_3(O_2CMe)_4(dbm)_3]$ (**48**) by controlled potential electrolysis of the butterfly-type complex $[Mn_4O_2(O_2CMe)_6(py)_2(dbm)_2]$ [112]. Complex **48** (which was subsequently also prepared from a simple one-pot reaction [113]) was the first derivative of the series not to contain halides in the core. Instead, one of the acetate groups now acts as the η^1,μ_3-ligand "X". This acetate group is amenable to selective substitution by other η^1,μ_3-ligands, and thus complex **48** is the basis from which a large group of compounds of formulae $[Mn_4O_3X(O_2CMe)_3(dbm)_3]$ (X = F, Br, MeO, OH, NO_3, N_3, NCO, etc.) [113–115] can be made. In addition, the preparation of complex **48** could be reproduced with a variety of carboxylates, leading to an analogous series of

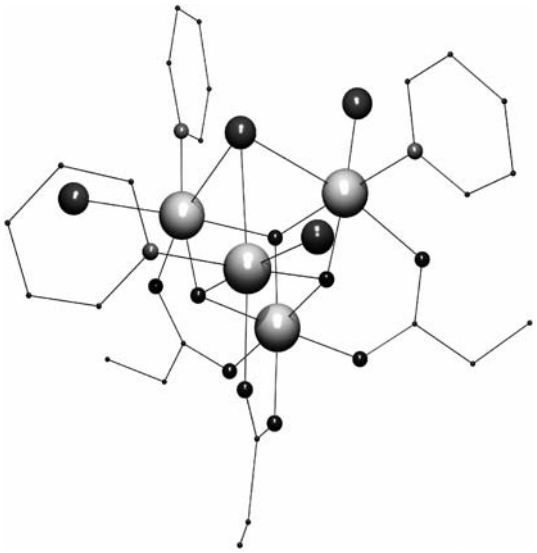

Fig. 28 PovRay representation of $[Mn_4O_3Cl_4(O_2CEt)_3(py)_3]$ (**49**). Hydrogen atoms are omitted for clarity. Code for atoms as in Fig. 4

compounds of formula $[Mn_4O_3(O_2CPh-R)_4(dbm)_3]$ (R = H, *p*-Me, *p*-OMe, *o*-Cl) [116, 117]. These families of compounds have proved highly useful for the detailed study of SMM properties. For example, the latter family established a relationship between the molecular symmetry (or degree of distortion) of the cluster with the dynamics of relaxation of magnetisation through quantum tunnelling [118]. In another instance, some compounds of the series $[Mn_4O_3X(O_2CMe)_3(dbm)_3]$ were studied by INS in order to determine the influence of the species "X" on the various parameters defining the ZFS [119]. More recently, the magnetic properties of one of the oldest members of this large group, $[Mn_4O_3Cl_4(O_2CEt)_3(py)_3]$ (**49**) [108], were investigated in detail. This complex ([Mn_4prop], Fig. 28) crystallises in the hexagonal space group R-3 with pairs of [Mn_4prop] molecules lying head to head on a crystallographic S_6 axis. The two units are held together by six C – H · · · Cl hydrogen bonds between the pyridine rings on one [Mn_4prop] and the Cl^- ions on the other to form $[Mn_4prop]_2$ dimers. This has an important consequence on the observed magnetic properties as these H-bonds introduce a weak inter-molecular antiferromagnetic exchange interaction that greatly changes the observed quantum behaviour [120, 121]. Each [Mn_4prop] unit acts as an exchange bias upon its neighbour which shifts the tunnel resonances from zero field, where they are seen in the isolated cubanes. The absence of tunnelling at zero field is an important issue, if SMMs are to be considered as serious candidates for information storage.

3
SMMs of Iron

Iron coordination clusters constitute the second largest family of SMMs after the group of manganese aggregates. In this context, the properties of some compounds of Fe(III) have been described in detail in a recent review [41]. However, a few polynuclear complexes of iron in the oxidation state 2 + have also been shown to display slow relaxation of the magnetisation. The proliferation of SMMs of this metal has benefited from the fact that synthesis of high-spin iron cages had been an intense area of investigation for a long time before the discovery of magnetic bistability in molecules. Such early work stemmed from (i) the quest for building blocks for the construction of molecule-based magnetic materials, (ii) the interest in modelling the properties of ferritin (the iron storage protein in cells) [122], (iii) the use of the synthetic analogue approach for the study of iron containing enzymes [123].

3.1
The $[Fe_8O_2(OH)_{12}(tacn)_6]^{8+}$ (50); The Prototype Fe SMM

It is generally agreed that the complex cation $[Fe_8O_2(OH)_{12}(tacn)_6]^{8+}$ (**50**, Fig. 29) was the first properly identified SMM of iron, and it was the second molecular species after the class of $[Mn_{12}]$ clusters, where this behaviour was firmly established [124]. First evidence of superparamagnetic relaxation phenomena arising from nanosised Fe(III) molecular species had been suggested by Mössbauer spectroscopy on a $[Fe_{11}]$ and a $[Fe_{16}Mn]$ cluster [125]. Such dynamics of relaxation were determined with a measuring time of $\sim 10^{-8}$ s and the existence of intramolecular magnetic ordering was attributed to the pseudo three-dimensional structure of the cluster. The ground spin state of these clusters, however, was not unambiguously determined, and it was proven later with the $[Mn_{12}]$ family and subsequently with the $[Fe_8]$ cluster **50** that a "globular" shape was not responsible for the slow relaxation in molecular species.

As with the case of $[Mn_{12}OAc]$ (**1**), the preparation of cluster **50** was reported more than a decade before its properties as SMM were discovered [126]. Obtained from the reaction of $[Fe(tacn)Cl_3]$ with NaBr in H_2O and formulated as $[Fe_8O_2(OH)_{12}(tacn)_6]Br_8$, it was claimed to be the first oxo/hydroxo bridged Fe(III) cluster with a nuclearity higher than three. Trapping such discreet species in aqueous medium without rapid precipitation of insoluble Fe_2O_3 is very difficult and can only be achieved by blocking core growth with chelating ligands while carefully controlling the pH. Since then, reports of polynuclear oxide/hydroxide iron clusters have become increasingly frequent [127], in particular after organic solvents started to be used for the syntheses [85, 128, 129]. The structure of **50** (Fig. 29) shows a central unit of four Fe(III) ions linked by two $\mu_3 - O^{2-}$ ligands in a "butterfly" ar-

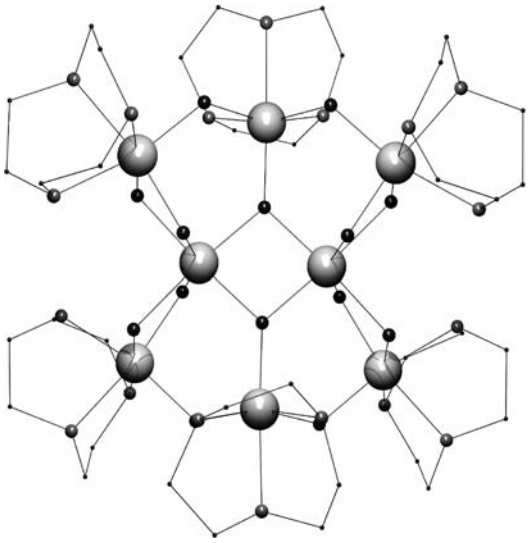

Fig. 29 PovRay representation of the complex cation $[Fe_8O_2(OH)_{12}(tacn)_6]^{8+}$ (**50**). Hydrogen atoms are omitted for clarity. Code for atoms: *largest grey*, Fe; *medium black*, O; *medium grey*, N; *rest*, C

rangement. Bound to the metals of this central core *via* hydroxide bridges are four additional Fe(III) centres. These and the wing metals of the "butterfly" are capped by tridentate tacn (triazacyclononane) ligands. A pioneering study using the irreducible tensor operator (ITO) approach for the calculation of the spin Hamiltonian matrix and magnetic susceptibility of large clusters allowed the spin value of the ground state of **50** ($S = 10$) to be established [130]. This spin number is the consequence of spin frustration effects arising from the presence of several competing antiferromagnetic interactions within the cluster. The superparamagnetic-like behaviour of **50** was established by use of both, Mössbauer and AC magnetic susceptibility measurements [124], and the electronic nature of the ground state was described in detail by use of HF EPR, polarised neutron diffraction (PND) [131] and INS [132]. Compound **50** was only the second system to show hysteresis of molecular origin and displaying quantum tunnelling of the magnetisation [133]. The mechanism of the quantum tunnelling in **50** has been investigated in detail [124, 134–136], and this work has been paramount in the understanding of this phenomenon, inherent to SMMs.

The breakthroughs described above have turned the octanuclear iron cluster **50** into a major reference molecule within the family of SMMs. This has undoubtedly stimulated the search for other polynuclear iron clusters displaying similar properties. Following this, a growing group of compounds has been prepared or revisited, the study of which has thrown light to other important aspects on the physical properties of SMMs. The number of iron

clusters displaying this behaviour remains, however, very small when compared with the existing examples based on Mn.

3.2 $[Fe_{19}(metheidi)_{10}(OH)_4O_6(H_2O)_{12}](NO_3)$ (51); The Largest Nuclearity and Spin Fe SMM

The complex $[Fe_{19}(metheidi)_{10}(OH)_4O_6(H_2O)_{12}](NO_3)$ (**51**, Fig. 30) belongs to a family of $[Fe^{III}_{19}]$ clusters whose first example was made in 1992 within a pair of co-crystallised Fe_{17}/Fe_{19} species. At the time this was a rare example of a polynuclear hydroxo/oxo/iron aggregate stabilised by peripheral organic ligands, made in order to mimic the properties of ferritin and still is the largest synthesised since then. The multi-dentate ligand used to prevent core growth into an infinite "$Fe(OH)_3$" array was H_3heidi (Scheme 1). Despite the ambiguities related to the fact that both components of this pair could not be studied separately, it was established that the spin ground state of at least one of them was $S = 33/2$. This remained the largest spin ground

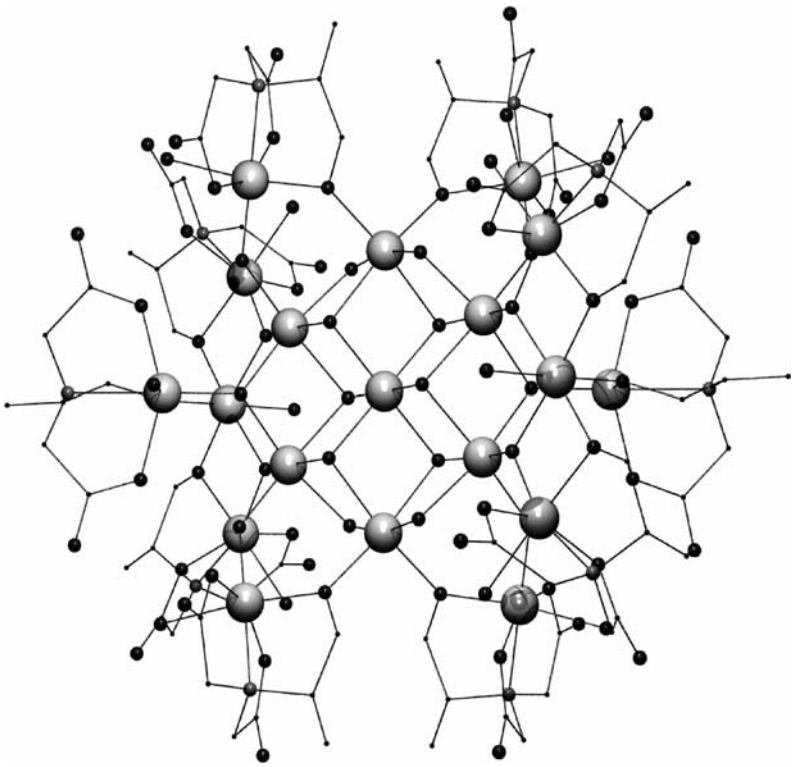

Fig. 30 PovRay representation of $[Fe_{19}(metheidi)_{10}(OH)_4O_6(H_2O)_{12}](NO_3)$ (**51**). Hydrogen atoms are omitted for clarity. Code for atoms as in Fig. 29

state observed in any molecular species for some time [86]. Although it could be shown that the Fe_{17}/Fe_{19} pair was responsible for hysteresis phenomena at low temperatures [137], its molecular origin was not confirmed until the independent synthesis of only one member of the pair in form of compound **51**, which led to the proper characterisation of the largest iron SMM *hitherto* studied [138]. Such description was made by means of powder and single-crystal bulk magnetisation studies, as well as HF-EPR. Stabilisation of **51** as a unique compound was achieved by introducing a small modification to the H_3heidi ligand (Scheme 1). The structure of this cluster (Fig. 30) can be described as a central disk-like $[Fe_7(\mu_3-OH)_4(\mu_2-OH)_4((\mu_3-O)Fe)_2]^{13+}$ unit, surrounded by Fe/metheidi units and bound to it by a combination of μ_2-OH, μ_3-O, and alkoxo groups. Recent studies have revealed intercluster antiferromagnetic ordering within the lattice of compound **51** [139]. This represents an important contribution to the understanding of long range effects in SMMs – a topic of great relevance in this field [120, 140].

3.3
$[Fe_4(OR)_6(dpm)_6]$; Insights into the Origin of ZFS

The tetranuclear Fe(III) cluster $[Fe_4(OMe)_6(dpm)_6]$ (**52**, Fig. 31) is the smallest nuclearity Fe SMM. Compound **52** is one of a number of alkoxide bridged Fe aggregates stabilised by β-diketones [141, 142]. The identity of the isolated product depends on the exact type of chelate and the solvent system employed during the reaction and crystallisation processes. Complex **52** was prepared from the reaction in MeOH of $FeCl_3$ with Hdpm in the presence of NaOMe, followed by recrystallisation from Et_2O/MeOH [143]. The structure of this cluster comprises a centred triangle of four Fe(III) ions bridged by six μ_2-OMe^- ligands, with the peripheral Fe ions each chelated by two dpm^- ligands. The nearest and second-nearest neighbour magnetic interactions between iron centres ($S = 5/2$) within the molecule can be modelled using the Heisenberg spin-Hamiltonian $H = -2J(S_1S_2 + S_1S_3 + S_1S_4) - J'(S_2S_3 + S_2S_4 + S_3S_4)$, where S_1 is the spin of the central metal in Fig. 31 and the S_2 to S_4 are the spins of the other metals. The $\chi_M T$ vs. T curve obtained from bulk magnetisation measurements is typical of a ferrimagnetic system and a good fit was obtained for parameters $g = 1.97$, $J = -10.5\ cm^{-1}$ and $J' = 0.6\ cm^{-1}$, leading to an $S = 5$ spin ground state, in addition to a ZFS term of $D = -0.20\ cm^{-1}$. The above description was confirmed by a HF-EPR investigation whereas dynamic susceptibility measurements demonstrated that compound **52** exhibits slow relaxation of its magnetisation. This complex being among the smallest polynuclear SMMs observed to date, it could be subject to a semi-quantitative treatment in the characterisation of its ZFS parameters *via* angular-overlap model (AOM) calculations. The single ion and spin-spin contributions to the total D parameter of the cluster were established, and these results then helped to rationalise the enhanced magnetoanisotropy ($D = -0.4\ cm^{-1}$) of

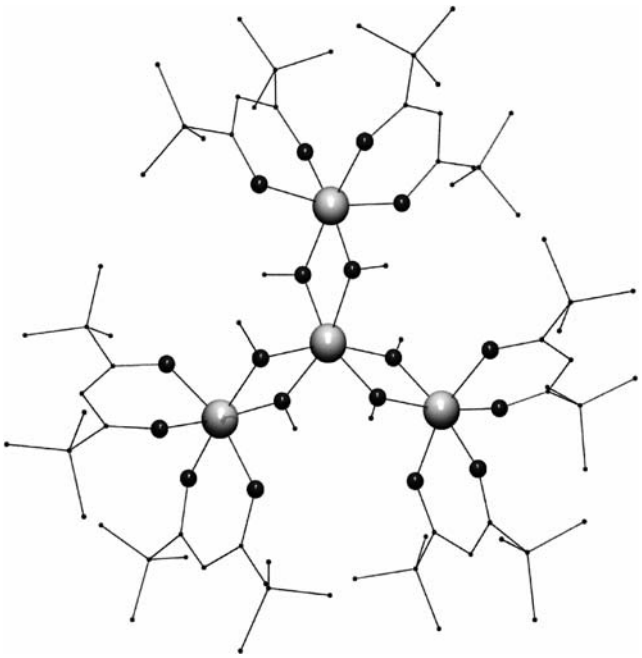

Fig. 31 PovRay representation of $[Fe_4(OMe)_6(dpm)_6]$ (**52**). Hydrogen atoms are omitted for clarity. Code for atoms as in Fig. 29

the analogous cluster $[Fe_4(thme)_2(dpm)_6]$ (**53**), obtained from **52** by ligand substitution [144]. Compound **53** exhibits hysteresis loops featuring very marked steps as a result of increased relaxation by quantum tunnelling, occurring at certain values of the external magnetic fields. The related complex $[Fe_4(thme)_2(CH_3CH_2CH_2OH)_6Cl_6]$ (**54**) [145], reported simultaneously as **53**, is also a SMM. It was made from the reaction of $FeCl_3$, H_3thme and NaOMe in alcohol. This compound was proven to undergo quantum tunnelling of the magnetisation, but the hysteresis loops do not show the clear steps seen in **53**. The smearing out of the steps has been ascribed to a combination of the disorder associated with the terminal alcohols and the presence of weak ferromagnetic ordering within the crystal, mediated through a network of intermolecular Cl · · · Cl interactions. Such interactions are not present in **53**.

3.4
Control of Anisotropy in Ferrous Cubes $[Fe_4(sae)_4(MeOH)_4]$ (55)

Tetranuclear clusters with a cubane structure are common in 3*d*-metal coordination chemistry. The relative disposition of orbitals from metal and bridging ligands within such structures favour orthogonality between metallic magnetic orbitals and consequently, ferromagnetic interactions leading

to high spin ground states. Thus, ferromagnetic $[Cu_4]$ [146], $[Ni_4]$ [147], $[Mn_4]$ [113], $[Fe_4]$ [148] or $[Co_4]$ [149] cubane complexes have been described.

The first alkoxide bridged ferrous cube was reported in 1992 [150]; however, no details of its magnetisation properties were given. The complex $[Fe_4(sae)_4(MeOH)_4]$ (**55**) is the first ferrous cubane identified as a SMM [151]. The core of the cube (Fig. 32) is formed by four Fe(II) ions and the μ_3-alkoxide moiety of four sae^{2-} ligands which also chelate one metal each through the remaining N and O donor atoms. The sixth coordination sites on the iron ions are completed by MeOH molecules. The formation of **55** takes place through a self assembly process following the reaction in methanol between $FeCl_2$ and H_2sae in strictly anaerobic conditions.

The Fe – O – Fe bridging angles within the core of **55** fall within the range expected to facilitate ferromagnetic superexchange interactions between the Fe(II) centres ($S = 2$). This results in a total spin ground state of $S = 8$. Ac magnetic susceptibility measurements revealed that this complex exhibits slow relaxation of the magnetisation. The D parameter was subsequently estimated to be $-0.64\ cm^{-1}$, from fitting variable field reduced magnetisation data. The importance of a negative value of D for observing the properties of SMMs was elegantly shown by a study of a family of compounds related to complex **55** [102]. This series of complexes was prepared using three derivatives of H_2sae and three forms of the related ligand H_2sap. All complexes being

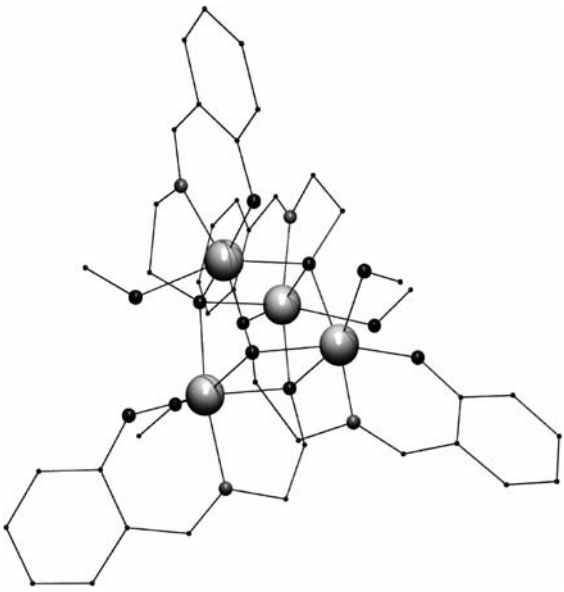

Fig. 32 PovRay representation of $[Fe_4(sae)_4(MeOH)_4]$ (**55**). Hydrogen atoms are omitted for clarity. Code for atoms as in Fig. 29

structurally analogous, they are divided into two groups that crystallise in the space groups $P\bar{1}$ and $I4_1/a$, respectively, depending on the type of ligand. The two groups present small differences in the JT distortions of the octahedral coordination geometry around Fe(II). The six complexes are all ferromagnetically coupled and therefore, display an $S = 8$ spin ground state, but the structural differences induced by the two types of ligands cause the ZFS D parameter for the complexes of both groups to be of opposite sign. Complexes with the H_2sae ligand have negative D and thus behave as SMMs, whereas the other group of compounds possess a positive D value and do not show SMM behaviour. In all cases, AOM calculations allowed the determination of the single ion D values in both groups of compounds and the total D values could be rationalised from the crystallographic symmetry of each system.

3.5 $[Fe_9(N_3)_2(O_2CMe)_8(pdol)_4]$ (56); An Azido Bridged Fe(II) SMM

The compound $[Fe_9(N_3)_2(O_2CMe)_8(pdol)_4]$ (**56**) is the first crystallographically characterised nonanuclear Fe(II) cluster [152]. This molecule (Fig. 33) comprises two groups of four Fe(II) centres, linked *via* a central Fe(II) by four $pdol^{2-}$ ligands. Within each group, the Fe(II) atoms are bridged by a rare $\mu_4 - N_3^-$ ion and four $\mu_2 - OAc^-$ ligands. This complex was prepared from the structurally related cluster $[Fe_9(OH)_2(O_2CMe)_8(pdol)_4]$

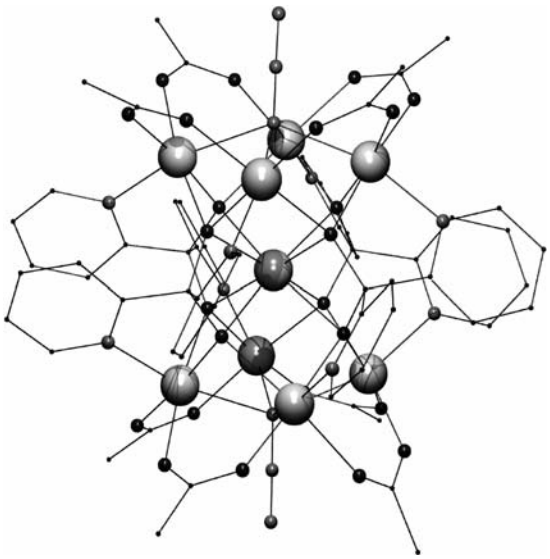

Fig. 33 PovRay representation of $[Fe_9(N_3)_2(O_2CMe)_8(pdol)_4]$ (**56**). Hydrogen atoms are omitted for clarity. Code for atoms as in Fig. 29

(**57**) *via* the selective replacement of two $\mu_4 - OH^-$ ligands by $\mu_4 - N_3^-$ groups. This synthetic approach had been previously implemented successfully for the preparation of the Co(II) and Ni(II) analogues of **56** from the corresponding hydroxide parent complexes [153, 154]. This led to the formation of clusters that exhibit spin numbers 7 and 9 times higher, respectively, than their corresponding precursors [153, 155]. The reason for this dramatic increase of spin is that the end-on $\mu_4 - N_3^-$ bridge induces ferromagnetic exchange interactions that previously were antiferromagnetic. However, neither the $[Co_9]$ nor the $[Ni_9]$ cluster show SMM behaviour. Bulk magnetisation measurements show that the $[Fe_9]$ congener (**56**) also possesses a high spin ground state number ($S = 14$), and the presence of an out-of-phase ac signal indicates that this compound exhibits slow relaxation of the magnetisation and therefore behaves as an SMM. This system is an excellent example of where chemistry has been wisely used for the design of a molecular species with desired properties, in this case the generation of a high-spin ground state through N_3^- ligand substitution.

3.6 $[Fe_{10}Na_2O_6(OH)_4(O_2CPh)_{10}(chp)_6(H_2O)_2(Me_2CO)_2]$ (58); A Decanuclear Fe SMM with $S = 11$

The magnetic properties of the compound $[Fe_{10}Na_2O_6(OH)_4(O_2CPh)_{10}(chp)_6(H_2O)_2(Me_2CO)_2]$ (**58**) were revisited 5 years after it was first reported [156]. The preparation of this complex was the result of a programme aimed at

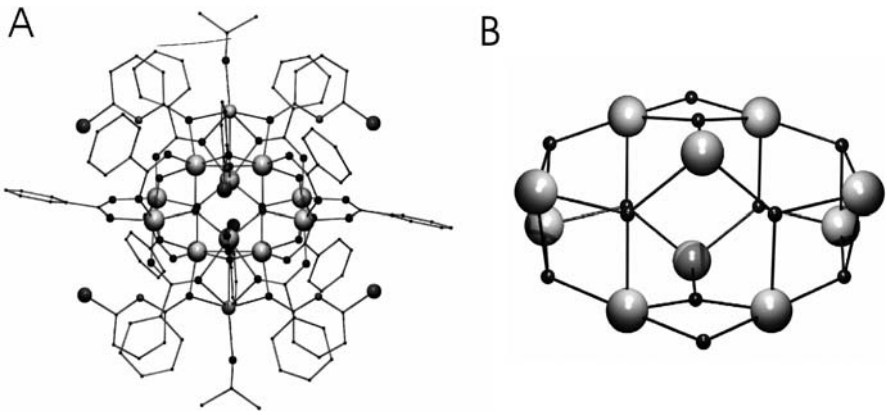

Fig. 34 **A** PovRay representation of the molecular cluster $[Fe_{10}Na_2O_6(OH)_4(O_2CPh)_{10}(chp)_6(H_2O)_2(Me_2CO)_2]$ (**58**). Hydrogen atoms are omitted for clarity. **B** Representation of the $[Fe_{10}O_{12}]$ core of the cluster. Code for atoms: *largest grey*, Fe; *second largest dark grey*, Cl; *second largest light grey*, Na; *medium black*, O; *medium grey*, N; *rest*, C

the formation of polynuclear metal clusters containing a combination of carboxylate and pyridonate ligands [32]. Crystals of **58** can be obtained from the addition of acetone to the filtrate resulting from the reaction between the dimer $[NEt_4]_2[Fe_2OCl_6]$, NaO_2CPh and Na(chp) in acetonitrile. The structure of the cluster (Fig. 34A) consists of a heterometallic aggregate of ten Fe(III) centres and two Na^+ ions, bridged by two μ_4-oxo, four μ_3-oxo and four μ_3-hydroxo ligands, in addition to bridging benzoate and chp^- ligands. The core (Fig. 34B) can be described as two distorted $[Fe_6O_6]^{6+}$ hexagonal prisms sharing one "square" face. Original susceptibility and reduced magnetisation studies led to the conclusion that the spin ground state is $S = 11$, as a result of spin frustration caused by competing antiferromagnetic interactions within the cluster. During the re-examination of the magnetic properties of **58**, it was found that this cluster is an SMM and the intramolecular magnetic exchange was properly described by use of a Monte Carlo methodology [24]. A good fit of the experimental $\chi_M T$ versus T curve could be obtained for $J_1 = -22\ cm^{-1}$, $J_2 = -6.5\ cm^{-1}$ and $J_3 = -5\ cm^{-1}$, where J_1, J_2 and J_3 are the coupling constants describing the Fe···Fe interactions mediated through two oxygen atoms, a single hydroxide group and a single oxide bridge, respectively.

3.7 $(NEt_4)[Fe_{11}O_4(O_2CPh)_{10}(thme)_4(dmhp)_2Cl_4]$ (59); An Undecanuclear Fe(III) SMM

Complex **59** is only the second class of undecanuclear iron clusters described in the literature [157] and it exhibits a spin ground state ($S = 11/2$) 11 times higher than its predecessors [158]. This complex constitutes another example of the series of aggregates [69, 159] formed with the tripodal ligand H_3thme. The cluster was obtained, in a procedure very similar to that used for complex **58** (*vide supra*), by reaction of the dimer $[NEt_4]_2[Fe_2OCl_6]$ with NaO_2CPh, dmhp and H_3thme in acetonitrile. The core of **59** (Fig. 35) comprises four fused butterfly $[Fe_4O_2]^{8+}$ subunits, thereby incorporating many competing antiferromagnetic $Fe^{III}\cdots Fe^{III}$ interactions into the structure. Thus, the spin number of the ground state, shown to be 11/2 by susceptibility and reduced magnetisation measurements is the consequence of spin frustration. Low temperature magnetisation studies revealed the presence of hysteresis loops, demonstrating **59** to be a new example of SMM. The study of the hysteresis as a function of the field sweep rate showed that this complex is subject to strong quantum tunneling of the magnetisation. In what is a very rare case for SMMs, the ground state of **59** could be characterised by means of Q-band EPR spectroscopy. Most EPR investigations on SMMs have been conducted using high fields and frequencies. The simulation of the spectrum provided the following parameters; $g = 2.03$, $D = -0.38\ cm^{-1}$ and $E = 0.055\ cm^{-1}$. These results were found to be in good agreement with the values obtained from bulk magnetisation measurements.

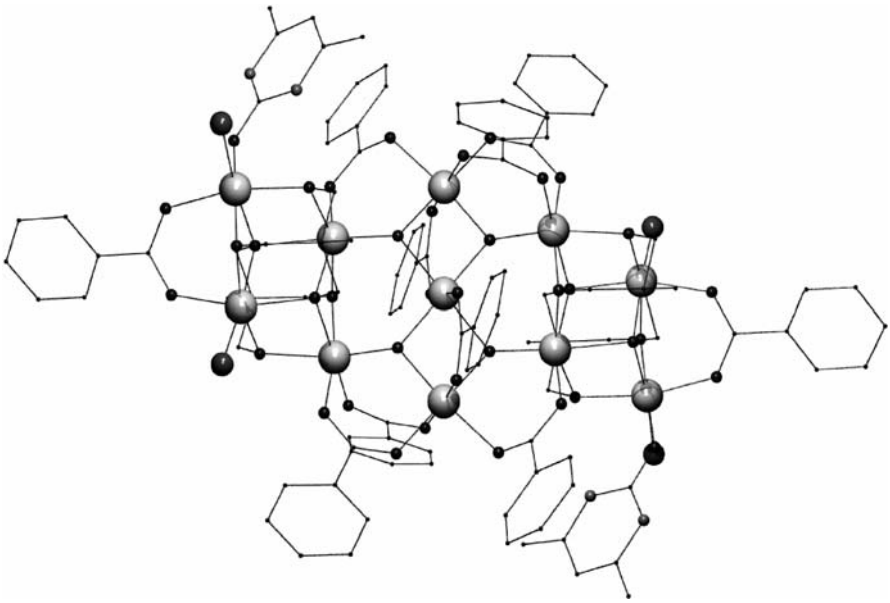

Fig. 35 PovRay representation of the anion of $(NEt_4)[Fe_{11}O_4(O_2CPh)_{10}(thme)_4(dmhp)_2Cl_4]$ (**59**). Hydrogen atoms are omitted for clarity. Code for atoms as in Fig. 34

3.8 $[Fe_9O_4(OH)_5(heia)_6(Hheia)_2]$ (60); A Piece of All-Ferric Molecular Magnetite

The cluster $[Fe_9O_4(OH)_5(heia)_6(Hheia)_2]$ (**60**, Fig. 36) [160] was prepared in methanol from $Fe(NO_3)_3 \cdot 9H_2O$ and H_2heia in the presence of tetramethyammonium hydroxide. The structure features a central tetrahedral Fe(III) ion bound by four $\mu_3 - O^{2-}$ groups to eight peripheral octahedral ferric centres. Further bridging and peripheral ligation of the outer Fe(III) metals is ensured by six $heia^{2-}$ and two $Hheia^-$ ligands, in addition to five $\mu_2 - OH^-$ groups. The core of the complex is related to the lattice of magnetite. Fitting of the low temperature magnetisation data was consistent with a ground state of $S = 25/2$ with $g = 1.99$ and $D = -0.07\ cm^{-1}$. The ground state was rationalised by the antiferromagnetic interaction between the central Fe(III) ion and all of the external Fe(III) ions except one. The coupling scheme is that expected from consideration of the Fe – O – Fe angles within the various Fe_2 pairs. Single crystal magnetisation measurements performed on an array of micro-SQUID show the temperature and sweep rate dependent hysteresis loops expected for an SMM with an effective barrier for the re-orientation of the magnetisation of approximately $5.4\ cm^{-1}$.

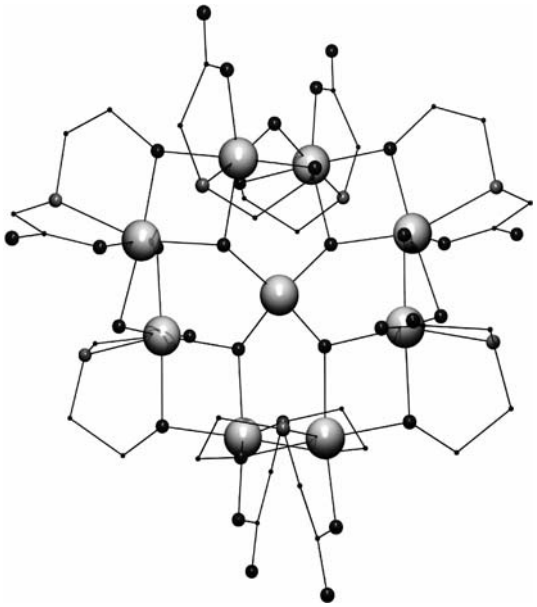

Fig. 36 PovRay representation of $[Fe_9O_4(OH)_5(heia)_6(Hheia)_2]$ (**60**). Hydrogen atoms are omitted for clarity. Code for atoms as in Fig. 29

4
SMMs of Nickel

The synthesis of large polynuclear cages featuring Ni(II) has been studied for a long time as a potential route to high-spin molecules [127, 161], and SMMs since Ni(II) is known to display large single-ion anisotropy [162, 163]. Thus, the magnetic properties of new and pre-existing Ni clusters have been examined with this in mind.

4.1
$[Ni_{12}(chp)_{12}(O_2CMe)_{12}(thf)_6(H_2O)_6]$ (61); The First Ni SMM

The cyclic complex $[Ni_{12}(chp)_{12}(O_2CMe)_{12}(thf)_6(H_2O)_6]$ (**61**) was first prepared in 1994 [164]. In the structure of **61** (Fig. 37) there are only two independent Ni(II) centres and thus two types of nearest-neighbour Ni $\cdots$ Ni interactions: one *via* two μ_2 – O atoms from chp^- and one *syn*,*syn*-carboxylate, and the other *via* one μ_2 – O atom from an H_2O molecule, one from a carboxylate and one *syn*,*syn*-acetate. Crystals of **61** form from the melt reaction of $Ni(AcO)_2$ with Hchp at 130 °C followed by crystallisation from THF [165]. Interestingly, most reactions involving nickel and cobalt carboxylates and pyridonate ligands produce compact cages [166], rather than cyclic compounds like **61**. Initial bulk magnetisation studies [164] revealed the presence

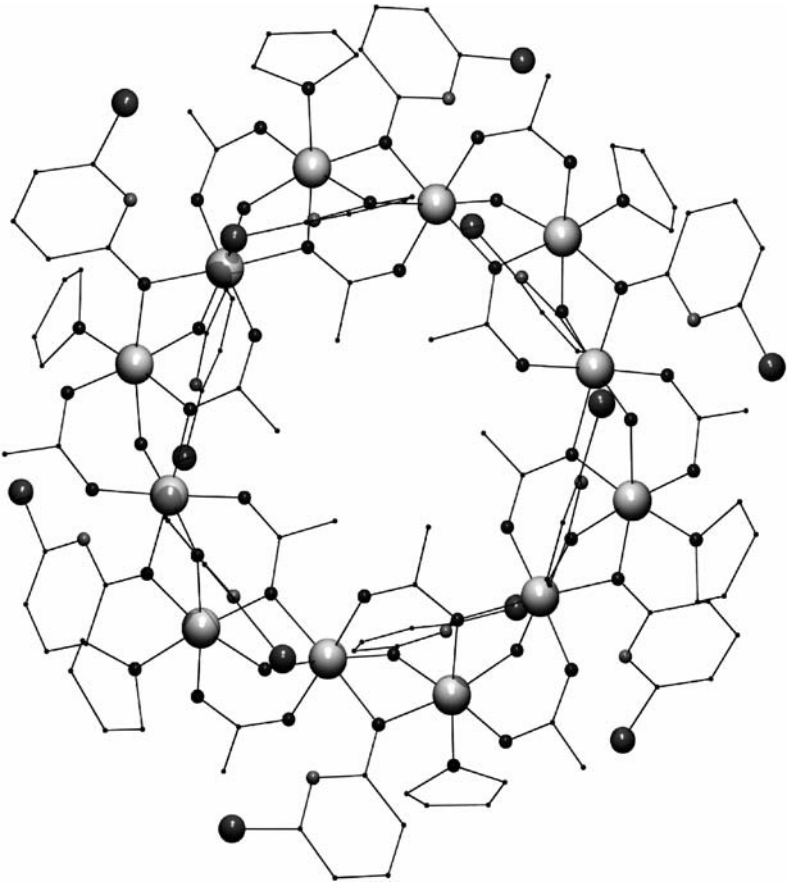

Fig. 37 PovRay representation of $[Ni_{12}(chp)_{12}(O_2CMe)_{12}(thf)_6(H_2O)_6]$ (**61**). Hydrogen atoms are omitted for clarity. Code for atoms: *largest grey*, Ni; *second largest dark grey*, Cl; *medium black*, O; *medium grey*, N; *rest*, C

of ferromagnetic interactions within the wheel and the presence of a spin ground state of high multiplicity. A more detailed analysis allowed a good recreation of the $\chi_m T$ vs. T curve using a Heisenberg exchange coupling model with a unique J value of $J = 4.7\,cm^{-1}$ [164]. Very low temperature magnetisation measurements confirmed the presence of an $S = 12$ ground state and a small amount of Ising-type magnetoanisotropy ($D = -0.05\,cm^{-1}$), making this compound the first SMM of Ni [167]. This condition was confirmed by ac magnetic susceptibility studies and by the presence of hysteresis in the curve of magnetisation *versus* field. The latter also revealed the existence of QTM. The dynamics of relaxation has been the object of more recent studies through micro-SQUID measurements on single crystals. An INS investigation unveiled the necessity of using two J values to describe

the exchange coupling between the two different nearest Ni · · · Ni vectors existing in the ring and a third J exchange coupling constant for the second-nearest Ni · · · Ni interactions. The best parameters were $J_1 = 5.7$, $J_2 = 0.95$ and $J_3 = -0.45\ \mathrm{cm}^{-1}$.

4.2 [Ni(hmp)(ROH)Cl]$_4$ (62–64); A Family of Exchange-Biased SMMs

The family of tetranuclear Ni(II) cubanes **62** to **64** represent a recent and very interesting addition to the group of Ni SMMs. Clusters with a $[Ni_4O_4]$ cubane core are relatively common. Complexes with all antiferromagnetic [168], both ferro- and antiferromagnetic [169, 170] or all ferromagnetic interactions [171] have been described. The first category displays $S = 0$ and the last $S = 4$ ground states, whereas the spin of the intermediate case depends on the symmetry of the cluster and the relative strength of the competing interactions. The compounds $[Ni(hmp)(ROH)Cl]_4$ (R = CH_3, **62**; CH_2CH_3, **63**; $CH_2CH_2C(CH_3)_3$, **64**) are the first family of Ni(II) cubanes to be confirmed as SMMs. In all cases, the structure (Fig. 38) consists of a cube formed by four crystallographically equivalent Ni(II) cations and the alkoxide O atom from four hmp^- ligands. The coordination around each Ni centre is completed by the N atom from hmp^-, one Cl^- ion and one molecule of ROH. The three compounds were prepared from the reaction of $NiCl_2$,

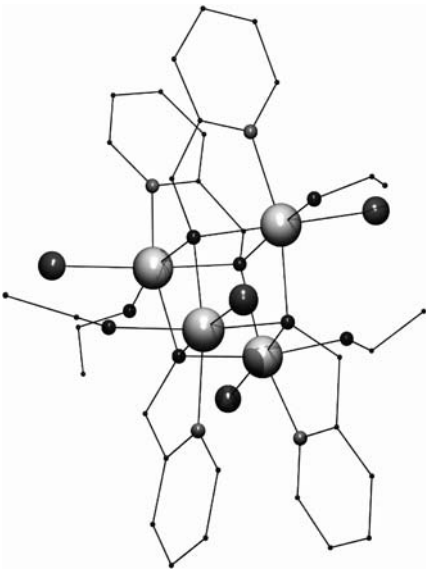

Fig. 38 PovRay representation of $[Ni(hmp)(EtOH)Cl]_4$ (**63**). Hydrogen atoms are omitted for clarity. Code for atoms as in Fig. 37

Hhmp and NaOR in the corresponding alcohol. Variable temperature bulk magnetisation measurements revealed the presence of intramolecular ferromagnetic exchange and a spin ground state $S = 4$. This series of compounds are among the few clusters that allow the use of the Kambe vector coupling approach [172] to obtain the coupling constants describing the intramolecular magnetic exchange. For this, the appropriate spin Hamiltonian is $H = -2J(S_1S_2 + S_1S_3 + S_1S_4 + S_2S_3 + S_2S_4 + S_3S_4)$, which yields the following expression for the energies of the various spin states; $E(S_T) = -J[S_T(S_T + 1)]$. The J value obtained by fitting the Van Vleck equation to the experimental data was $+5.2\ cm^{-1}$. Confirmation of the ground state and the ZFS parameters D and B_4^0 (e.g. $D = -0.60$ and $B_4^0 = -4.6 \times 10^{-5}\ cm^{-1}$, respectively, in **62**) could be obtained by fitting reduced magnetisation measurements by means of a full matrix diagonalisation. The results were consistent with those obtained from a HF-EPR investigation. Particularly interesting about this EPR study was the finding that all the signals were split in two. This could be due to the presence of different local environments around the cluster within the crystal or the existence of intermolecular exchange. The latter suggestion was confirmed from the hysteresis loops of the complexes. The magnetisation *versus* field curves showed steps due to faster relaxation at certain fields caused by the presence of quantum tunnelling. This is a normal feature in SMMs, but in complexes **62–64** the first step occurs before H = 0 due to the presence of an exchange bias effect. This is a very rare phenomenon, only recently discovered in tetranuclear SMMs [120]. The exchange bias originates from intercluster magnetic interactions, and consequently its effect on the hysteresis and EPR, has been found to decrease as the bulk around the cluster increases ($R = CH_3 > CH_3CH_2 > CH_2CH_2C(CH_3)_3$).

The most recent example of a $[Ni_4]$ cubane acting as an SMM is the compound $[Ni(H_2thme)(MeCN)]_4(NO_3)_4$ (**65**) [171]. In this complex, only one alcohol arm of each thme ligand is deprotonated and acts as a μ_3-O group within the cubane core. The other two alcohol arms of each ligand coordinate to Ni(II) terminally. The coordination around the metal ions is completed by one molecule of MeCN. The charge of the cluster cation (+ 4) is compensated by four NO_3^- anions. The ground state of **65** was found to be $S = 4$ as a result of intramolecular ferromagnetic interactions of magnitude $J_1 = 7.5\ cm^{-1}$ and $J_2 = 4\ cm^{-1}$; with $D = -0.43\ cm^{-1}$ and $E/D = 0.04$. Hysteresis loops featuring steps caused by quantum tunnelling of the magnetisation were also observed in single crystal micro-SQUID measurements.

4.3
The $[Ni_{21}(cit)_{12}(OH)_{10}(H_2O)_{10}]^{16-}$ (66); The Largest Ni SMM

The use of carboxylates as co-ligands has been one of the most successful strategies in the production high-nuclearity transition metal aggregates [39, 127]. The method has been extended to the use of polycarboxylates such

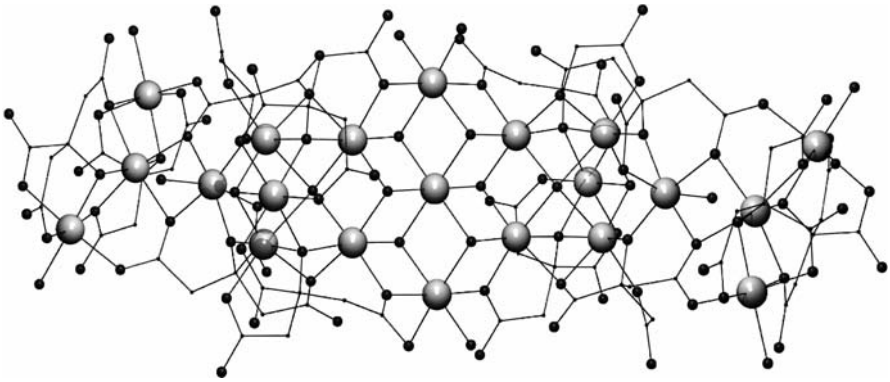

Fig. 39 PovRay representation of the cluster anion $[Ni_{21}(cit)_{12}(OH)_{10}(H_2O)_{10}]^{16-}$ (**66**). Hydrogen atoms are omitted for clarity. Code for atoms as in Fig. 37

as citric acid [173]. Among the compounds with Ni(II) is **66** [174], one of the largest Ni clusters known [175]. The structure (Fig. 39) contains a planar central unit $[Ni_7(\mu_3 - OH)_6]$, similar to that seen in a layer of $Ni(OH)_2$, and comparable with that found in $[Fe_{19}]$ [138] or $[Co_{24}]$ [176] clusters. Twelve bridging citrate ligands in five different binding modes link the remaining metal centres to this unit. Cluster **66** displays two chiral centres on Ni(II) atoms at both ends of the molecule. Originally the compound was isolated as the $\Delta - \Lambda$ isomer, whereas further research on the system allowed the formation of the enantiomeric pair $\Delta - \Delta + \Lambda - \Lambda$ (**67**), by simply changing the amounts of reagents used during the synthesis. The magnetic properties of both diastereoisomers were found to be identical. The $\chi_m T$ vs. T curve revealed domination of antiferromagnetism within the cluster leading to a spin ground state of $S = 3$. Ac magnetic susceptibility measurements revealed the presence of a frequency dependent out-of-phase signals suggesting slow relaxation of the magnetisation. The relaxation of the magnetisation at the lowest temperature occurs mainly through quantum tunnelling caused, at least in part, by the presence of a rhombic term (E) of the magnetic anisotropy. The value of the D parameter obtained by fitting the linear part of the Arrhenius plot ($-0.22\ cm^{-1}$) can only be a lower limit of the actual value, since it represents an energy barrier smaller than the true one.

4.4 $[Ni_8Na_2(N_3)_{12}(^tBuPhCO_2)_2(mpo)_4(Hmpo)_6(EtOAc)_6]$ (68); Ferromagnetism Induced by Azide Bridges

It is now well known that end-on bridging azide ligands mediate the ferromagnetic exchange between paramagnetic centers [177]. Magnetostructural

correlations between the strength of the interaction and the $M - N - M$ angle in these bridges have been reported for Cu(II) [178] and Mn(II) [179]. This property has only recently started to be exploited in the preparation of SMMs. An elegant example was the substitution of $\mu_4 - OH^-$ by $\mu_4 - N_3^-$ on a preformed $[Fe_9]$ cluster, resulting in the change from antiferro- to ferromagnetic interactions and thus leading to a new example of SMM [152]. The compound $[Ni_8Na_2(N_3)_{12}(^t BuPhCO_2)_2(mpo)_4(Hmpo)_6(EtOAc)_6]$ (**68**) (Fig. 40) is another of the very rare SMMs whose high spin state ($S = 8$) is caused by the ferromagnetic coupling induced by end-on azide ligands. Complex **68** was prepared [180] by refluxing in MeOH $Ni(BF_4)_2$, Hmpo, $^t BuPhCO_2H$, NaOMe, and NaN_3, followed by evaporation of the solvent and extraction with ethylacetate. The core of **68** is a $[Ni_8(N_3)_{12}]^{4+}$ rod where the peripheral ligation is completed by bridging or terminal carboxylate and pyrazolinolate ligands, which also link this core to two Na^+ at both ends. Magnetic susceptibility measurements revealed ferromagnetic intramolecular coupling and a spin ground state of $S = 8$ with $D = -0.07\ cm^{-1}$. The SMM behaviour at very low temperature was confirmed by the presence of temperature and sweep rate dependent hysteresis loops (Fig. 41).

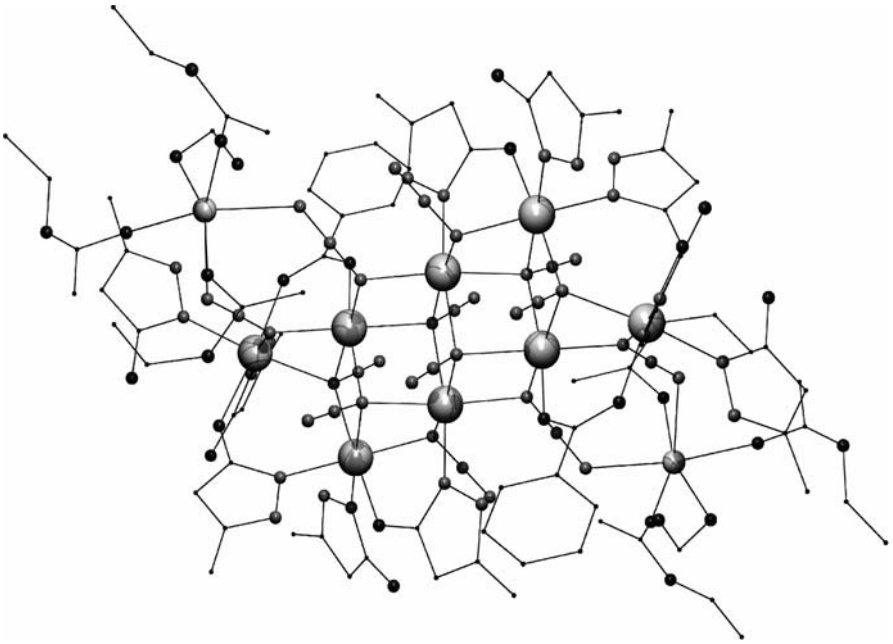

Fig. 40 PovRay representation of the cluster $[Ni_8Na_2(N_3)_{12}(^t BuPhCO_2)_2(mpo)_4(Hmpo)_6(EtOAc)_6]$ (**68**). Hydrogen atoms are omitted for clarity. Code for atoms: *largest grey*, Ni; *second largest grey*, Na; *medium black*, O; *medium grey*, N; *rest*, C

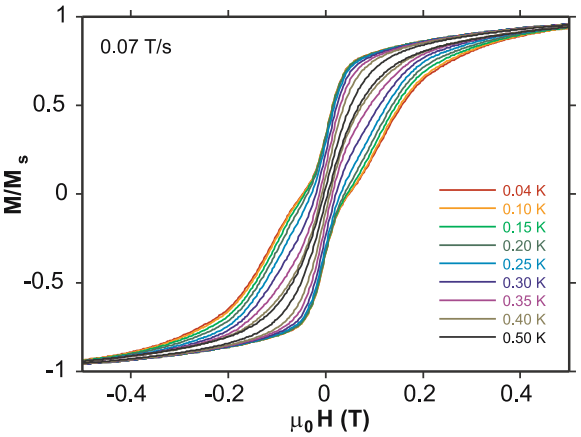

Fig. 41 Variable field isothermal magnetisation curves, recorded at different temperatures, for complex $[Ni_8Na_2(N_3)_{12}(^tBuPhCO_2)_2(mpo)_4(Hmpo)_6(EtOAc)_6]$ (**68**), emphasising the hysteresis loops caused by slow relaxation of the magnetisation and showing large steps as a result of enhanced relaxation due to quantum tunneling at zero field

5
SMMs of Co

The chemistry of polynuclear Co(II) complexes is quite rich [32, 161, 181] and has been particularly exploited in the context of molecular magnetism [154, 182]. Since this ion can possess up to three unpaired electrons ($S = 3/2$) and display large single-ion anisotropy, it is a suitable candidate for SMM synthesis. However, only two SMMs of Co(II) have been reported to date, although the first identified single-chain magnet (SCM) [183] also contains Co(II).

5.1
$[Co_4(hmp)_4(MeOH)_4Cl_4]$ (69); The First Co SMM

A number of complexes with a $[Co(II)_4O_4]$ cubane topology exist in the literature [184, 185], but only a few have been shown to exhibit intramolecular ferromagnetic coupling [154, 186]. Compound **69** is the only to have been identified as an SMM [149]. This complex was prepared from the reaction of $CoCl_2$ with Hhmp in MeOH, in the presence of NaOMe. The structure of $[Co_4(hmp)_4(MeOH)_4Cl_4]$ has four Co(II) ions arranged in a cube with the alkoxide O-atoms from four hmp^- ligands. Six-coordination around each metal is completed by the N-atom of hmp^-, one Cl^- and one MeOH molecule. Variable temperature magnetisation data recorded at various magnetic fields were fit to the Van Vleck equation, including ZFS effects, by means of a full matrix diagonalisation of the Hamiltonian. The results were consistent with

the presence of an $S = 6$ spin ground state resulting from dominant ferromagnetic interactions within the cluster, and a negative ZFS parameter of $D = -2.78\,cm^{-1}$. SMM behaviour was confirmed by the presence of temperature dependent hysteresis loops in micro-SQUID measurements, which showed evidence of quantum tunnelling of the magnetisation.

5.2 $(NMe_4)_3Na[Co_6(cit)_4(H_2O)_{10}]$ (70); A SMM Assembled by Citrate

The second SMM of Co reported, $(NMe_4)_3Na[Co_6(cit)_4(H_2O)_{10}]$ (**70**) [187], is a hexanuclear cluster (Fig. 42) bridged by four cit^{4-} ligands. It comprises a central $[Co_4O_4]$ cubane core where the μ_3-O donors are the alkoxide O-atoms from cit^{4-}. The three carboxylate groups of each ligand act as monodentate donors that complete the coordination around these four Co(II) centres. Two of these carboxylate groups bind, in a *syn,anti* manner to the free coordination site of two peripheral $[Co(H_2O)_5]^{2+}$ moieties. Variable temperature bulk magnetisation data are difficult to model due to the existence of first order spin-orbit coupling effects. At low temperatures, each Co(II) may be treated as an effective spin $S = 1/2$. In this manner, the reduced magnetisation curve was interpreted as that produced by a cluster with total spin of $S = 3$ and average g value of $g > 3$, suggesting ferromagnetic coupling between the six Co(II) ions. Evidence that this cluster is a new SMM came from

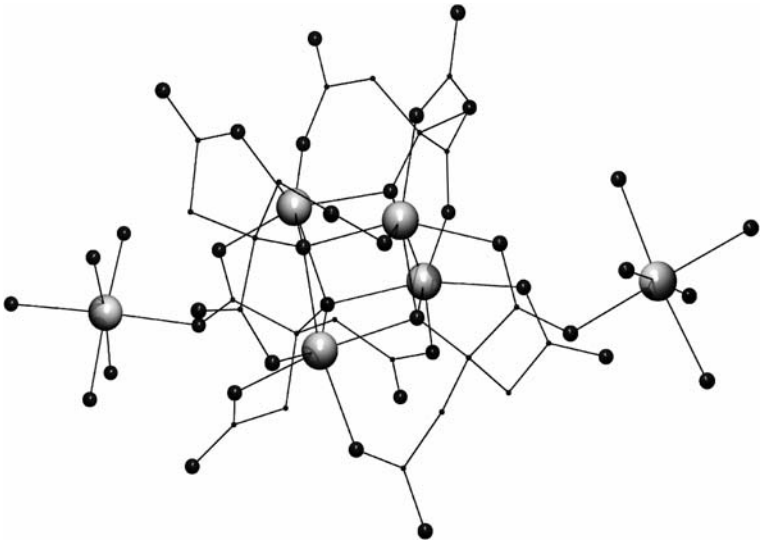

Fig. 42 PovRay representation of the cluster anion of $(NMe_4)_3Na[Co_6(cit)_4(H_2O)_{10}]$ (**70**). Hydrogen atoms are omitted for clarity. Code for atoms: *largest grey*, Co; *medium black*, O; *rest*, C

the presence of frequency dependent signals in the out-of-phase component of ac susceptibility. Changes in the degree of solvation of the molecule had important effects on the dynamics of the relaxation of the magnetisation, presumably caused by the subtle changes in geometry as a result of solvent loss. Such solvent dependent effects had been previously observed on Mn-based SMMs [68].

6 SMMs of Vanadium

Polynuclear aggregates of octahedral V(III) (d^2, $S = 1$) are also a potential source of SMMs. The fact that the number of known V(III) clusters is small is due to its air-sensitivity, which adds some difficulty to their preparation and handling. Among the relatively few paramagnetic vanadium clusters reported [188–190], only one structural type has proved to be a SMM.

6.1 Complex Ions $[V_4O_2(O_2CEt)_7(L–L)_2]^z$ (L–L = pic$^-$, $z = –1$, **71a**; L–L = bpy, $z = +1$, **71b**); The Only Vanadium SMMs

Complexes **71** possess a $[V_4O_2]$ butterfly-type core. They are prepared from the reaction in acetone of $VCl_3(THF)_3$, the corresponding chelate and NaO_2CEt under anaerobic conditions, followed by addition of the appropriate counter-ion. This is a common motif in 3*d* M(III) clusters, including Mn [191], Fe [192], Cr [193], and/or mixtures of these [194], and one that can often lead to spin frustration effects. Complex **71a** (ClO_4) [195] exhibits spin frustration as a result of "body-body" *versus* "body-wing" competing exchange interactions leading to a ground state of $S = 3$ with $D = -1.5\ cm^{-1}$. A re-investigation [196] of the magnetic properties of **71a** (ClO_4) and the related complex (NEt_4) **71b** established this family of compounds as the only class of vanadium-based SMMs identified to date. Ac magnetisation measurements revealed the presence of frequency dependent out-of-phase signals and slow relaxation of the magnetisation.

7 SMMs with Other Metals

Despite the success in the preparation of SMMs achieved during the last decade, it is significant that the first identified member $[Mn_{12}OAc]$ (**1**) [2] remains the one with the highest observed blocking temperature. In the search for new and improved SMMs, synthesis has been expanded toward heterometallic complexes and other synthetic methods.

7.1 Cyanide-Bridged SMMs

Cyanide bridged coordination compounds early became a cornerstone in molecular magnetism, in particular, those related to Prussian blue solids [197]. This has inspired attempts to prepare molecular CN^- bridged transition metal compounds, using polydentate capping ligands to prevent the growth of infinite arrays. The predictable geometry of the final compound and the nature of the resulting magnetic interactions make these systems suited for the design of molecules with desired properties. Recent reviews illustrate the remarkable progress made with cyanide-based complexes at the molecular level [42, 43]. In the context of SMMs, this work has resulted in the synthesis of the first examples of such type of compounds made by rational design. The first reported cyano-bridged SMM is the complex cation $[(Me_3tacn)_6MnMo_6(CN)_{18}]^{2+}$ (**72**) [27], being also the first molecule of this type incorporating 4*d* metals in the structure. Complex **72** possesses a spin ground state of $S = 13/2$, by virtue of antiferromagnetic coupling between a central Mn(II) metal ($S = 5/2$) and six peripheral Mo(III) centres ($S = 3/2$). Another related molecule with SMM properties is the mixed valence cluster $[Mn^{II}(tmphen)_2]_3[Mn^{III}(CN)_6]_2$ (**73**), with a $S = 11/2$ spin ground state resulting from strong antiferromagnetic coupling between three high spin Mn^{II} centres ($S = 5/2$) and two low spin Mn^{III} ions ($S = 1$) [198]. The two heterometallic trinuclear complexes, $K[(5-Brsalen)_2(H_2O)_2Mn^{III}{}_2M^{III}(CN)_6]$ (M = Cr, **74**; Fe, **75**) [199], have been also made in this manner, and exhibit ground states of $S = 5/2$ and $9/2$ as a result of intramolecular antiferro- and ferromagnetic coupling, respectively. Both species displaying negative values of the ZFS parameter *D*, they behave as SMMs. To these, a new example has been added very recently, with formula $(NEt_4)[(salmen)_2(MeOH)_2Mn_2Fe(CN)_6]$ (**76**), $S = 9/2$ and $D = -0.87\ cm^{-1}$, which has been used as a precursor to build a single chain magnet [130]. In the same manner, the tetranuclear ion $[(dipropy2)_2Ni_3Cr(CN)_3]^{3+}$ (**77**) has been shown to have a spin ground state of $S = 9/2$ arising from $Cr\cdots Ni$ ferromagnetic interactions and the magnetisation *versus* field curve shows a hysteresis loop [42]. Recently, spectacular molecular cubes have been prepared. The first has formula $[(MnCl)_4(Re(triphos)(CN)_3)_4]$ (**78**) and is the only existing example of SMM with a 5*d* element [28]. The most recent is $[(Tp)(H_2O)_6Cu_6Fe_8(CN)_{24}](ClO_4)_4$ (**79**) [200], with a spin ground state of $S = 7$. Finally, two octacyanometallate-based clusters with formulae $[Co^{II}{}_9(M^V(CN)_8)_6(CH_3OH)_{24}]$ (M = W, **80**; Mo, **81**) have been prepared [201], which display SMM behaviour by virtue of their high spin ground state of $S = 21/2$, as a result of antiferromagnetic coupling between Co and M ions. The slow relaxation of **80** and **81** is in contrast with the behaviour observed for the Mn^{II} analogues, synthesised a few years earlier [86, 202, 203].

7.2 Heterometallic 3*d*–4*f* Single-Molecule Magnets

It is surprising that to date, very few 3*d*–4*f* compounds have been shown to act as SMMs. 4*f* elements can provide up to seven unpaired electrons and introduce large magnetic anisotropy. Recent developments indicate that this situation is beginning to change with reports of a few hybrid 3*d*–4*f* SMMs. The first such species was the complex $[CuTbL(hfac)_2]_2$ (**82**) [29], which, as a result of ferromagnetic coupling between its paramagnetic centres, exhibits very large magnetisation and the properties characteristic of SMMs. However, a detailed study of the variable temperature magnetisation is hampered by first order spin-orbit coupling effects of the lanthanide ions.

The cluster $[Dy_6Mn_6(H_2shi)_4(Hshi)_{10}(CH_3OH)_{10}(H_2O)_2]$ (**83**) [30] is prepared from the self-assembly of the components in methanol, involving the oxidation of Mn(II) to Mn(III/IV). Finally, a family of mixed manganese-lanthanide SMMs with a $[Mn_{11}Ln_4]^{45+}$ (Ln = Nd, Gd, Dy, Ho, Eu) core has been recently prepared. Of these, the magnetic properties of compound $[Mn_{11}Dy_4O_8(OH)_6(OMe)_2(O_2Ph)_{16}(NO_3)_5(H_2O)_3]$ (**84**) have been discussed in detail in a recent report [31].

7.3 The Smallest Possible Heterometallic SMM

Mixing the chloride salts of Mn(II) and Cu(II) with the Schiff base ligand $H_2$5 – Br – sap leads, following air oxidation of manganese, to the SMM $[MnCu(5 – Br – sap)_2(MeOH)]$ (**85**) instead of the corresponding homometallic analogues [204]. Complex **85** exhibits strong intramolecular ferromagnetic coupling as a result of strict orthogonality between magnetic orbitals and is the smallest possible heterometallic SMM. A slightly larger partner in this new family of compounds is the tetranuclear cluster $[Mn_2Ni_2Cl_2(salpa)_2]$ (**86**) [205], which shows $S = 6$ spin ground state, resulting from dominant ferromagnetic interactions within the cluster. The ground state could be also confirmed from single-crystal HF-EPR spectra and their simulation. The compound $[Mn_8Fe_4O_{12}(O_2CCH_2Cl)_{16}(H_2O)_4]$ (**87**) [206] is the first heterometallic derivative of the $[Mn_{12}]$ family to display properties of SMM. A previously reported compound [207], only differing from **87** in the nature of the carboxylate (O_2CCH_3 instead of O_2CCH_2Cl) did not show slow relaxation of the magnetisation.

7.4 Mononuclear SMMs

A remarkable novelty in the area of investigation covered by this review is the discovery of SMM behaviour on the mononuclear compounds $(NBu_2)[Pc_2Ln]$

(Ln = Tb, **88**; Dy, **89**) [208]. It is shown that the origin of the slow relaxation of the magnetisation in **88** and **89** is the energy barrier necessary to equilibrate the spin-orbit ground state $\pm J_z$ upon removal of an external magnetic field. This barrier would result from the necessity to climb over certain of the various J_z sublevels of the ground multiplet of the lanthanide, in order to toggle between the $\pm J_z$ sublevels of the ground state. A recent report offers details on the mechanisms of relaxation of the magnetisation of these compounds for each temperature range [209]. This discovery is substantial, and it is surprising that such behaviour has not been noted before, on other mononuclear lanthanide complexes.

7.5
Photomagnetic Creation of a SMM

The use of light irradiation in order to trigger changes of the magnetic properties in materials has been pursued with intensity and has led to important subtopics of investigation [210–212]. At the molecular level, an important development was the formation of a high-spin molecule in this manner [213]. It has now been shown that the compound $[Co(SCN)_2(dabp)_4]$ (**90**, dabp = 4-(α-diazobenzyl)pyridine) can be transformed into an SMM upon exposure to light [214]. Thus, the carbene ligand-radicals ($S = 1/2$) originating from irradiation of the diazo compound couple ferromagnetically with the central Co(II) ions, and the resulting high spin-entity, because of the anisotropy induced by the Co(II) ion, behaves as SMM.

8
Conclusions

In this review, we have shown that the intense synthetic effort made during the approximately 10 years elapsed since the discovery of SMMs has led to the preparation of a large number of new and very diverse examples, most of them based on 3*d* metals. This work and the large number of physical studies that have derived from its fruits have undoubtedly provided a very good understanding of the phenomenon and of the necessary requirements to observe it. This has in turn opened new and original lines of research such as the quest for poly-functional materials including the property of single-molecule magnetism, the search for magneto-chiral dichroism based on SMMs, or attempts to organise these species on surfaces of different nature, as well as stimulating many new synthetic investigations. It was early recognised that increasing the spin ground state and the magnetoanisotropy were among the necessary conditions if the temperature for observing memory effects on single molecules was to be raised. While there has been considerable progress in improving the first condition with the preparation of SMMs ex-

hibiting larger and larger spin numbers, it is interesting to note that the first identified SMM, $[Mn_{12}AcO]$ (**1**), still remains that with the highest blocking temperature observed *hitherto*. It is thus clear that a huge amount of work still lies ahead before the possibility of using this property for routine applications in the context of nano-technologies can be considered. As has been summarised in the last section of this manuscript, new synthetic methodologies and approaches are beginning to be explored in order to expand the area relevant to SMM research. This has led to the first members of what will undoubtedly be new generations of SMMs, such as 3*d*–4*f* mixed-metal aggregates, only 4*f* or 5*d* clusters, or systems prepared using a rationally designed approach. The speed at which progress is being made in this area might soon render this review outdated. We think that it will nevertheless be an adequate reference as a compilation of the first consolidated family of SMMs.

Table 1 Complexes cited in this review

$[Mn_{12}O_{12}(O_2CMe)_{16}(H_2O)_4]$	**(1)**
$[Mn_{12}O_{12}(O_2CCH_2Br)_{16}(H_2O)_4]$	**(2)**
$[Mn_{12}O_{12}(O_2CPh)_{16}(H_2O)_4]$	**(3)**
$[Mn_{12}O_{12}(O_2CPh)_{12}(NO_3)_4(H_2O)_4]$	**(4)**
$[Mn_{12}O_{12}(O_2CMe)_8(O_2PPh_2)_8(H_2O)_4]$	**(5)**
$[Mn_{12}O_{12}(O_2CMe)_8(O_3SPh)_8(H_2O)_4]$	**(6)**
$[Mn_{12}O_{12}(O_2CPh)_8(L1)_4(H_2O)_4]$	**(7)**
$(PPh_4)[Mn_{12}O_{12}(O_2CEt)_{16}(H_2O)_4]$	**(8)**
$[Mn_{12}O_{12}(O_2CEt)_{16}(H_2O)_3]$	**(9)**
$(PPh_4)_2[Mn_{12}O_{12}(O_2CCHCl_2)_{16}(H_2O)_4]$	**(10)**
$[Mn_{84}O_{72}(O_2CMe)_{78}(OMe)_{24}(OH)_6(MeOH)_{12}(H_2O)_{42}]$	**(11)**
$[Mn_{12}O_{12}(O_2CCH_2{}^tBu)_{16}(H_2O)_4]$	**(12)**
$[Mn_{30}O_{24}(OH)_8(O_2CCH_2{}^tBu)_{32}(H_2O)_2(MeNO_2)_4]$	**(13)**
$[Mn_{12}O_8Cl_4(O_2CPh)_8(hmp)_6]$	**(14)**
$[Mn_{12}O_8Cl_4(O_2CPh)_8(hep)_6]$	**(15)**
$[Mn_9O_7(thme)(O_2CMe)_{11}(py)_3(H_2O)_2]$	**(16)**
$[Mn_{12}O_4(OH)_2(O_2CPh)_{12}(thme)_4(py)_2]$	**(17)**
$[Mn_{22}O_6(OMe)_{14}(O_2CMe)_{16}(tmp)_8(HIm)_2]$	**(18)**
$[Mn_{18}O_{14}(O_2CMe)_{18}(hep)_4(hepH)_2(H_2O)_2]$	**(19)**
$[Mn_6(teaH)_2(teaH_2)_2(O_2CCHPh_2)_8]$	**(20)**
$[Mn_4(O_2CMe)_2(pdmH)_6]^{2+}$	**(21)**
$[Mn_4(hmp)_6(NO_3)_4]$	**(22)**
$[Mn_4(hmp)_6Br_2(H_2O)_2]Br_2$	**(23)**
$[Mn_4(hmp)_6(NO_3)_2(MeCN)_2](ClO_4)_2$	**(24)**
$[Mn_4(hmp)_4(acac)_2(MeO)_2](ClO_4)_2$	**(25)**

Table 1 (continued)

$[Mn_4(O_2CPh)_4(mda)_2(mdaH)_2]$	**(26)**
$[Mn_4O_2(MeO)(O_2CPh)_2(bis-bpy)_2(MeOH)](ClO_4)_2$	**(27)**
$[Mn_2(H_2thme)_2(bpy)_4](ClO_4)_2$	**(28)**
$[Mn_3(Hcht)_2(bpy)_4](ClO_4)_2$	**(29)**
$[CeMn_8O_8(O_2CMe)_{12}(H_2O)_4]$	**(30)**
$[Mn_{25}O_{18}(OH)_2(N_3)_{12}(pdm)_6(pdmH)_6](Cl)_2$	**(31)**
$[Mn_{26}(pdol)_{12}(OMe)_{12}O_{16}(N_3)_6]$	**(32)**
$[Mn_{16}(O_2CMe)_{16}(teaH)_{12}]$	**(33)**
$[Mn_{12}(O_2CMe)_{14}(mda)_8]$	**(34)**
$(TBA)_2[Mn_{12}O_{12}(OMe)_2(O_2CPh)_{16}(H_2O)_2]$	**(35)**
$[Mn_{16}O_{16}(OMe)_6(O_2CCH_2Ph)_{16}(MeOH)_6]$	**(36)**
$[Mn_{16}O_{16}(OMe)_6(O_2CCH_2Cl)_{16}(MeOH)_6]$	**(37)**
$[Mn_{16}O_{16}(OMe)_6(O_2CCH_2Br)_{16}(MeOH)_6]$	**(38)**
$[Mn_{16}O_{16}(OMe)_6(O_2CMe)_{16}(MeOH)_3(H_2O)_3]$	**(39)**
$(Et_3NH)_2[Mn(CH_3CN)_4(H_2O)_2][Mn_{10}O_4(biphen)_4Br_{12}]$	**(40)**
$[Mn^{III}_4Mn^{II}_3(L2)_6]$	**(41)**
$[Mn_6O_2(O_2CMe)_2(salox)_6(EtOH)_4]$	**(42)**
$[Mn_4Cl_4sal_4]$	**(43)**
$[Mn_2(saltmen)_2(ReO_4)_2]$	**(44)**
$[Mn_{26}O_{17}(OH)_8(OMe)_4F_{10}(bta)_{22}(MeOH)_{14}(H_2O)_2]$	**(45)**
$(HIm)_2[Mn_4O_3Cl_6(O_2CMe)_3(Im)]$	**(46)**
$[Mn_4O_3Cl(O_2CMe)_3(dbm)_3]$	**(47)**
$[Mn_4O_3(O_2CMe)_4(dbm)_3]$	**(48)**
$[Mn_4O_3Cl_4(O_2CEt)_3(py)_3]$	**(49)**
$[Fe_8O_2(OH)_{12}(tacn)_6]^{8+}$	**(50)**
$[Fe_{19}(metheidi)_{10}(OH)_4O_6(H_2O)_{12}](NO_3)$	**(51)**
$[Fe_4(OMe)_6(dpm)_6]$	**(52)**
$[Fe_4(thme)_2(dpm)_6]$	**(53)**
$[Fe_4(thme)_2(CH_3CH_2CH_2OH)_6Cl_6]$	**(54)**
$[Fe_4(sae)_4(MeOH)_4]$	**(55)**
$[Fe_9(N_3)_2(O_2CMe)_8(pdol)_4]$	**(56)**
$[Fe_9(OH)_2(O_2CMe)_8(pdol)_4]$	**(57)**
$[Fe_{10}Na_2O_6(OH)_4(O_2CPh)_{10}(chp)_6(H_2O)_2(Me_2CO)_2]$	**(58)**
$(NEt_4)[Fe_{11}O_4(O_2CPh)_{10}(thme)_4(dmhp)_2Cl_4]$	**(59)**
$[Fe_9O_4(OH)_5(heia)_6(Hheia)_2]$	**(60)**
$[Ni_{12}(chp)_{12}(O_2CMe)_{12}(thf)_6(H_2O)_6]$	**(61)**
$[Ni(hmp)(CH_3OH)Cl]_4$	**(62)**
$[Ni(hmp)(CH_3CH_2OH)Cl]_4$	**(63)**
$[Ni(hmp)((CH_3)_3CCH_2CH_2OH)Cl]_4$	**(64)**
$[Ni(H_2thme)(MeCN)]_4(NO_3)_4$	**(65)**

Table 1 (continued)

$[Ni_{21}(cit)_{12}(OH)_{10}(H_2O)_{10}]^{16-}$ (Δ – Λ)	**(66)**
$[Ni_{21}(cit)_{12}(OH)_{10}(H_2O)_{10}]^{16-}$ (Δ – Δ + Λ – Λ)	**(67)**
$[Ni_8Na_2(N_3)_{12}(^t BuPhCO_2)_2(mpo)_4(Hmpo)_6(EtOAc)_6]$	**(68)**
$[Co_4(hmp)_4(MeOH)_4Cl_4]$	**(69)**
$(NMe_4)_3Na[Co_6(cit)_4(H_2O)_{10}]$	**(70)**
$[V_4O_2(O_2CEt)_7(pic)_2]^-$	**(71a)**
$[V_4O_2(O_2CEt)_7(bpy)_2]^+$	**(71b)**
$[(Me_3tacn)_6MnMo_6(CN)_{18}]^{2+}$	**(72)**
$[Mn^{II}(tmphen)_2]_3[Mn^{III}(CN)_6]_2$	**(73)**
$K[(5-Brsalen)_2(H_2O)_2Mn_2Cr(CN)_6]$	**(74)**
$K[(5-Brsalen)_2(H_2O)_2Mn_2Fe(CN)_6]$	**(75)**
$(NEt_4)[(salmen)_2(MeOH)_2Mn_2Fe(CN)_6]$	**(76)**
$[(dipropy2)_2Ni_3Cr(CN)_3]^{3+}$	**(77)**
$[(MnCl)_4(Re(triphos)(CN)_3)_4]$	**(78)**
$[(Tp)(H_2O)_6Cu_6Fe_8(CN)_{24}](ClO_4)_4$	**(79)**
$[Co^{II}_9(W^V(CN)_8)_6(CH_3OH)_{24}]$	**(80)**
$[Co^{II}_9(Mo^V(CN)_8)_6(CH_3OH)_{24}]$	**(81)**
$[CuTbL(hfac)_2]_2$	**(82)**
$[Dy_6Mn_6(H_2shi)_4(Hshi)_{10}(CH_3OH)_{10}(H_2O)_2]$	**(83)**
$[Mn_{11}Dy_4O_8(OH)_6(OMe)_2(O_2Ph)_{16}(NO_3)_5(H_2O)_3]$	**(84)**
$[MnCu(5-Br-sap)_2(MeOH)]$	**(85)**
$[Mn_2Ni_2Cl_2(salpa)_2]$	**(86)**
$[Mn_8Fe_4O_{12}(O_2CCH_2Cl)_{16}(H_2O)_4]$	**(87)**
$(NBu_2)[Pc_2Tb]$	**(88)**
$(NBu_2)[Pc_2Dy]$	**(89)**
$[Co(SCN)_2(dabp)_4]$	**(90)**

References

1. Caneschi A, Gatteschi D, Sessoli R, Barra AL, Brunel LC, Guillot M (1991) J Am Chem Soc 113:5873
2. Sessoli R, Tsai HL, Schake AR, Wang SY, Vincent JB, Folting K, Gatteschi D, Christou G, Hendrickson DN (1993) J Am Chem Soc 115:1804
3. Sessoli R, Gatteschi D, Caneschi A, Novak MA (1993) Nature 365:141
4. Lis T (1980) Acta Cryst B36:2042
5. Hendrickson DN, Christou G, Ishimoto H, Yoo J, Brechin EK, Yamaguchi A, Rumberger EM, Aubin SMJ, Sun ZM, Aromí G (2001) Polyhedron 20:1479
6. Fernandez JF, Luis F, Bartolome J (1998) Phys Rev Lett 80:5659
7. Bokacheva L, Kent AD, Walters MA (2001) Polyhedron 20:1717
8. Wernsdorfer W, Bhaduri S, Tiron R, Hendrickson DN, Christou G (2002) Phys Rev Lett 89
9. Leuenberger MN, Loss D (2001) Nature 410:789

10. Barra AL, Gatteschi D, Sessoli R (2000) Chem-Eur J 6:1608
11. Barra AL (2001) Appl Magn Reson 21:619
12. Bouwen A, Caneschi A, Gatteschi D, Goovaerts E, Schoemaker D, Sorace L, Stefan M (2001) J Phys Chem B 105:2658
13. Zipse D, North JM, Dalal NS, Hill S, Edwards RS (2003) Phys Rev B 68
14. Morello A, Bakharev ON, Brom HB, de Jongh L (2004) J Magn Magn Mater 272–276:1015
15. Morello A, Bakharev ON, Brom HB, de Jongh LJ (2003) Polyhedron 22:1745
16. Procissi D, Suh BJ, Lascialfari A, Borsa F, Caneschi A, Cornia A (2002) J Appl Phys 91:7173
17. Achey RM, Kuhns PL, Moulton WG, Reyes AP, Dalal NS (2001) Polyhedron 20:1745
18. Carretta S, Liviotti E, Amoretti G, Caciuffo R, Caneschi A, Gatteschi D (2002) Phys Rev B 65
19. Andres H, Basler R, Güdel HU, Aromí G, Christou G, Buttner H, Ruffle B (2000) J Am Chem Soc 122:12469
20. McInnes EJL, Pidcock E, Oganesyan VS, Cheesman MR, Powell AK, Thomson AJ (2002) J Am Chem Soc 124:9219
21. Ruiz E, Cano J, Alvarez S (2005) Chem-Eur J 11:4767
22. Kortus J, Pederson MR, Baruah T, Bernstein N, Hellberg CS (2003) Polyhedron 22:1871
23. Park K, Pederson MR, Richardson SL, Aliaga-Alcalde N, Christou G (2003) Phys Rev B 68
24. Benelli C, Cano J, Journaux Y, Sessoli R, Solan GA, Winpenny REP (2001) Inorg Chem 40:188
25. Clark AE, Davidson ER (2001) J Chem Phys 115:7382
26. Murugesu M, Habrych M, Wernsdorfer W, Abboud KA, Christou G (2004) J Am Chem Soc 126:4766
27. Sokol JJ, Hee AG, Long JR (2002) J Am Chem Soc 124:7656
28. Schelter EJ, Prosvirin AV, Dunbar KR (2004) J Am Chem Soc 126:15004
29. Osa S, Kido T, Matsumoto N, Re N, Pochaba A, Mrozinski J (2004) J Am Chem Soc 126:420
30. Zaleski CM, Depperman EC, Kampf JW, Kirk ML, Pecoraro VL (2004) Angew Chem Int Ed 43:3912
31. Mishra A, Wernsdorfer W, Abboud KA, Christou G (2004) J Am Chem Soc 126:15648
32. Winpenny REP (2002) J Chem Soc-Dalton Trans 1
33. Mallah T, Auberger C, Verdaguer M, Veillet P (1995) J Chem Soc-Chem Commun 61
34. Marvaud V, Decroix C, Scuiller A, Tuyeras F, Guyardduhayon C, Vaissermann J, Marrot M, Gonnet F, Verdaguer M (2003) Chem-Eur J 9:1692
35. Breuning E, Ruben M, Lehn JM, Renz F, Garcia Y, Ksenofontov V, Gutlich P, Wegelius E, Rissanen K (2000) Angew Chem Int Ed 39:2504
36. Peng SM, Wang CC, Jang YL, Chen YH, Li FY, Mou CY, Leung MK (2000) J Magn Magn Mater 209:80
37. Zhao L, Xu ZQ, Grove H, Milway VA, Dawe LN, Abedin TSM, Thompson LK, Kelly TL, Harvey RG, Miller DO, Weeks L, Shapter JG, Pope KJ (2004) Inorg Chem 43:3812
38. Pardo E, Morales-Osorio I, Julve M, Lloret F, Cano J, Ruiz-García R, Pasán J, Ruiz-Perez C, Ottenwaelder X, Jurneaux Y (2004) Inorg Chem 43:7594
39. Aromí G, Aubin SMJ, Bolcar MA, Christou G, Eppley HJ, Folting K, Hendrickson DN, Huffman JC, Squire RC, Tsai HL, Wang S, Wemple MW (1998) Polyhedron 17:3005

40. Eppley HJ, Aubin SMJ, Wemple MW, Adams DM, Tsai HL, Grillo VA, Castro SL, Sun ZM, Folting K, Huffman JC, Hendrickson DN, Christou G (1997) Mol Cryst Liq Cryst Sci Technol Sect A: Mol Cryst Liq Cryst 305:167
41. Gatteschi D, Sessoli R, Cornia A (2000) Chem Commun 725
42. Marvaud V, Herrera JM, Barilero T, Tuyeras F, Garde R, Scuiller A, Decroix C, Cantuel M, Desplanches C (2003) Mon Chem 134:149
43. Long JR In: Yang P (ed) (2003) Chemistry of Nanostructural Materials. World Scientific, Hong Kong
44. Barra AL, Brunel LC, Gatteschi D, Pardi L, Sessoli R (1998) Accounts Chem Res 31:460
45. Gatteschi D (2000) J Phys Chem B 104:9780
46. Basler R, Boskovic C, Chaboussant G, Güdel HU, Murrie M, Ochsenbein ST, Sieber A (2003) Chem Phys Chem 4:910
47. Mertes KM, Suzuki Y, Sarachik MP, Myasoedov Y, Shtrikman H, Zeldov E, Rumberger EM, Hendrickson DN, Christou G (2003) Solid State Commun 127:131
48. Thomas L, Lionti F, Ballou R, Gatteschi D, Sessoli R, Barbara B (1996) Nature 383:145
49. Friedman JR, Sarachik MP, Tejada J, Maciejewski J, Ziolo R (1996) J Appl Phys 79:6031
50. Wernsdorfer W, Sessoli R (1999) Science 284:133
51. Eppley HJ, Tsai HL, de Vries N, Folting K, Christou G, Hendrickson DN (1995) Am Chem Soc J 117:301
52. Aubin SMJ, Sun ZM, Eppley HJ, Rumberger EM, Guzei IA, Folting K, Gantzel PK, Rheingold AL, Christou G, Hendrickson DN (2001) Inorg Chem 40:2127
53. Petukhov K, Hill S, Chakov NE, Abboud KA, Christou G (2004) Phys Rev B 70:054426
54. Coronado E, Torment-Aliaga A, Gaita-Arino A, Giminez-Saiz C, Romero FM, Wernsdorfer W (2004) Angew Chem Int Ed 43:6152
55. Condorelli GG, Motta A, Fragala IL, Giannazzo F, Raineri V, Caneschi A, Gatteschi D (2004) Angew Chem Int Ed 43:4081
56. Cornia A, Fabretti AC, Pacchioni M, Zobbi L, Bonacchi D, Caneschi A, Gatteschi D, Biagi R, Del Pennino U, De Renzi V, Gurevich L, Van der Zant HSJ (2003) Angew Chem Int Ed 42:1645
57. Artus P, Boskovic C, Yoo J, Streib WE, Brunel LC, Hendrickson DN, Christou G (2001) Inorg Chem 40:4199
58. Boskovic C, Pink M, Huffman JC, Hendrickson DN, Christou G (2001) J Am Chem Soc 123:9914
59. Chakov NE, Wernsdorfer W, Abboud KA, Hendrickson DN, Christou G (2003) Dalton Trans 2243
60. Pacchioni M, Cornia A, Fabretti AC, Zobbi L, Bonacchi D, Caneschi A, Chastanet G, Gatteschi D, Sessoli R (2004) Chem Commun 2604
61. Loss D, Divincenzo DP, Grinstein G, Awschalom DD, Smyth JF (1993) Physica B 189:189
62. Soler M, Chandra SK, Ruiz D, Huffman JC, Hendrickson DN, Christou G (2001) Polyhedron 20:1279
63. Soler M, Wernsdorfer W, Abboud KA, Huffman JC, Davidson ER, Hendrickson DN, Christou G (2003) J Am Chem Soc 125:3576
64. Christou G (1989) Accounts Chem Res 22:328
65. Tasiopoulos AT, Vinslava A, Wernsdorfer W, Abboud KA, Christou G (2004) Angew Chem Int Ed 43:2117
66. Sun ZM, Ruiz D, Rumberger E, Incarvito CD, Folting K, Rheingold AL, Christou G, Hendrickson DN (1998) Inorg Chem 37:4758

67. Soler M, Wernsdorfer W, Folting K, Pink M, Christou G (2004) J Am Chem Soc 126:2156
68. Boskovic C, Brechin EK, Streib WE, Folting K, Bollinger JC, Hendrickson DN, Christou G (2002) J Am Chem Soc 124:3725
69. Brechin EK, Soler M, Davidson J, Hendrickson DN, Parsons S, Christou G (2002) Chem Commun 2252
70. Piligkos S, Rajaraman G, Soler M, Kirchner N, van Slageren J, Bircher R, Parsons S, Güdel H-U, Kortus K, Wernsdorfer W, Christou G, Brechin EK (2005) J Am Chem Soc 127:5572
71. Brechin EK, Soler M, Christou G, Helliwell M, Teat SJ, Wernsdorfer W (2003) Chem Commun 1276
72. Rajaraman G, Murugesu M, Sanudo EC, Soler M, Wernsdorfer W, Helliwell M, Muryn C, Raftery J, Teat SJ, Christou G, Brechin EK (2004) J Am Chem Soc 126:15445
73. Murugesu M, Raftery J, Wernsdorfer W, Christou G, Brechin EK (2004) Inorg Chem 43:4203
74. Brechin EK, Sanudo EC, Wernsdorfer W, Boskovic C, Yoo J, Hendrickson DN, Yamaguchi A, Ishimoto H, Concolino TR, Rheingold AL, Christou G (2005) Inorg Chem 44:502
75. Murugesu M, Wernsdorfer W, Abboud KA, Christou G (2005) Angew Chem Int Ed 44:892
76. Yoo J, Brechin EK, Yamaguchi A, Nakano M, Huffman JC, Maniero AL, Brunel LC, Awaga K, Ishimoto H, Christou G, Hendrickson DN (2000) Inorg Chem 39:3615
77. Yang EC, Harden N, Wernsdorfer W, Zakharov L, Brechin EK, Rheingold AL, Christou G, Hendrickson DN (2003) Polyhedron 22:1857
78. Yoo J, Yamaguchi A, Nakano M, Krzystek J, Streib WE, Brunel LC, Ishimoto H, Christou G, Hendrickson DN (2001) Inorg Chem 40:4604
79. Foguet-Albiol D, O'Brien TA, Wernsdorfer W, Moulton B, Zaworotko MJ, Abboud KA, Christou G (2005) Angew Chem Int Ed 44:897
80. Sanudo EC, Grillo VA, Knapp MJ, Bollinger JC, Huffman JC, Hendrickson DN, Christou G (2002) Inorg Chem 41:2441
81. Cooper SR, Calvin M (1977) J Am Chem Soc 99:6623
82. Rajaraman G, Sanudo EC, Helliwell M, Piligkos S, Wernsdorfer W, Christou G, Brechin EK (2005) Polyhedron 24:2450
83. Scott RTW, Parsons S, Murugesu M, Wernsdorfer W, Christou G, Brechin EK (2005) Chem Commun 2083
84. Tasiopoulos AJ, Wernsdorfer W, Moulton B, Zaworotko MJ, Christou G (2003) J Am Chem Soc 125:15274
85. Low DM, Jones LF, Bell A, Brechin EK, Mallah T, Riviere E, Teat SJ, McInnes EJL (2003) Angew Chem Int Ed 42:3781
86. Zhong ZJ, Seino H, Mizobe Y, Hidai M, Fujishima A, Ohkoshi S, Hashimoto K (2000) J Am Chem Soc 122:2952
87. Dendrinou-Samara C, Alexiou M, Zaleski CM, Kampf JW, Kirk ML, Kessissoglou DP, Pecoraro VL (2003) Angew Chem Int Ed 42:3763
88. Rumberger EM, Zakharov LN, Rheingold AL, Hendrickson DN (2004) Inorg Chem 43:6531
89. Tasiopoulos AJ, Wernsdorfer W, Abboud KA, Christou G (2004) Angew Chem Int Ed 43:6338
90. King P, Wernsdorfer W, Abboud KA, Christou G (2004) Inorg Chem 43:7315
91. Price DJ, Batten SR, Moubaraki B, Murray KS (2002) Chem Commun 762

92. Barra AL, Caneschi A, Gatteschi D, Goldberg DP, Sessoli R (1999) J Solid State Chem 145:484
93. Dance I, Fisher K (1994) Prog Inorg Chem 41:637
94. Koizumi S, Nihei M, Nakano M, Oshio H (2005) Inorg Chem 44:1208
95. Harden NC, Bolcar MA, Wernsdorfer W, Abboud KA, Streib WE, Christou G (2003) Inorg Chem 42:7067
96. Oshio H, Hoshino N, Ito T, Nakano M, Renz F, Gutlich P (2003) Angew Chem Int Ed 42:223
97. Milios CJ, Raptopoulou CP, Terzis A, Lloret F, Vicente R, Perlepes SP, Escuer A (2004) Angew Chem Int Ed 43:210
98. Telfer SG, Kuroda R (2003) Coord Chem Rev 242:33
99. Gavrilova AL, Bosnich B (2004) Chem Rev 104:349
100. van Koningsbruggen PJ, Maeda Y, Oshio H (2004) In: Spin Crossover in Transition Metal Compounds I. Topics in Current Chemistry 233:259
101. Cozzi PG (2004) Chem Soc Rev 33:410
102. Oshio H, Hoshino N, Ito T, Nakano M (2004) J Am Chem Soc 126:8805
103. Boskovic C, Bircher R, Tregenna-Piggott PLW, Güdel HU, Paulsen C, Wernsdorfer W, Barra AL, Khatsko E, Neels A, Stoeckli-Evans H (2003) J Am Chem Soc 125:14046
104. Miyakasa H, Clérac R, Wernsdorfer W, Lecren L, Bonhomme C, K S, Yamashita M (2004) Angew Chem Int Ed 43:2801
105. Jones LF, Rajaraman G, Brockman J, Murugesu M, Sanudo EC, Raftery J, Teat SJ, Wernsdorfer W, Christou G, Brechin EK, Collison D (2004) Chem-Eur J 10:5180
106. Bashkin JS, Chang HR, Streib WE, Huffman JC, Hendrickson DN, Christou G (1987) J Am Chem Soc 109:6502
107. Li Q, Vincent JB, Libby E, Chang HR, Huffman JC, Boyd PDW, Christou G, Hendrickson DN (1988) Angew Chem Int Ed Engl 27:1731
108. Hendrickson DN, Christou G, Schmitt EA, Libby E, Bashkin JS, Wang SY, Tsai HL, Vincent JB, Boyd PDW, Huffman JC, Folting K, Li QY, Streib WE (1992) J Am Chem Soc 114:2455
109. Wemple MW, Tsai HL, Folting K, Hendrickson DN, Christou G (1993) Inorg Chem 32:2025
110. Wang SY, Folting K, Streib WE, Schmitt EA, McCusker JK, Hendrickson DN, Christou G (1991) Angew Chem Int Ed Engl 30:305
111. Aubin SMJD, Dilley NR, Wemple MW, Maple MB, Christou G, Hendrickson DN (1998) J Am Chem Soc 120:839
112. Wemple MW, Tsai H-L, Folting K, Hendrickson DN, Christou G (1995) J Am Chem Soc 117:7275
113. Aromí G, Bhaduri S, Artus P, Folting K, Christou G (2002) Inorg Chem 41:805
114. Wemple MW, Adams DM, Hagen KS, Folting K, Hendrickson DN, Christou G (1995) J Chem Soc Chem Commun 1591
115. Aromí G, Wemple WM, Aubin JS, Folting K, Hendrickson ND, Christou G (1998) J Am Chem Soc 120:5850
116. Wang SW, Wemple WM, Yoo J, Folting K, Huffman JC, Hagen KS, Hendrickson DN, Christou G (2000) Inorg Chem 39:1501
117. Aliaga-Alcalde N, Edwards RS, Hill SO, Wernsdorfer W, Folting K, Christou G (2004) J Am Chem Soc 126:12503
118. Evangelisti M, Luis F, Mettes FL, Aliaga N, Aromí G, Christou G, de Jongh LJ (2003) Polyhedron 22:2169
119. Andres H, Basler R, Güdel HU, Aromí G, Christou G, Buttner H, Ruffle B (2000) J Am Chem Soc 122:12469

120. Wernsdorfer W, Aliaga-Alcalde N, Hendrickson DN, Christou G (2002) Nature 416:406
121. Hill S, Edwards RS, Aliaga-Alcalde N, Christou G (2003) Science 302:1015
122. Xu B, Chasteen ND (1991) J Biol Chem 266:19965
123. Feig AL, Lippard SJ (1994) Chem Rev 94:759
124. Barra AL, Debrunner P, Gatteschi D, Schulz CE, Sessoli R (1996) Europhys Lett 35:133
125. Papaefthymiou GC (1992) Phys Rev B 46:10366
126. Wieghardt K, Pohl K, Jibril I, Huttner G (1984) Angew Chem Int Ed 23:77
127. Winpenny REP (2001) Adv Inorg Chem 52:1
128. Tabernor J, Jones LF, Heath SL, Muryn C, Aromí G, Ribas J, Brechin EK, Collison D (2004) Dalton Trans 975
129. Canada-Vilalta C, O'Brien TA, Brechin EK, Pink M, Davidson ER, Christou G (2004) Inorg Chem 43:5505
130. Delfs C, Gatteschi D, Pardi L, Sessoli R, Wieghardt K, Hanke D (1993) Inorg Chem 32:3099
131. Pontillon Y, Caneschi A, Gatteschi D, Sessoli R, Ressouche E, Schweizer J, Lelievre-Berna E (1999) J Am Chem Soc 121:5342
132. Caciuffo R, Amoretti G, Murani A, Sessoli R, Caneschi A, Gatteschi D (1998) Phys Rev Lett 81:4744
133. Sangregorio C, Ohm T, Paulsen C, Sessoli R, Gatteschi D (1997) Phys Rev Lett 78:4645
134. Ohm T, Sangregorio C, Paulsen C (1998) Eur Phys J B 6:195
135. Ohm T, Sangregorio C, Paulsen C (1998) J Low Temp Phys 113:1141
136. Wernsdorfer W, Ohm T, Sangregorio C, Sessoli R, Mailly D, Paulsen C (1999) Phys Rev Lett 82:3903
137. Price DJ, Lionti F, Ballou R, Wood PT, Powell AK (1999) Philos Trans R Soc Lond Ser A-Math Phys Eng Sci 357:3099
138. Goodwin JC, Sessoli R, Gatteschi D, Wernsdorfer W, Powell AK, Heath SL (2000) J Chem Soc-Dalton Trans 1835
139. Affronte A, Sessoli R, Gatteschi D, Wernsdorfer W, Lasjaunias JC, Heath SL, Powell AK, Fort A, Rettori A (2004) J Phys Chem Solids 65:745
140. Evangelisti M, Luis F, Mettes FL, Aliaga N, Aromí G, Alonso JJ, Christou G, de Jongh LJ (2004) Phys Rev Lett 93
141. Caneschi A, Cornia A, Fabretti AC, Foner S, Gatteschi D, Grandi R, Schenetti L (1996) Chem-Eur J 2:1379
142. Abbati GL, Cornia A, Fabretti AC, Malavasi W, Schenetti L, Caneschi A, Gatteschi D (1997) Inorg Chem 36:6443
143. Barra AL, Caneschi A, Cornia A, de Biani FF, Gatteschi D, Sangregorio C, Sessoli R, Sorace L (1999) J Am Chem Soc 121:5302
144. Cornia A, Fabretti AC, Garrisi P, Mortalo C, Bonacchi D, Gatteschi D, Sessoli R, Sorace L, Wernsdorfer W, Barra AL (2004) Angew Chem Int Ed 43:1136
145. Moragues-Canovas M, Riviere P, Ricard L, Paulsen C, Wernsdorfer W, Rajaraman G, Brechin EK, Mallah T (2004) Adv Mater 16:1101
146. Nihei M, Hoshino N, Ito T, Oshio H (2003) Polyhedron 22:2359
147. Yang EC, Wernsdorfer W, Hill S, Edwards RS, Nakano M, Maccagnano S, Zakharov LN, Rheingold AL, Christou G, Hendrickson DN (2003) Polyhedron 22:1727
148. Taft KL, Caneschi A, Pence LE, Delfs CD, Papaefthymiou GC, Lippard SJ (1993) J Am Chem Soc 115:11753
149. Yang EC, Hendrickson DN, Wernsdorfer W, Nakano M, Zakharov LN, Sommer RD, Rheingold AL, Ledezma-Gairaud M, Christou G (2002) J Appl Phys 91:7382

150. Shoner SC, Power PP (1992) Inorg Chem 31:1001
151. Oshio H, Hoshino N, Ito T (2000) J Am Chem Soc 122:12602
152. Boudalis AK, Donnadieu B, Nastopoulos V, Modesto Clemente-Juan J, Mari A, Sanakis Y, Tuchagues J-P, Perlepes SP (2004) Angew Chem Int Ed 43:2266
153. Papaefstathiou GS, Escuer A, Vicente R, Font-Bardia M, Solans X, Perlepes SP (2001) Chem Commun 2414
154. Tsohos A, Dionyssopoulou S, Raptopoulou CP, Terzis A, Bakalbassis EG, Perlepes SP (1999) Angew Chem Int Ed 38:983
155. Papaefstathiou GS, Perlepes SP, Escuer A, Vicente R, Font-Bardia M, Solans X (2001) Angew Chem Int Ed 40:884
156. Benelli C, Parsons S, Solan GA, Winpenny REP (1996) Angew Chem Int Ed Engl 35:1825
157. Jones LF, Brechin EK, Collison D, Helliwell M, Mallah T, Piligkos S, Rajaraman G, Wernsdorfer W (2003) Inorg Chem 42:6601
158. Gorun SM, Papaefthymiou GC, Frankel RB, Lippard SJ (1987) J Am Chem Soc 109:3337
159. Jones LE, Batsanov A, Brechin EK, Collison D, Helliwell M, Mallah T, McInnes EJL, Piligkos S (2002) Angew Chem Int Ed 41:4318
160. Powell GW, Lancashire HN, Brechin EK, Collison D, Heath SL, Mallah T, Wernsdorfer W (2004) Angew Chem Int Ed 43:5772
161. Papaefstathiou GS, Perlepes SP (2002) Comments Inorganic Chem 23:249
162. Krzystek J, Park JH, Meisel MW, Hitchman MA, Stratemeier H, Brunel LC, Telser J (2002) Inorg Chem 41:4478
163. Rogez G, Rebilly JN, Barra AL, Sorace L, Blondin G, Kirchner N, Duran M, van Slageren J, Parsons S, Ricard L, Marvilliers A, Mallah T (2005) Angew Chem Int Ed 44:1876
164. Blake AJ, Grant CM, Parsons S, Rawson JM, Winpenny REP (1994) J Chem Soc-Chem Commun 2363
165. Andres H, Basler R, Blake AJ, Cadiou C, Chaboussant G, Grant CM, Güdel HU, Murrie M, Parsons S, Paulsen C, Semadini F, Villar V, Wernsdorfer W, Winpenny REP (2002) Chem-Eur J 8:4867
166. Benelli C, Blake AJ, Brechin EK, Coles SJ, Graham A, Harris SG, Meier S, Parkin A, Parsons S, Seddon AM, Winpenny REP (2000) Chem-Eur J 6:883
167. Cadiou C, Murrie M, Paulsen C, Villar V, Wernsdorfer W, Winpenny REP (2001) Chem Commun 2666
168. Boyd PDW, Martin RL, Schwarzenbach G (1988) Aust J Chem 41:1449
169. Halcrow MA, Sun JS, Huffman JC, Christou G (1995) Inorg Chem 34:4167
170. Aromí G, Batsanov AS, Christian P, Helliwell M, Roubeau O, Timco GA, Winpenny REP (2003) Dalton Trans 4466
171. Moragues-Cánovas M, Helliwell M, Ricard L, Rivière E, Wernsdorfer W, Brechin EK, Mallah T (2004) Eur J Inorg Chem 2219
172. Kambe K (1950) J Phys Soc Jpn 5:48
173. Bino A, Shweky I, Cohen S, Bauminger ER, Lippard SJ (1998) Inorg Chem 37:5168
174. Ochsenbein ST, Murrie M, Rusanov E, Stoeckli-Evans H, Sekine C, Güdel HU (2002) Inorg Chem 41:5133
175. Dearden AL, Parsons S, Winpenny REP (2001) Angew Chem Int Ed 40:151
176. Brechin EK, Harris SG, Harrison A, Parsons S, Whittaker AG, Winpenny REP (1997) Chem Commun 653
177. Ribas J, Escuer A, Monfort M, Vicente R, Cortes R, Lezama L, Rojo T (1999) Coord Chem Rev 195:1027

178. Tandon SS, Thompson LK, Manuel ME, Bridson JN (1994) Inorg Chem 33:5555
179. Karmakar TK, Ghosh BK, Usman A, Fun H-K, Rivière E, Mallah T, Aromí G, Chandra SK (2005) Inorg Chem 44:2391
180. Bell A, Aromí G, Teat SJ, Wernsdorfer W, Winpenny REP (2005) Chem Commun 2808
181. Aromí G, Batsanov AS, Christian P, Helliwell M, Parkin A, Parsons S, Smith AA, Timco GA, Winpenny REP (2003) Chem-Eur J 9:5142
182. Dimitrou K, Sun JS, Folting K, Christou G (1995) Inorg Chem 34:4160
183. Caneschi A, Gatteschi D, Lalioti N, Sessoli R, Sorace L, Tangoulis V, Vindigni A (2002) Chem-Eur J 8:286
184. Gubina KE, Ovchynnikov VA, Swiatek-Kozlowska J, Amirkhanov VM, Sliva TY, Domasevitch KV (2002) Polyhedron 21:963
185. Brechin EK, Harris SG, Parsons S, Winpenny REP (1996) Chem Commun 1439
186. Tong ML, Zheng SL, Shi JX, Tong YX, Lee HK, Chen XM (2002) J Chem Soc-Dalton Trans 1727
187. Murrie M, Teat SJ, Stoeckli-Evans H, Güdel HU (2003) Angew Chem Int Ed 42:4653
188. Castro SL, Streib WE, Sun JS, Christou G (1996) Inorg Chem 35:4462
189. Karet GB, Sun ZM, Heinrich DD, McCusker JK, Folting K, Streib WE, Huffman JC, Hendrickson DN, Christou G (1996) Inorg Chem 35:6450
190. Page EM (1998) Coord Chem Rev 172:111
191. Aromí G, Bhaduri S, Artus P, Huffman JC, Hendrickson DN, Christou G (2002) Polyhedron 21:1779
192. McCusker JK, Vincent JB, Schmitt EA, Mino ML, Shin K, Coggin DK, Hagen PM, Huffman JC, Christou G, Hendrickson DN (1991) J Am Chem Soc 113:3012
193. Ellis T, Glass M, Harton A, Folting K, Huffman JC, Vincent JB (1994) Inorg Chem 33:5522
194. Chaudhuri P, Rentschler E, Birkelbach F, Krebs C, Bill E, Weyhermuller T, Florke U (2003) Eur J Inorg Chem 541
195. Castro SL, Sun ZM, Bollinger JC, Hendrickson DN, Christou G (1995) J Chem Soc-Chem Commun 2517
196. Sun ZM, Grant CM, Castro SL, Hendrickson DN, Christou G (1998) Chem Commun 721
197. Ferlay S, Mallah T, Ouahes R, Veillet P, Verdaguer M (1995) Nature 378:701
198. Berlinguette CP, Vaughn D, Canada-Vilalta C, Galan-Mascaros JR, Dunbar KR (2003) Angew Chem Int Ed 42:1523
199. Choi HJ, Sokol JJ, Long JR (2004) Inorg Chem 43:1606
200. Wang S, Zuo JL, Zhou HC, Choi HJ, Ke YX, Long JR, You XZ (2004) Angew Chem Int Ed 43:5940
201. Song Y, Zhang P, Ren X-M, Shen X-F, Li Y-Z, You X-Z (2005) J Am Chem Soc 127:3708
202. Larionova J, Gross M, Pilkington M, Andres H, Stoeckli-Evans H, Güdel HU, Decurtins S (2000) Angew Chem Int Ed 39:1605
203. Ruiz E, Rajaraman G, Alvarez S, Gillon B, Stride J, Clerac R, Larionova J, Decurtins S (2005) Angew Chem Int Ed 44:2711
204. Oshio H, Nihei M, Yoshida A, Nojiri H, Nakano M, Yamaguchi A, Karaki Y, Ishimoto H (2005) Chem-Eur J 11:843
205. Oshio H, Nihei M, Koizumi S, Shiga T, Nojiri H, Nakano M, Shirakawa N, Akatsu M (2005) J Am Chem Soc 127:4568
206. Yang C-I, Hui-Lien Tsai H-L, Lee G-H, Wur C-S, Yang S-F (2005) Chem Lett 34:288
207. Schake AR, Tsai HL, Webb RJ, Folting K, Christou G, Hendrickson DN (1994) Inorg Chem 33:6020

208. Ishikawa N, Sugita M, Ishikawa T, Koshihara S, Kaizu Y (2003) J Am Chem Soc 125:8694
209. Ishikawa N, Sugita M, Ishikawa T, Koshihara S, Kaizu Y (2004) J Phys Chem B 108:11265
210. Gutlich P, Hauser A (1990) Coord Chem Rev 97:1
211. Bleuzen A, Lomenech C, Escax V, Villain F, Varret F, Moulin CCD, Verdaguer M (2000) J Am Chem Soc 122:6648
212. Takayama K, Matsuda K, Irie M (2003) Chem-Eur J 9:5605
213. Herrera JM, Marvaud V, Verdaguer M, Marrot J, Kalisz M, Mathoniere C (2004) Angew Chem Int Ed 43:5468
214. Karasawa S, Zhou GY, Morikawa H, Koga N (2003) J Am Chem Soc 125:13676

Struct Bond (2006) 122: 69–102
DOI 10.1007/430_034

Published online: 7 April 2006

Spectroscopy of Single-Molecule Magnets

Eric J.L. McInnes

School of Chemistry, The University of Manchester, Manchester M13 9PL, UK
eric.mcinnes@manchester.ac.uk

Abstract A review of spectroscopic studies of single-molecule magnets (SMMs) is presented, covering Electron Paramagnetic Resonance (EPR; field and frequency swept), Nuclear Magnetic Resonance (NMR), Inelastic Neutron Scattering (INS), and Magnetic Circular Dichroism (MCD; UV/Vis and X-ray) spectroscopies. The range of important information available from each technique on this class of compounds is highlighted, including, for example, cluster spin states, zero-field splitting parameters, exchange coupling constants, nuclear spin dynamics, etc. The review covers the literature from the first spectroscopic studies of SMMs (ca. 1990) to date (May 2005).

Keywords Single molecule magnets · Spectroscopy · EPR · NMR · INS · MCD

1 Introduction

The spectroscopic techniques covered in this review are: Electron Paramagnetic Resonance (EPR), Nuclear Magnetic Resonance (NMR), Inelastic

Neutron Scattering (INS), and Magnetic Circular Dichroism (MCD) spectroscopies. The main advantage of spectroscopic techniques in the study of single molecule magnets (SMMs) is their ability to probe molecular or even single-ion magnetic or electronic properties *directly*, as opposed to techniques that measure bulk properties such as magnetic susceptibility or magnetisation. This allows much more accurate determination of, for example, the spin-Hamiltonian parameters that control magnetic memory or quantum tunnelling of magnetisation (QTM) effects in SMMs. This review is not intended to give an in-depth overview of the principles of these techniques or their instrumentation, rather to highlight important work that has been done exploiting these techniques as applied to SMMs and related molecules. Some of their particular advantages (and disadvantages) in this area are discussed. The vast majority of spectroscopic studies of SMMs have been performed on just two molecules, namely $[Mn_{12}O_{12}(O_2CMe)_{16}(H_2O)_4]\cdot 2MeCO_2H\cdot 4H_2O$ ("Mn12") and $[Fe_8O_2(OH)_{12}(tacn)_6]Br_8\cdot 9H_2O$ ("Fe8"), and these are reviewed separately under each spectroscopic heading below, followed by reviews of work on other SMMs and other relevant large spin ground state systems. I have not tried to be exhaustive in listing every paper that has been published on SMMs using these techniques, nor have I attempted to cover every spectroscopic technique used to probe SMMs (e.g., Mossbauer spectroscopy is only mentioned in passing). Inevitably, I may have missed some papers that the reader deems to be important in such a large literature.

2 EPR Spectroscopy

SMMs have an energy barrier to relaxation of magnetisation due to the combination of a large ground state electronic spin S with a significant negative zero-field splitting (ZFS) within this ground state. Because both S and the ZFS parameters D, E, etc. are in principle EPR observables, in addition to the electronic g-values, EPR spectroscopy was one of the first spectroscopic techniques to be exploited for probing the electronic and therefore magnetic structure of these molecules directly. For example, EPR gave the first direct measurement of D in the $S = 10$ ground state of Mn12 and gave the first unambiguous determination of the ground state value of S in Fe8 (see below). The $\Delta M_S = \pm 1$ selection rule implies that in the high-field limit 2S allowed transitions will be observed for a molecule with spin state S at a given orientation with respect to the applied magnetic field. The separations of these lines are a function of the ZFS parameters. Moreover, at sufficiently high magnetic fields and consequently large Zeeman splittings, cf. the available thermal energy kT (k = Boltzmann constant, T = temperature), Boltzmann depopulation effects as a function of temperature can be used to determine the sign of D directly. In addition, single crystal measurements can give the orientation of

the principal axes of the D-tensor and g-matrix with respect to the crystal and molecular geometries. Single crystal measurements are only possible because of the high sensitivity of EPR and this requirement of only small amounts of material is a major advantage of EPR over complementary techniques such as INS (see below). The development of high-frequency/field (HF) EPR techniques in the last two decades has been of crucial importance to the study of SMMs, and indeed these materials have been one of the drivers for the development of HF techniques. Because of the large values of S and/or $|D|$, the EPR spectra can be spread over many Tesla in magnetic field. Therefore, in principle, EPR at sufficiently high frequency and extending to sufficiently high magnetic fields allows measurement of the entire spectrum and/or measurement in the high field limit to simplify the spectra. Many of the advantages of HF-EPR as applied to high spin ground state molecules and large $|D|$ systems have been laid out in an excellent review article by Gatteschi and co-workers [1].

2.1 EPR of Mn12 and Related Compounds

The first reported EPR study of Mn12, and the first of any SMM, was by Caneschi et al. [2] on a loose-powdered sample at frequencies and applied magnetic fields in the ranges 246 to 525 GHz (using a far-infrared laser source) and 0 to 12 T, respectively. Although they only observed a limited number of features, they were able to conclude that they were observing the fine structure arising from transitions within the $S = 10$ cluster ground state, that the axial ZFS parameter $|D|$ was ca. 0.5 cm^{-1} in magnitude, and that it was negative in sign. Barra et al. reported a more complete study on a pressed pellet of Mn12 (to prevent orientation in the applied magnetic field) at frequencies and fields up to 525 GHz and 25 T, respectively (Fig. 1) [3].

The spectra appear axial with the lowest and highest field components of the parallel and perpendicular manifolds, respectively, most intense. At 4 K and at 525 GHz the Zeeman splittings are sufficiently large that only the $M = -10$ sublevel of the cluster $S = 10$ ground state is significantly populated, and the only observed transitions are $M = -10$ to -9 for the parallel and perpendicular field orientations (note M_S is not a good quantum number for the perpendicular manifold). On warming the sample, new features grow in to higher field in the parallel manifold, and to lower field in the perpendicular manifold. These are EPR transitions originating from higher energy M sublevels (-9, -8, ...) which become successively thermally populated. The thermal population/depopulation behaviour can be used to determine the sign of D; in Mn12 this is confirmed as negative. The spectra were simulated using the spin-Hamiltonian:

$$H = \beta \mathbf{H} \cdot \mathbf{g} \cdot \mathbf{S} + D\left[S_z^2 - \frac{1}{3}S(S+1)\right] + B_4^0 O_4^0 + B_4^4 O_4^4 , \quad (1)$$

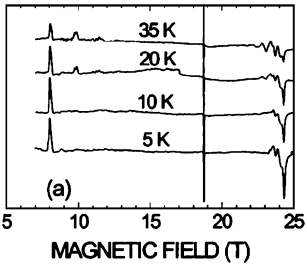

Fig. 1 525 GHz EPR spectra of an immobilized powder sample of Mn12 at variable temperature. The *narrow signal* is a dpph marker ($g = 2.0037$). At 5 K, only the $M = -10$ sublevel of the $S = 10$ ground state is populated, and only two transitions are observed. The low-field feature corresponds to $M_S = -10$ to -9 transition for the subset of molecules with their molecular z axes parallel to the applied magnetic field; the high-field feature corresponds to the equivalent transition for the subset of molecules with their z axes perpendicular to the applied field. As the temperature increases, higher energy M states are populated successively, and further transitions are observed ($M = -9$ to -8, etc.). Figure from [3]

where β is the electronic Bohr magneton, and

$$O_4^0 = 35S_z^4 - [30S(S+1) - 25]\, S_z^2 - 6S(S+1) + 3S^2(S+1)^2$$

$$O_4^4 = \frac{1}{2}\left(S_+^4 + S_-^4\right) ,$$

with $g_{||} = 1.93$, $g_\perp = 1.96$, $D = -0.46\ \mathrm{cm}^{-1}$, $B_4^0 = -2.2 \times 10^{-5}\ \mathrm{cm}^{-1}$ and $B_4^4 = \pm 4 \times 10^{-5}\ \mathrm{cm}^{-1}$. They could not fit the spectra without inclusion of the 4th order terms, and found that B_4^0 and B_4^4 mostly affected the parallel and perpendicular regions of the spectra, respectively. The importance of the 4^{th} order terms for the mechanism of QTM is discussed in this work: B_4^4 mixes sublevels differing in M_S by multiples of four and, hence, can connect sublevels on either side of the barrier to reversal of magnetization, as is necessary for QTM. The first single crystal EPR study of Mn12 was reported by Hill et al. [4]. They studied the frequency (35–115 GHz in regular increments) dependence of the resonances (applied field parallel to the molecular z axis) to construct a field-frequency diagram, and determine $D = -0.53\ \mathrm{cm}^{-1}$, $B_4^0 = -1.8 \times 10^{-5}\ \mathrm{cm}^{-1}$ and $B_4^4 = -8.8 \times 10^{-5}\ \mathrm{cm}^{-1}$, although they later revised these values based on more detailed single crystal work (see below). [Note these values are for the parameters as defined in spin-Hamiltonian (Eq. 1); [4] uses a different form of Eq. 1.] However, they state that the fit to the data is not as good for the transitions between the M_S sublevels at the top of the energy barrier, and in particular noted several peaks that could not be fit with the standard $S = 10$ Hamiltonian, and suggested that this implied an inadequacy of this model (see below).

Hill, Dalal and co-workers have published a series of papers studying linewidth and line position effects in single crystals of Mn12 and Fe8, oriented

with the applied field along the molecules' easy axis of magnetization [5–9], and have reviewed this work themselves [10].

In both SMMs they find a strong increase in linewidth with increasing $|M_S|$ (the sublevel from which the EPR transition originates), due to D-strain effects—a discrete distribution of D-values in the clusters. In Mn12 there is only a weak temperature dependence on linewidth in the range 10–40 K (cf. Fe8, see below). Fitting the linewidths gives a distribution in D of ca. 1.8% for Mn12, although the authors note that this can vary from sample to sample which suggests that crystal defects may be a possible source of the strain effects. The same authors also present a model for the slight asymmetry observed in the EPR lineshapes, based on a random (static) distribution of the orientation of molecular z axes with respect to the crystal c axis (in addition to D-strain) [9]. Cornia et al. discussed one possible source of crystal "defects" by showing that disorder in the hydrogen bonding network due to the solvents of crystallisation in crystals of Mn12 gives rise to a symmetry breaking effect on the global 4-fold symmetry of the molecule [11]. The two $MeCO_2H$ molecules are disordered over the four possible positions on the in-plane 2-fold axes perpendicular to the C_4. This leads to six different isomers of Mn12 in the lattice, only 2 of which retain 4-fold symmetry. Using angular overlap calculations, they estimate the spin-Hamiltonian parameters for each of these sites, and the misorientation between the molecular z axes and the crystal c axis (0–0.4°), and use these to provide an improved simulation of the 525 GHz EPR spectra. D-values are calculated ranging from – 0.527 to – 0.554 cm^{-1} and importantly the lower symmetry sites can have an additional, non-zero rhombic term $E(S_x^2 - S_y^2)$ in spin-Hamiltonian (Eq. 1). The significant calculated values of E (in the range 0 to 0.003 cm^{-1}) have potentially important consequences for QTM because this rhombic term can mix M_S sublevels differing by ± 2.

Further EPR spectroscopic support for this model came from Hill et al. [12, 13], from detailed single crystal measurements in transverse applied magnetic fields. In this work a fourfold symmetry in the resonance field variations with angle was observed, thus providing good evidence for, and a direct measure of, the B_4^4 term as 3.2×10^{-5} cm^{-1} (they also give $D = -0.455$ and $B_4^0 = -2.0 \times 10^{-5}$ cm^{-1}) [12]. Furthermore, they detected a partially resolved splitting of the main EPR transitions, and plots of the EPR linewidths and splittings (shoulders were observed on each main resonance) versus angle in the hard plane also revealed a fourfold symmetric pattern. They argue that this effect is actually disorder-induced twofold rhombic distortions ($E \neq 0$) as described by Cornia. Because the four possible (in-plane) $MeCO_2H$ sites are 90° apart, a 50 : 50 mixture is produced of molecules with their hard axes of magnetization along one of two perpendicular axes and an apparent fourfold symmetry is observed in the angular variation. The same group performed a much more detailed study of this phenomenon and further incorporated discrete angles of tilting of the molecular, with respect to the crystal, easy

axes of magnetization into their model [13]. These were necessary in order to reproduce their single crystal (0.1° resolution) data in the hard plane of the crystal and selected narrow (±10°) ranges of angles from this hard plane towards the easy axis. With the magnetic field applied in the hard plane, the EPR transitions can be considered in two groups: those between states originating from the same zero-field ($\pm M_S$; M_S ceases to be a good quantum number in non zero-field) doublet, and those between states which originate from adjacent zero-field doublets. These two types of resonance should have very different applied frequency dependences – specifically, the latter should not be observable below frequencies of ca. 90 GHz. However, they are. The same authors had observed these "anomalous" EPR peaks previously (see above) [4], and had argued that they were due to a low lying $S = 9$ excited state with a very similar D to the $S = 10$ ground state [14]. Amigó had argued that that such anomalous peaks could be due to stress induced dislocations in the crystal lattice introducing a rhombic E term [15]. In this latest work, Hill argued that this behaviour could be explained by the tilting of the molecular z axes, and the consequent longitudinal component of the transverse applied field for the subsets of tilted molecules [13]. Modelling the single crystal data revealed the tilting to be in two distinct orthogonal orientations from the crystal easy axis, as predicted by the Cornia model. The authors conclude that this tilting, which when the applied field is along the crystal easy axis of magnetization would give rise to subsets of molecules with transverse field components, could be the mechanism allowing QTM between M_S sublevels differing by an odd integer value (which cannot be explained by non-zero E or B_4^4).

Aubin et al. have probed the effect of "Jahn–Teller isomerism" in Mn12 – isomers differing by the orientation of the Jahn–Teller distortion axis of one or more of the Mn(III) ions – on the cluster spin-Hamiltonian parameters by EPR on $[Mn_{12}O_{12}(O_2C_6H_4\text{-}p\text{-}Me)_{16}(H_2O)_4].HO_2C_6H_4Me$ and $[Mn_{12}O_{12}(O_2C_6H_4\text{-}p\text{-}Me)_{16}(H_2O)_4].3H_2O$ [16]. The former material has one Jahn–Teller axis approximately perpendicular to the easy axis of magnetization of the molecule, leading to much faster magnetization relaxation properties, and is found to have a slightly lower axial ZFS parameter D compared to the latter form (– 0.46 and – 0.49 cm^{-1}, respectively).

Two EPR studies have appeared on one-electron reduced forms of Mn12. Kuroda–Sawa et al. [17] determined that $[Fe(C_5Me_5)][Mn_{12}O_{12}(O_2C_6F_5)_{16}(H_2O)_4].2H_2O$ has a $S = 21/2$ ground state from magnetisation data, and HF-EPR gave $D = -0.35\ cm^{-1}$. [Note that later studies on a salt of $[Mn_{12}O_{12}(O_2C_6F_5)_{16}(H_2O)_4]^-$ showed the ground state to be $S = 19/2$, although the INS determined D value agrees well. See below.] In contrast, Aubin found $(PPh_4)[Mn_{12}O_{12}(O_2CEt)_{16}(H_2O)_4]$ to have a $S = 19/2$ ground state [18]. They measured the ZFS from EPR at 328 and 438 GHz on a polycrystalline sample that had been oriented in a 10 T magnetic field, and then applied a correction to account for the misalignment of the molecular and crystal easy axes

of magnetisation to give $D = -0.62\ \mathrm{cm}^{-1}$, considerably larger than accepted values for Mn12 variants.

Finally, HF-EPR spectra have been reported for some interesting chemical variants of Mn12 (other than simple substitution of carboxylates). Artues et al. have substituted four carboxylates for four nitrates in $[Mn_{12}O_{12}(NO_3)_4(O_2CCH_2^tBu)_{12}(H_2O)_4]$, which still has an $S = 10$ ground state, and find $g = 1.99$, $D = -0.46\ \mathrm{cm}^{-1}$ and $B_4^0 = -2.0 \times 10^{-5}\ \mathrm{cm}^{-1}$, very similar to Mn12 itself, from 330 GHz EPR [19]. Hachisuka et al. have prepared $[Mn_{11}CrO_{12}(O_2CMe)_{16}(H_2O)_4].2MeCO_2H.4H_2O$, where one of the Mn(III) ions in Mn12 has been replaced by Cr(III) [20]. This material has an $S = 19/2$ ground state, as expected from replacement of an $S = 2$ ion with $S = 3/2$, but the ZFS parameters are identical within experimental error. This is unexpected because an isotropic Cr(III) has replaced an anisotropic Mn(III) – they suggest that the Cr(III) ions only substitute one of the two distinct Mn(III) sites, and this site does not contribute to the cluster anisotropy.

2.2 EPR of Fe8 and Related Compounds

The first HF-EPR (245 GHz) study of Fe8 was reported in 1996 by Barra et al. [21]. In this important study, EPR was used to confirm unambiguously the nature of the cluster ground state as $S = 10$ (previous magnetic studies had left $S = 9$ as a possibility). Powder spectra at 5 K gave an essentially *three* line spectrum (due to significant population of only the $M = S$ sublevels, as with Mn12), and this immediately reveals the *rhombic* nature of the ZFS – the x and y manifolds are no longer degenerate, in contrast to the higher symmetry Mn12. At higher temperatures the fine structure grows in a pattern which confirms the value of $S = 10$ and the sign of D as negative (Fig. 2).

Simulations using the Hamiltonian (Eq. 1), but including the rhombic E term and neglecting 4th order terms, gave $D = -0.191\ \mathrm{cm}^{-1}$, $|E| = 0.032\ \mathrm{cm}^{-1}$, and $g_x = g_y = 2.00$, $g_z = 2.04$. The same group later published single crystal studies at 95 to 285 GHz [22]. Simulations now included the rhombic and 4th order terms in Hamiltonian (Eq. 2),

$$H = \beta \mathbf{H} \cdot \mathbf{g} \cdot \mathbf{S} + D\left[S_z^2 - \frac{1}{3}S(S+1)\right] + E\left(S_x^2 - S_y^2\right) + B_4^0 O_4^0 + B_4^2 O_4^2 + B_4^4 O_4^4\,, \tag{2}$$

where the additional operator is

$$O_4^2 = \frac{1}{4}\left\{\left[7S_z^2 - S(S+1) - 5\right]\left(S_+^2 + S_-^2\right) + \left(S_+^2 + S_-^2\right)\left[7S_z^2 - S(S+1) - 5\right]\right\}\,,$$

giving much better fits than previously reported, with $D = -0.205\ \mathrm{cm}^{-1}$, $|E| = 0.038\ \mathrm{cm}^{-1}$, $B_4^0 = 1.6 \times 10^{-6}\ \mathrm{cm}^{-1}$, $B_4^2 = -5 \times 10^{-6}\ \mathrm{cm}^{-1}$, $B_4^4 = -8 \times 10^{-6}\ \mathrm{cm}^{-1}$, and $g_x = g_y = g_z = 2.00$. However, they noted significant discrepancies in the

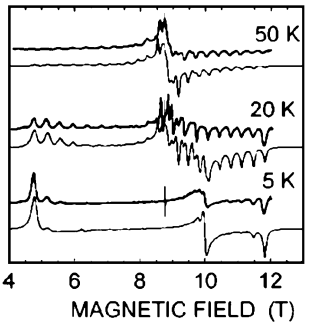

Fig. 2 245 GHz EPR spectra of a polycrystalline sample of Fe8 at variable temperature. In contrast to Mn12, which has global axial symmetry ($x = y$), in Fig. 1, three transitions are observed at the lowest temperature ($M = -10$ to -9 within the $S = 10$ ground state) for the lower symmetry Fe8, corresponding to the x, y and z orientations of the ZFS tensor, giving direct evidence for a non-zero E term in the spin-Hamiltonian. Upper spectra are experimental, lower spectra are simulated. Figure from [21]

high field region of the spectra, which they suggested may be due to a breakdown of the single spin model and the presence of a relatively low-lying $S = 9$ excited state. From the single crystal studies, the principal axis of the ZFS (the easy axis of magnetization for negative D) is found to be approximately perpendicular to the best plane of the 8 Fe(III) ions. Maccagnano et al. reported single crystal studies in the same year, using multiple frequencies between ca. 60 and 160 GHz at low temperatures [23]. By constructing frequency-resonance field plots and extrapolating back to zero-field, they claim much greater accuracy in measurement of ZFS parameters.

Both Barra [22] and Hill [23] had noted pronounced D-strain effects in the single-crystal spectra of Fe8, as were also observed in Mn12 (see above). However, in contrast to Mn12, the linewidths and line positions of Fe8 are strongly temperature dependent as well, as discussed by Hill, Dalal et al. [5–10]. In Mn12 these temperature effects are masked by the much larger distribution in D (ca. threefold larger than in Fe8). Both the linewidths and the line positions (measured at 116 GHz between 2 and 35 K) show a complicated temperature dependence that also depends on the transition (i.e., M_S values) involved. Importantly, they argue that both effects are due to inter-cluster spin–spin interactions, and find that in order to quantitatively fit these behaviours they had to invoke both dipolar and exchange interactions, and the best fit was found with an effective dipole field of 20 G (an antiferromagnetic interaction) and an exchange coupling constant of – 7 G (a ferromagnetic interaction).

Further, direct, evidence of the $S = 9$ excited state in Fe8 came form Zipse et al. [24]. In single crystal studies at 131 GHz with the applied field along the easy axis of magnetization, a regular series of peaks was observed between

the $S = 10$ peaks and with considerably lower intensity. The temperature dependence of the weaker peaks was consistent with a thermally populated excited state ca. 17 cm^{-1} above the $S = 10$ ground state (much lower energy than had been suggested from magnetic susceptibility data). The ZFS parameters for the $S = 9$ state were found to be $D = -0.19$ cm^{-1}, $E = 0.03$ cm^{-1} and $B_4^4 = -0.9 \times 10^{-6}$ cm^{-1}.

Finally, Barra et al. studied the effect on the spin-Hamiltonian parameters of substitution of the counter-ions in Fe8, in $[Fe_8O_2(OH)_{12}(tacn)_6]Br_{4.3}(ClO_4)_{3.7}.6H_2O$ [25]. This material has a higher molecular symmetry (C_i) than the parent (all bromide) salt, although the disorder of the counter-ions leads to four different isomers in the lattice. EPR spectra at 190 GHz behave similarly to those of Fe8 itself, and analysis leads to the parameters $D = -0.200$ cm^{-1}, $E = -0.042$ cm^{-1}, $B_4^0 = 3 \times 10^{-7}$ cm^{-1}, $B_4^2 = -4 \times 10^{-6}$ cm^{-1} and $B_4^4 = -8 \times 10^{-6}$ cm^{-1}. The major difference with Fe8 is the significantly larger rhombic term E, which is consistent with the much larger QTM rate observed for the perchlorate analogue at very low temperatures.

2.3 EPR of other SMMs and Molecules of Interest

Several interesting studies have been reported on the tetranuclear Fe(III) SMM $[Fe_4(OMe)_6(dpm)_6]$ ("Fe4"; Hdpm = dipivaloylmethane) and derivatives, which are based on a centered triangle of Fe(III) ions and have an $S = 5$ ground state that arises from the antiferromagnetic coupling between the central and apical irons [26–29]. Barra et al. determined the ground state ZFS parameters $D = -0.2$ cm^{-1} and $E = 0$ with $g_{||} = 2.003$ and $g_\perp = 2.023$ from 245 GHz spectra on a pressed pellet, and they determined that the dipolar contribution to this ground state ZFS was significant [26]. Single crystal 95 GHz studies were performed on the same molecule by Bouwen et al. [27], who showed that the principal axis of the cluster ZFS tensor, and hence the molecular easy axis of magnetization, was approximately perpendicular to the plane of the four Fe(III) ions. Their studies also revealed the presence of three distinct molecular species resulting from disorder of the ligand sets on two of the apical Fe(III) ions. These isomers have subtly distinct D-values ranging from -0.175 to -0.206 cm^{-1}. The full set of spin-Hamiltonian terms was determined for the dominant species as: $g_z = 2.009$, $g_x = 1.995$, $g_y = 1.997$, $D = -0.206$ cm^{-1}, $E = 0.010$ cm^{-1}, $B_4^0 = -1.1 \times 10^{-5}$ cm^{-1}, $B_4^2 = -0.8 \times 10^{-4}$ cm^{-1} and $B_4^4 = -0.4 \times 10^{-4}$ cm^{-1}. D-strain effects were also studied in this work. Cornia et al. prepared the analogous complexes $[Fe_4L_2(dpm)_6]$ where the six methoxides that bridge the central and apical Fe(III) ions in Fe4 have been replaced by the deprotonated tris-alcohol ligands $MeC(CH_2OH)_3$ and $PhC(CH_2OH)_3$ [28]. 230 GHz EPR shows these clusters to have much larger ground state $|D|$-values than the parent Fe4, with $D = -0.445$ and -0.42 cm^{-1}, respectively, in agreement with the higher

blocking temperatures found for these complexes. They ascribed this effect to the different trigonal distortions, and consequent different single-ion ZFSs, of the central Fe(III) ions [29].

Several tetranuclear Mn clusters have been found to behave as SMMs, and several of these have been studied by EPR. Christou and co-workers report the heterovalent $Mn(III)_3Mn(IV)$ cluster $[Mn_4O_3Cl(O_2CMe)_3(dbm)_3]$ (Hdbm = dibenzoylmethane) which is based on a $\{Mn_4O_3Cl\}$ heterocubane structure with a pseudo-C_3 axis passing through the Mn(IV) ion and Cl, and the Cl^- ion sitting at the intersection of the 3 Mn(III) Jahn–Teller distortion axes [30]. EPR at frequencies between 220 and 440 GHz on oriented (by strong magnetic field) polycrystalline samples, corrected for the canting angle of 4.5° between the C_3 axes of the individual molecules (expected to be the principal axes of their *D*-tensors) and the external magnetic field, gives $D = -0.53\ cm^{-1}$ and $B_4^0 = -7.5 \times 10^{-5}\ cm^{-1}$ in the $S = 9/2$ ground state. The related $Mn(III)_3Mn(IV)$, $S = 9/2$ ground-state clusters $[Mn_4O_3(O_2CC_6H_4\text{-}p\text{-}R)_4(dbm)_3]$ (R = H, Me) have lower symmetry (approximately C_S) due to replacement of Cl^- with a η^2,μ_3-carboxylate, opening up one edge of the cubane [31]. This results in a better alignment of the Mn(III) Jahn–Teller axes with the cluster easy axis of magnetization, and hence significantly larger *D*-values ($D = -0.567$ and $-0.646\ cm^{-1}$ for X = H and Me, respectively), as determined by EPR. The second consequence of the lower symmetry is to allow a significant *E*-term ($E = 0.140\ cm^{-1}$ for X = Me), leading to very fast QTM in zero-field. Other members of the $Mn(III)_3Mn(IV)$ family of SMMs include $[Mn_4O_3(OSiMe_3)_3(O_2CEt)_3(dbm)_3]$ and $[Mn_4O_3Cl_4(O_2CEt)_3(py)_3]_2$ (py = pyridine) [32, 33], both of which have crystallographic or pseudo-threefold symmetry. In the former, the molecules are well isolated in the crystal lattice and single crystal studies at 138 GHz give the parameters $D = -0.484\ cm^{-1}$, $B_4^4 = -6.2 \times 10^{-5}\ cm^{-1}$, $g = 2.00$ for the $S = 9/2$ ground state [32]. (Related molecules had been studied previously at X-band [34].) In the latter, the molecules exist as discrete head-to-head dimers (the dimer having S_6 symmetry), H-bonded via intermolecular terminal Mn – Cl ... H – C(pyridine) contacts [33]. This results in a weak antiferromagnetic exchange interaction between the two halves of the dimer. Thus, each molecule experiences an "exchange bias" field due to the other half of the dimer. This had been proposed previously as the reason that QTM steps are *not* observed at zero magnetic field in single crystal magnetization vs. applied field loops [35]. Single crystal EPR spectra at 145 GHz in the temperature range 2–20 K, with the applied field parallel to the dimer S_6 axis, reveal extra structure over that expected for isolated $S = 9/2$ molecules, due to transitions between coupled states of the dimer. The spectra can be modeled by including an isotropic exchange term JS_1S_2 in the spin-Hamiltonian (where S_1 and S_2 refer to the ground-state spins of the independent Mn_4 clusters), giving: $D = -0.521\ cm^{-1}$, $B_4^0 = -4 \times 10^{-5}\ cm^{-1}$, $g_z = 2$ with $J = 0.083\ cm^{-1}$. They note that, although the derived *J* is isotropic, it is the transverse part of the exchange interaction

that gives rise to the extra structure. Thus EPR gives a direct measure of the "exchange bias" interaction, and the possibility of exploiting such interactions for construction of quantum logic gates is discussed. The same group present evidence (unexpected structure in single crystal EPR spectra) for a similar phenomenon in the tetranuclear, heterocubane Ni(II) SMMs, $[Ni(hmp)_4(ROH)_4Cl_4]$ (Hhmp = 2-hydroxy-6-methylpyridine; R = Me, Et, ^{t}Bu), where the isolated clusters have $S = 4$ ground states and are arranged in a diamond-like topology in the crystal lattice [36, 37]. However, the authors also state that the extra structure may alternatively be due to more than one distinct form of the cluster in the lattices. The dominant species (for R = ^{t}Bu) gives $D = -0.577\ cm^{-1}$, $B_4^0 = -1.2 \times 10^{-4}\ cm^{-1}$, $g_z = 2.3$. They argue from complementary magnetization studies, and because the extra EPR structure is more pronounced (and linewidths broader) for smaller R groups, that the former explanation is more likely.

Non-cubane based Mn4 SMMs have been reported by Yoo et al. [38, 39] and Boskovic et al. [40]. Yoo's compounds $[Mn_4(O_2CMe)_2(Hpdm)_6](ClO_4)_2$ (H_2pdm = pyridine-2,6-dimethanol) [38] and $[Mn_4(hmp)_6Br_2(H_2O)_2]Br_2.2H_2O$ [39], are based on planar $Mn(II)_2Mn(III)_2$ rhombus-like cores. The former complex was isolated as its $2MeCN.Et_2O$ solvate. However, this was found to desolvate, and subsequently to form the $2.5H_2O$ hydrate, on exposure to air. Magnetic susceptibility and magnetization studies indicated the desolvated complex had an $S = 8$ ground state while the hydrate had $S = 9$. Fits of HF-EPR spectra of a magnetic field-oriented powder sample of the hydrate were attempted assuming both $S = 8$ and 9 ground states. The latter was favoured on the basis of the more sensible determined g-values, giving $S = 9$, $D = -0.31\ cm^{-1}$, $B_4^0 = 2.0 \times 10^{-5}\ cm^{-1}$, $g_z = 1.99$ ($g_z = 2.10$ was found assuming $S = 8$). $[Mn_4(hmp)_6Br_2(H_2O)_2]Br_2.2H_2O$ is also found to have an $S = 9$ ground state from magnetization and HF-EPR studies, with $D = -0.346\ cm^{-1}$, $E = 0.086$, $B_4^0 = 1.2 \times 10^{-5}\ cm^{-1}$, $g_z = 1.999$. The authors note that the rhombicity parameter $|E/D| = 0.25$ is unusually high for Mn clusters. Boskovic's $[Mn_4X_4L_4]$ (X = Cl or Br; H_2L = salicylidene-2-ethanolamine) are based on $Mn(III)_4$ squares, where ferromagnetic exchange gives $S = 8$ ground states [40]. HF-EPR on oriented polycrystalline samples, although limited in resolution, give a good estimate of the ground state ZFS, at $D \approx -0.2\ cm^{-1}$ with $g_z = 1.96$. Like Christou's Mn4 SMMs [33], these complexes are "exchange biased" by intermolecular interactions although these are not manifest in the EPR spectra.

Possibly the highest spin state to give rise to a fine structure resolved EPR spectrum to date is from the $Mn(II)_6Mn(III)_4$ cluster $(Me_4N)[Mn_{10}O_4(biphen)_4Cl_{12}]$, studied by Barra et al. [41]. Previous magnetic susceptibility and magnetization measurements revealed a large spin ground state, but the exact value was ambiguous with $12 \leq S \leq 14$. EPR at 245 GHz on a magnetic field-oriented polycrystalline sample unambiguously gave $S = 12$ with $D = -0.047\ cm^{-1}$, $E = 0$, $g_{||} = 1.974$ and $g_\perp = 1.983$. Despite the very high S,

no SMM behaviour was observed for this complex down to 1.5 K, due to the very low value of $|D|$. The $S = 6$ ground state dodecametallic Cr(III) cluster $[Cr_{12}O_9(OH)_3(O_2CCMe_3)_{15}]$ has been studied by EPR [42–44]. 90 and 180 GHz data on powders and single crystals confirm the value of S and give $D = +0.088\ cm^{-1}$, $E = 0$, $g_{||} = 1.965$ and $g_{\perp} = 1.960$ (consistent with the high D_3 molecular symmetry) – here, the positive sign of D prevents SMM behaviour, and the authors argue that this is due to the relative orientations of the local and cluster ZFS axes where the single-ion ZFS (estimated from optical data) is negative in sign [42, 43]. Piligkos et al. have studied the same molecule by parallel mode EPR, at X-band on a single crystal at 5 K (the first parallel modulation study of non-biological very high spin clusters), demonstrating the possible selection of different transitions at a given EPR frequency by exploiting the different selection rules of perpendicular and parallel mode modulation [44]. There have been a few recent reports of heterometallic SMMs, some of which have been studied by EPR. A notable recent example, which is also one of the smallest SMMs, is the bimetallic Mn(III)Cu(II) complex $[MnCu(5\text{-Br-sap})_2(MeOH)]$ where 5-Br-sapH_2 = 5-bromo-2-salicylideneamino-1-propanol [45]. The metal ions are strongly ferromagnetically coupled, giving an $S = 5/2$ ground state, due to the orthogonality of the magnetic orbitals [the Mn(III) Jahn–Teller axis being perpendicular to the Cu(II) coordination plane]. Nicely resolved EPR spectra at 342 GHz between 4.2 and 60 K are presented, allowing characterization of the ground state $D = -1.81\ cm^{-1}$. The data are analysed using a microscopic spin-Hamiltonian – possible because of the small size of the problem – allowing determination of the single-ion Mn and Cu g-values, and the Mn(III) ZFS using vector coupling techniques in the assumption that this is the only contribution to the observed cluster ZFS. The S and D values are consistent with the molecule behaving as an SMM at very low temperatures.

2.4 Frequency Domain EPR Spectroscopy of SMMs

One very powerful variant on the EPR technique is the frequency swept, static field experiment. This has become possible at the high frequencies suitable for studying many SMMs, in the range ca. 30 GHz to 1.5 THz (ca. 1 to 50 cm^{-1} energy range). Of course this experiment can be performed in zero applied magnetic field, allowing determination of ZFS parameters in zero-field, without the considerable demands on amount and nature of sample in other zero-field techniques such as INS. A short review of the benefits of this technique in the study of molecular magnetic materials has been published by van Slageren et al. [46]. The first report of frequency-swept EPR on a SMM was Muhkin's Mn12 study in 1998 [47]. They reported 3–33 cm^{-1} spectra, between 2 and 20 K, on a pressed polycrystalline sample in zero applied field. At the lowest temperatures, at which only the $M_S = \pm 10$ sublevels of the clus-

ter ground state are populated, only one transition is observed, at ca. 10 cm^{-1} which corresponds well to the expected energy gap between the $M_S = \pm 10$ and ± 9 sublevels with D of ca. – 0.5 cm^{-1}. As the temperature is increased new peaks are found to lower energy as higher energy sublevels are populated (Fig. 3).

The data were fitted to give $D = -0.460$ cm^{-1} and $B_4^0 = -2.19 \times 10^{-5}$ cm^{-1} [parameters as defined in Hamiltonian (Eq. 1); converted from the equivalent Hamiltonian used in [47]. Note the Zeeman term is redundant in zero-field.], in excellent agreement with Barra's [3] EPR data. The authors also noted much higher energy transitions between 30–35 cm^{-1}, which they suggest may be due to an excited spin state. Dressel et al. explored the frequency domain EPR spectra in static, non-zero applied magnetic fields [48]. They monitored the $M_S = +10$ to $+9$ transition at 2.6 K in an applied magnetic field of + 0.45 T (only $M_S = +10$ is populated). This occurs at ca. 10.4 cm^{-1}, shifted from its zero-field position of 10.1 cm^{-1} due to the Zeeman effect. On rapid reversal of the applied field to – 0.45 T, the transition from the metastable $M_S = +10$ sublevel to + 9 occurs at ca. – 9.8 cm^{-1}; the intensity of this transition decreases with time as the system relaxes to the $M_S = -10$ ground state, and the $M_S = -10$ to – 9 transition grows in at ca. 10.4 cm^{-1}. This experiment was then repeated at 1.96 K, below the blocking temperature, and using larger

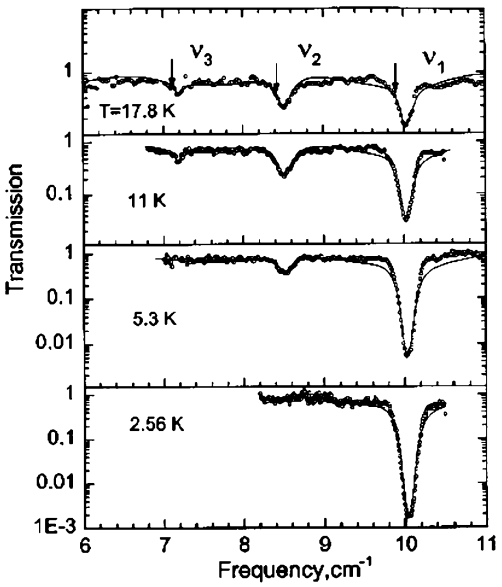

Fig. 3 Frequency domain EPR spectra of pressed pellet of Mn12 at variable temperature and zero applied magnetic field. At 2 K, only $M_S = \pm 10$ are populated and only the $M_S = \pm 10$ to ± 9 transition is observed; $M_S = \pm 9$ to ± 8, etc. observed on warming. Figure from [46]

applied fields (±0.9 T). Now, at specific frequencies above and below the zero-field frequency, dips or peaks in the spectra are observed which correspond to faster relaxation from the metastable state. These "tunnel dips" are due to QTM effects at the sublevel crossing between $M_S = +10$ and -9. Vongtragool et al. [49, 50] have studied the linewidths of the frequency domain EPR spectra of Mn12, including *D*-strain effects and their consequences on inhomogeneous broadening.

Fe8 and its partially perchlorate substituted counter-ion form, $[Fe_8O_2(OH)_{12}(tacn)_6]Br_{4.3}(ClO_4)_{3.7}.6H_2O$, have also been studied by frequency domain EPR, by Gorshunov and co-workers [51]. As had been found previously via field-swept EPR [25], the most significant difference between the two derivatives was in the rhombic *E* parameters: $D = -0.205\ cm^{-1}$, $E = 0.0307\ cm^{-1}$ for Fe8 and $D = -0.207\ cm^{-1}$, $E = 0.05\ cm^{-1}$ for the perchlorate analogue.

Brechin and co-workers have recently reported a new manganese-based SMM, the ennanuclear $[Mn_9O_7(O_2CMe)_{11}(thme)(py)_3(H_2O)_2].MeCN.Et_2O$ [H_3thme = tris-(hydroxymethyl)ethane], based on a $\{Mn(III)_4Mn(II)_2O_6\}$ ring centered on a triangular $\{Mn(IV)_3O\}$ fragment, including zero-field frequency domain EPR studies of the ZFS in the $S = 17/2$ ground state [52]. This gives $D = -0.247\ cm^{-1}$ and $B_4^0 = 4.6 \times 10^{-6}\ cm^{-1}$, in excellent agreement with INS studies (see below).

2.5
Magnetization-detected EPR of Fe8

One very recently published result must be mentioned. Petukhov et al. have reported the detection of the "EPR spectrum" of micron-sized crystals of Fe8 via their magnetization response as a function of applied magnetic field, using a Hall-probe magnetometer under either continuous wave or pulsed microwave irradiation at 118 GHz and between 1.4 and 50 K [53]. Dips are observed in the magnetization vs. field curves corresponding to resonant absorption – that is, EPR transitions. This method offers potentially extraordinary sensitivity and, furthermore, manipulation of the magnetization data in the absence and presence of the microwave radiation allows determination of the spin temperature.

3
NMR Spectroscopy

NMR has proved to be an enormously powerful tool in the study of SMMs, over and above the obvious use of characterising clusters in solution by ^1H, ^{13}C NMR studies of coordinated ligands (not covered in this review). NMR is a direct probe of the local spin dynamics of magnetic nuclei, al-

lowing determination of, for example, nuclear spin relaxation rates and their mechanism. NMR is also a microscopic probe to investigate the internal magnetic structure of the cluster, providing direct information on nuclear hyperfine interactions with the local magnetic moments (information not readily available from EPR due to the large experimental linewidths). Although the review below is focussed on SMMs (as ever the literature is dominated by Mn12 and Fe8) it should be noted that some of the very important early work on NMR of cluster complexes regarding, for example, the effect of fluctuations of local magnetic moments on nuclear spin-lattice relaxation rates [54] and $1/T_1$ enhancement due to spin level crossings [55], were on antiferromagnetically coupled rings such as the "ferric wheel" $[Fe_{10}(O_2CCH_2Cl)_{10}(OMe)_{20}]$.

3.1
NMR of Mn12 and Related Compounds

^1H and ^2D NMR studies on the archetypal SMM Mn12 appeared in 1998. Lascialfari et al. reported ^1H nuclear spin-lattice relaxation rate ($1/T_1$) studies measured as a function of temperature (10–400 K) on pressed (to avoid orientation effects in applied magnetic fields) polycrystalline samples of Mn12 [56]. The determined values were assumed be averages for the 56 protons in each cluster (which are not resolved experimentally). $1/T_1$ increased rapidly at temperatures below 100 K, which tracks the increase in χT in this temperature range due to the ordering of the local electron spins (slowing of the local spin fluctuations) towards the $S = 10$ ground state. However, on further cooling $1/T_1$ went through a maximum at ca. 60 K (observed at 87 and 200 MHz NMR frequency). No definitive explanation was offered for this, although it was suggested that it may be due to the frequency of the local spin fluctuations matching the nuclear Larmor frequency. The same group reported further $1/T_1$ studies to lower temperature (3 K) and as a function of applied magnetic field, on polycrystalline samples that had been oriented in a strong field (molecular z axes parallel to applied field) [57]. Two peaks are observed in the low temperature ^1H NMR spectra (measured at 4.7 T), due to the sixteen $-C\underline{H}_3$ groups (assumed to be coupled to Mn by a dipolar hyperfine interaction only, because the peak is unshifted from the Larmor frequency) and to coordinated $\underline{H}_2O$ (significantly shifted, and assumed to be coupled to Mn by an isotropic hyperfine interaction), respectively. The shift of the latter line plateaus below ca. 5 K indicating that the local hyperfine field is now constant as the cluster is in its $S = 10$ ground state. They further observed a maximum in $1/T_1$ (as measured by ^{1}NMR and μSR) at ca. 10–20 K, a different maximum to that observed at higher temperatures/fields. This behaviour was modeled as due to thermal fluctuations of the orientation of the total magnetization of the cluster, i.e., spin-phonon transitions between the M_S components of the $S = 10$ ground state. Such transitions re-

sult in changes in the transverse component of the local hyperfine fields at the nuclear spins via the dipolar interactions with the electronic spins. A model was derived which allows determination of the lifetimes of the individual M_S states.

In related studies, two maxima were observed in the deuteron $1/T_1$ as a function of temperature (at ca. 60 and 10 K; measured at 9 T, 58 MHz) in the ^{2}D NMR of the fully deuterated form of Mn12 by Dalal and co-workers, and they suggested that molecular motion (rotation of CD_3 groups) could be responsible for the high temperature maximum [58, 59]. Although they subsequently supported this conclusion with ^{13}C NMR studies on oriented samples of the $^{13}\underline{C}H_3$-labelled analogue of Mn12 (in which a peak is also observed in ^{13}C $1/T_1$ versus temperature at ca. 60 K) [60], they later concluded that both maxima were due to magnetization reversal processes and that the higher temperature maximum was associated with the M_S states at the top of the energy barrier [61]. In their ^{13}C NMR study, they resolved and assigned the four different $\underline{C}H_3$ group environments and concluded that there is significant electron spin density at the C nuclei on the basis that there is a significant isotropic contribution to the local hyperfine fields (determined from the orientation dependence of the spectrum, with the applied field varied from the molecular *z* axis).

Jang et al. [62] reported a method for monitoring the relaxation rate of magnetization of Mn12 (in an oriented powder) by following the NMR intensity of the unshifted ^{1}H NMR signal (see above) as a function of time after switching on a longitudinal applied field (i.e., along the molecular *z* axis, 0.5 T) at 2.5 K starting from a thermally equilibrated sample at zero-field (zero net magnetization). The same authors extended this method by monitoring the NMR intensity of the shifted lines (see below) at 2.4 K and 30.8 MHz, after starting in equilibrium conditions in an applied field and then sudden reversal of the direction of the field (by rotating the sample through 180°) [63]. The NMR spectrum is inverted because of the inversion of the local hyperfine fields, and the recovery of the system to equilibrium can be monitored at a field corresponding to one of the (Larmor) shifted NMR transitions (because these are much more strongly effected than the unshifted line). This was also monitored as a function of applied field at 2.4 K, and they found minima in T_1 at fields that correspond to M_S sublevel crossings within the $S = 10$ ground state. Thus, they had observed QTM effects via the ^{1}H NMR response. In this work they also observed better resolved ^{1}H NMR spectra (160.5 MHz and 2.4 K) than previously, with several new, weaker peaks significantly shifted from the Larmor frequency. The magnetic field shifts of all these peaks as a function of applied frequency are identical at 2.4 K, which implies that the shifts arise from the hyperfine field at the ^{1}H nuclei due to the frozen orientation of the molecular magnetization ($M_S = -10$ in the positive applied magnetic fields). The spectra could be simulated assuming the local hyperfine fields are due entirely to dipolar interactions between the nu-

clear spins and the local magnetic moments of the Mn(III) and Mn(IV) ions, modeled using the known crystal structure. This also allows assignment of the spectrum and confirmation that the local magnetic moments at Mn(IV) are oppositely aligned to those at Mn(III), as in the common description of the $S = 10$ ground state with four Mn(IV) ions "spin down" and eight Mn(III) ions "spin up".

The first ^{55}Mn NMR studies of Mn12 were reported by Goto et al. [64], recorded on a powder sample at 1.4 K in zero external field. They observed a beautifully simple spectrum, with just three resonances, related to the three different Mn sites in the Mn12 structure. The Mn(IV) ion gives a relatively sharp signal at ca. 230 MHz while the two inequivalent Mn(III) sites give broader peaks at 280 and 365 MHz. They argue that the Mn(IV) line is much sharper because of its orbital singlet nature cf., the orbital doublet Mn(III) ions (although this neglects the Jahn–Teller distortions of these ions). These conclusions were extended shortly after by Furukawa et al. by measurements on oriented powders (Fig. 4) [65].

They point out that the observation of a spectrum in zero magnetic field at 1.5 K verifies that the magnetic moment is frozen on the NMR timescale at this temperature. They argue that the Mn(IV) line is much sharper due to the much weaker quadrupole coupling due to the more symmetric electron density distribution in this near-octahedrally coordinated ion. In contrast the Jahn–Teller distortions of the Mn(III) ions gives rise to much greater

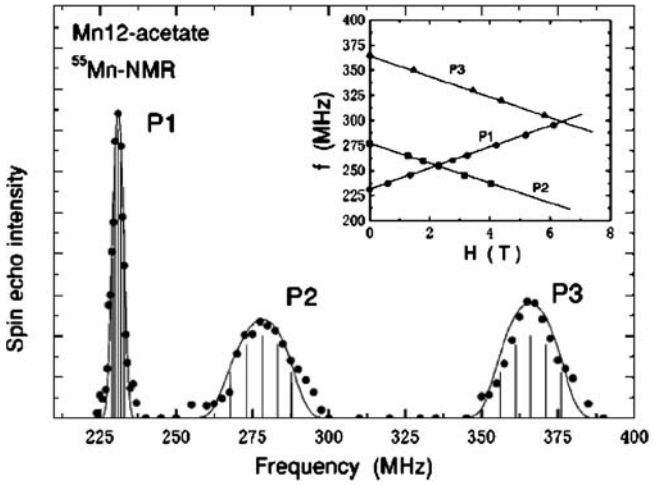

Fig. 4 ^{55}Mn NMR spectrum of an oriented polycrystalline sample of Mn12 at 1.4 K in zero applied magnetic field. The three peaks correspond to the three different Mn environments in Mn12; P1 is Mn(IV). *Inset*: applied magnetic field dependence of the resonance frequencies for P1 to P3. The Mn(IV) peak shifts in the opposite sense to the two Mn(III) peaks, indicating opposite signs of the internal magnetic fields. Figure from [63]

electric field gradients at the nuclei, and hence much larger quadrupole couplings. The two Mn(III) resonances shifted to lower frequencies on application of a longitudinal magnetic field. In contrast, the Mn(IV) peak shifts to higher frequencies (Fig. 4, inset). This implies that the internal magnetic field, and hence electron spin direction, at Mn(IV) is opposite in sign to those at Mn(III), and again this confirms the simple picture of the magnetic structure of Mn12. The local hyperfine fields at Mn are concluded to be dominated by core polarization in each case (3d orbital spin density at Mn). $1/T_1$ was measured by saturation recovery for each of the three peaks and were all found to have the same temperature dependence, as expected if the spin dynamics are controlled by the total cluster $S = 10$ moment. The temperature dependence could again by described by the fluctuating magnetic moment model – this is now being probed much more directly by monitoring the Mn nuclei rather than remote ^{1}H or ^{13}C. Kubo et al. later observed thermally assisted QTM in ^{55}Mn NMR by magnetization recovery experiments at the Mn(IV) ion at 1.65 K in crystals in a longitudinal field (Fig. 5) [66, 67].

Two Mn(IV) lines are observed in zero-field cooled samples corresponding to clusters frozen in the $M_S = +10$ and -10 sublevels (resulting in different signs of the local fields) – only one peak is observed for a field-cooled sample (only $M_S = -10$ populated). They probed cluster magnetization recovery by field cooling (1 T) a sample, sudden reversal of the field and monitoring the growth of the "second" Mn(IV) line. T_1 generally decreases with applied field due to destruction of the barrier to relaxation of magnetization, and also

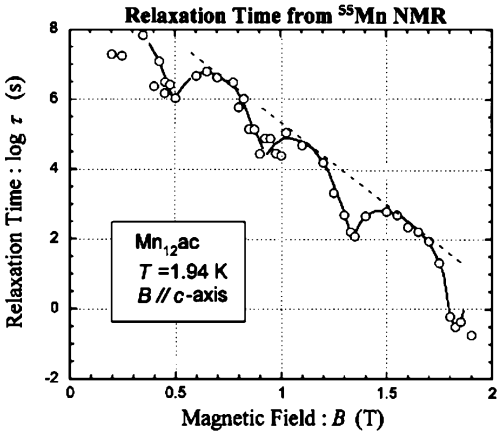

Fig. 5 Relaxation times τ for magnetization of an oriented single crystal of Mn12 at 1.94 K as a function of applied longitudinal magnetic field H. τ values are determined by monitoring the recovery in intensity of the ^{55}Mn NMR signal from Mn(IV) after field cooling (1 T) and sudden reversal of the applied magnetic field. The dips in τ vs. H are at fields corresponding to M_S sublevel crossings and are due to QTM effects. Figure from [64]

shows characteristic minima due to QTM at applied fields corresponding to M_S sublevel crossings. The same authors also argue that there is a significant dipolar contribution to the local hyperfine at Mn(III), and analyse the hyperfines in terms of the covalency of the Mn ions [68]. They estimate the hyperfine interaction in the $S = 10$ ground state at 324 G, implying a total spread of energy in each M_S level of ca. 0.3 cm^{-1}.

^{55}Mn NMR studies down to 20 mK were reported by de Jongh and coworkers [69, 70]. At these temperatures only the $M_S = \pm 10$ sublevels are populated and the magnetization relaxation is expected to be dominated by QTM between these sublevels (the "quantum regime"). Thus, the ^{55}Mn $1/T_1$ [for Mn(IV)] becomes essentially independent of temperature below 0.75 K at ca. 0.03 s^{-1}, and they note that below this temperature magnetization vs. external field hysteresis loops for Mn12 also become temperature independent. Thus, above 0.75 K the nuclear spin relaxation is dominated by spin-phonon driven fluctuations in M_S, and below this temperature it is dominated by QTM between $M_S = \pm 10$. They also express surprise at the magnitude of the relaxation rate, too large to be solely due to QTM, and suggest that an additional relaxation process is possible via inter-cluster nuclear spin diffusion to a small (defect) amount of fast relaxing molecules in the lattice (as have been observed in ac magnetic susceptibility studies) that act as a heat sink for the nuclear spin system. Evidence for this was presented later from the transverse spin–spin relaxation rate, $1/T_2$, measurements on the ^{55}Mn(IV) NMR spectrum of field-cooled and zero field-cooled samples of Mn12 [71].

Kubo et al. [72] and Furukawa et al. [73] published ^{55}Mn NMR studies on the effect of transverse (to the molecular z axis) applied magnetic fields (H_x) on T_1. Kubo observed a decrease in T_1 with increasing H_x, measured at 1.95 K and static longitudinal fields (H_z), which is explicable in terms of the reduction of the energy barrier [74]. They also observed that this decrease in T_1 with H_x is suppressed when H_z corresponds to a M_S sublevel crossing field. Furukawa also observed a general decrease in T_1 with H_x but did not observe any significant change in the difference in T_1 measured at H_z on and off these special field values [73]. Thus, there appeared to be no significant enhancement of QTM with applied H_x. The same authors extended this study and reported that $1/T_1$ increases rapidly with increasing H_x [at 1.5 K, measured at Mn(IV)] but then goes through a broad maximum at 5.5 T [74]. This behaviour is explained qualitatively by the decrease in the energy gap between the ground and first excited sublevels (which can no longer be accurately described by M_S) and the consequent increase in spin-phonon driven fluctuations of the magnetization. However, in order to quantitatively reproduce this behaviour it was also necessary to include the effect of H_x on the canting of the total cluster magnetization versus the local internal field and hence the different axes of quantization of the electron and nuclear spins. H_x gives rise to perpendicular (with respect to the nuclear spin quantisation)

components of the local field, the fluctuations of which provide an additional enhancement of $1/T_1$.

Finally, Kubo et al. [75] and Dalal et al. [76] have published comparative ^{55}Mn NMR studies of chemical variants of Mn12, namely $[Mn_{12}(O_2CPh)_{16}(H_2O)_4].2PhCO_2H$ ("Mn12Ph") and $[Mn_{12}(O_2CCH_2Br)_{16}(H_2O)_4].4CH_2Cl_2$ ("Mn12BrAc"), respectively. Seven distinct Mn resonances are observed in the NMR spectrum of an oriented powder of Mn12Ph at 1.3 K and zero field, consistent with the lower molecular symmetry cf. Mn12 [75]. Dalal demonstrates the enhanced resolution of the quadrupole structure in the three Mn peaks (Mn12BrAc also has four-fold symmetry) available from single crystal studies compared to oriented powders [76].

3.2 NMR of Fe8

The first reported NMR study of Fe8 was from Gatteschi, Lascialfari and Borsa [77] who studied the ^{1}H spectra of a powdered sample and probed the temperature dependence of the ^{1}H $1/T_1$ (by saturation recovery) down to 4 K. $1/T_1$ (an average of the values for all the inequivalent ^{1}H nuclei in the molecule) goes through a maximum with decreasing temperature, and this behaviour was used to estimate the relaxation time of the molecular magnetisation (related to the fluctuations of the local Fe magnetic moments) and compared to magnetic susceptibility data. The same group reported detailed low temperature (down to 1.3 K) ^{1}H and ^{2}D NMR studies of natural abundance and partially deuterated (all non-aliphatic protons substituted) Fe8, on collections of aligned single crystals and oriented powders [78]. At high temperatures broad single lines were observed (field-swept/fixed-frequency spectra), which resolved into highly structured spectra on decreasing temperature, with the peaks shifted significantly from the Larmor frequency as the magnetisation of the cluster is "frozen" in its $S = 10$ ground state. At the lowest temperature studied, only the $M_S = 10$ sublevels are significantly populated. The differences between the spectra of the protonated and partially deuterated samples allowed assignment of the different proton environments. The authors were not able to simulate the spectra based on simple models where only the dipolar component of the local hyperfine fields was considered (between H and the individual Fe magnetic moments, using coordinates from a neutron scattering derived structure), and thus concluded that the contact hyperfine contributions cannot be ignored, i.e., the spin densities must be delocalised beyond the Fe(III) ions to the H nuclei to some extent. Reasonable simulations were obtained by including significant contact terms to the 8 O<u>H</u> nuclei, with smaller terms to the N<u>H</u> and C<u>H</u>$_2$, and none to the unbound <u>H</u>$_2$O. These largest values correspond to a ca. 1% delocalisation of spin density to each H. The temperature dependence of the proton $1/T_1$ was interpreted in terms of the M_S sublevel transitions within the $S = 10$ ground state, using

the same model as developed for Mn12. The paper concludes by stating that low temperature (< 360 mK) NMR experiments were underway to study T_1 in the pure quantum regime. In the same year Ueda et al. reported ^{1}H nuclear spin T_1 studies on single crystals of Fe8 down to 15 mK [79, 80]. They demonstrated that T_1 becomes temperature independent below 300 mK, at a value of longer than 100 ms. They further detected QTM enhancement of ^{1}H nuclear spin relaxation at applied magnetic fields corresponding to M_S level crossings, where the QTM transitions cause fluctuations of the local fields of the ^{1}H nuclei.

Borsa and co-workers studied the effect of QTM on ^{1}H nuclear spin relaxation rates in an oriented powder of Fe8 at 1.5 K [81]. They measured T_1 as a function of an external magnetic field applied perpendicular to the easy axis of magnetisation of the molecule. $1/T_1$ was found to decrease on increasing transverse field up to ca. 2 T (due to transitions between the M_S sublevels), then to increase to a maximum between 2 and 5 T. The transverse field is expected to increase the tunnel splitting Δ_T (and hence enhance QTM) between the $M_S = \pm 10$ sublevels. At a certain field between 2 and 5 T (depending on the orientation of the applied field within the molecular plane perpendicular to the easy axis) the magnitude of Δ_T will equal the ^{1}H Larmor frequency and the resulting fluctuation of the hyperfine fields gives rise to an efficient nuclear spin relaxation mechanism. This was later confirmed by single-crystal studies from the same group [82]. Furukawa et al. showed that isotopic substitution in 96% ^{57}Fe-enriched samples of Fe_8 has no effect on the ^{1}H NMR spectrum at 1.5 K, nor on the ^{1}H nuclear spin T_1 at 1.5 K [27]. This confirms that the spin–phonon coupling, the dominant relaxation mechanism at this temperature, is not perturbed by the metal nuclear spin.

The first ^{57}Fe NMR studies of Fe8 were reported on the same ^{57}Fe-enriched material by Furukawa et al. [83, 84]. At 1.5 K and zero applied magnetic field, beautiful eight-line spectra were observed corresponding to the 8 Fe(III) ions in the structure of Fe8 and revealing that all the metal ions are magnetically distinct consistent with the crystallographic symmetry (Fig. 6).

Furthermore, when an external magnetic field was applied parallel to the easy axis of the molecule, two of the eight signals shift to a higher frequency with increasing field, while the other six shift to lower field, thus indicating the internal fields at these two sites are opposite in sign (direction) to the other six. This is consistent with the simple six “spin up”, two “spin down” description of the $S = 10$ ground state of Fe8 and also aids the assignment of the individual peaks in the spectra. The calculated internal fields at the different Fe sites agreed well with those determined previously by Mossbauer spectroscopy [85], and were used to gain insight into the differences in covalency of the chemically distinct Fe(III) sites. Finally, Dalal and co-workers have reported a ^{81}Br NMR study of Fe8, which clearly distinguishes between the seven bromide anions which are H-bonded to the cluster cation (via OH and NH), and the single bromide which is isolated from the cluster [86]. They

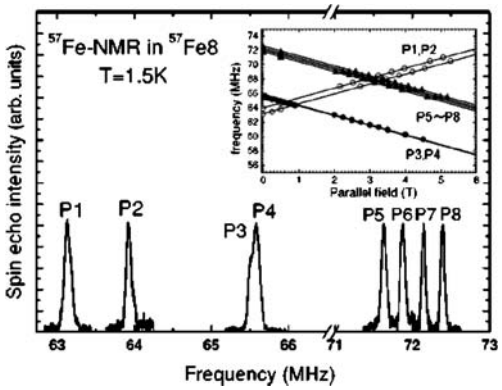

Fig. 6 ^{57}Fe NMR spectrum of a powder sample of 96% ^{57}Fe-enriched Fe8 at 1.5 K in zero applied magnetic field. The eight peaks correspond to the eight different Fe(III) environments. *Inset*: applied magnetic field dependence of the resonance frequencies, indicating opposite signs of the internal magnetic field for two of the eight Fe(III) ions. Figure from [81]

estimate that there is a small amount of unpaired electron density (0.3%) on the seven H-bound bromides.

4 INS Spectroscopy

In an INS experiment energy and momentum are transferred (gain and loss) between incident neutrons and the sample under study which undergoes excitations dictated by the selection rules $\Delta S = 0, \pm 1$ and $\Delta M_S = 0, \pm 1$. Thus, INS can give detailed information on the fine structure (ZFS parameters; including sign of D) of cluster spin states, in common with and complementary to EPR. However, in contrast to field-swept EPR, the INS experiment is performed in zero-field, thus allowing determination of the ZFS parameters without the perturbing influence of an applied magnetic field. It has been argued that this gives far greater accuracy in determining the relatively small magnitude, 4th order ZFS parameters in SMMs. Another major advantage is given by the $\Delta S = 0, \pm 1$ selection rule which means that INS transitions can be observed *between* cluster total spin states – this gives a direct measure of their energy separations and therefore, with an appropriate model, information on the isotropic exchange couplings J within the cluster. The main disadvantage of INS is the requirement of gramme-scale quantities of material. This is compounded further by the large cross-section of ^{1}H for incoherent neutron scattering which often necessitates at least partial deuteration of the sample (the incoherent cross section of ^{2}D is ca. 1/40th that of ^{1}H), although several well-resolved INS studies of SMMs on non-deuterated

materials in relatively low energy transfer ranges have been reported recently (see below). An excellent tutorial on the applications of INS to magnetically exchange coupled clusters has been published recently by Güdel and co-workers, together with a review of the important work in the field by this group [87].

4.1 INS of Mn12 and Related Compounds

The first INS study of Mn12 was reported by Hennion et al. in 1997 [88]. They studied a partially (ca. 70%) deuterated powder sample in the neutron excitation energy range 0–14.5 meV at temperatures down to 1.6 K. They observed a sharp peak at 1.24 meV due to excitations from the $S = 10$, $M_S = \pm 10$ ground state (the only significantly populated state at 1.6 K) to $S = 10$, $M_S = \pm 9$ (the only allowed transition within the $S = 10$ state starting from $M_S = \pm 10$). With this assignment the axial ZFS parameter D was determined as 0.52 cm^{-1}. This peak broadened on warming the sample, with intensity shifting to the low energy side, as lower values of $|M_S|$ are successively populated and more (lower energy) transitions become allowed. They also observed several higher energy peaks centered at ca. 5.0 and 9.1 meV. These are far too high in energy to be transitions within the cluster ground state, and were assigned as transitions between $S = 10$ and cluster spin excited states. Finally, they observed a broad, weak peak at ca. 0.83 meV that was later [89] assigned to a fast relaxing isomer of Mn12 in the sample. This new INS study of Mn12, on a 93% deuterated powder sample using a high energy resolution time-of-flight spectrometer, gave spectacular resolution of the transitions within the $S = 10$ ground state (Fig. 7).

At 1.5 K only the $|M_S| = 10$ to 9 transition is observed as before, and further peaks are resolved as the temperature is increased and higher energy $|M_S|$ states are populated. At 24 K, seven of the possible nine peaks are clearly resolved on either side of the elastic scattering. The data were fitted to the (axial symmetry) spin-Hamiltonian (Eq. 1), where the Zeeman term is neglected because of the zero applied field, to give $D = -0.457\ cm^{-1}$, $B_4^0 = -2.33 \times 10^{-5}\ cm^{-1}$ and $B_4^4 = \pm 3.0 \times 10^{-5}\ cm^{-1}$. The off-diagonal 4th order term B_4^4 has the effect of making the spacing between the peaks uneven – this is observed experimentally and thus this parameter is determined with good accuracy. Ground state fine structure resolution in Mn12, albeit with poorer resolution, was also reported by Zhong et al. in the same year [90], and they gave values equivalent to $|D| = 0.45\ cm^{-1}$ and $|B_4^0| = 2.4 \times 10^{-5}\ cm^{-1}$. Higher resolution studies still, from Bircher et al. [91], allowed far better definition of the lowest energy transitions, i.e., those between sublevels of low $|M_S|$. These transitions were not reproduced well using the previously determined (axial) parameters above, and it was necessary to introduce a small rhombic term, $E(S_x^2 - S_y^2)$, in the spin-Hamiltonian – this splits the

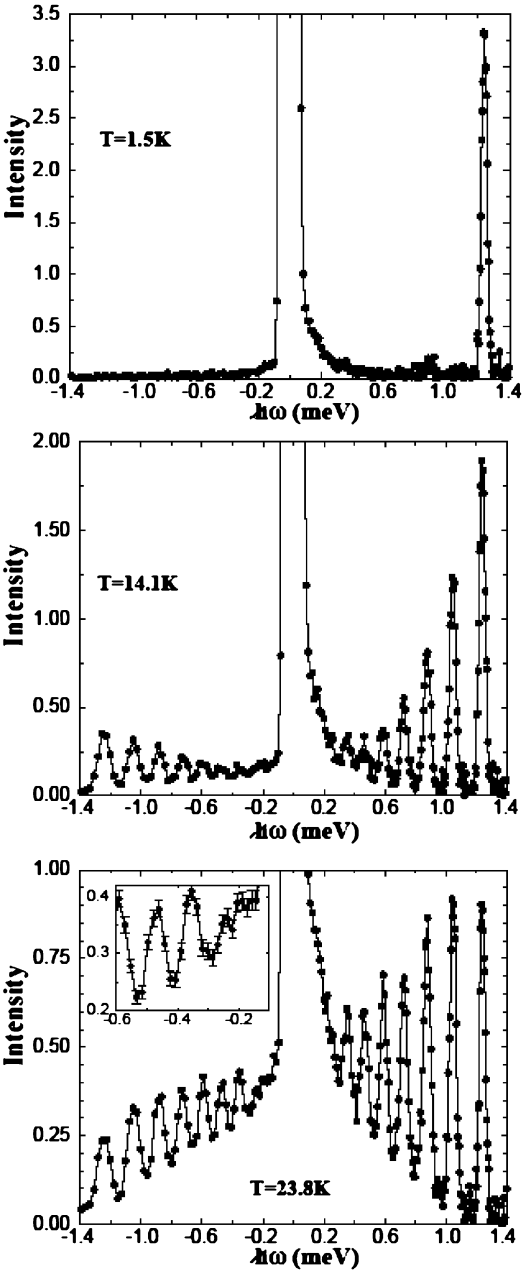

Fig. 7 INS spectra of 93% deuterated powder sample of Mn12 at variable temperature. At 1.5 K, only $M_S = \pm 10$ are populated and only the $M_S = \pm 10$ to ± 9 transition is observed, on the energy gain side of the spectrum at 1.24 meV; $M_S = \pm 9$ to ± 8, etc. are observed on warming, as are the energy loss transitions ($M_S = \pm 9$ to ± 10, etc.). The *intense central peak* is due to elastic scattering. Figure from [87]

$M_S = \pm 1$ sublevels and hence the low energy INS transitions are very sensitive to this term. The authors found that they could best model the data, assuming a single species, with $D = -0.460\ \text{cm}^{-1}$, $B_4^0 = -2.24 \times 10^{-5}\ \text{cm}^{-1}$ and $B_4^4 = \pm 2.58 \times 10^{-5}\ \text{cm}^{-1}$ and $|E| = 5.5 \times 10^{-3}\ \text{cm}^{-1}$. They could also get a good agreement assuming six different site symmetries in the lattice, due to disorder in the molecules of solvation as proposed by Cornia [11], and with $|E|$ parameters ranging from 0 to $0.011\ \text{cm}^{-1}$, thus providing support to this model.

Chaboussant et al. [92] returned to the problem of the very high energy peaks observed in the original [88] INS study of Mn12, extending the excitation energy range studied up to 45 meV. They observed discrete sets of high energy peaks in the ranges 5–6.5 and 8–10.5 meV at 8 K, and, from the temperature and Q dependence data, argue that they are resolving $S = 10$, $M_S = \pm 10$ to $S = 9$, $M_S = \pm 9$ transitions for five different $S = 9$ states all within 30 meV of the $S = 10$ ground state. Furthermore, they determined that the first transition that could feasibly be assigned to an $S = 10$ or 11 excited state was at 27 meV. They then considered the values of the isotropic exchange coupling constants (J) within the cluster that would reproduce the ground and low lying excited total spin states consistent with this INS data (and of course be consistent with susceptibility and magnetization data). They modelled the molecule with four unique J values, between Mn(IV) and Mn(III) via two μ-oxo bridges (J_1) and via one μ-oxo bridge (J_2), between Mn(IV) and Mn(IV) via two μ-oxo bridges (J_3) and between Mn(III) and Mn(III) via one μ-oxo and two μ-carboxylato bridges (J_4), and find the best match to the INS data is with $J_1 = 67.2$, $J_2 = 61.8$, $J_3 = 7.8$ and $J_4 = 5.6$ K. Exact diagonalisation with these parameters, considering only the ground and low-lying excited states, gives the seven lowest lying excited states as $S = 9$ (including two sets of doubly degenerate states) with the first $S > 9$ excited state being $S = 11$ at 24.6 meV (starting from the $S = 10$ ground state, only transitions to $S = 9$, 10, 11 are allowed by INS) [93].

Basler et al. have probed the effect of successive one-electron reductions on the ground state ZFS by INS studies on the family $[Mn_{12}O_{12}(O_2C_6F_5)_{16}(H_2O)_4]^{0/-/2-}$ (the counter-ions are not specified), which have ground states of $S = 10$, 19/2 and 10, respectively [94]. INS spectra at 2 K spectra show similar behaviour to that of Mn12 itself (only the $|M_S| = S$ sublevels are populated) and increasing the temperature leads to the growth of new intra-ground state transitions to lower energy. They find that the parent (unreduced) complex has $D = -0.463\ \text{cm}^{-1}$ and $B_4^0 = -2.09 \times 10^{-5}\ \text{cm}^{-1}$, while the mono- and di-reduced species have $D = -0.368\ \text{cm}^{-1}$ and $B_4^0 = -1.59 \times 10^{-5}\ \text{cm}^{-1}$ and $D = -0.274\ \text{cm}^{-1}$ (B_4^0 not determined), respectively (approximating to axial symmetry, and quoting data only for the dominant isomers). Thus, reduction leads to a reduction of $|D|$, consistent with the reduction of anisotropic Mn(III) ions to pseudo-isotropic Mn(II).

4.2 INS of Fe8 and Related Compounds

The first INS study of Fe8 was in 1998 from Caciuffo et al. [95]. They recorded remarkably well resolved data on a powder sample of *non*-deuterated material, measured between 1 and 10 K. As with Mn12 a single peak is found at 1.3 K corresponding to the $S = 10$, $M_S = \pm 10$ to $S = 9$, $M_S = \pm 9$ transition, at 0.465 meV, with lower energy peaks growing in on raising the temperature. They fit the data to the rhombic Hamiltonian (Eq. 2), giving the parameters $D = -0.203\ cm^{-1}$, $E = -3.24 \times 10^{-2}\ cm^{-1}$, $B_4^0 = 7.0 \times 10^{-7}\ cm^{-1}$, $B_4^2 = 8.1 \times 10^{-8}\ cm^{-1}$ and $B_4^4 = \pm 6.0 \times 10^{-6}\ cm^{-1}$. Again, the low energy region of the spectrum was found to be more sensitive to the non-diagonal terms in the Hamiltonian, as the higher energy sublevels are substantially mixed by these terms and many transitions become allowed. They later provided support for the values of the higher order terms, which were significantly different from those determined by HF-EPR, with a higher resolution experiment in the energy transfer region below 0.085 meV [96]. Carretta et al. studied the partially counter-ion substituted version of Fe8, $[Fe_8O_2(OH)_{12}(tacn)_6]Br_{4.3}(ClO_4)_{3.7}.6H_2O$ [97]. INS spectra in the temperature range 2–10 K behave similarly to those of Fe8 itself, and analysis leads to the parameters $D = -0.204\ cm^{-1}$, $E = -4.5 \times 10^{-2}\ cm^{-1}$, $B_4^0 = 5.6 \times 10^{-7}\ cm^{-1}$, $B_4^2 = 0$ and $B_4^4 = -1.6 \times 10^{-5}\ cm^{-1}$. As found by EPR, there is a significantly larger rhombic term E than in Fe8 itself.

4.3 INS of other SMMs

Andres et al. reported INS studies on the family of tetranuclear Mn(IV) $Mn(III)_3$ SMMs, $[Mn_4O_3X(O_2CMe)_3(dbm)_3]$ where X = Cl, Br, O_2CMe and F, and Hdbm = dibenzoylmethane [98], previously studied by EPR (see above). All the family have a ground state spin of $S = 9/2$. The transitions within this ground state are well resolved by INS in the temperature range 2–20 K. There is a significant variation of the ground state D, ranging from $-0.529\ cm^{-1}$ for X = Cl to $-0.379\ cm^{-1}$ for X = F, which the authors rationalized in terms of the Mn(III) single-ion contribution to the cluster ZFS. They conclude that the single-ion Mn(III) $|D|$ decreased down the halogen group due to the reduction of the spin-orbit coupling of the Mn(III) ions due to covalency effects. They also show the X = Cl analogue is significantly more rhombic than X = Br ($E = 0.022$ and $0.017\ cm^{-1}$, respectively) and that this has a direct consequence on the QTM rates and energy barriers to reversal of magnetization. Sieber et al. also studied the pressure dependence of the ZFS parameters in the deuterated form of the X = Br compound by INS spectroscopy [99]. They found that D decreases from −0.505 to $-0.486\ cm^{-1}$ on applying 12 kbar pressure. They argue that the pressure

induces a shrinkage of the Mn(III)-Br bonds and thus an increase in the angle between the Mn(III) Jahn–Teller axes and the easy axis of magnetization of the cluster hence the reduction in the cluster ground state *D*. Piligkos et al. probed the ZFS in the $S = 17/2$ ground state of the ennanuclear SMM, $[Mn_9O_7(O_2CMe)_{11}(thme)(py)_3(H_2O)_2].MeCN.Et_2O$ (see above), by INS on the non-deuterated material [52]. The INS values of $D = -0.249\ cm^{-1}$, $B_4^0 = 7 \times 10^{-6}\ cm^{-1}$ are in excellent agreement with frequency domain EPR, and this study provides another example of beautiful INS resolution (in the relatively low energy transfer window corresponding to intra-ground state transitions), on a non-deuterated material.

The tetranuclear SMM $[Fe_4(OMe)_6(dpm)_6]$ ($S = 5$ ground state) has been studied by INS by Amoretti et al. [100]. The spectra could only be modeled by including rhombic terms in the Hamiltonian, whereas previous powder HF-EPR measurements had been modeled as axial. Furthermore, they had to consider three different isomers of the clusters as previously observed by single crystal HF-EPR studies.

Finally, the Ni(II) SMM $[Ni_{12}(chp)_{12}(O_2CMe)_{12}(thf)_6(H_2O)_6]$ (Hchp = chlorohydroxypyridine) has been probed by INS by the Winpenny and Güdel groups [101]. The cluster has an $S = 12$ ground state due to ferromagnetic coupling between the Ni(II) ions. Fitting of susceptibility data, assuming a single unique *J* value, had given J = ca. $+6\ cm^{-1}$, although there is no requirement for this as there are two unique Ni(II) ions by symmetry. Two inelastic transitions were observed in the INS spectra at 1.5 K (at 2.85 and 3.35 meV), and from their temperature dependence these were assigned to transitions between the $S = 12$ ground state and two $S = 11$ excited states. The data could only be fitted by considering two unique nearest neighbour *J*-values of + 11.3 and + 1.9 cm^{-1} and also a next-nearest neighbour exchange of $-0.9\ cm^{-1}$. Thus, INS gives a much more direct, and therefore accurate, measure of the *J*-values than was possible by modeling of susceptibility data.

5 MCD and XMCD Spectroscopies

Magnetic Circular Dichroism (MCD) spectroscopy is the differential absorption of left and right circularly polarized light by a substance in an applied magnetic field. Thus, the sign (and intensity) of the MCD spectrum is dependent on the spin polarization of the sample induced by the applied field. Therefore, this magneto-optical technique has great potential in the study of SMMs because transitions originating from the $M_S = +S$ and $-S$ sublevels will have opposite sign. The first MCD study of an SMM was from Cheeseman et al., on a dmf/MeCN glass (dmf = N,N-dimethylformamide) at 1.7 K between 400 and 800 nm [102]. The MCD spectrum in 5 T applied field shows spectacular resolution of the optical transitions [Mn(III) and Mn(IV)

dd transitions and charge transfer transitions] in contrast to the rather featureless absorption spectra in the same wavelength region. They found that after removal of the field a strong CD spectrum remains with ca. 30% of its original intensity, and furthermore that the sign of this CD signal was dependent on the sign of the original applied field. Thus they had optically detected the magnetic bistability of Mn12. They also measured hysteresis loops by monitoring the MCD intensity as a function of applied field at fixed wavelengths. This work was extended by the same group, to studies of a long-chain carboxylate version of Mn12, $[Mn_{12}O_{12}(O_2CC_{15}H_{29})_{16}]$, doped in a thin poly(methylmethacrylate) (PMM) film and in a $CHCl_3$/toluene glass (Fig. 8) [103].

By modeling the MCD magnetisation curves at fixed wavelengths, the optical polarizations of the individual electronic transitions could be determined, and the extent of retention of magnetization as monitored by the CD spectrum after removal of the applied field was found to be dependent on these polarizations. This effect is also observed in the different remanent fields of the hysteresis loops measured at different wavelengths. Steps were seen in these hysteresis loops at zero field, which are due to QTM. Similar MCD studies on Mn12 in glasses were reported later by Domingo et al., who also showed that the magnetization vs external field loops measured on the glasses by MCD and by SQUID were essentially identical [104]. Collison et al. have probed the local electronic structure of the Cr(III) ions in the $S = 6$ ground state cluster $[Cr_{12}O_9(OH)_3(O_2CCMe_3)_{15}]$ by low temperature MCD [105]. Although the room temperature UV/Vis spectrum looks similar to that of a monomeric Cr(III) ion, with two of the three allowed dd transitions resolved ($^4A_2 \rightarrow {}^4T_2$ and $^4T_1$), the MCD spectrum at 4 K reveals that these are split (into ^4E and ^4A terms) in the lower than O_h symmetry, and also enhances the intensity of the spin forbidden transitions (e.g., $^4A_2 \rightarrow {}^2E$). This resolution allowed an estimate of the single-ion ZFS from crystal field models developed for the Cr(III) ion in ruby. The authors concluded that although the single-ion ZFS is negative in sign and the cluster ground state ZFS is dominated by the single-ion contribution, the cluster ZFS is positive in sign due to mis-alignment of the local and cluster ZFS axes at 9 of the 12 sites.

Two reports have appeared on the use of X-ray MCD (XMCD) to probe the relative contributions of the spin and orbital contributions of the angular momentum to the local magnetic moments on Mn12 and Fe8 [106, 107] – this is possible, in principle, by the application of sum rules. Ghigna et al. report Mn-$L_{II,III}$ and Fe-$L_{II,III}$ edge studies on Mn12 and Fe8, respectively [106]. XMCD spectra on Mn12 are reported at 5 K in an applied magnetic field of 5 T, and show partial resolution of the different absorption edges due to Mn(III) and Mn(IV), with the latter at higher energy (642.5 and 643.5 eV, respectively, for the L_{III} edge). The authors note that the integral of the XMCD spectrum over a complete core-level edge is proportional to the expectation value of the orbital angular momentum in the ground state. In Mn12 the total

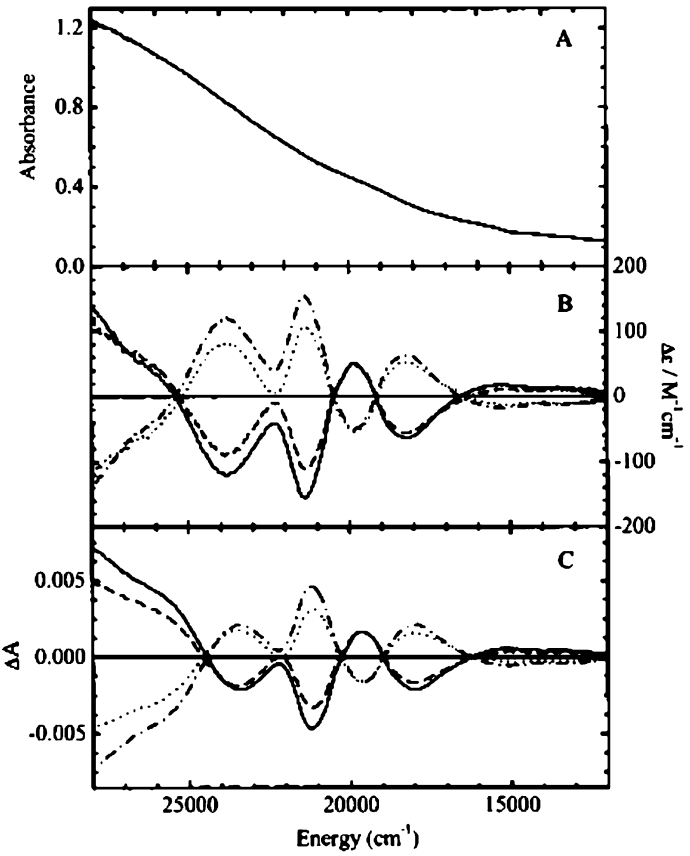

Fig. 8 (A) Electronic absorption spectra at room temperature of a doped PMM film, (B) MCD spectra at 1.8 K of a $CHCl_3$ glass, and (C) MCD spectra at 1.8 K of a doped PMM film of $[Mn_{12}O_{12}(O_2CC_{15}H_{29})_{16}]$. In (B) and (C) applied magnetic fields are: (–) + 5 T, (···) – 5 T, (– – –) 0 T after application of + 5 T, (· · ·) 0 T after application of – 5 T. The sign of the retained CD spectrum in zero-field depends on the sign of the original applied field. The retention of magnetization depends on the polarization of the optical transition monitored. Figure from [101]

integral over the $L_{II,III}$ edges is zero and this confirms the quenching of the orbital angular momentum in this molecule. Independent analysis of the two different oxidation states via the sum rules was hampered by their incomplete resolution. The integral of the total XMCD spectrum of Fe8 at 4 K and 7 T is also small. The spin angular momentum was estimated from the difference between the integrals of L_{II} and L_{III} edges, and the ratio of the orbital to spin moments was found to be ca. 0.02, again confirming almost complete quenching of orbital angular momentum in Fe8. Moroni et al. studied Mn12 in more detail, and addressed the problem of the overlapping Mn(III) and Mn(IV) spectra by comparison with the model compounds $[Mn(dbm)_3]$ and

$[Mn_2L_2O(O_2BPh)_2](ClO_4)_2$ (L = 1,4,7-trimethyl-1,4,7-triazacyclononane), respectively [107]. They used crystal field multiplet calculations to simulate the XMCD spectra of the reference complexes, thus obtaining their crystal field parameters, and use these data as a starting point in the analysis of Mn12. Thus, the ratios of the ground state expectation values of the spin and orbital moments along the easy axis of magnetization of the cluster were determined to be < 0.005 and – 0.03 for Mn(III) and Mn(IV), respectively, where the difference in sign implies anti-parallel orientations of the magnetic moments. Thus, the orbital contributions to the magnetic moments are largely quenched for both ions in Mn12.

6 Conclusions

The extraordinary number of studies on (and battery of techniques applied to) the two best known SMMs, Mn12 and Fe8, has led to a detailed understanding of the origin and mechanism of their unique physics and by extension that of SMMs in general. It is to be hoped that further exciting discoveries will be forthcoming as attention turns to the rapidly increasing number of new SMMs (for example, see the review elsewhere in this volume by Arómi and Brechin).

References

1. Barra AL, Brunel LC, Gatteschi D, Pardi LA, Sessoli R (1998) Acc Chem Res 31:460
2. Caneschi A, Gatteschi D, Sessoli R (1991) J Am Chem Soc 113:5873
3. Barra AL, Gatteschi D, Sessoli R (1997) Phys Rev B 56:8192
4. Hill S, Perenboom JAAJ, Dalal NS, Hathaway T, Stalcup T, Brooks JS (1998) Phys Rev Lett 80:2453
5. Park K, Novotny MA, Dalal NS, Hill S, Rikvold PA (2002) J Appl Phys 91:7167
6. Park K, Novotny MA, Dalal NS, Hill S, Rikvold PA (2001) Phys Rev B 65:014426
7. Park K, Novotny MA, Dalal NS, Hill S, Rikvold PA (2002) Phys Rev B 66:144409
8. Hill S, Maccagnano S, Park K, Achey RM, North JM, Dalal NS (2002) Phys Rev B 65:224410
9. Park K, Dalal NS, Rikvold PA (2002) J Chem Phys 117:11292
10. Hill S, Edwards RS, North JM, Park K, Dalal NS (2003) Polyhedron 22:1889
11. Cornia A, Sessoli R, Sorace L, Gatteschi D, Barra AL, Daiguebonne C (2002) Phys Rev Lett 89:257201
12. Hill S, Edwards RS, Jones SI, Dalal DS, North JM (2003) Phys Rev Lett 90:217204
13. Takahashi S, Edwards RS, North JM, Hill S, Dalal NS (2004) Phys Rev B 70:094429
14. Hill S, Edwards RS, North JM, Maccagnano S, Dalal NS (2003) Polyhedron 22:1897
15. Amigó R, del Barco E, Casas Ll, Molins E, Tejada J, Rutel IB, Mommouton B, Dalal N, Brooks J (2002) Phys Rev B 65:172403

16. Aubin SMJ, Sun Z, Rumberger EM, Hendrickson DN, Christou G (2002) J Appl Phys 91:7158
17. Kuroda-Sowa T, Lam M, Rheingold AL, Frommen C, Reiff WM, Nakano M, Yoo J, Maniero AL, Brunel LC, Christou G, Hendrickson DN (2001) Inorg Chem 40:6469
18. Aubin SMJ, Sun Z, Pardi L, Krzystek J, Folting K, Brunel LC, Rheingold AL, Christou G, Hendrickson DN (1999) Inorg Chem 38:5329
19. Artus P, Boskovic C, Yoo J, Streib WE, Brunel LC, Hendrickson DN, Christou G (2001) Inorg Chem 40:4199
20. Hachisuka H, Awaga K, Yokoyama T, Kubo T, Goto T, Nojiri H (2004) Phys Rev B 70:104427
21. Barra AL, Debrunner P, Gatteschi D, Shulz ChE, Sessoli R (1996) Europhys Lett 135:133
22. Barra AL, Gatteschi D, Sessoli R (2000) Chem Eur J 6:1608
23. Maccagnano S, Achey R, Negusse E, Lussier A, Mola MM, Hill S, Dalal NS (2001) Polyhedron 20:1441
24. Zipse D, North JM, Dalal NS, Hill S, Edwards RS (2003) Phys Rev B 68:184408
25. Barra AL, Bencini F, Caneschi A, Gatteschi D, Paulsen C, Sangregorio C, Sessoli R, Sorace L (2001) Chem Phys Chem 2:523
26. Barra AL, Caneschi A, Cornia A, Fabrizi de Biani F, Gatteschi D, Sangregorio C, Sessoli R, Sorace L (1999) J Am Chem Soc 121:5302
27. Bouwen A, Caneschi A, Gatteschi D, Goovaerts E, Schoemaker D, Sorace L, Stefan M (2001) J Phys Chem B 105:2658
28. Cornia A, Fabretti AC, Garrisi P, Mortalò C, Bonacchi D, Sessoli R, Sorace L, Barra AL, Wernsdorfer W (2004) J Magn Mag Mat 272–276:e749
29. Cornia A, Fabretti AC, Garrisi P, Mortalò C, Bonacchi D, Gatteschi D, Sessoli R, Sorace L, Wernsdorfer W, Barra AL (2004) Angew Chem Int Ed 43:1136
30. Aubin SMJ, Dilley NR, Pardi L, Krzystek J, Wemple MW, Brunel LC, Maple MB, Christou G, Hendrickson DN (1998) J Am Chem Soc 120:4991
31. Aliaga-Alcade N, Edwards RS, Hill SO, Wernsdorfer W, Folting K, Christou G (2004) J Am Chem Soc 126:12503
32. Edwards RS, Hill S, Bhaduri S, Aliaga-Alcade N, Bolin E, Maccagnano S, Christou G, Hendrickson DN (2003) Polyhedron 22:1911
33. Hill S, Edwards RS, Aliaga-Alcade N, Christou G (2003) Science 302:1015
34. Hendrickson DN, Christou G, Schmitt EA, Libby E, Bashkin JS, Wang S, Tsai HL, Vincent JB, Boyd PDW, Huffman JC, Folting K, Li Q, Streib WE (1992) J Am Chem Soc 114:2455
35. Wernsdorfer W, Aliaga-Alcalde N, Hendrickson D, Christou G (2002) Nature 416:406
36. Edwards RS, Maccagnano S, Yang EC, Hill S, Wernsdorfer W, Hendrickson D, Christou G (2003) J Appl Phys 93:7807
37. Yang EC, Wernsdorfer W, Hill S, Edwards RS, Nakano M, Maccagnano S, Zakharov LN, Rheingold AL, Christou G, Hendrickson DN (2003) Polyhedron 22:1727
38. Yoo J, Brechin EK, Yamaguchi A, Nakano M, Huffman JC, Maniero AL, Brunel LC, Awaga K, Ishimoto H, Christou G, Hendrickson DN (2000) Inorg Chem 39:3615
39. Yoo J, Yamaguchi A, Nakano M, Kyzystek J, Streib WE, Brunel LC, Ishimoto H, Christou G, Hendrickson DN (2001) Inorg Chem 40:4604
40. Boskovic C, Bircher R, Treggenna-Piggott PLW, Güdel HU, Paulsen C, Wernsdorfer W, Barra AL, Khatsko E, Neels A, Stoeckli-Evans H (2003) J Am Chem Soc 125:14046
41. Barra AL, Caneschi A, Gatteschi D, Sessoli R (1995) J Am Chem Soc 117:8855

42. Mabbs FE, McInnes EJL, Murrie M, Parsons S, Smith GM, Wilson CC, Winpenny REP (1999) Chem Commun 643
43. Collison D, Murrie M, Oganesyan VS, Piligkos S, Poolton NRJ, Rajaraman G, Smith GM, Thomson AJ, Timko GA, Wernsdorfer W, Winpenny REP, McInnes EJL (2003) Inorg Chem 42:5293
44. Piligkos S, Collison D, Oganesyan VS, Rajaraman G, Timko GA, Thomson AJ, Winpenny REP, McInnes EJL (2004) Phys Rev B 69:134424
45. Oshio H, Nihei M, Yoshida A, Nojiri H, Nakano M, Yamaguchi A, Karaki Y, Ishimoto H (2005) Chem Eur J 11:843
46. van Slageren J, Vongtragool S, Gorshunov B, Mukhin AA, Karl N, Krzystek J, Telser J, Müller A, Sangregorio C, Gatteschi D, Dressel M (2003) Phys Chem Chem Phys 5:3837
47. Mukhin AA, Travkin VD, Zvezdin AK, Lebedev SP, Caneschi A, Gatteschi D (1998) Europhys Lett 44:778
48. Dressel M, Gorshunov B, Rajagopal K, Voontragool S, Muhkin AA (2003) Phys Rev B 67:060405
49. Vontragool S, Muhkin A, Gorshunov B, Dressel M (2004) Phys Rev B 69:104410
50. Vontragool S, Gorshunov B, van Slageren J, Dressel M, Muhkin AA (2004) Polyhedron 272–276:e769
51. Mukhin A, Gorshunov V, Dressel M, Sangregorio C, Gatteschi D (1998) Phys Rev B 63:214411
52. Piligkos S, Rajaraman G, Soler M, Kirchner N, van Slageren J, Bircher R, Parsons S, Güdel HU, Kortus J, Wernsdorfer W, Christou G, Brechin EK (2005) J Am Chem Soc 127:5572
53. Petukhov K, Wernsdorfer W, Barra A-L, Mosser V (2005) Phys Rev B 72:052401
54. Lascialfari A, Gatteschi D, Borsa F, Cornia A (1997) Phys Rev B 55:14341
55. Julien MH, Jang ZH, Lascialfari A, Borsa F, Horvatic M, Caneschi A, Gatteschi D (1999) Phys Rev Lett 83:227
56. Lascialfari A, Gatteschi D, Borsa F, Shastri A, Jang ZH, Carretta P (1998) Phys Rev B 57:514
57. Lascialfari A, Jang ZH, Borsa F, Carretta P, Gatteschi D (1998) Phys Rev Lett 81:3773
58. Dolinšek J, Arčon D, Blinc R, Vonlanthen P, Gavilano JL, Otto HR, Achey RM, Dalal NS (1998) Europhys Lett 42:691
59. Arčon D, Dolinšek J, Apih T, Blinc R, Dalal NS, Achey RM (1998) Phys Rev B 58:R2941
60. Achey RM, Kuhns PL, Reyes AP, Moulton WG, Dalal NS (2001) Phys Rev B 64:064420
61. Blinc R, Zalar B, Gregorovič A, Arčon D, Kutnjak Z, Filipič C, Levstik A, Achey RM, Dalal NS (2003) Phys Rev B 67:094401
62. Jang ZH, Lascialfari A, Borsa F, Gatteschi D (2000) Phys Rev Lett 84:2997
63. Furukawa Y, Watanabe K, Kumagai K, Jang ZH, Lascialfari A, Borsa F, Gatteschi D (2000) Phys Rev B 62:14246
64. Goto T, Kubo T, Koshiba T, Fujii Y, Oyamada A, Arai J, Takeda K, Awaga K (2000) Physica B 284–288:1227
65. Furukawa Y, Watanabe K, Kumagai K, Borsa F, Gatteschi D (2001) Phys Rev B 64:104401
66. Kubo T, Koshiba T, Goto T, Oyamada A, Fujii Y, Takeda K, Awaga K (2001) Physica B 294–295:310
67. Kubo T, Goto T, Koshiba T, Takeda K, Awaga K (2002) Phys Rev B 65:224425
68. Morello A, Bakharev ON, Brom HB, de Jongh LJ (2003) Polyhedron 22:1745

69. Morello A, Bakharev ON, Brom HB, de Jongh LJ (2004) J Magn Mag Mat 272–276:1015
70. Morello A, Bakharev ON, Brom HB, Sessoli R, de Jongh LJ (2004) Phys Rev Lett 93:197202
71. Kubo T, Doi H, Imanari B, Goto T, Takeda K, Awaga K (2003) Physica B 329–333:1172
72. Furukawa Y, Watanabe K, Kumagai K, Borsa F, Gatteschi D (2003) Physica B 329–333:1146
73. Furukawa Y, Watanabe K, Kumagai K, Borsa F, Sasaki T, Kobayashi N, Gatteschi D (2003) Phys Rev B 67:064426
74. Kubo T, Nagano A, Goto T, Takeda K, Awaga K (2004) J Magn Mag Mat 272–276:e727
75. Harter AG, Chakov NE, Roberts B, Achey R, Reyes A, Kuhns P, Christou G, Dalal NS (2005) Inorg Chem 44:2212
76. Gatteschi D, Lascialfari A, Borsa F (1998) J Magn Mag Mat 185:238
77. Furukawa Y, Kumagai K, Lascialfari A, Aldrovandi S, Borsa F, Sessoli R, Gatteschi D (2001) Phys Rev B 64:094439
78. Ueda M, Maegawa S, Kitagawa S (2002) Phys Rev B 66:073309
79. Maegawa S, Ueda M (2003) Physica B 329–333:1144
80. Furukawa Y, Aizawa K, Kumagai K, Ullu R, Lascialfari A, Borsa F (2003) J Appl Phys 93:7813
81. Furukawa Y, Aizawa K, Kumagai K, Lascialfari A, Borsa F (2004) J Magn Mag Mat 272–276:1013
82. Furukawa Y, Kawakami S, Aizawa K, Kumagai K, Borsa F (2003) Polyhedron 22:2277
83. Furukawa Y, Kawakami S, Kumagai K, Baek SH, Borsa F (2003) Phys Rev B 68:180405
84. Baek SH, Kawakami S, Furukawa Y, Suh BJ, Borsa F, Kumagai K, Cornia A (2004) J Magn Mag Mat 272–276:E771
85. Cianchi L, Giallo FD, Spina G, Reiff W, Caneschi A (2002) Phys Rev B 65:064415
86. Zipse D, North JM, Achey RM, Dalal NS, Hill S, Edwards RS, Choi ES, Brooks JS (2004) J Appl Phys 95:6900
87. Basler R, Boskovic C, Chaboussant G, Güdel HU, Murrie M, Ochsenbein ST, Sieber A (2003) Chem Phys Chem 4:910
88. Hennion M, Pardi L, Mirebeau I, Suard E, Sessoli R, Caneschi A (1997) Phys Rev B 56:8819
89. Mirebeau I, Hennion M, Casalta H, Andres H, Güdel HU, Irodova AV, Caneschi A (1999) Phys Rev Lett 83:628
90. Zhong Y, Sarachik MP, Friedman JR, Robinson RA, Kelly TM, Nakotte H, Christianson AC, Truow F, Aubin SMJ, Hendrickson DN (1999) J Appl Phys 85:5636
91. Bircher R, Chaboussant G, Sieber A, Güdel HU, Mutka H (2004) Phys Rev B 70:212413
92. Chaboussant G, Sieber A, Ochsenbein S, Güdel HU, Murrie M, Honecker A, Fukushiwa N, Normand B (2004) Phys Rev B 70:104422
93. Honecker A, Fukushiwa N, Normand B, Chaboussant G, Güdel HU (2005) J Magn Mag Mat 290–291:966
94. Basler R, Sieber A, Chaboussant G, Güdel HU, Chakov NE, Soler M, Christou G, Desmedt A, Lechner R (2005) Inorg Chem 44:649
95. Caciuffo R, Amoretti G, Murani A, Sessoli R, Caneschi A, Gatteschi D (1998) Phys Rev Lett 81:4744
96. Amoretti G, Caciuffo R, Combet J, Murani A, Caneschi A (2000) Phys Rev B 62:3022
97. Carretta S, Liviotti E, Amoretti G, Caciuffo R, Caneschi A, Gatteschi D (2002) Phys Rev B 65:052411

98. Andres H, Basler R, Güdel HU, Aromi G, Christou G, Büttner H, Rufflé B (2000) J Am Chem Soc 122:12469
99. Sieber A, Chaboussant G, Bircher R, Boskovic C, Güdel HU, Christou G, Mutka H (2004) Phys Rev B 70:172413
100. Amoretti G, Carretta S, Caciuffo R, Casalta H, Cornia A, Affronte M, Gatteshi D (2001) Phys Rev B 64:104403
101. Andres H, Basler R, Blake AJ, Cadiou C, Chaboussant G, Grant CM, Güdel HU, Murrie M, Parsons S, Paulsen C, Semadini F, Villar V, Wernsdorfer W, Winpenny REP (2002) Chem Eur J 8:4867
102. Cheeseman MR, Oganesyan VS, Sessoli R, Gatteschi D, Thomson AJ (1997) Chem Commun 1677
103. McInnes EJL, Pidcock E, Oganesyan VS, Cheeseman MR, Powell AK, Thomson AJ (2002) J Am Chem Soc 124:9219
104. Domingo N, Williamson BE, Gómez-Segura J, Gerbier Ph, Ruiz-Molina D, Amabilino DB, Veciana J, Tejada J (2004) Phys Rev B 69:052405
105. Collison D, Oganesyan VS, Piligkos S, Thomson AJ, Winpenny REP, McInnes EJL (2003) J Am Chem Soc 125:1168
106. Ghigna P, Campana A, Lascialfari A, Caneschi A, Gatteschi D, Tagliaferri A, Borgatti A (2001) Phys Rev B 64:132413
107. Moroni R, Cartier dit Moulin Ch, Champion G, Arrio MA, Sainctavit Ph, Verdaguer M, Gatteschi D (2003) Phys Rev B 68:064407

Struct Bond (2006) 122: 103–131
DOI 10.1007/430_032

Published online: 29 April 2006

Synthesis of Single-molecule Magnets Using Metallocyanates

Jean-Noël Rebilly · Talal Mallah (✉)

Laboratoire de Chimie Inorganique, UMR CNRS 8613, Université Paris-Sud, 91405 Orsay, France
mallah@icmo.u-psud.fr

Abstract Cyanometallate building blocks are inert and stable molecules that may act as ligands towards metal complexes. A stepwise approach allows preparing polynuclear complexes with predictable architectures. The knowledge of the nature of the exchange interaction through the cyanide bridge enables chemists to reasonably predict the spin of the ground state and in some cases the magnitude of the magnetic anisotropy. During the last 10 years, hexacyanometallates led to the discovery of polynuclear complexes that behave as single-molecule magnets (SMMs). For such low-nuclearity complexes, these SMMs have a relatively high anisotropy barrier in comparison to other metal–oxo-based clusters with larger spin ground state. On the other hand, the introduction of tricyanometallates led to different architectures in complexes with higher nuclearity (up to 14). Chemists took advantage of the step by step approach to introduce within the polynuclear complexes metal ions of the first or second transition metal series that have large spin–orbit coupling. All the cyanometallate clusters with such ions have been shown to behave as SMMs.

Keywords Hexacyanometallate · Magnetic anisotropy · Single-molecule magnets · Tricyanometallate

1 Introduction

At the beginning of the 1990s, Gatteschi and coworkers discovered that a manganese mixed valence ($Mn_4^{IV}Mn_8^{III}$, Fig. 1) complex synthesized a decade before by Lis shows slow relaxation of the magnetization of the order of a few months at $T = 2\,K$ [1, 2]. The complex of formula $[Mn_{12}O_{12}(CH_3COO)_{16}(H_2O)_4]$, i.e. Mn12-ac, has a $S = 10$ ground state and behaves, due to the presence of a hysteresis cycle in the $M = f(H)$ plot, as a tiny magnet [3]. Mn12-ac has a $S = 10$ ground state and a non-zero uniaxial magnetic anisotropy ($D = -0.5\ cm^{-1}$) that lead to an energy barrier ($|D|S2$) of $50\ cm^{-1}$. Its structure consists of a Mn_4O_4 cubane surrounded by eight other Mn atoms bridged by oxo and acetate groups. The four central Mn atoms are at the oxidation state IV while the eight peripheral ones are Mn^{III} (Fig. 1). The molecule that has a disk-like shape possesses a S_4 symmetry axis that is responsible for the uniaxial anisotropy. Within the crystal, the Mn_{12} molecules are stacked with their anisotropy axes parallel to the *c* direction, leading to an easy magnetization axis for the crystal.

Other related complexes (where the acetate can be replaced by another carboxylate) and new complexes were synthesized and found to have similar behavior; they are now called "single-molecule magnets", SMMs [4–8].

What is the origin of the SMM behavior? Let us assume, for a given molecule, a spin ground state *S*. At sufficiently low temperature only the ground state is populated. If the molecule has a relatively high symmetry, the

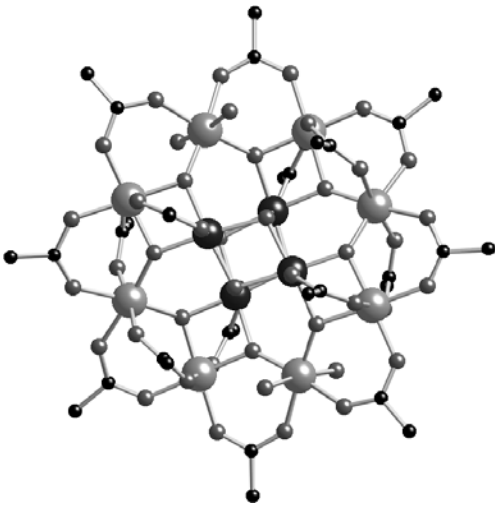

Fig. 1 View of the structure of Mn12-ac along the S_4 symmetry axis

$2S + 1M_S$ sublevels are likely to have the same energy (or very close) and the reversal from the M_S – S state (prepared by applying a sufficiently high magnetic field) to the $M_S = + S$ state will cost no energy; the molecule will behave as a simple paramagnet. In other words, when the magnetization is saturated by applying an external magnetic field, the return to equilibrium when the field is switched off is very fast and no hysteresis loop is observed. If, for structural reasons, the molecule has an axial symmetry (presence of a principal symmetry axis ≥ 3), the degeneracy of the $2S + 1M_S$ levels is lifted in zero field (zero-field splitting) to give pairs of M_S levels of the same energy. In some particular cases the energy of the degenerate + S and – S levels can be the lowest. In such cases, when the molecule is prepared in the $M_S = - S$ state and then the field is switched off, the reversal of the magnetization to the + S state implies overcoming an energy barrier with a magnitude that is proportional to the square of the spin value and to the magnitude of the axial anisotropy. The anisotropy can be described in a phenomenological manner by the following spin Hamiltonian:

$$H = D(S_z^2 - S(S + 1)/3) + E(S_x^2 - S_y^2), \quad (1)$$

where S is the spin value and S_z, S_x, and S_y are the three components of the spin operator; D and E are scalars (related to the anisotropy tensor) and express the magnitude of the axial and the rhombic anisotropies, respectively.

In the simple case of a strictly axial anisotropy, E is equal to zero and the energy levels calculated from Eq. 1 for a spin $S = 5$, for example, and a negative D value are shown in Scheme 1.

Another way is to plot the energy vs. M_S for a negative value, which allows us to show the presence of a barrier between the $M_S = - S$ and + S sublevels (Scheme 2).

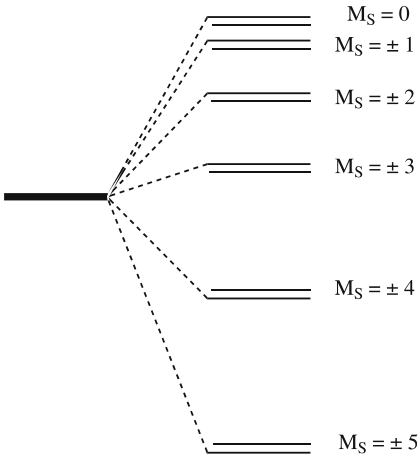

Scheme 1

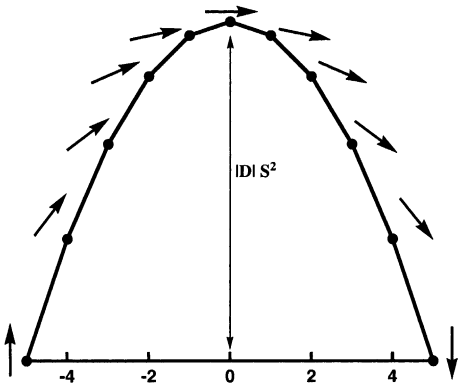

Scheme 2

The height of the energy barrier is equal to $|D|S^2$. In such a case, the magnetization energy is minimum when the spin is along a single axis. When a magnetic field is applied along such an axis, the saturation is reached for a very small value of the applied magnetic field; one can say that the molecule has an easy axis of magnetization and thus a hard plane of magnetization. The presence of the barrier leads to the blocking behavior and the hysteresis curve. In the case where D is positive, the magnetization energy is minimum when it is perpendicular to the anisotropy axis and can thus have any orientation within the perpendicular plane; thus, no barrier to the reorientation of the magnetization within the plane can exist and the blocking of the magnetization cannot occur.

The requirements to observe the blocking of the magnetization associated with a single molecule are

- a spin ground state as large as possible well separated from the first excited state;
- a large uniaxial (Ising-type) anisotropy.

However, even though the single molecule may have uniaxial anisotropy, one must insure that the molecules are organized in the crystal so that all their axes are in the same direction in order to maximize the overall anisotropy of the crystal.

Most of the synthetic work in this area has focused on metal–oxo clusters using a serendipitous assembly approach [9]. The general synthetic approach is to build up oxo-type cores in the presence of organic ligands that play simultaneously the roles of bridging and peripheral ligands and enable the stabilization of discrete molecular species. Christou and Winpenny [9–13] are the most active in this area and they succeeded in preparing a large variety of clusters among which some behave as SMMs. Among the numerous compounds, three are particularly interesting because they combine large

nuclearity and a high spin ground state. The first is a complex based on Fe^{III} of formula $[Fe_{14}(bta)_6O_6(OMe)_{18}Cl_6]$ obtained by a solvothermal route using benzatriazole (bta) as the bridging/capping ligand [14]. Preliminary magnetic studies suggest a spin ground state S between 23 and 25 and a positive axial parameter D, so no blocking of the magnetization was observed despite the large spin ground state of this complex. The second compound is a Mn_{25} complex of formula $[Mn_{25}O_{18}(OH)_2(N_3)_{12}(pdm)_6(pdmH)_6Cl_2]$, where $pmdH_2$ is pyridine-2,6-dimethanol [10]. It contains six Mn^{II} ions, 18 Mn^{III} ions, and one Mn^{VI} ion. The spin ground state of this complex was found to be as large as 51/2 based mainly on the susceptibility value at low temperature. The fit of the $M = f(H)$ data at different temperatures confirms the $S = 51/2$ value but with a rather small g value that may suggest a smaller spin value for the ground state. The D value extracted from the magnetization data was found to be negative and the height of the anisotropy barrier to be equal to 8.3 cm^{-1}. The SMM behavior was thus observed only at very low temperature. The third compound is a Mn_{20} complex of formula $[EtNH]_2[Mn_{18}{}^{III}Mn_2{}^{II}(O)_{12}(OH)_2(O_3PCH_2Ph)_{12}(O_2CCMe_3)_{10}(py)_2]$ obtained from the reaction of the mixed valence trinuclear $[Mn_3O(O_2CCMe_3)_6(py)_3]$ complex and $PhCH_2PO_3H_2$ in the presence of triethylamine [11]. The structural analysis shows that 12 Mn atoms (including the two Mn^{II}) lie in one plane with four Mn atoms above and four below giving a cigar shape to the molecule. Magnetization studies at very low temperature confirm the susceptibility data that indicates that the ground state is equal to 19 or 20. A SMM behavior is observed at a temperature higher than the former Mn_{25} complex but still below 4 K. Other metal–oxo complexes with high nuclearity (Mn_{84}...) have been reported but, unfortunately, the spin ground state is always relatively low [12, 13].

Even if the serendipitous assembly approach has produced most of the SMM complexes, none has an anisotropy barrier as high as those of the Mn_{12}-carboxylate derivatives. On the other hand, due to the synthetic approach itself, it is difficult to have a control on the nature of the spin ground state and on the orientation of the anisotropy axes of the individual metal centers within the molecules. In metal–oxo clusters, the presence of metal ions in a triangular geometry leads to a competition between the exchange coupling interactions, making the prediction of the value of the spin ground state very difficult. Furthermore, when the number of metal ions becomes large, the first excited states with large spin values are very close to the ground state, making the exact determination of the value of the spin ground state very difficult.

One alternative is to construct molecular clusters with already preformed mononuclear or polynuclear species with well-known electronic structure, so that the nature of the ground state and even in some cases the magnitude and the nature of the magnetic anisotropy may be easier to predict. Such a step by step approach was first used by Kahn and coworkers to prepare the very

first complexes that have a high spin ground state using $Cr^{III}(C_2O_4)_3^{3-}$ as a "complex as ligand" [15]. These ideas were exploited further when chemists succeeded for the first time in using hexacyanometallates as an inert building block to construct molecules with nuclearity higher than 4.

In the following, we will mainly focus on the different synthetic routes that allowed obtaining discrete species with a high spin ground state using cyanometallates. Particular attention will be given to the molecules that turned out to behave as single-molecule magnets.

2
Nature of the Exchange Coupling Interaction Through the Cyanide Bridge

Exchange coupling interaction through the cyanide bridge was perfectly well studied from the theoretical point of view by Weihe and Güdel [16]. We would like here to just give simple rules that help to predict the nature of the exchange coupling interaction between two metal ions through the cyanide bridge. The synthesis of polynuclear complexes with the cyanide as a bridge is carried out using inert $M(CN)_6^{3-}$($M = Cr^{III}, Fe^{III}$...) complexes as building blocks. Since the cyanide induces a strong crystal field, all mononuclear cyanometallates are at the low-spin state with the single electrons in the d_{xy}, d_{xz}, and d_{yz} orbitals. Even though the M – CN – M′ linkage is almost never linear in molecular species, the C – N – M′ angle is usually larger than 160° in most complexes. Thus, the prediction of the nature of the magnetic coupling follows simple rules such as overlap and orthogonality. In systems with octahedral geometry, one may safely assume that the single electrons are described by t_{2g} orbitals for the metal ions linked to the carbon end of the cyanide. For the metal ions linked to the nitrogen end, a high spin state occurs in most cases and, depending on the nature of the M′ metal ion, the t_{2g} and e_g orbitals may have single electrons. When M′ is Ni^{II} or Cu^{II} with respectively one and two single electrons in the e_g orbitals, one expects to observe a ferromagnetic interaction because of the orthogonality of the magnetic orbitals (Scheme 3). For M′ = V^{II}, V^{III}, or V^{IV} only the t_{2g} orbitals are filled and because of the overlap between the magnetic orbitals the interaction is expected to be antiferromagnetic (Scheme 4).

In the case of high-spin Cr^{II} (d^4), Mn^{III} (d^4), Mn^{II} (d^5), Fe^{II} (d^6), and Co^{II} (d^7) ions the prediction is not straightforward, because the overall exchange interaction is the result of the antiferromagnetic contribution coming from the t_{2g} – t_{2g} overlap and the ferromagnetic one resulting from the orthogonality of the t_{2g} – e_g orbitals (Scheme 5). However, the experimental results can be qualitatively rationalized on the basis of the number of exchange pathways expected for the different configurations of the metal ions.

Let us consider the case of a hexacyanochromate(III) with a t_{2g}^3 configuration. For a Cr^{III} – CN – Mn^{II} linkage, the Mn^{II} ion has five d electrons

($t_{2g}^3 e_g^2$) and the number of exchange pathways is equal to 15 (3×5). There are nine $t_{2g} - t_{2g}$ pathways; among them only two, the $d_{xz} - d_{xz}$ and $d_{yz} - d_{yz}$, are effective (we assume the z direction along the Cr – CN – Mn linkage) and are responsible for the antiferromagnetic contribution arising from the $t_{2g} - t_{2g}$ overlap. The remaining six pathways correspond to the $t_{2g} - e_g$ interaction and only the two $d_{xz} - d_{z2}$ and $d_{yz} - d_{z2}$ pathways are effective for the ferromagnetic contribution. Thus, when the M′ metal ion has single electrons in the t_{2g} and e_g orbitals it is difficult to predict easily the nature of

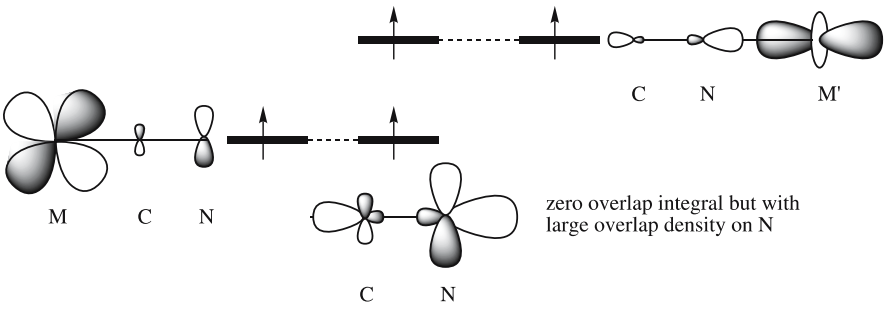

Scheme 3

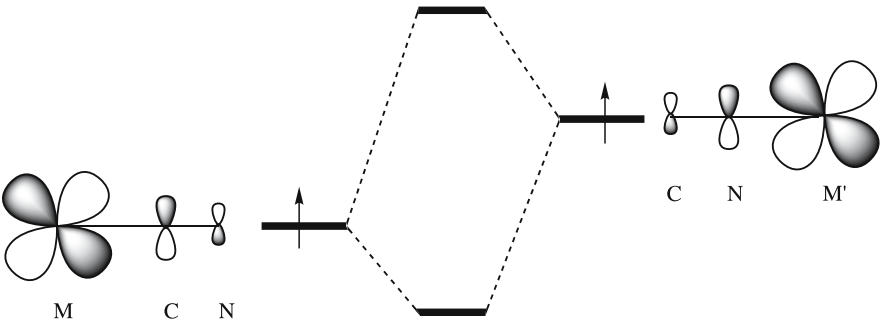

Scheme 4

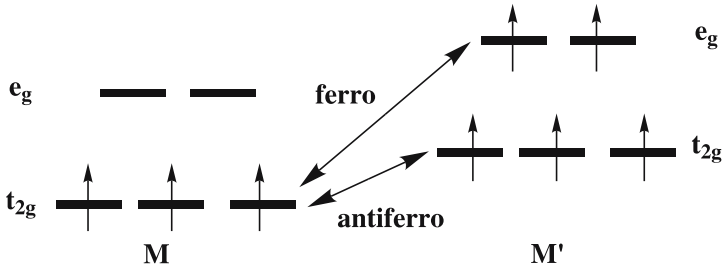

Scheme 5

the overall exchange coupling interaction. Experimental studies show that, in the case of the $Cr^{III} - CN - Mn^{II}$ linkage, the interaction is antiferromagnetic, which means that $t_{2g} - t_{2g}$ contribution dominates. The exchange coupling parameter J (based on the spin Hamiltonian $H = -JS_1 \cdot S_2$) was found to be equal to -8 and $-5\,cm^{-1}$ for two similar heptanuclear $Cr^{III}Mn^{II}_6$ complexes [17, 18]. When Mn^{II} is replaced by Fe^{II} or Co^{II} that possess two and one single electrons respectively in their t_{2g} orbitals, the overall interaction is found to be ferromagnetic in the corresponding three-dimensional Prussian blue analogues [19]. Clearly, the ferromagnetic contribution dominates because the number of $t_{2g} - t_{2g}$ antiferromagnetic exchange pathways has decreased (six for the Cr^{III}–Fe^{II} linkage and three for $Cr^{III} - Co^{II}$), while the number of ferromagnetic $t_{2g} - e_g$ pathways is still maximal.

It is interesting at this stage to consider the case where Cr^{III} is replaced by low-spin Fe^{III} with the t_{2g}^5 configuration and thus one single electron in the t_{2g} orbitals. For the $Fe^{III} - CN - Fe^{III}(HS)$ linkage, the number of antiferromagnetic and ferromagnetic exchange pathways is three and two respectively and the overall interaction was found to be ferromagnetic in three reported cases [20–22]. Because of the presence of one single electron in the low-spin Fe^{III} t_{2g} orbitals, only one antiferromagnetic exchange pathway is operative and the ferromagnetic contribution dominates. If the number of e_g electrons on the M′ metal ion is reduced (as for high-spin Mn^{III}), the nature of the interaction may well be ferromagnetic or antiferromagnetic; this will in such a case highly depend on the $Mn^{III} - N - C$ angle. However, one will expect in

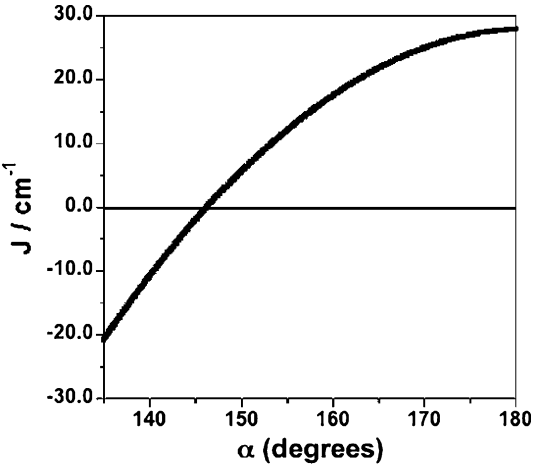

Fig. 2 Variation of the exchange coupling parameter J as a function of the $Ni - N - C$ angle in the case of the $Ni^{II} - CN - Cr^{III}$ linkage

either case a rather weak overall magnetic coupling, because the two contributions can be very close in magnitude.

In order to complete this rather qualitative analysis of the nature of the exchange coupling interaction through the cyanide bridge, it is interesting to mention the results obtained by Julve, Cano and coworkers for the dependence of the magnitude of the ferromagnetic interaction in the case of the $Cr^{III} - CN - Ni^{II}$ linkage [23]. As stated above when the linkage is linear, a ferromagnetic interaction is expected and observed due to the orthogonality of the magnetic orbitals. However, when the Ni – N – C angle starts to be bent, the overlap between the magnetic orbitals is not zero any more and an antiferromagnetic contribution arises that weakens the magnitude of the ferromagnetic magnetic coupling. Density Functional Theory (DFT) calculations showed that the Ni – N – C angle must be lower than 140° in order to overcome the ferromagnetic coupling (Fig. 2).

The analysis we have made is clearly qualitative; however, it explains well almost all the experimental results reported in the literature. When the number of exchange pathways leads to ferromagnetic and antiferromagnetic contributions that are very close in magnitude, a small variation of the M′ – N – C angle and the nature of the M and M′ metal ions start to be the important factors that determine the nature of the exchange interaction.

3
SMMs Based on Hexacyanometallates

Cyanometallates are probably the most adapted building blocks that allow chemists to carry out a stepwise approach in order to prepare molecular clusters. Two prerequisite conditions have to be fulfilled in order to put into practice the stepwise approach. Firstly, the building block molecular complex must be able to play the role of a ligand (complex as ligand), i.e. must possess on its periphery atoms bearing lone electron pairs able to coordinate to a metal ion; this complex must be stable and inert since all reactions are performed in solution. Secondly, the molecule that plays the role of complex towards the lone pairs of the ligands must bear chelating organic ligands that cannot be substituted by the nitrogen end of the cyanide and available sites in order to link to the hexacyanometallate.

3.1
Heptanuclear Complexes

Applying the simple ideas developed above and reacting a “complex as metal” bearing a pentadentate ligand with hexacyanochromate(III) lead to the formation of the first heptanuclear complex of formula $[Cr^{III}(CNNi(tetren))_6](ClO_4^-)_9(CrNi_6)$ (tetren is $H_2NC_2H_4(HNC_2H_4)_3NH_2$) that has a spin ground

state $S = 15/2$ as a result of the ferromagnetic interaction between the central Cr^{III} ($S = 3/2$) ion and the six peripheral Ni^{II} ($S = 1$) metal ions, as was expected [24]. Unfortunately, the crystal structure of this compound has not been fully solved mainly because of a large disorder on the organic ligands. However, the magnetic properties below 1 K were investigated and a slow relaxation of the magnetization was evidenced [25].

The best way to probe the dynamic properties consists in measuring the magnetic susceptibility in the presence of an oscillating ac magnetic field at different frequencies. Alternating current (ac) measurements allow probing the relaxation time of the magnetization. For a simple paramagnet, the magnetization of the system stays in phase with the oscillating magnetic field that gives the magnetic susceptibility. When the relaxation time of the magnetization of the system probed and the frequency of the oscillating field become of the same order of magnitude, the magnetization does not follow the magnetic field and the susceptibility will exhibit two components: the real in-phase part (χ') and the imaginary out of phase part (χ''). For $CrNi_6$, ac measurements show, at a frequency of 1000 Hz, a maximum for χ' at $T = 0.38$ K. Associated with this maximum, the out of phase component (χ'') increases and, on cooling, reaches a maximum at 0.24 K. Measurements at different frequencies (1000, 300, and 30 Hz) show that the maxima of χ' and χ'' are frequency dependent and shift to low temperature when the frequency of the oscillating field is decreased (Fig. 3).

The magnetization relaxation time (τ) is proportional to the inverse of the frequency (f) of the oscillating field: $\tau = 1/2\pi f$. The blocking temperature (T_B) at a given frequency corresponds to the temperature of the maximum of

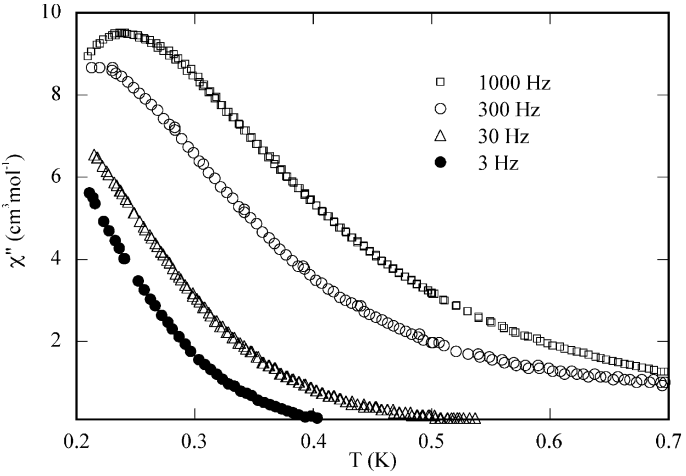

Fig. 3 $\chi''_M = f(T)$ for different frequencies of the magnetic oscillating field in zero dc field for $CrNi_6$

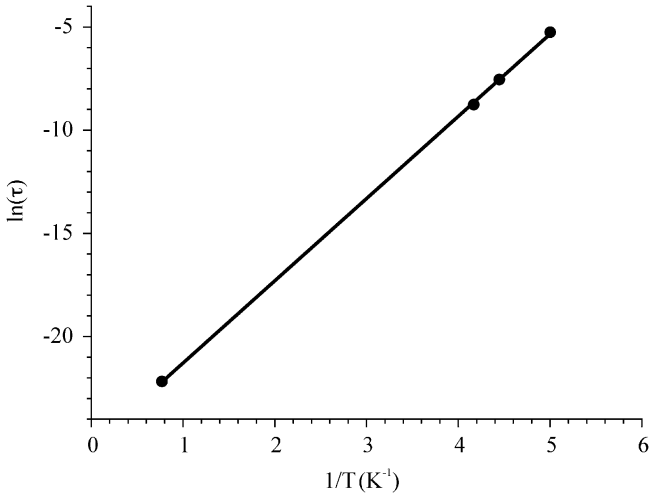

Fig. 4 $\ln(\tau) = f(1/T)$ for $CrNi_6$

the χ'' signal. Plotting $\ln(\tau)$ against $1/T_B$ (including a measurement made at 680 MHz using a different apparatus) gives a straight line (Fig. 4). The blocking phenomenon is thus thermally activated (Arrhenius type). The relaxation time can be expressed as $\tau = \tau_o \exp(E_A/kT_B)$, where τ_o is the relaxation time at infinite temperature and E_A/k is the activation energy. τ_o and E_A are found equal to 1.1×10^{-11} s and 3.98 cm^{-1}, respectively, for $CrNi_6$. This complex is the first based on a cyanometallate that exhibits a SMM behavior, even though around 200 mK [25]. This result is intriguing since an octahedral complex does not possess an axial magnetic anisotropy.

Actually, Marvaud and coworkers have recently reported a complex with the same composition but that crystallizes in a different space group of the original complex [26]. One possible explanation of this difference and of the difficulty in refining fully the crystal structure of the original complex is the presence of different isomers of tetren capping the Ni^{II} ions, which lowers the symmetry of the heptanuclear complex and thus leads to the presence of a very small but non-zero Ising-type magnetic anisotropy within the original complex. Even though several heptanuclear complexes based on $Fe(CN)_6^{3-}$ and $Cr(CN)_6^{3-}$ with a relatively high spin ground state ($S = 27/2$ for the $Cr^{III}Mn_6^{II}$) or using high-spin Mn^{III} complexes to introduce anisotropy were prepared, none has shown the SMM behavior to date [18, 27, 28].

3.2 Pentanuclear Complexes

The use of pentadentate ligands restricts the architecture of the polynuclear complexes to that of a central ion surrounded by up to six peripheral ones.

One possible tactic to access new architectures is to use organic ligands with less than five chelating sites to stabilize a molecular complex. This is a difficult task because of the propensity of the cyanide bridge to form extended networks.

In 1997, Murray and coworkers reported the structure of a pentanuclear complex obtained from the reaction of ferricyanide and $[Ni(bpm)_2]^{2+}$ (bpm = bis(1-pyrazolyl)methane) of formula $[Fe(CN)_6]_2[Ni(bpm)_2]_3 \cdot 7H_2O$ (Fig. 5) [29].

The $[Ni(bpm)_2]^{2+}$ complex has two available sites in cis position and may form with a hexacyanometallate a linear chain structure. However, a molecular discrete species was isolated. The complex has a trigonal bipyramidal shape with the three $[Ni(bpm)_2]^{2+}$ bridging two ferricyanides. The complex has a spin ground state $S = 4$, but a long-range ferromagnetic order due the ferromagnetic intermolecular interactions mediated by a three-dimensional network of hydrogen bonds was observed below 23 K. The formation of a polynuclear complex instead of an extended network can be understood by looking at the steric hindrance of the organic ligand, which precludes the extension of the molecule in one dimension by bridging the cyanide on its periphery. Since then, several complexes with the trigonal bipyramidal structure were synthesized. Very recently, Dunbar and coworkers reported a similar structure by using low-spin $Mn^{III}(CN)_6^{3-}$ as building block and $Mn^{II}(tmphen)_2^{2+}$ as the assembling metal complex (Fig. 6) [30].

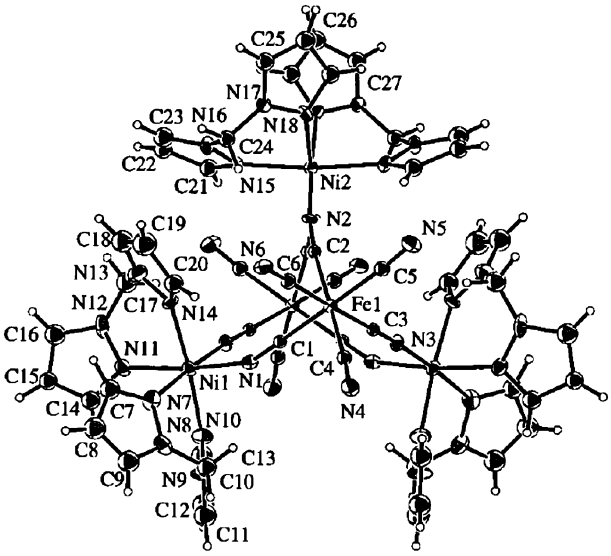

Fig. 5 View of the molecular structure of the pentanuclear complex $[(Ni(bpm)_2)_3(Fe(CN)_6)_2]$

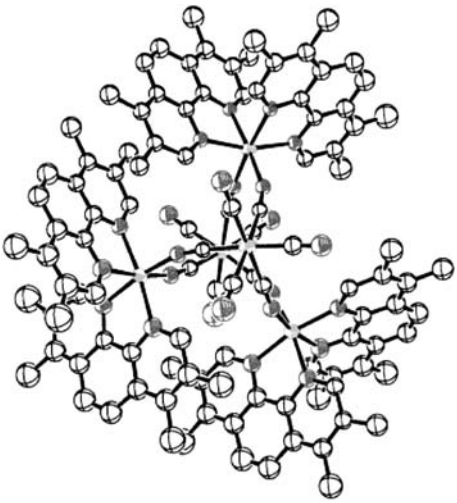

Fig. 6 View of the molecular structure of the pentanuclear complex $[(Mn^{II}(tmphen)_2)_3(Mn^{III}(CN)_6)_2]$

The magnetic studies performed on this complex showed an antiferromagnetic interaction through the cyanide bridge that leads to a high-spin ground state. The study of the magnetization indicates a $S = 11/2$ ground state with an effective D parameter equal to $-0.348\ cm^{-1}$. Alternating current susceptibility studies show an out of phase χ'' susceptibility signal above $T = 2$ K that depends on the frequency of the oscillating magnetic field. Even though no measurements below 1.8 K were carried out, the frequency dependence already observed indicates that the complex behaves as a SMM. The presence of spin–orbit coupling for the $Mn^{III}(CN)_6^{3-}$ complex is probably responsible for the relatively large magnetic anisotropy of the complex especially since the high-spin $d^5 Mn^{II}$ ions have negligible magnetic anisotropy.

3.3 Tetranuclear and Trinuclear Complexes

In some particular cases, it is possible to stabilize tetranuclear complexes with hexacyanometallates taking advantage of the neutrality of the polynuclear complex and isolate them in a given solvent. To the best of our knowledge, the first tetranuclear complexes obtained using this tactic and where anisotropic high-spin Mn^{III} ions were introduced were obtained from the reaction of $M(CN)_6^{3-}$ ($M = Fe^{III}$ or Cr^{III}) and mononuclear complexes of general formula $M'L_5Cl$ ($M' = Fe^{III}$, Mn^{III}; for L_5 see Scheme 6) [21].

Unfortunately, no crystals suitable for structural determination were obtained. It is interesting to note that when the building block was hexacyanochromate(III), the exchange interaction with the Fe^{III} and the Mn^{III}

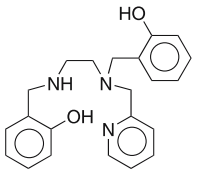

Scheme 6

ions was found to be antiferromagnetic while, for $Fe(CN)_6^{3-}$, the interaction is ferromagnetic. Since no structure was available for the four compounds, no ac studies were carried out.

Very recently, Miyasaka, Clérac and coworkers reported the synthesis and the crystal structure of two tetranuclear complexes of formula $[(NC)_3M(CNMn(salen))_3]$ with M = Fe^{III} and Cr^{III} obtained from the reaction of $\{NH_2(n\text{-}C_{12}H_{25})_2\}_3[M(CN)_6]$ and $[Mn(salen)(H_2O)]ClO_4$ (salen = *N*,*N*′-ethylene bis(salicylideneiminate)) in a 1 : 1 mixing ratio in EtOH/MeOH solution [31]. The two complexes are isostructural with the Mn units surrounding the central cyanometallate in a meridional fashion through the cyanide bridge. The Mn^{III} ions have as expected a Jahn–Teller distortion leading to Mn – N(NC) distances ranging from 2.29 to 2.32 Å (Fig. 7).

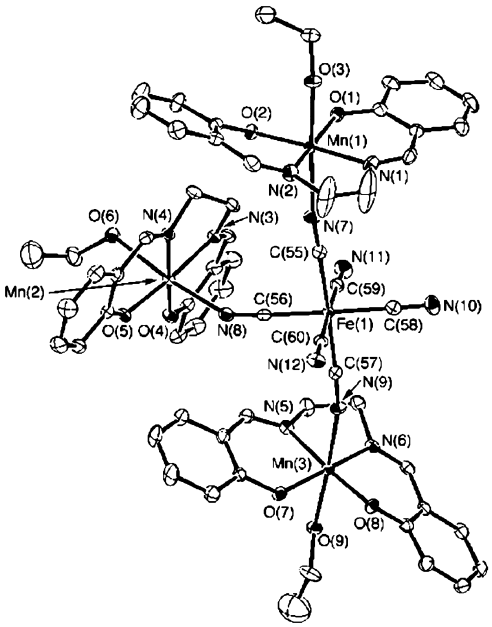

Fig. 7 View of the molecular structure of the tetranuclear complex $[(CN)_3Fe^{III}(CNMn^{III}(salen))_3]$

The magnetic studies showed clearly that the exchange interaction between Cr^{III} and Mn^{III} is antiferromagnetic with an exchange parameter $J_{Cr-Mn} = -4.6\ cm^{-1}$. The exchange interaction within the $FeMn_3^{III}$ compound was found to be antiferromagnetic along two of the three bridges and ferromagnetic for the third one. This was rationalized as due to a Mn – N – C angle equal to 149°, much smaller than the other two (> 161°). Such an interaction (Scheme 7) leads to a spin ground state $S = 3/2$ for the $FeMn_3^{III}$ complex.

The dynamics of the magnetization of the two complexes were probed by ac susceptibility measurements. Only the $FeMn_3^{III}$ complex showed the presence of an out of phase signal. The ac studies were performed above $T = 1.8$ K, so the maximum of the susceptibility curves could not be observed; however, a hysteresis loop occurs in the magnetization vs. field studies at $T = 0.5$ K confirming the characteristics of a SMM behavior for this compound. Detailed studies at lower temperatures are necessary for this compound in order to confirm without doubt the SMM behavior; this is important because of the rather low value of the spin ground state ($S = 3/2$). However, since the anisotropy plays a determinant role, we examined for this particular compound the contribution of the local anisotropy to the $S = 3/2$ ground state relative to the $S = 11/2$ state that is stabilized in the case where the magnetic coupling is antiferromagnetic for the three Fe – CN – Mn linkages (see Sect. 5).

The use of $[Mn^{III}(salen)(H_2O)]^+$ with the potassium salt of hexacyanometallate(III) leads to heptanuclear complexes [27, 28]. In one case, however, a trinuclear $FeMn_2^{III}$ complex was isolated by Long and coworkers [27]; however, the crystal contains dimeric $[Mn(salen)(H_2O)]_2$ species, two mononuclear Mn complexes, and one $Fe(CN)_6^{3-}$ molecule. It is interesting to note here that the stoichiometry corresponds to a neutral $FeMn_3$ compound. The same situation is found for the heptanuclear complex based on hexacyanoferrate that cocrystallizes with one molecule of $Fe(CN)_6^{3-}$ to lead to the $FeMn_3$ neutral stoichiometry as well [28].

Isolated trinuclear complexes were obtained by using 5-X-salen (X = Cl, Br) derivatives [32]. Recently, Long and coworkers investigated the behavior of trinuclear complexes obtained from the reaction of hexacyanometallate(III) (Fe and Cr) and $[Mn(5\text{-Br-salen})(H_2O)]^+$ in MeOH and water (Fig. 8) [33].

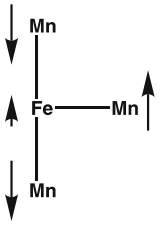

Scheme 7

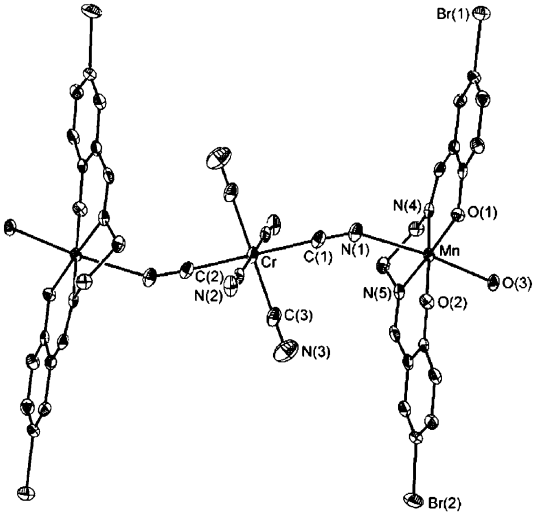

Fig. 8 View of the molecular structure of the trinuclear complex $[(CN)_4Fe^{III}(CNMn^{III}(5\text{-Br-salen}))_2]^-$

The dc magnetic studies indicate a ferromagnetic exchange coupling (J = 4.6 cm^{-1}) between the low-spin Fe^{III} and the Mn^{III} ion through the cyanide bridge, leading to a spin ground state $S = 9/2$. An antiferromagnetic coupling was found for the $CrMn_3$ complex, leading to a spin ground state $S = 5/2$. The two complexes show slow relaxation of the magnetization. The maxima of the out of phase signal of the Fe-based compound are present above $T = 2$ K. An estimation of the anisotropy barrier for this complex ($|D|S^2$) gives a value of 25 cm^{-1}. However, the out of phase signals (χ'') for the two compounds are extremely weak in comparison to the χ' signals when compared to other fully characterized SMM complexes.

Very recently, a report by Miyasaka and Clérac on a FeM_2^{III} complex using a modified salen ligand (N,N'-(1-methyethylene)bis(salicylideneiminate)) showed that the complex has a $S = 9/2$ spin ground state that undergoes a slow relaxation of the magnetization. Very low temperature magnetization studies on one single crystal using a micro-squid array show a hysteresis for the $M = f(H)$ curves but with fast relaxation at zero field [34].

4
SMMs Based on Tricyanometallates

Tricyanometallates with the three cyanide ligands in facial positions were first used by Long and coworkers in order to stabilize new polynuclear complexes with cubic architecture [35]. They used an inert diamagnetic

Co^{III} complex with the triazacyclononane (tacn) ligand blocking three facial positions of the octahedron; the three remaining sites were occupied by cyanides: $[(tacn)Co(CN)_3]$. The reaction of this complex with $[(tacn)Cr(H_2O)_3](CF_3SO_3)_3$ leads to the octanuclear $[Cr_4Co_4(CN)_{12}(tacn)_8](CF_3SO_3)_{12} \cdot 8H_2O$ compound. The structure of the cation showed a cubic complex with the vertices occupied by Co and Cr atoms (Fig. 9).

This complex is not interesting from the magnetic point of view because of the presence of diamagnetic Co^{III} ions, but its preparation can be considered as a precursor work for a new class of compounds based on tricyanometallate among which some behave as SMMs. It is noteworthy that the synthesis of this complex was possible mainly because of the inertness of the building blocks that allowed carrying on the reaction in boiling water in order to reach the thermodynamic compound. The use of assembling paramagnetic complexes bearing an organic ligand will generally not allow us to perform reactions in such extreme conditions, because paramagnetic complexes with metal of the first transition metal series are generally labile.

Long and coworkers extended their tactic by using a similar paramagnetic building block based on Cr^{III}, i.e. $[(Me_3tacn)Cr(CN)_3]$. The reaction between this complex and $Ni(H_2O)_6^{2+}$ in boiling water allowed us to isolate another cubic architecture for the complex of formula $[(Me_3tacn)_8Cr_8Ni_6(CN)_{24}]^{12+}$ (Cr_8Ni_6) (Fig. 10) [36].

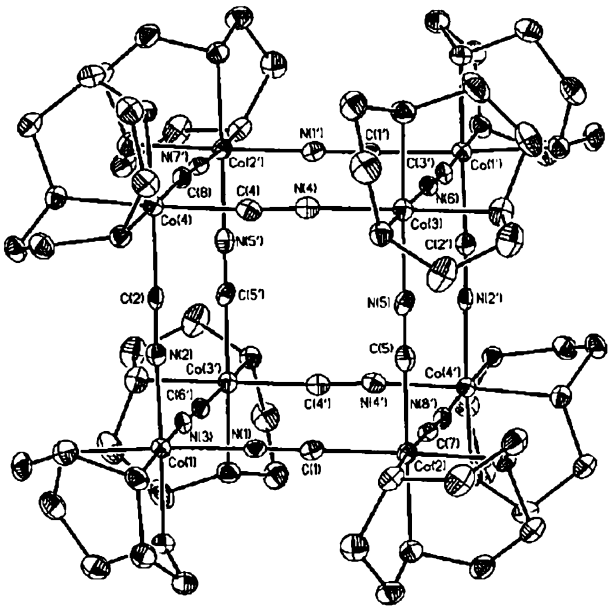

Fig. 9 View of the cubic structure of $[Co_8^{III}(CN)_{12}(tacn)_8]^{12+}$

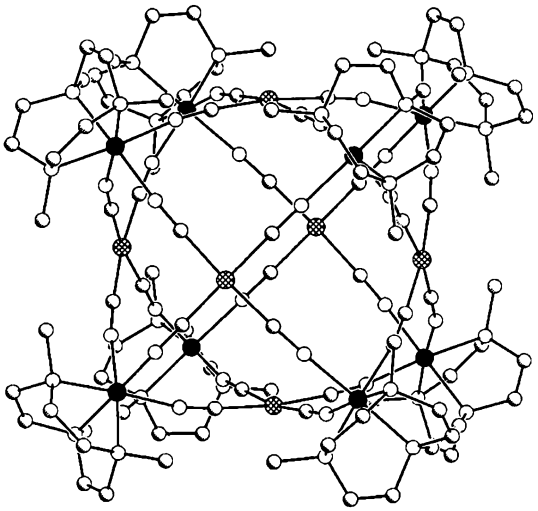

Fig. 10 View of the cubic structure of $[(Me_3tacn)_8Cr^{III}_8Ni_6(CN)_{24}]^{12+}$

The Cr atoms occupy the vertices of the cube and the Ni atoms the centers of the six faces. Unfortunately, because of the relative lability of Cr^{III} and particularly because of the stability of the $Ni(CN)_4^{2-}$ complex, linkage isomerism occurs, leading to Ni atoms linked to the carbon end and Cr atoms to the nitrogen end of the cyanide bridge. Such a structure where an atom occupies the center of the cube's faces stabilizes strongly a square planar geometry, especially when the assembling paramagnetic ion is Ni^{II}. Even if this result is at first view deceiving from the magnetic point of view (square planar Ni^{II} complexes are diamagnetic), it opens new perspectives in the chemistry of cyanide bridged clusters.

4.1 Cubic Complexes

One of the main problems with the chemistry based on $[(Me_3tacn)M(CN)_3]$ is the insolubility of the building blocks in almost any solvent. A new type of anionic and soluble building block must therefore be prepared. An interesting paramagnetic complex was reported recently by Julve and coworkers [22]. It has the same facial structure but the tacn-type ligand was replaced by the monoanion $HB(pz)_3^-$ ($HB(pz)_3^-$ = hydrotris-(1-pyrazolyl)borate) and Cr by Fe, i.e. $[(HB(pz)_3)Fe^{III}(CN)_3]^-$ (Fig. 11) [22].

Very recently, the reaction between $(Bu_4N)[(HB(pz)_3)Fe^{III}(CN)_3]$ and $[Cu(H_2O)_6](ClO_4)_2$ in acetonitrile and water led to the formation of a complex of formula $[(HB(pz)_3)_8(H_2O)_6Fe_8Cu_6(CN)_{24}](ClO_4)_4$ (Fe_8Cu_6) [37]. This complex has the same structure as the cubic Cr_8Ni_6 with the Fe atoms oc-

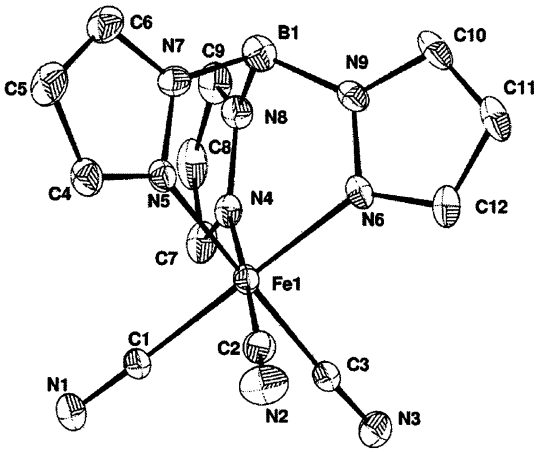

Fig. 11 View of the structure of *fac*-$[Fe(HB(pz)_3)(CN)_3]^-$

cupying the vertices of the cube and the Cu atoms the centers of the faces. The important difference is that d^9 Cu^{II} is paramagnetic ($S = 1/2$) and, since $Cu(CN)_4^{2-}$ is not particularly stable, no linkage isomerism occurs. The magnetic studies reveal, as expected, a ferromagnetic exchange coupling between the low-spin Fe^{III} and Cu^{II}, leading to a spin ground state $S = 7$ for the complex. The magnetization studies as a function of field at different temperatures suggest that the axial D parameter is negative ($D = -0.16\,cm^{-1}$) with a very small rhombic parameter E ($E/D = 0.03$). The investigation of the dynamic behavior shows the presence of a non-zero out of phase signal below 3 K. Even though no maximum was observed above $T = 1.8$ K, there is a frequency dependence of χ'' that strongly suggests a blocking of the magnetization at lower temperatures. However, low-temperature studies are necessary to confirm the SMM behavior. The determination of the anisotropy axes by magnetic measurements on single crystals will add to the understanding of the slow relaxation observed.

Efforts to incorporate transition-metal ions of the second or third series that possess large spin–orbit coupling in order to enhance the overall anisotropy of the molecular clusters is one of the possibilities that chemists try to explore. Dunbar and coworkers reported the preparation of an octanuclear complex of formula $[(MnCl)_4(Re(triphos)(CN)_3)_4]$ from the reaction of $(Et_4N)[Re(triphos)(CN)_3]$ and $MnCl_2$ in a mixture of acetone and acetonitrile under reflux. The complex has a cubic structure similar to Cr_4Co_4, where the metal ions occupy the vertices of the molecular cube (Fig. 12) [38].

This complex seems to have a SMM behavior suggested by the presence of an out of phase susceptibility signal which is frequency dependent. It is interesting to note that the Mn atoms are tetracoordinated and bonding the nitrogen end of three cyanides and a Cl atom. The local symmetry on the Mn

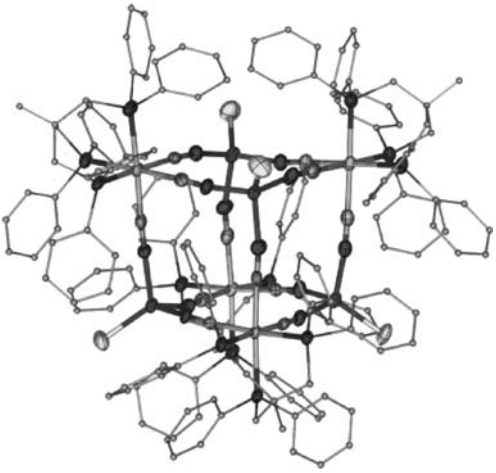

Fig. 12 View of the cubic structure of $[(MnCl)_4(Re(triphos)(CN)_3)_4]$

is close to C_{3v}, which lowers the overall symmetry of the cube due to a C_3 symmetry axis. This structural distortion is thought to be the origin of the axial magnetic anisotropy responsible for the anisotropy barrier of the compound. Again, in this case lower magnetic studies are necessary in order to confirm the suggested SMM behavior.

4.2 Square Complexes

Even though not based on tricyanometallates, one of the first examples of paramagnetic molecular squares based on the cyanide bridge was reported by Oshio and coworkers [39] by reacting the $[(bpy)_2Fe^{III}(CN)_2](PF_6)$ building block with $[Cu(bpy)(MeOH)_2](NO_3)$ in MeOH. The outcome of such a reaction may be either a zigzag cationic FeCu chain, or a molecular square with six positive charges. It is clear that thermodynamically the molecular square is more stable, because all the bonds are fulfilled and the entropy of the reaction is maximal. The important point is to avoid the precipitation of the chain before reaching the thermodynamic conditions. Oshio and coworkers left the reactants to stir for three days and then added NH_4PF_6 in order to isolate the tetranuclear molecular square complex $[Fe^{III}_2Cu^{II}_2(\mu\text{-}CN)_4(bpy)_6](PF_6)_6$ from solution (Fig. 13) [39].

Recently, Holmes and coworkers succeeded in stabilizing molecular squares by reacting $[Tp^*Fe(CN)_3]^-$ (Tp^* = hydridotris(3,5-dimethylpyrazol-1-yl)borate) is a derivative of $(HB(pz)_3)$ and $M^{II}(OTf)^{2+}_2$ (OTf = trifluoromethanesulfonate, M = Mn, Co, and Ni) in DMF and obtained tetranuclear Fe_2M_2 complexes (Fig. 14) [40]. The metal ions occupy the vertices of the square; the coordination sphere of the Ni atom is completed by four DMF

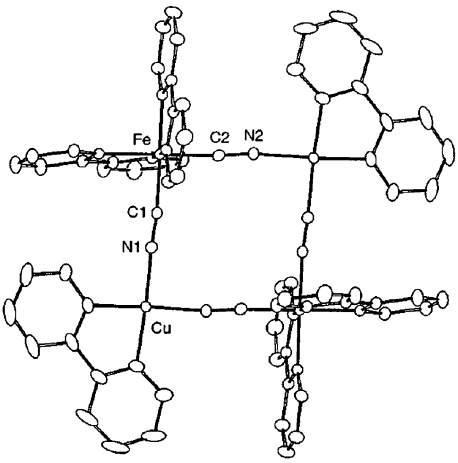

Fig. 13 View of the structure of the molecular square $[(Fe^{III}(bpy)_2)_2(Cu^{II}(bpy))_2(CN)_4]^{6+}$

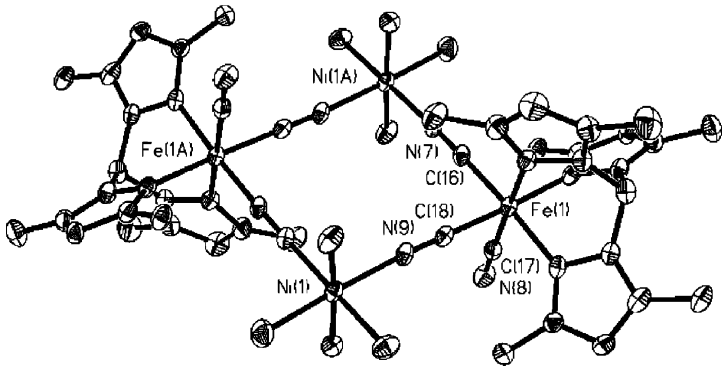

Fig. 14 View of the structure of the molecular square $[Tp^*Fe^{III}(CN)_3Ni^{II}(DMF)_4]_2^{2+}$

molecules and each Fe atom has one pendant cyanide ligand. The complex containing the Ni atoms has a $S = 3$ ground state and presents an out of phase ac signal. The height of the anisotropy barrier was estimated from a magnetization study to be equal to about 36 cm^{-1}, the largest value reported for a cyanide bridged complex. This is a relatively large value when compared to other SMMs even though it is still lower than that of Mn12-ac. However, the spin ground state is only 3 in this complex while it is equal to 10 for Mn12-ac.

4.3
Heptanuclear Trigonal Prismatic Complex

Introducing transition-metal ions of the second series that has large spin–orbit coupling seems to be an interesting route to prepare new SMMs. Long

and coworkers succeeded in isolating a heptanuclear complex of formula $K[(Me_3tacn)_6Mn^{II}Mo_6^{III}(CN)_{18}](ClO_4)_3$ from the reaction of $[(Me_3tacn)_6Mo^{III}(CN)_3]$ and $Mn(ClO_4)_2 \cdot 6H_2O$ in the presence of $KClO_4$ (Fig. 15) [41].

The structure of the complex consists of a central Mn atom surrounded by six nitrogen atoms from six $(Me_3tacn)Mo^{III}(CN)_3$; each Mo complex has two non-bridging cyanide ligands. The geometry of the complex is close to trigonal prismatic with parallel faces twisted about the three-fold axis 22.6° away from the fully eclipsed position. The antiferromagnetic exchange coupling interaction found leads to a $S = 13/2$ spin ground state. The D value extracted from the fit of the magnetization was found to be equal to $-0.33\ cm^{-1}$ with $E/D = 0.05$, indicating a relatively axial anisotropy. A maximum in the χ' signal was observed; it is associated with an out of phase signal. The χ'' frequency dependence leads to an activation barrier of $10\ cm^{-1}$, much smaller than for other complexes with lower spin states and metal ions which have weaker single-ion anisotropy such as for Fe_2Ni_2 (see Sect. 4.2).

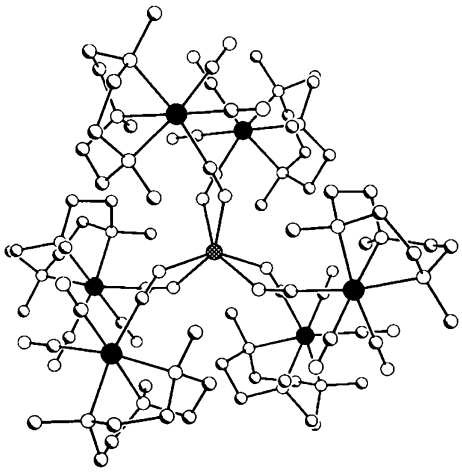

Fig. 15 View of the structure of the trigonal prismatic complex $[(Me_3tacn)_6Mn^{II}Mo_6^{III}(CN)_{18}]^{2+}$

5
Predicting the Magnetic Anisotropy

For cyanide bridged systems, the prediction of the nature and even the magnitude of the exchange coupling parameters between the different magnetic ions is relatively well established and the behavior of most of the reported molecular clusters follows quite well the simple rules expressed in Sect. 2. These rules have been successfully used to build clusters with relatively high-

spin ground states. Magnetic anisotropy is the other ingredient necessary to achieve a large activation barrier for the reversal of the magnetization.

When looking at all the SMMs reported in the literature, it is quite deceiving to conclude that to date Mn12-ac (and the other Mn12 belonging to the same family) still have the record for the value of the anisotropy barrier (50 cm^{-1}) and actually very few compounds have a value larger than 30 cm^{-1}.

The molecular clusters based on cyanide offer a simple example to predict the nature and the magnitude of the magnetic anisotropy of the ground spin state.

In order to compute the anisotropy of a given spin state in a molecular cluster, one must take into account different contributions: (i) the contribution of the single-ion anisotropy for the relevant spin state, (ii) the contribution coming for dipolar interaction, and (iii) the contribution coming from the exchange itself. We will assume in the following that the exchange interaction within the complexes we will consider is relatively large, so that we can thus express the anisotropy of the total spin states resulting from the interaction between the local spins in the case of a dinuclear complex A – B as

$$\boldsymbol{D} = d_1\boldsymbol{D}_A + d_2\boldsymbol{D}_B + d_{12}\boldsymbol{D}_{AB}\,. \tag{2}$$

Here $\boldsymbol{D}_A$, $\boldsymbol{D}_B$, and $\boldsymbol{D}_{AB}$ are the tensors corresponding to the single ion A, to the single ion B, and to the anisotropic interaction, respectively; d_1, d_2, and d_{12} give the contributions of each tensor [42]. Since Eq. 2 is a tensorial relation, the orientation of each tensor must be known. The metal–metal distance through the cyanide bridge is around 5 Å, so one can safely neglect the contribution to anisotropy coming from the dipolar interaction; furthermore, the exchange interaction between the metal ions even though not negligible is still relatively weak for the anisotropic term to be considered. So, for cyanide bridged systems, we assume that mainly the single-ion anisotropy contributes to the overall anisotropy. This approximation is not valid for metal–oxo clusters for instance, since the M – M distances are much shorter so that the anisotropy coming from dipolar interaction cannot be neglected. Furthermore, the exchange anisotropy may be important because of the large exchange coupling parameter that can be present for such cases.

We will, in the following, consider a "T"-like geometry with a central $S = 1/2$ (metal M) ion and three peripheral $S = 2$ (metal M′) ions (Scheme 8).

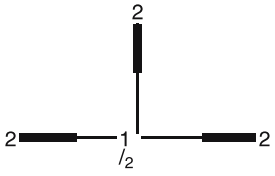

Scheme 8

We will assume that the peripheral metal ions have axial anisotropy ($E = 0$) and that the principal axis is along the M – M′ bonds. We will assume as well that the exchange interaction between the central M and the peripheral M′ ions is of the same nature, either ferromagnetic or antiferromagnetic. Such a situation can be found, for example, if the peripheral atoms are high-spin Mn^{III} with a Jahn–Teller distortion along the M – M′ bond and the central metal ion has only three bridging cyanides in meridional fashion. The computation of the total $\boldsymbol{D}$ tensor for the tetranuclear "T"-like complex leads to a maximum rhombicity for the anisotropy, which means that the axiality of the peripheral M′ ions is completely lost [43]. This result does not depend of course on the sign (easy axis or easy plane of magnetization) of the local D parameter. If the same calculations are performed in the similar case as above but with the M′ – M – M′ angles equal to 120° instead of 90 and 180° (Scheme 9) and considering a negative D value (easy axis of magnetization) for M′, the $\boldsymbol{D}$ tensor of the complex remains axial ($E = 0$) but the D value becomes positive (an easy plane of magnetization). Thus, using a metal ion with a negative D_{local} value does not insure the same sign for D_{total} of the polynuclear complex. A local easy axis of magnetization may well lead to an easy plane for the molecule.

Let us consider again the "T"-like complex but now the local anisotropy axes of the M′ ions are perpendicular to the plane formed by the four MM'_3 metal ions. This can be the case if M′ are Mn^{III} ions with their Jahn–Teller axes perpendicular to the M – M′ bonds. In such a case, the anisotropy axes of the three peripheral M′ ions are parallel and clearly the overall anisotropy axis keeps the same direction. Thus, the sign of D_{total} will be the same as that of D_{local}. This result is true, of course, in the case of a planar complex for any value of the M′ – M – M′ angle.

When the three peripheral M′ metal ions have the same spin orientation i.e. ferromagnetic exchange coupling, the d_n (d_1, d_2, and d_3 for the particular case we considered) coefficients are all equal. However, these values depend on the spin state considered. In the case of a ferromagnetic interaction between the central and the peripheral ions (case A, Scheme 10), the ground spin state will be equal to 13/2 and d_1 (= d_2 = d_3) is found equal to 0.076923.

In the case of an antiferromagnetic coupling where the ground spin state is $S = 9/2$ (case B, Scheme 11), d_1 is equal to 0.104895. Numerical calculations

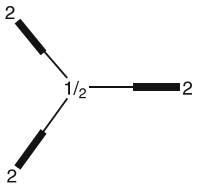

Scheme 9

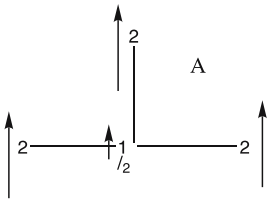

Scheme 10

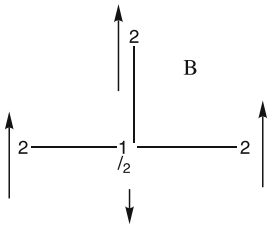

Scheme 11

for the case where all the local anisotropy axes of the M′ ions are perpendicular to the plane of the molecule for a spin ground state $S = 13/2$, $D = -4\ \mathrm{cm}^{-1}$, and $E = 0$ (case A) lead to $D_{13/2} = -0.93\ \mathrm{cm}^{-1}$, and in the case of $S = 11/2$ (case B) to $D_{11/2} = -1.27\ \mathrm{cm}^{-1}$.

So, the antiferromagnetic interaction leads to a larger magnetic anisotropy. However, the activation barrier (given by $|D_S|S^2$) is found equal to 39 and $38.4\ \mathrm{cm}^{-1}$ for the spin states 13/2 and 11/2, respectively. The gain in anisotropy in the case of the antiferromagnetic coupling is lost by the weaker spin value of the ground state.

In order to complete this discussion, we computed the value of the anisotropy parameters for an intermediate spin ground state $S = 3/2$ arising from an antiferromagnetic coupling between the central $S = 1/2$ and the two peripheral ions that are at opposite sides and a ferromagnetic interaction with the third M′ ion (case C, Scheme 12).

In such a case, we have $d_1 = d_2 = 0.7857$ and $d_3 = 0.4$. The value of $D_{3/2}$ was found to be equal to $-7.88\ \mathrm{cm}^{-1}$ with $E = 0$ assuming the same conditions as

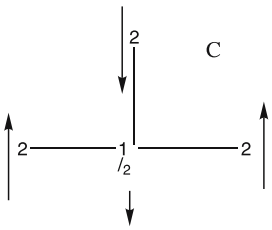

Scheme 12

for the other spin states. Everything being equal, the D_S value depends highly on the interaction scheme and for intermediate spin states this value can be very large. However, the increase in the value of the anisotropy parameter does not compensate at all the decrease of the S value since, despite the large D value, the anisotropy barrier is reduced to 17 cm^{-1}.

The qualitative results found concerning the orientation and the degree of rhombicity of the total $\boldsymbol{D}$ tensor in different cases can be considered as general and can be easily understood. Parallel local anisotropy axes for the single ions keep the same axial anisotropy for the total tensor. Non-parallel local anisotropy axes lead to a rhombic total tensor if the M′ – M – M′ angles are different. Only in the case where the angles are equal (120°) is the axiality retained for the molecule but the sign of the D parameter is changed. This is not surprising because, for equal angles, the molecule possesses a three-fold symmetry axis that imposes the axiality of the global $\boldsymbol{D}$ tensor. The calculations for particular cases show that a decrease of the spin ground state increases the value of the D parameter but reduces the anisotropy barrier. It is thus difficult to draw general conclusions on the relation between the nature of the ground state and the height of the anisotropy barrier; each particular case must be considered.

6 Concluding Remarks

In this review, we mainly focused on the cyanide-based complexes that behave as SMMs; however, during the last 10 years many compounds based on bridging cyanides have been reported using the same synthetic stepwise approach [44–57]. The stepwise approach allows us to prepare molecules where the spin ground state can be relatively easily predicted. Even when the architecture of the polynuclear complex is not expected, the determination of the nature of the ground state is straightforward, since the nature of the cyanide bridge does not lead to competition between different exchange interactions as for metal–oxo complexes where triangular units are usually present. Furthermore, it is possible to calculate the orientation of the $\boldsymbol{D}$ tensor for the spin ground state, providing a good knowledge of the local tensors. This is where probably the stepwise approach is rewarding, because one can carry out a detailed study by different spectroscopic techniques to determine precisely the nature of the magnetic anisotropy on the precursors used to build up the final polynuclear complexes.

One of the important issues in the domain of SMMs is the temperature of the blocking of the magnetization. To date, the Mn12 derivatives hold the record with a relaxation time of the order of a few months at $T = 2$ K. One of the challenges is to be able to increase the temperature of the blocking of the magnetization in order to access slow relaxation times at higher

temperatures. Considering the results of the last 10 years, a blocking of the magnetization at a temperature of 10 K is a real challenge. To reach such a blocking temperature, a molecule with an easy magnetization axis and an anisotropy barrier larger than 200 K is needed. The calculations of the *D* values for the spin ground state of a polynuclear complex (see Sect. 5) show clearly that for high-spin states the total anisotropy is dramatically reduced. This leads to the conclusion that in order to obtain a reasonably large activation barrier so that a molecule would store information at a temperature around 10 K, one must build up molecules with very large spin ground states (100 of higher) and at the same time use metal ions with very large single-ion anisotropy. This is probably not out of reach of chemists. However, a molecule with a slow relaxation of the magnetization at room temperature is, for the time being, just a dream.

Acknowledgements We thank the CNRS (Centre National de la Recherche Scientifique) and the European community for financial support (Contract No. MRTN-CT-2003-504880/RTN Network "QuEMolNa" and NoE "MAGMANET"). The authors are grateful to Roberta Sessoli for providing the necessary numerical information for the computation of the *D* tensors.

References

1. Lis T (1980) Acta Crystallogr B 36:2042
2. Caneschi A, Gatteschi D, Sessoli R, Barra AL, Brunel LC, Guillot M (1991) J Am Chem Soc 113:5873
3. Sessoli R, Gatteschi D, Caneschi A, Novak MA (1993) Nature 365:141
4. Sessoli R, Hui-Lien Tsai AR, Schake AR, Sheyi Wang JB, Vincent JB, Folting K, Gatteschi D, Christou G, Hendrickson DN (1993) J Am Chem Soc 115:1804
5. Barra AL, Gatteschi D, Sessoli R (2000) Chem Eur J 6:1608
6. (a) Blake AJ, Grant CM, Parsons S, Rawson JM (1994) J Chem Soc Chem Commun 2363; (b) Cadiou C, Murrie M, Paulsen C, Villar V, Wernsdorfer W, Winpenny REP (2001) Chem Commun 2666
7. Brechin EK, Boskovic C, Wernsdorfer W, Yoo J, Yamagushi A, Sañudo EC, Concolino TR, Rheingold AL, Ishimoto H, Hendrickson DN, Christou G (2002) J Am Chem Soc 33:9711
8. Oshio H, Hoshino N, Ito T (2000) J Am Chem Soc 122:12 602
9. Winpenny REP (2002) J Chem Soc Dalton Trans 1
10. Murugesu M, Habrych M, Wernsdorfer W, Abboud KA, Christou G (2004) J Am Chem Soc 126:4766
11. Maheswaran S, Chastanet G, Teat SJ, Mallah T, Sessoli R, Wernsdorfer W, Winpenny REP (2005) Angew Chem Int Ed 44:5044
12. Tasiopoulos AJ, Vinslava A, Wernsdorfer W, Abboud KA, Christou G (2004) Angew Chem Int Ed 116:2169
13. Soler M, Rumberger E, Folting K, Hendrickson DN, Christou G (2001) Polyhedron 20:1365
14. Low DM, Jones LF, Bell A, Brechin EK, Mallah T, Riviére E, Teat SJ, McInnes EJL (2003) Angew Chem Int Ed 42:3781

15. Yu P, Journaux Y, Kahn O (1989) Inorg Chem 28:100
16. Weihe H, Güdel HU (2000) Comments Inorg Chem 22:75
17. Scuiller A, Mallah T, Verdaguer M, Nivorozkhin A, Tholence JL, Veillet P (1996) New J Chem 20:1
18. Parker RJ, Spiccia L, Berry KJ, Fallon GD, Moubaraki B, Murray KS (2001) Chem Commun 333
19. Mallah T, Ferlay S, Auberger C, Hélary C, L'hermite F, Ouahès R, Vaissermann J, Verdaguer M, Veillet P (1995) Mol Cryst Liq Cryst 273:141
20. Colacio E, Dominguez-Vera JM, Ghazi M, Kivekäs R, Klinga M, Moreno JM (1998) Chem Commun 1071
21. Marvilliers A, Mallah T, Rivière E, Parsons S, Munoz C, Vostrikova KE (1999) Mol Cryst Liq Cryst 335:483
22. Lescouëzec R, Vaissermann J, Lloret F, Julve M, Verdaguer M (2002) Inorg Chem 41:5943
23. Toma L, Toma LM, Lescouëzec R, Armentano D, De Munno G, Andruh M, Cano J, Lloret F, Julve M (2005) J Chem Soc Dalton Trans 1357
24. Mallah T, Auberger C, Verdaguer M, Veillet P (1995) Chem Commun 61
25. Mallah T, Marvilliers A, Miller JS, Drillon M (2001) Magnetism: Molecules to Materials II. Wiley, Weinheim
26. Marvaud V, Decroix C, Scuiller A, Guyard-Duhayon C, Vaissermann J, Gonnet F, Verdaguer M (2003) Chem Eur J 9:1678
27. Choi HJ, Sokol JJ, Long JR (2004) J Phys Chem Solids 65:839
28. Shen X, Li B, Zou J, Hu H, Xu Z (2003) J Mol Struct 657:325
29. Van Landenberg K, Batten SR, Berry KJ, Hockless DCR, Moubaraki B, Murray KS (1997) Inorg Chem 36:5006
30. Berlinguette CP, Vaughn D, Cañada-Vilalta C, Galán-Mascarós JR, Dunbar KR (2003) Angew Chem Int Ed 42:1523
31. Miyasaka H, Takahashi H, Madanbashi T, Suguira K, Clérac R, Nojiri H (2005) Inorg Chem 44:5969
32. Miyasaka H, Matsumoto N, Re N, Gallo E, Floriani C (1997) Inorg Chem 36:670
33. Choi HJ, Sokol JJ, Long JR (2004) Inorg Chem 43:1606
34. Ferbnteanu M, Miyasaka H, Wernsdorfer W, Suguira K, Yamashita M, Coulon C, Clérac R (2005) J Am Chem Soc 127:3090
35. Heinrich JL, Berseth PA, Long JR (1998) Chem Commun 1231
36. Berseth PA, Sokol JJ, Shores MP, Heinrich JL, Long JR (2000) J Am Chem Soc 122:9655
37. Wang S, Zuo JL, Zhou HC, Choi HJ, Ke Y, Long JR, You XZ (2004) Angew Chem Int Ed 43:5940
38. Schelter EJ, Prosvirin AV, Dunbar KR (2004) J Am Chem Soc 126:15 004
39. Oshio H, Tamada O, Onodera H, Ito T, Ikoma T, Tero-Kubota S (1999) Inorg Chem 38:5686
40. Li D, Parkin S, Wang G, Yee GT, Prosvirin AV, Holmes SM (2005) Inorg Chem 44:4903
41. Sokol JJ, Hee AG, Long J (2002) J Am Chem Soc 124:7656
42. The d_n coefficients were calculated by R. Sessoli using the home-made software Genio based on the irreducible tensor operators (ITO) formalism as reported by Gatteschi and Bencini [Gatteschi D, Bencini A (1990) *EPR of Exchange Coupled Systems* (Springer, Berlin Heidelberg New York)]
43. The calculation of the total $\boldsymbol{D}$ tensor was performed by expressing the local tensors of each single ion in a common basis using adequate rotation matrices. Then the tensorial relation was applied and the resulting matrix diagonalized in order to obtain the D and E values and the orientation of the molecular tensor

44. Parker RJ, Hockless DCR, Moubaraki B, Murray KS, Spiccia L (1996) Chem Commun 2789
45. Marvilliers A, Pei Y, Cano Boquera J, Vostrikova KE, Paulsen C, Rivière E, Audière J-P, Mallah T (1999) Chem Commun 1951
46. Vostrikova KE, Luneau D, Wernsdorfer W, Rey P, Verdaguer M (2000) J Am Chem Soc 122:718
47. Sokol JJ, Shores MP, Long JR (2001) Angew Chem Int Ed 40:236
48. Oshio H, Yamamoto M, Hoshino N, Ito T (2001) Polyhedron 20:1621
49. Oshio H, Yamamoto M, Ito T (2002) Inorg Chem 41:5817
50. Berlinguette CP, Galán-Mascarós JR, Dunbar KR (2003) Inorg Chem 42:3416
51. Berlinguette CP, Dunbar KR (2005) Chem Commun 2451
52. Kou HZ, Zhou BC, Si SF, Wang RJ (2004) Eur J Inorg Chem 401
53. Berlinguette CP, Dunbar KR (2005) Chem Commun 2451
54. Zhong ZJ, Seino H, Mizobe Y, Hidai M, Fujishima A, Ohkoshi S, Hashimoto K (2000) J Am Chem Soc 122:2952
55. Larionova J, Gross M, Pilkington M, Andres H, Stoeckli-Evans H, Güdel HU, Descurtins S (2000) Angew Chem Int Ed 39:1605
56. Rombaud G, Verelst M, Golhen S, Ouahab L, Mathonière C, Kahn O (2001) Inorg Chem 40:1151
57. Herrera JM, Marvaud V, Verdaguer M, Marrot J, Kalisz M, Mathonière C (2003) Angew Chem Int Ed 43:5468

Struct Bond (2006) ■: 133–161
DOI 10.1007/430_029

Published online: 24 March 2006

Preparation of Novel Materials Using SMMs

Andrea Cornia[1] (✉) · Antonio Fabretti Costantino[1] · Laura Zobbi[1] · Andrea Caneschi[2] · Dante Gatteschi[2] · Matteo Mannini[2] · Roberta Sessoli[2]

[1]INSTM & Department of Chemistry, University of Modena and Reggio Emilia, via G. Campi 183, 41100 Modena, Italy
acornia@unimore.it, fabretti@unimore.it, lzobbi@unimore.it

[2]INSTM & Department of Chemistry, University of Florence, via della Lastruccia 3, 50019 Sesto Fiorentino (FI), Italy
andrea.caneschi@unifi.it, dante.gatteschi@unifi.it, matteo.mannini@unifi.it, roberta.sessoli@unifi.it

Abstract Magnetic hysteresis is considered a distinctive feature of bulk magnetic materials, where it arises from long-range ordering and irreversible motion of domain walls. However, many anisotropic high-spin molecules, referred to as Single-Molecule Magnets (SMMs), display a hysteresis loop at low temperature and have the potential of being used as molecular-scale units for information storage. This work reviews recent advances in the realization of new bulk materials and low-dimensional nanostructures based on SMMs. Particular reference will be made to mixed-valence Mn_{12} complexes, which comprise the most versatile and best-performing SMMs available to date. Nonetheless, the described criteria for structure tailoring as well as the guiding principles in material design are of general value and applicability. Examples are given of multifunctional materials of either inorganic or hybrid nature which combine in a unique fashion the magnetic properties of embedded SMMs with the conductive, optical and mechanical characteristics of a polymeric host. In the framework of the molecular approach to electronics,

successful attempts to organize SMMs into bidimensional arrays on surfaces and to address them individually have been reported. Recent results in this area will be treated exemplarily, with emphasis on molecular design and surface functionalization. The construction of molecular-scale electronic devices embodying SMMs as active components is finally highlighted among the future developments of this lively research area, which straddles the interface between chemistry and physics.

Keywords Molecular magnetism · Molecular electronics · Manganese · Surface science

Abbreviations

AC	alternating current
AFM	atomic force microscopy
ATR-FT/IR	attenuated transmission reflection Fourier transform infrared spectroscopy
DC	direct current
DVD	digital video disk
FET	field effect transistor
H_2adc	anthracene-1,8-dicarboxylic acid (and its derivatives)
Hbet	betaine
Hdph	diphenylphosphinic acid
Hdpp	diphenylphosphate
HF-EPR	high frequency electron paramagnetic resonance
HL	16-(acetylthio)hexadecanoic acid
HL′	16-mercaptohexadecanoic acid
Hmtb	4-(methylthio)benzoic acid
Hmet	methacrylic acid
Htc	3-thiophenecarboxylic acid
HZ	(4-carboxybenzyl)tributylammonium
hTPD	*N*,*N*′-diphenyl-*N*,*N*′-bis(4-hexylphenyl)-[1,1′-biphenyl]-4,4′-diamine
JT	Jahn–Teller
LB	Langmuir–Blodgett
MAPLE	matrix assisted pulsed laser evaporation
MES	sodium 2-mercaptoethanesulfonate
μCP	micro-contact printing
MFM	magnetic force microscopy
ML	monolayer
MMA	methyl methacrylate
mpyNIT	*m*-*N*-methylpyridinium nitronylnitroxide
PC	polycarbonate
PDMS	poly(dimethylsiloxane)
PLD	pulsed laser deposition
PMMA	poly(methyl methacrylate)
PS	polystyrene
pTPD	poly(*N*,*N*′-diphenyl-*N*,*N*′-bis(4-hexylphenyl)-[1,1′-biphenyl]-4,4′-diamine)
QCM	quartz crystal microbalance
QT	quantum tunneling
SAM	self-assembled monolayer
SMM	single-molecule magnet
SQUID	superconducting quantum interference device
STM	scanning tunneling microscopy

TEM	transmission electron microscopy
ToF-SIMS	time of flight secondary ion mass spectrometry
UHV	ultra high vacuum
XPS	X-ray photoelectron spectroscopy
XRD	X-ray diffraction

1
The Chemistry and Physics of Single-Molecule Magnets (SMMs)

1.1
Introductory Remarks

The investigation of molecular materials has clearly demonstrated that properties traditionally associated with inorganic materials, such as conductivity, superconductivity and non-linear optical behavior, can be observed even in discrete molecular entities or in crystal lattices assembled from molecular building blocks. Magnetic materials [1–3] make no exception to this trend and RT molecular magnets have been available since the early nineties of the last century [4, 5]. Also during this time it was discovered that molecular nanosize assemblies of paramagnetic metal ions may show magnetic hysteresis below a certain temperature (T_B), from which the acronym single-molecule magnets (SMMs) was coined [6, 7]. Unlike in traditional ferro- or ferrimagnetic materials, however, the hysteresis loop of SMMs does not originate from long-range ordering of magnetic moments and irreversible motion of domain walls, since each molecule effectively acts as a monodomain particle. Rather, it is the outcome of an exceedingly slow paramagnetic relaxation observed when intramolecular magnetic interactions produce a high spin ground state and a large Ising-type anisotropy. For both conditions to be fulfilled, not only the constituent ions have to be chosen correctly, but also molecular architecture must be properly designed. In this respect, synthetic chemistry has massively contributed to the development of *molecular nanomagnetism*, which has rapidly matured into a unique discipline at the interface between chemistry and solid-state physics.

The main advantages of a molecular approach to nanomagnetism [8, 9] lie in the high reproducibility and monodispersity of the molecular building blocks, naturally identical to each other and with well-defined sizes and electronic levels. Furthermore, molecular magnetic properties can be finely tuned at the synthetic level and combined with mechanical, electrical and/or optical properties to give multifunctional systems [10]. As a result, molecular nanomagnetism is now further expanding toward neighboring areas, including material science [11], molecular electronics [12] and information technology [13].

Herein we review recent progress in the rational moulding of SMMs into new materials and devices. Many different structural types have been shown to lead to SMM behavior, and the interested reader is addressed to dedicated reviews [14–17] and the remainder of this volume. Our choice has been to focus on the family of Mn_{12} complexes, which exhibit the highest T_B and the greatest chemical versatility among known SMMs. Their synthesis, structure, reactivity and physical behavior are briefly outlined in Sects. 1.2 and 1.3. Section 2 is devoted to the preparation of new bulk materials containing SMMs, whereas Sect. 3 focusses on the organization of SMMs into bidimensional nanostructures. A perspective view of the future developments in the field is eventually provided in Sect. 4.

1.2
Synthesis, Structure and Reactivity of Mn_{12}-type SMMs

The chemical methods applicable to the synthesis of SMMs rely on concepts pertaining to the wider realm of supramolecular chemistry, such as molecular recognition, host-guest interactions and self-assembly [18]. As will be illustrated in Sect. 1.3, however, the structural and electronic requirements for SMM behavior are so demanding that truly general synthetic routes to SMMs have not yet been developed. Instead, the vast majority of SMMs known to date have been obtained using serendipitous/combinatorial methods not dissimilar from those widely used in pharmaceutical drug discovery [19, 20]. By contrast, the reactivity of *preformed* cluster cores has been widely exploited to design new molecular compounds endowed with additional properties and functionalities, as discussed in the next sections.

The prototypal SMM was synthesized and structurally characterized by XRD in 1980 [21], though its unusual magnetic properties were uncovered only about a decade later [6, 7]. It is a crystalline, molecular compound with formula $[Mn_{12}O_{12}(OAc)_{16}(H_2O)_4] \cdot 4H_2O \cdot 2AcOH$ (Mn_{12}-*acetate*) and can be isolated in high yield ($\sim$ 80%) by reaction of manganese(II) acetate tetrahydrate with potassium permanganate in a 60% v/v AcOH-water mixture (the possible occurrence of dodecanuclear manganese acetate complexes had been anticipated by Weinland and Fischer as early as in 1921, see [22]). Each Mn_{12} cluster contains eight manganese(III) and four manganese(IV) ions, which are produced by comproportionation of the reactants [15, 16], as described by the Eq. 1:

$$44Mn(OAc)_2 + 16MnO_4^- + 16H_2O + 8H^+ \longrightarrow 5[Mn_{12}O_{12}(OAc)_{16}(H_2O)_4] + 8AcO^- . \quad (1)$$

The disk-like Mn_{12} molecule, whose structure is schematically depicted in Fig. 1, has crystallographic S_4 symmetry. The four manganese(IV) ions are found in a central cubane unit, which is surrounded by a ring of eight

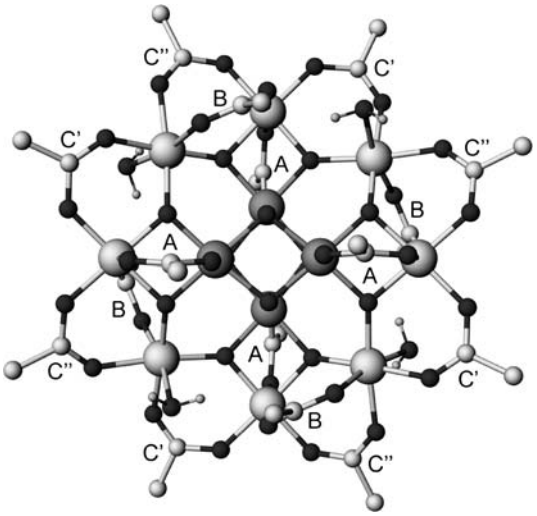

Fig. 1 Structure of the $[Mn_{12}O_{12}(OAc)_{16}(H_2O)_4]$ cluster in Mn_{12}-*acetate* viewed along the S_4 axis, with the labelling scheme for acetate ligands. Atom code (size/color): Mn^{III} = *large/light-gray*; Mn^{IV} = *large/gray*; O = *medium/black*; C = *medium/light-gray*; H = *small/gray*. Methyl hydrogen atoms omitted for clarity

manganese(III) ions. The resulting $[Mn_{12}O_{12}(OAc)_{16}(H_2O)_4]$ core is held together by 12 μ_3-O^{2-} ions and 16 μ-acetates, while the four water molecules provide terminal ligation to every second manganese(III) ion. The acetate bridges are partitioned into three chemically distinct sets, labelled with A, B and C in Fig. 1. A-type and B-type acetates provide axial ligation to Mn^{IV}–Mn^{III} and Mn^{III}–Mn^{III} pairs, respectively, whereas C-type acetates bridge Mn^{III}–Mn^{III} pairs equatorially. Notice that C-type acetates comprise two crystallographically independent subsets, labelled with C′ and C″ in Fig. 1. All the constituent ions reside in distorted octahedral environments, the eight manganese(III) centers displaying pronounced JT distortion by tetragonal elongation. The elongated Mn – O bonds involve exclusively axial acetate (A,B) and water ligands, so that the JT axes are essentially collinear with the unique S_4 molecular axis. Such peculiar arrangement of the JT axes has important consequences on the magnetic properties, as discussed in Sect. 1.3. The crystal lattice of Mn_{12}-*acetate* also comprises non-coordinated water and acetic acid molecules, which are hydrogen bonded to the dodecamanganese unit. The acetic acid molecules, in particular, are disordered over two equally-populated positions and determine a local symmetry lowering [23, 24], as recently confirmed by detailed spectroscopic investigations [25].

Mn_{12}-*acetate* is soluble and perfectly stable in organic solvents such as acetonitrile and DMF.

The ^{1}H-NMR spectrum in acetonitrile, for instance, shows three resonances at 48.2, 41.8 and 13.9 ppm (vs. tetramethylsilane) with integrated in-

tensities in a 1 : 2 : 1 ratio. The signals arise from the CH_3 groups of B-, C- and A-type acetates, respectively, and demonstrate that the solid-state structure is preserved in solution [26]. However, Mn_{12}-*acetate* easily undergoes ligand exchange reactions when treated with suitable carboxylate or non-carboxylate ligands, such as those gathered in Fig. 2. In fact, the total replacement of AcO^- groups (Eq. 2) has been widely exploited to access new homocarboxylate derivatives, like $[Mn_{12}O_{12}(O_2CPh)_{16}(H_2O)_4]$ (Mn_{12}-*benzoate*) [27], the second member of the Mn_{12} family to be reported after Mn_{12}-*acetate*:

$$[Mn_{12}O_{12}(OAc)_{16}(H_2O)_4] + 16RCO_2H \rightleftharpoons [Mn_{12}O_{12}(O_2CR)_{16}(H_2O)_4] + 16AcOH\,. \quad (2)$$

In order to drive the equilibrium to the right, it is advisable to use a large excess of incoming ligand and to remove the produced acetic acid

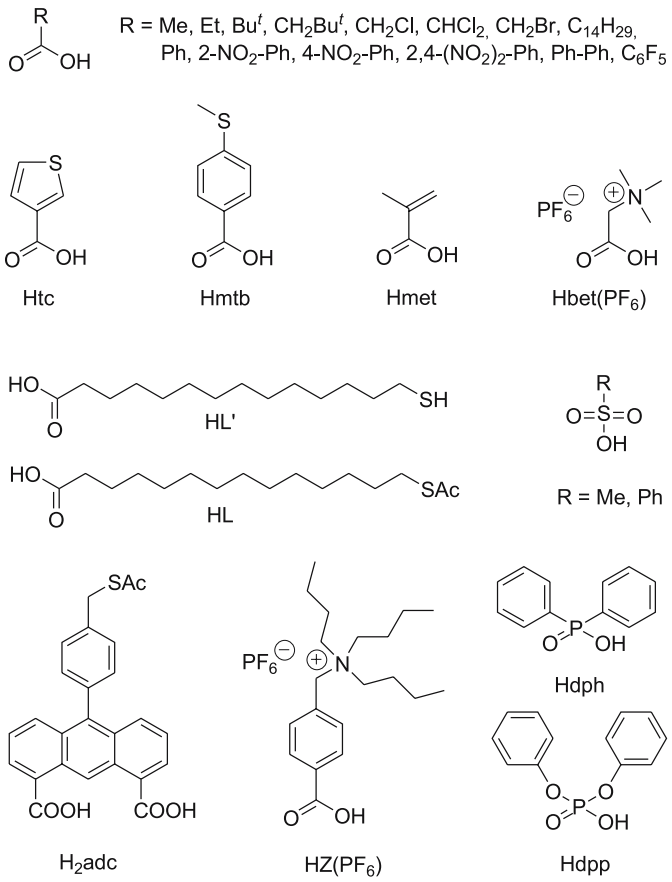

Fig. 2 A selection of ligands used in Mn_{12} chemistry

by azeotropic distillation with toluene[1]. It is important to notice here that, although the basic structure of the $Mn_{12}O_{12}$ core is preserved upon ligand replacement, the arrangement of axial water and carboxylate ligands may differ from that observed in Mn_{12}-*acetate*. For instance, whereas for R = Me one water ligand is present every second manganese(III) ion, in Mn_{12}-*benzoate* two *trans* H_2O ligands are found every fourth manganese(III) center [27]. For R = Et, the cluster features three water ligands and one five-coordinated manganese(III) ion [26]. Derivatives with no coordinated water are also known [28].

As compared with homocarboxylates, the preparation of mixed-ligand complexes is considerably more challenging. In favorable cases, they are accessible by direct comproportionation of manganese(II) and permanganate salts. For instance, the complex $[Mn_{12}O_{12}(OAc)_4(O_2CEt)_{12}(H_2O)_4]$ was conveniently prepared by reaction between $Mn(OAc)_2 \cdot 4H_2O$ and $KMnO_4$ in a mixture of propionic acid and water [29]. Heterocarboxylate species have also been synthesized by ligand redistribution as in Eq. 3 (R = Et or CH_2Bu^t and R′ = $CHCl_2$) [30]:

$$[Mn_{12}O_{12}(O_2CR)_{16}(H_2O)_4] + [Mn_{12}O_{12}(O_2CR')_{16}(H_2O)_4] \rightleftharpoons 2[Mn_{12}O_{12}(O_2CR)_8(O_2CR')_8(H_2O)_4] \quad (3)$$

However, the simplest route to mixed-ligand Mn_{12} complexes involves treatment of a homocarboxylate with a stoichiometric amount of the proper incoming ligand. This strategy proved to be successful for the introduction, among others, of nitrates, sulfonates, phosphates and phosphinates, as shown exemplarily in Eq. 4:

$$[Mn_{12}O_{12}(O_2CCH_2Bu^t)_{16}(H_2O)_4] + 4HNO_3 \rightleftharpoons [Mn_{12}O_{12}(O_2CCH_2Bu^t)_{12}(NO_3)_4(H_2O)_4] + 4Bu^tCH_2CO_2H \quad (4)$$

Interestingly, the exchange reaction is usually site selective, i.e. the different ligands are located at specific sites rather than being disordered. Table 1 lists the distribution of the ligands amongst A, B and C coordination sites for a selection of Mn_{12} derivatives. For each ligand, the pK_a of the conjugated acid is also reported in parentheses. The weaker bases (lower pK_a for the conjugated acid) are most often found in B-type axial sites, i.e. those bridging a pair of Mn^{III} ions, whereas stronger bases usually occupy A-type axial or C-type equatorial positions. The observed trend is ascribed to the strength of the ligand-to-metal interaction, which is minimal for B-sites due to the larger Mn – O distances along the Mn^{III} JT elongation axes [30, 34]. However, Table 1 also reveals exceptions to this rule. For instance, in $[Mn_{12}O_{12}(dph)_8(O_2CMe)_8(H_2O)_4]$ and $[Mn_{12}O_{12}(dph)_9(O_2CPh)_7(H_2O)_4]$ the weaker diphenylphosphinate base is distributed among axial (B) and

[1] Toluene and acetic acid form a negative azeotrope which contains 28 wt % of the acid and boils at 100.6 °C at 1 atm vs. 110.7 and 118.1 °C for pure toluene and acetic acid, respectively.

Table 1 Distribution of the ligands among A, B, and C coordination sites in mixed-ligand Mn_{12} complexes

Formula [a]	A-sites	B-sites	C-sites	Refs.
$[Mn_{12}O_{12}(O_3SPh)_8(O_2CMe)_8(H_2O)_4]$	$PhSO_3$ (∼ – 2.5)	$PhSO_3$ (∼ – 2.5)	$MeCO_2$ (4.76)	[31, 32]
$[Mn_{12}O_{12}(O_3SMe)_4(O_2CMe)_{12}(H_2O)_3]$	$MeCO_2$ (4.76)	$MeSO_3$ (∼ – 2)	$MeCO_2$ (4.76)	[33]
$[Mn_{12}O_{12}(NO_3)_4(O_2CCH_2Bu^t)_{12}(H_2O)_4]$	$Bu^tCH_2CO_2$ (5.24)	NO_3 (∼ – 1.4)	$Bu^tCH_2CO_2$ (5.24)	[34]
$[Mn_{12}O_{12}(dpp)_4(O_2CMe)_{12}]$	$MeCO_2$ (4.76)	dpp (∼ 1.1)	$MeCO_2$ (4.76)	[28]
$[Mn_{12}O_{12}(dpp)_4(O_2CPh)_{12}(H_2O)_4]$	$PhCO_2$ (4.20)	dpp (∼ 1.1)	$PhCO_2$ (4.20)	[35]
$[Mn_{12}O_{12}(O_2CCHCl_2)_8(O_2CCH_2Bu^t)_8(H_2O)_3]$	$CHCl_2CO_2$ (1.48)	$CHCl_2CO_2$ (1.48)	$Bu^tCH_2CO_2$ (5.24)	[30]
$[Mn_{12}O_{12}(O_2CCHCl_2)_8(O_2CEt)_8(H_2O)_3]$	$CHCl_2CO_2$ (1.48)	$CHCl_2CO_2$ (1.48)	$EtCO_2$ (4.86)	[30]
$[Mn_{12}O_{12}(dph)_8(O_2CMe)_8(H_2O)_4]$	$MeCO_2$ (4.76)	dph (∼ 2.3)	4dph + $4MeCO_2$	[36]
$[Mn_{12}O_{12}(dph)_9(O_2CPh)_7(H_2O)_4]$	$PhCO_2$ (4.20)	dph (∼ 2.3)	5dph + $3PhCO_2$	[37]
$[Mn_{12}O_{12}(O_2CMe)_4(O_2CEt)_{12}(H_2O)_4]$	$MeCO_2$ (4.76)	$EtCO_2$ (4.86)	$EtCO_2$ (4.86)	[29]

[a] Crystallization solvent omitted.

equatorial (C) sites. Beside ligand basicity, other factors like steric hindrance and crystal packing must therefore play a role. It is important to notice here that ligand redistribution between the available coordination sites has been clearly detected in solutions of heterocarboxylate derivatives by NMR spectroscopy [30].

To overcome these difficulties, an alternative strategy for site-selective ligand replacement has been recently proposed. It is based on conformationally rigid dicarboxylate ligands derived from anthracene-1,8-dicarboxylic acid (H_2adc), which are capable of exclusive axial coordination because of geometric reasons. The ligands act in a bis-bidentate fashion and occupy A + B sites only. As an additional advantage, the anthracene moiety can be readily functionalized in the 10-position. Figure 3 illustrates the structure of the complex $[Mn_{12}O_{12}(O_2CPh)_8(adc)_4(H_2O)_4]$, which contains eight benzoates in equatorial sites and four adc-derived ligands in axial sites [38].

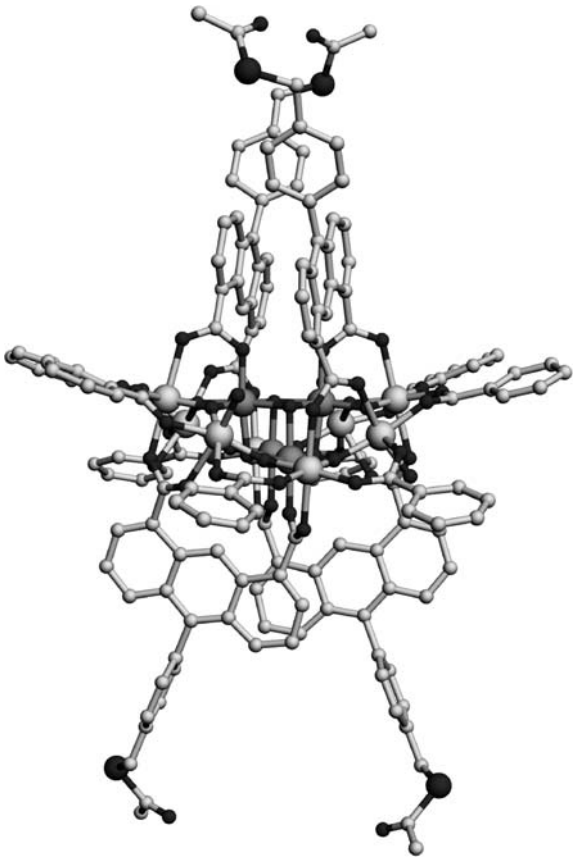

Fig. 3 Structure of $[Mn_{12}O_{12}(O_2CPh)_8(adc)_4(H_2O)_4]$ [38]. Atom code as in Fig. 1 *plus*: S = *large/black*. Hydrogen atoms omitted for clarity

Table 2 First- and second-reduction potentials for $[Mn_{12}O_{12}(O_2CR)_{16}(H_2O)_4]$ complexes (adapted from [41]) [a]

R	E_1 (V)	E_2 (V)
C_6H_5 [b]	+ 0.12	– 0.23
Me	+ 0.18	– 0.06
2-NO_2 – Ph	+ 0.47	+ 0.19
4-NO_2 – Ph [b]	+ 0.49	+ 0.23
CH_2Cl	+ 0.60	+ 0.30
C_6F_5	+ 0.64	+ 0.46
2,4-$(NO_2)_2$ – Ph	+ 0.74	+ 0.45
$CHCl_2$	+ 0.91	+ 0.61

[a] Determined by Differential Pulse Voltammetry in acetonitrile unless otherwise indicated, vs. ferrocene
[b] In CH_2Cl_2

Another important aspect of the reactivity of Mn_{12} complexes emerges clearly from their cyclic voltammograms in organic solution. Most $[Mn_{12}O_{12}(O_2CR)_{16}(H_2O)_4]$ derivatives show multiple redox waves, the 1st oxidation and the 1st reduction being usually reversible. The first-reduction potential generally lies in the range 0.0–1.0 V vs. Fc^+/Fc and the actual value depends predictably on the electron-withdrawing capability of the carboxylate ligands (Table 2). Many one- and two-electron reduced species have indeed been isolated in crystalline form by reacting preformed Mn_{12} complexes with mild reducing agents, such as iodides [26, 39–43] or metallocenes [40, 44], as exemplarily reported in Eqs. 5–7 (M = Fe, Co).

$$[Mn_{12}O_{12}(O_2CEt)_{16}(H_2O)_3] + H_2O + PPh_4I \longrightarrow (PPh_4)[Mn_{12}O_{12}(O_2CEt)_{16}(H_2O)_4] + 1/2I_2 \quad (5)$$

$$[Mn_{12}O_{12}(O_2CCHCl_2)_{16}(H_2O)_4] + 2PPh_4I \longrightarrow (PPh_4)_2[Mn_{12}O_{12}(O_2CCHCl_2)_{16}(H_2O)_4] + I_2 \quad (6)$$

$$[Mn_{12}O_{12}(O_2CC_6F_5)_{16}(H_2O)_4] + M(C_5Me_5)_2 \longrightarrow [M(C_5Me_5)_2][Mn_{12}O_{12}(O_2CC_6F_5)_{16}(H_2O)_4]\,. \quad (7)$$

In the reduced variants, the extra electron usually resides on former manganese(III) ions, affording trapped-valence $Mn^{II}Mn^{III}_7Mn^{IV}_4$ and $Mn^{II}_2Mn^{III}_6Mn^{IV}_4$ cores. Interestingly, a two-electron reduction occurs concomitantly with ligand replacement when Hbet is used as an incoming ligand, presumably due to the strong electron-withdrawing ability of the trimethylammonium substituents [45].

1.3 The Physics of SMMs in a Nutshell

The distinctive property of SMMs is the occurrence of magnetic hysteresis at low temperature [6, 7, 46, 47]. When the magnetization of a single crystal of Mn_{12}-*acetate* is measured at 2 K by applying the magnetic field along the tetragonal Z axis, the zero-field magnetization depends on the previous history of the sample (Fig. 4). If the sample is first magnetically saturated in a 3 T magnetic field (1) and the field is subsequently reduced to zero, the magnetization is maintained essentially unaltered (2). In order to bring the magnetization back to zero, a magnetic field exceeding 1 T (coercive field) has to be applied in the opposite direction (3). By further increasing the applied field to 3 T, saturation is achieved again (4). Switching off the field the magnetization largely persists (5), but now lies in the opposite direction as compared with (2). Again, demagnetizing the system requires the application of a substantial field (6). The resulting hysteresis loop (1) → (2) → (3) → (4) → (5) → (6) → (1) recalls the magnetic behavior of bulk ferromagnetic materials, but the underlying physics is completely different. In fact, no long-range order is established in the crystal lattice due to the efficient magnetic shielding provided by the organic ligands which surround the cluster core.

Rather, magnetic bistability originates purely from intramolecular magnetic interactions, as firmly established by dilution experiments [48–50]. In essence, SMM behavior arises from the association of a high-spin ground

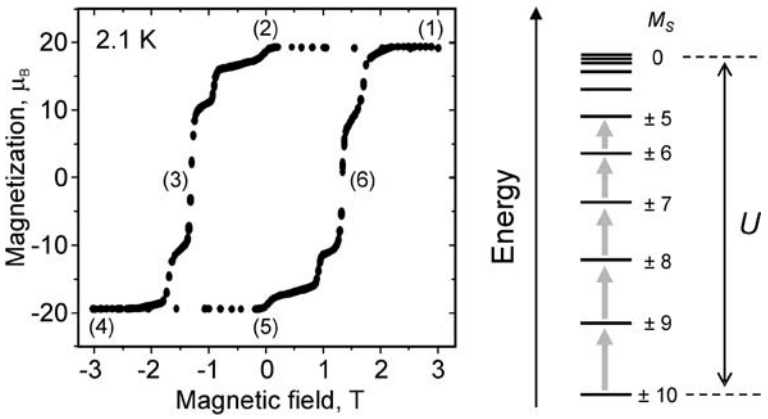

Fig. 4 (*Left*) Hysteresis loop recorded at 2.1 K on a single crystal of Mn_{12}-*acetate*, with the magnetic field directed along the tetragonal axis. (*Right*) Splitting of the $S = 10$ ground spin state in Mn_{12}-*acetate*. The lowest-lying substates are labelled with the M_S quantum number. The *arrows* indicate the successive spin transitions required to overcome the anisotropy barrier U

state with an easy-axis (i.e. Ising-type) magnetic anisotropy. In the vast majority of Mn_{12} complexes, superexchange interactions transmitted by the bridging oxide ligands result in an $S = 10$ ground state, which can be pictorially (but not rigorously) described by arranging the Mn^{III} $S = 2$ spins antiparallel to the Mn^{IV} $S = 3/2$ spins [51]. The second ingredient required for SMM behavior is an easy-axis anisotropy, which in Mn_{12} complexes is brought about by the manganese(III) ions. HF-EPR investigations on simple model complexes [52] have established that the JT elongation axis of manganese(III) corresponds to an easy magnetic direction for the $S = 2$ spin. Since the eight JT axes in Mn_{12}-*acetate* are roughly collinear (see Sect. 1.2), the local anisotropies sum up and determine a huge Ising-type anisotropy in the $S = 10$ ground state of the molecule. The magnetic moment then preferably lies along the tetragonal axis and much less favorably perpendicular to it. In other terms, the energy of the $2S + 1 = 21$ substates pertaining to the $S = 10$ multiplet decreases with increasing $|M_S|$ in a way most simply described by Eq. 8:

$$E(M_S) = DM_S^2 \qquad M_S = -S, -S+1, \ldots, S-1, S, \tag{8}$$

where $D < 0$ is called the axial zero-field splitting parameter. Evidently, the total splitting of the multiplet is $U = |D|S^2$ for integer S and $|D|(S^2 - 1/4)$ for half-integer S (Fig. 4).

Experimentally, at temperatures such that $k_B T \ll U$ the magnetization relaxes with a characteristic time τ which follows the Arrhenius law:

$$\tau = \tau_0 \exp(U_{eff}/k_B T), \tag{9}$$

where $U_{eff} \leq U$ is the *effective* anisotropy barrier. The value of τ can be measured either in DC mode, i.e. by following the time dependence of the magnetization as the field is switched off, or more commonly in AC mode, i.e. by applying a small, oscillating magnetic field with frequency ν. When the condition:

$$\tau = (2\pi\nu)^{-1} \tag{10}$$

is fulfilled, the out-of-phase component of magnetic susceptibility, χ'', is a maximum. Though Eq. 10 can be satisfied by varying ν at constant T, in practice the temperature dependence of χ'' is measured for a set of different frequencies ν. When the results are plotted in the form of $\ln \tau$-vs.-T^{-1}, the slope and intercept of the best straight line through experimental datapoints directly provide U_{eff} and τ_0 (61 K and 2.1×10^{-7} s in Mn_{12}-*acetate* [7]). The activation parameters, and in particular the height of the anisotropy barrier, are distinctive features of Mn_{12} complexes and have been often used to probe their structural integrity in a variety of organic or inorganic matrices (vide infra).

From Eq. 9, it is clear that the relaxation time increases exponentially upon cooling. At sufficiently low temperatures, the relaxation of the magnetization

becomes so slow that hysteresis appears (Fig. 4). More generally, a characteristic temperature T_B exists for each investigation technique, below which the magnetization is blocked on the timescale of the experiment (T_B = 3 K in SQUID measurements).

The temperature dependence of τ in SMMs has been theoretically explained by Villain et al., who described thermally activated magnetization reversal as a step-by-step process driven by spin-phonon interactions [53]. By successive exchange of phonons, the system undergoes the transition from $M_S = -S$ to $-S + 1$, to $M_S = -S + 2$, etc. climbing up the ladder of states and then descending to $M_S = S$ (Fig. 4). Quite simply, the total splitting of the multiplet, U, can be perceived as an energy barrier which must be overcome for spin reversal to occur. For integer S, the pre-exponential factor τ_0 is given by

$$\tau_0^{-1} \approx \frac{1}{\hbar^4 c_s^5 \rho} \left| \langle \pm 1 \left| \widehat{V}_{sp} \right| 0 \rangle \right|^2 \left(E_0 - E_{\pm 1} \right)^3 , \tag{11}$$

where c_s is the speed of sound in the material, whose density is ρ, and V_{sp} is the Hamiltonian describing spin-phonon interaction. Because of the phonon distribution and Eq. 8, the transitions between $M_S = 0$ and $M_S = \pm 1$ states at the top of the anisotropy barrier are the slowest and thus represent the rate-determining step of the whole relaxation process. For this reason, τ_0 depends exclusively on the energy separation between the $M_S = 0$ and $M_S = \pm 1$ states ($E_0 - E_{\pm 1}$) and on the corresponding spin-phonon matrix element.

What makes SMMs unique magnetic systems, however, is the coexistence of classical and quantum mechanisms for spin reversal. In fact, beside the above-described thermally activated process, spin reversal in SMMs may also occur by QT [46, 47, 54]. Whenever two states lying on opposite sides of the barrier have the same energy *and* are quantum-mechanically admixed, a direct underbarrier transition is in principle permitted. QT effects are indeed responsible for the stepped hysteresis loops of Mn_{12}-*acetate* (Fig. 4) and explain why the effective anisotropy barrier probed by relaxation measurements (U_{eff}) is usually lower than U. Clearly, QT effects are of paramount importance for an accurate description of SMM behavior and their origin is among the most actively investigated topics in molecular nanomagnetism [54].

In the previous section we mentioned the possibility to isolate one- and two-electron reduced Mn_{12} complexes. These generally retain SMM behavior, but with different S values and activation parameters. Only two series of truly isostructural compounds have been isolated to date [55, 56], but a clear trend is already evident: the effective energy barrier decreases with the number of added electrons, consistently with a decreasing Mn^{III} content upon reduction. For instance, in the series $(NMe_4)_n[Mn_{12}O_{12}(O_2CC_6F_5)_{16}(H_2O)_4]$, the measured energy barriers are U_{eff} = 59 K, 49 K and 25 K for n = 0, 1 and 2, respectively while the ground spin value is S = 10 for n = 0, 2 and S = 19/2 for n = 1 [55].

2
New Bulk Materials Based on SMMs

The chemical versatility of Mn_{12} complexes and, in particular, their ability to undergo ligand-exchange and redox reactions without molecular disruption, has inspired the design and realization of new, multifunctional systems combining SMM behavior with additional properties (mechanical, optical, electrical, magnetic, etc.). Three main categories of materials have been conceived: salts with functional cations/anions, host-guest compounds with mesoporous silica and hybrid inorganic/organic materials.

2.1
Salts with Functional Cations/Anions

Positively charged Mn_{12} complexes can be most simply prepared by ligand substitution introducing cationic substituents on the incoming carboxylate. The cationic derivatives can be subsequently combined with functional anions to give new, multifunctional materials based on an ionic lattice. Following this strategy, a Mn_{12} derivative with 16 quaternary-ammonium substituents (HZ in Fig. 2) [57] has been used as a countercation in the preparation of hybrid salts with polyoxometalate anions, like $[W_6O_{19}]^{2-}$, $[PW_{12}O_{40}]^{3-}$, $[(H_3O)PW_{11}O_{39}Ni]^{4-}$ and $[(H_3O)PW_{11}O_{39}Co]^{4-}$ by metathesis reactions (see Eqs. 12 and 13) [58]:

$$[Mn_{12}O_{12}(OAc)_{16}(H_2O)_4] + 16HZ(PF_6) \longrightarrow [Mn_{12}O_{12}(Z)_{16}(H_2O)_4](PF_6)_{16} + 16AcOH \quad (12)$$

$$[Mn_{12}O_{12}(Z)_{16}(H_2O)_4](PF_6)_{16} + 4(NBu^n{}_4)_4[(H_3O)PW_{11}O_{39}Ni] \longrightarrow [Mn_{12}O_{12}(Z)_{16}(H_2O)_4][(H_3O)PW_{11}O_{39}Ni]_2 + 16(NBu^n{}_4)(PF_6)\,. \quad (13)$$

Conversely, one- and two-electron reduced Mn_{12} derivatives can be combined with functional cations, such as metallocenium ions [40, 44] and the organic radical mpyNIT ($S = 1/2$) in Fig. 5 [43]. The former have been prepared directly from neutral Mn_{12} complexes and metallocenes according to Eq. 7, while the compound $(mpyNIT)[Mn_{12}O_{12}(O_2CPh)_{16}(H_2O)_4]$ was synthesized by a one-pot reaction between $mpyNIT^+I^-$ and Mn_{12}-*benzoate* (Eq. 14).

$$[Mn_{12}O_{12}(O_2CPh)_{16}(H_2O)_4] + mpyNIT^+I^- \longrightarrow (mpyNIT)[Mn_{12}O_{12}(O_2CPh)_{16}(H_2O)_4] + 1/2I_2\,. \quad (14)$$

In materials containing open-shell polyoxoanions, ferrocenium ions or the organic radical mpyNIT great attention was devoted to the influence of the additional paramagnetic species on the relaxation of the Mn_{12} unit. However, the interpretation of the results is still controversial, due to the possible implication of JT isomerism and other environmental factors [44].

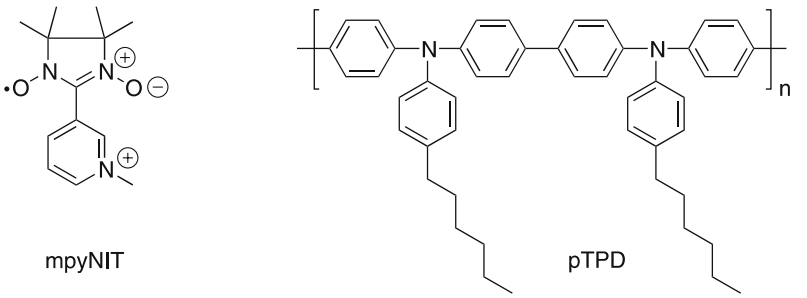

Fig. 5 A stable organic radical and an arylamine polymer used to prepare multifunctional Mn_{12}-containing bulk materials

2.2
Host-Guest Compounds with Mesoporous Silica

The non-covalent immobilization of Mn_{12} complexes (R = Me, Ph) into SBA-15-type mesoporous silica with pore sizes ranging from 25 to 100 Å was investigated by Coradin et al. [59, 60]. As expected, the pore size deeply affects the amount of embedded cluster. Silica with 60-Å pores was found to be the most efficient to incorporate the acetate derivative (36 wt %) as small aggregates which appear to fill the channels in TEM micrographs. Size selectivity of a silica host toward Mn_{12} complexes was reported by Coronado et al., who studied the incorporation of the R = Me, Et, Ph and C_6F_5 derivatives into MCM-41 silica (pore diameter ca. 26 Å) [61, 62]. Only the smaller Me and Et derivatives could be inserted into the mesoporous material, and no immobilization at all was observed after reduction of the pore diameter by trimethylsilylation. However, structural integrity was demonstrated for the R = Et derivative only and under special preparative conditions.

2.3
Hybrid Inorganic/Organic Materials

Hybrid inorganic/organic materials are assembled from molecular building blocks of different composition and combine (in a simply additive or synergic way) the properties of the inorganic and organic constituents into a single material [10, 63, 64]. Organic polymers represent a convenient choice for the design of hybrid materials because they provide excellent mechanical characteristics (toughness, low-temperature processability, etc.) and, in specific cases, optical and electrical properties. With these ideas in mind, SMMs of the Mn_{12} family were embedded into organic polymers exploiting either covalent or non-covalent interactions.

Following the former approach, Mn_{12} clusters functionalized with Hmet (Fig. 2) have been reported to act as cross-linkers in the radical copoly-

merization with MMA monomer, affording hybrid, reinforced copolymers [65]. The reaction was carried out at 60 °C with AIBN as the radical initiator, using a MMA-to-Mn_{12} molar ratio ranging from 100 to 1000. The embedded manganese clusters were shown not only to keep their chemical integrity and their characteristic SMM behavior, but also to display enhanced chemical and thermal stability, due to the effective shielding provided by the polymer matrix. Interestingly, the properties of the organic skeleton (glass transition temperature, solubility, swelling behavior) are also significantly affected by cross-linkage with the cluster.

As far as non-covalent embedding is concerned, organic polymers like PMMA, PC and PS have been widely used to prepare Mn_{12} dispersions. Thanks to the chemical inertness of the polymer, such nanocomposites provide the simplest method for diluting intact Mn_{12} complexes in a diamagnetic matrix suitable for optical studies [26, 48] or single-molecule addressing at the polymer-air interface [66, 67]. On the other hand, when the polymer is redox active the embedding of Mn_{12} complexes may occur with concomitant electron transfer, leading to a profound alteration of the electronic properties of both constituents. An arylamine-containing polymer, pTPD in Fig. 5, has been recently doped and made conductive with the complex $[Mn_{12}O_{12}(O_2CC_6F_5)_{16}(H_2O)_4]$ [11]. Because of the electron-withdrawing C_6F_5 substituents, the cluster $[Mn_{12}O_{12}(O_2CC_6F_5)_{16}(H_2O)_4]$ is able to oxidize pTPD, allowing the creation of free carriers in the polymer matrix. From the effective energy barrier of the embedded clusters, $U_{eff} \sim 28$ K, a concomitant two-electron reduction of the Mn_{12} complex

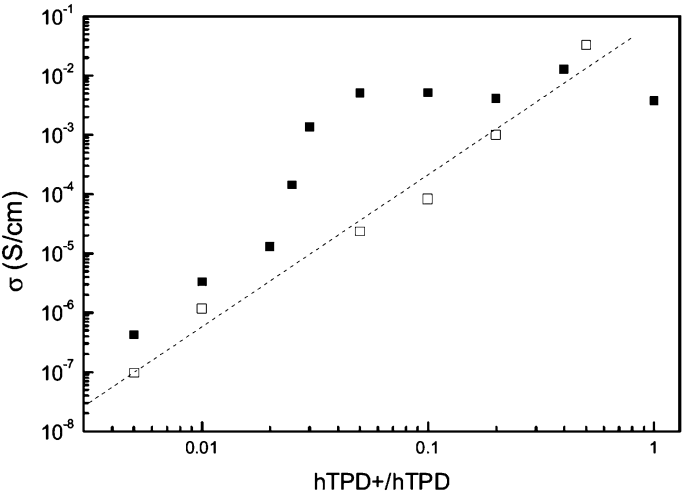

Fig. 6 Conductivity of pTPD films as a function of the fraction of oxidized hTPD units using Mn_{12} (■) and $AgSbF_6$ (□) as oxidant (reprinted from [11])

was inferred (see Sect. 1.3). The conductivity of the hybrid material was found to increase rapidly with the fraction of oxidized monomer units, $hTPD^+/hTPD$ (Fig. 6), reaching ca. $0.01\ S\,cm^{-1}$ for $hTPD^+/hTPD$ as low as 0.04 ($Mn_{12}/hTPD = 0.02$) and remaining essentially constant up to high doping ratios. Comparison with pTPD polymers doped using classical oxidants, like $AgSbF_6$, revealed a superior conductivity of the Mn_{12}-containing material at low levels of doping, suggesting that the manganese clusters not only function as oxidants, but also contribute to the charge-transport process.

3
Low-Dimensional Nanostructures

3.1
General Considerations

Assembling nanodevices and circuits directly from molecular constituents holds the premise to become a leading paradigm in electronics [68, 69]. The first single-molecule device idea, the "molecular diode", was theoretically proposed as early as in 1974 by Aviram and Ratner, who predicted that single molecules with a donor-spacer-acceptor structure would behave as electrical rectifiers [70]. Since that time, several fundamental devices containing single (or few) molecules as active components have been demonstrated and methods for contacting molecules to metallic electrodes have been contextually proposed. Quite simply, two-terminal conductance measurements can be performed by depositing the molecules of interest on a conducting substrate and using the metallic tip of an STM as a second, movable counterelectrode [71–73]. Alternative, more sophisticated methods are based on cross-wire or magnetic-bead junctions [73], on micromachined silicon nanopores [74] and on mercury-drop electrodes [75]. Lithographically fabricated electrodes [76, 77] and nanogaps [78, 79] are also widely utilized to probe individual nanotubes or molecules, with the possible addition of a third electrode (gate) which allows one to modulate the source-drain current in a molecular FET configuration [80–82].

The fast development of molecular electronics in the last decade has produced an increasing interest for probing and eventually manipulating the magnetic moment of individual SMMs, which act as true molecular-scale units for information storage (Sect. 1.3). A new direction in molecular nanomagnetism is therefore emerging, namely the organization of SMMs into low dimensional arrays suitable for single-molecule addressing and their investigation by scanning probe techniques. We herein review a selection of available strategies to assemble SMMs into 2D domains, starting from the earliest one: the incorporation of SMMs into LB films.

3.2
LB Films

The first-reported attempt to organize SMMs into an ultrathin film was undertaken by Clemente-León et al. using the LB technique [83, 84]. The ability of behenic acid $CH_3(CH_2)_{20}COOH$, an amphiphilic molecule, to form a ML at the air–water interface was exploited to prepare a hybrid film incorporating Mn_{12} complexes (R = Me, Ph) (Fig. 7). According to SQUID measurements performed on a multilayer sample, the LB films present some magnetic features reminiscent of SMM behavior, such as the appearance of magnetic hysteresis below 2 K. However, the coercive field is reduced by one order of magnitude and the saturation field is well above 5 T, at variance with crystalline samples. Apparently, the LB approach has not been developed any further, partially because of its inherent limitations, such as the instability of LB films.

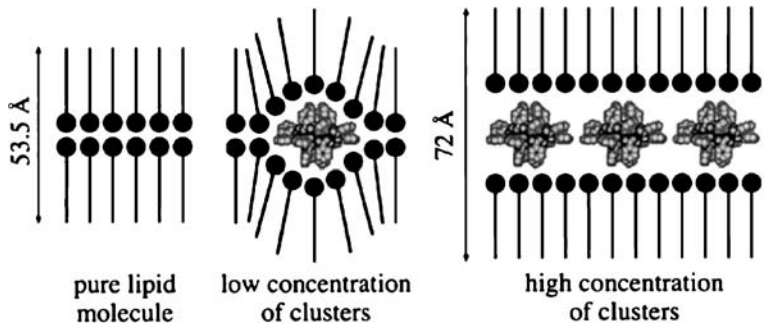

Fig. 7 LB films formed by behenic acid and Mn_{12} complexes as a function of the cluster concentration (reprinted from [83])

3.3
SMMs on Surfaces

The interactions between molecules and surfaces represent a central topic in modern surface science and have been extensively shown throughout biology, chemistry and physics. One of the most remarkable manifestations of molecule-substrate interactions is the spontaneous formation of ordered molecular arrays at surfaces (SAMs). SAMs are typically generated upon exposure of the substrate to molecules (in solution or in the gas phase) bearing suitable functional groups. Many different molecule/substrate combinations have been studied, ranging from amines on platinum [85] to alkyltrichlorosilanes on glass [86], from fatty acids on metal oxides [87] to sulfur-containing adsorbates (thiols, disulfides and sulfides) on gold [88]. The characterization of these MLs is far from trivial because the amount of active

material is extremely small. The use of surface-sensitive analytic techniques such as XPS, ATR-FT/IR, ToF-SIMS, STM and AFM is therefore mandatory.

Different strategies have been proposed for the preparation of MLs or sub-MLs of SMMs on surfaces based on either covalent, electrostatic or Van der Waals interactions. In each case, the required complementarity between the molecule and the surface can be attained by properly functionalizing the cluster periphery, the surface or both interacting pairs, as we now describe in detail.

3.3.1 Direct Deposition

Functionalization with sulfur groups is expected to promote chemical interaction of Mn_{12} clusters with native gold surfaces, thus providing the driving force for their spontaneous organization on the substrate. One major difficulty at the synthetic level arises from the redox instability of free thiols toward the $[Mn_{12}O_{12}]$ core during the ligand-exchange reaction. By contrast, acetyl-protected thiol or thioether groups are fully compatible with the Mn_{12} core and can be easily incorporated in the structure (HL and Hmtb, respectively, in Fig. 2) [89, 90].

As an example, the acetyl-protected derivative $[Mn_{12}O_{12}(L)_{16}(H_2O)_4]$ has been deposited on Au(111) by soaking the gold substrates in a diluted THF solution of the cluster, with the addition of a catalytic amount of NH_3 (aq) to facilitate deacylation of thioacetyl groups (Scheme 1) [89]. STM images and the chemical composition of the layers obtained from XPS measurements lend support to a successful deposition, although no structural ordering is observed (Fig. 8a).

At variance with thiols, thioether groups interact directly with the Au substrate, and the above-described protection/deprotection procedure is therefore unnecessary. In addition, they afford a more coordinative grafting, the Au – S bond energy being ca. 60 kJ mol^{-1} as compared with

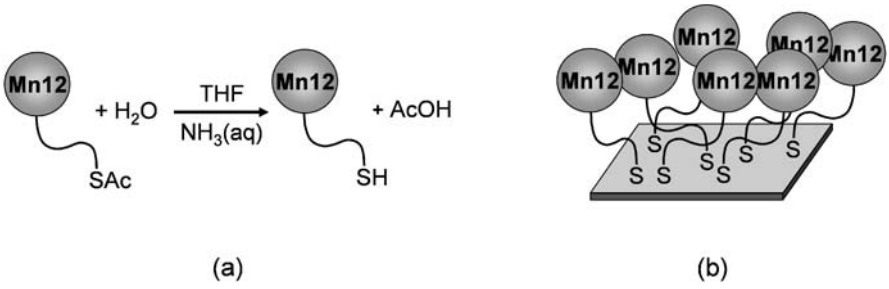

Scheme 1 Deposition of Mn_{12} derivatives on gold, based on in situ deprotection of thioacetyl groups (**a**) and subsequent interaction with the substrate (**b**)

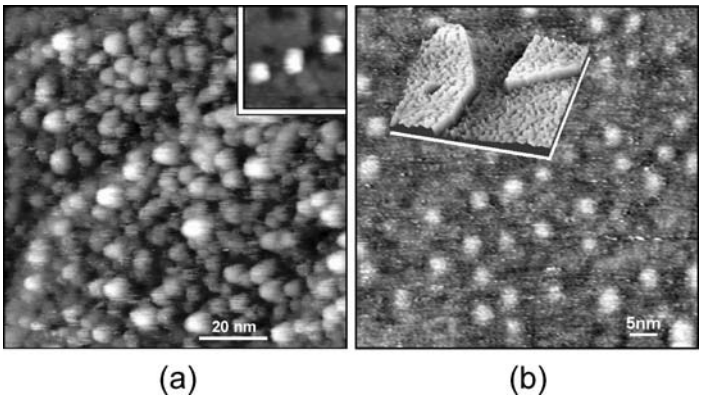

Fig. 8 Constant-current STM images of Au-bound Mn_{12} clusters containing the ligands L (**a**) and mtb (**b**). The *insets* show three isolated molecules (**a**) and a 3-D representation of a 200×200 nm^2 area with gold terraces and a triangular feature typical of Au(111) reconstruction (**b**) (adapted from [89] and [90])

ca. 120 kJ mol^{-1} for thiolates [91]. Following this strategy, adsorbates of $[Mn_{12}O_{12}(mtb)_{16}(H_2O)_4]$ have been prepared by simply soaking a Au(111) substrate in a THF solution of the cluster with no additives. STM investigations (Fig. 8b) have evidenced sub-ML coverage of the surface by well-isolated particles. The size distribution (2.7 ± 0.5 nm) is very narrow and fully compatible with the cluster's dimensions (2.8×2.1 nm), suggesting that aggregation is largely prevented and that single-molecule addressing is indeed achieved [90]. A similar deposition protocol, but leading to molecular aggregates rather than to isolated molecules, has been described by Phark et al., who used a Mn_{12} complex functionalized with Htc ligands [92].

3.3.2 Surface Prefunctionalization

The covalent anchoring of native SMMs can be alternatively carried out by surface prefunctionalization with carboxylate groups. As first reported by Condorelli et al. [93], the reaction of hydrogen-terminated Si(100) with methyl-10-undecenoate leads to the grafting of the ester by formation of a robust Si – C bond (Scheme 2). The use of long aliphatic chains is quite common in SAM preparation, since the Van der Waals interactions among hydrocarbon chains contribute to a significant amount of order of the assembly. The subsequent hydrolysis of the ester group atop the grafted ML leads to carboxylic functions which actively bind Mn_{12}-*acetate* clusters through a ligand exchange reaction. A detailed angle-dependent XPS investigation has been performed by the authors to monitor each reaction step. In particular, analysis of the valence state of manganese in the SMM layer pro-

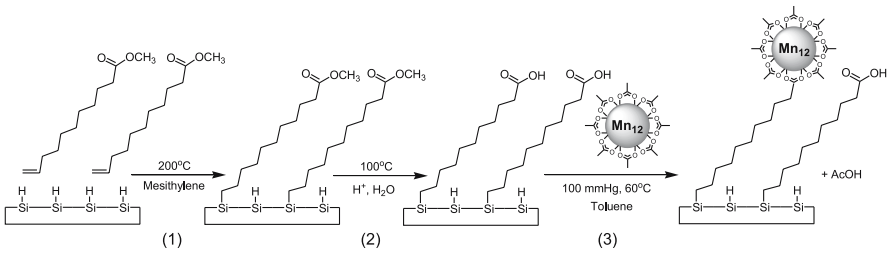

Scheme 2 Procedure used to anchor SMMs on a Si(100) surface: (**1**) reaction of the terminal double bond with the Si(100)-H surface; (**2**) hydrolysis of the ester groups; (**3**) reaction of the grafted carboxylic acid layer with Mn_{12}-*acetate* (adapted from [93])

vided clear evidence that the clusters remain intact during the grafting process.

A similar strategy has been followed by Fleury et al. to graft a mixed-ligand derivative, $[Mn_{12}O_{12}(CHCl_2CO_2)_8(Bu^tCH_2CO_2)_8(H_2O)_3]$ [30], on the Si(100) surface. In the crystalline material, the eight chloroacetate ligands occupy the axial A- and B-type sites whereas *tert*-butylacetate groups are found in equatorial C-positions (see Table 1). The Mn/Cl atomic ratio determined by XPS on the SAM is 0.75(4), hence identical with the solid-state value. This result was taken as evidence of preferential replacement of equatorial ligands and, as a consequence, of a partially oriented grafting [94].

The covalent anchoring of SMMs onto organically modified surfaces proved to be practicable for gold substrates as well. As a first step, long-chain ω-mercaptocarboxylic acids are deposited as a stable SAM on gold. This appears a favorable solution since *n*-alkanethiolate adsorbates on gold are generally well-ordered and crystalline [88]. Furthermore, gold-bound thiolates are redox inactive and fully compatible with the Mn_{12} core. Next, immobilization of Mn_{12} clusters on the prefunctionalized surface occurs as described for silicon substrates. Following this strategy Nait Abdi et al. succeeded in grafting $[Mn_{12}O_{12}(O_2CBu^t)_{16}(H_2O)_4]$ clusters [95] on Au(111) prefunctionalized with 11-mercaptoundecanoic acid [96] or HL′ [97]. This particular Mn_{12} complex was chosen because it easily undergoes ligand-exchange reactions and, in addition, shows optimal solubility in organic solvents. STM investigations in UHV conditions revealed the formation of ordered molecular domains with coherence length of ca. 40 nm when HL′ was employed [97]. However, the saturation magnetization evaluated by SQUID measurements pointed to the presence of more than one ML on the surface. For one sample with a number of Mn_{12} molecules comprised between 1 and 2 MLs simple paramagnetic behavior was observed at 1.8 K, in sharp contrast with the wide hysteresis loop shown by the bulk crystalline compound.

The same procedure was adopted by Steckel et al. who demonstrated through ellipsometric and QCM measurements the formation of a ML

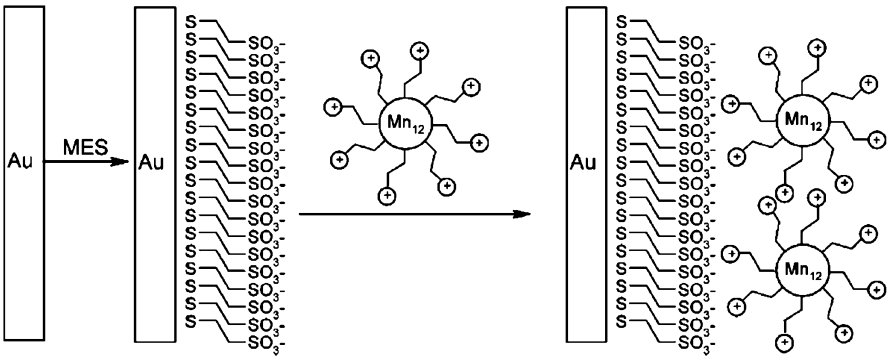

Scheme 3 Schematic representation of the two-steps electrostatic grafting of a cationic Mn_{12} derivative on a prefunctionalized gold surface (reprinted from [99])

of Mn_{12}-*acetate* clusters on a Au(111) surface prefunctionalized with 11-mercaptoundecanoic acid [98].

The pool of available methods for grafting Mn_{12} complexes on prefunctionalized surfaces has been recently enriched by the successful use of electrostatic interactions rather than coordination bonds to deposit a cationic derivative, $[Mn_{12}O_{12}(bet)_{16}(EtOH)_4]^{14+}$ [99]. As depicted in Scheme 3, the Au(111) surface is first treated with MES to give a densely packed SAM terminated with negatively charged sulfonate groups. The second step encompasses the electrostatic grafting of Mn_{12} complexes, which affords partial surface coverage by isolated molecules.

To conclude this section, we remark that sub-MLs of individually accessible clusters represent the conceptually simplest situation for a detailed study of single molecules in a STM configuration [12]. We have shown how these can be accessed by following two different strategies: a direct self-assembly of suitably functionalized clusters on native gold and a secondary self-assembly on a premodified gold surface. On the other hand, ordered patterns of micro- and nanoscale molecular arrays with characteristic sizes and positions may be more easily addressed and read differentially using a magnetic head or a magnetic scanning probe. In the next section the possibility to generate lithographically such structured Mn_{12} films will be discussed.

3.3.3 Lithography and Other Techniques

To date, a variety of lithographic techniques, including advanced soft- and photolithographic methods, have been extensively used for constructing molecular architectures at multiple length scales [100]. Thanks to their versatility, such approaches can be easily transferred to different substrates and molecular materials, including SMMs. For instance, solution-cast thin films of

Mn_{12}-*acetate* on Si/SiO_2 have been patterned by photolithography and characterized through spatially resolved XPS analysis [101]. The patterning has been extended down to the nanometer scale by Cavallini et al., who reported the stamp-assisted deposition of a hydrophobic Mn_{12} derivative on an oxidized Si(100) substrate [102]. In the adopted procedure, a patterned stamp is used to control the wetting/dewetting phenomena arising from molecule–substrate interactions. As shown in Fig. 9, the stamp is first brought in contact with a layer of solution which covers the substrate (1). As the solvent evaporates, capillary forces accumulate the solution below the protrusions of the stamp (2). When saturation is reached the clusters start to precipitate, resulting in parallel arrays of nanometer-sized SMM aggregates (3). Acting on the concentration of the solution and on the distance between the stamp and the substrate it is possible to control the droplet size and the interdroplet distance. Using very dilute solutions, split structures pinned to the edges of the protrusions can also be obtained (4). One of the advantages of this approach is the possibility to pattern length scales much smaller than the size of the stamp features. On the other hand, molecules are only physisorbed onto the surface and the resulting adsorbates have lower stability as compared with covalently grafted layers.

The patterning of chemically stable, washable Mn_{12} films has been reported by Mannini et al. using a combination of μCP and the direct-deposition method described in Sect. 3.3.1 [103]. μCP is a soft lithographic technique suited to pattern molecular stripes with a defined size and position on the surface and has been widely employed with organic molecules, biomolecules and nanoparticles but rarely used with polynuclear coordination compounds [104, 105]. The authors have prepared covalently bound nanostructures of $[Mn_{12}O_{12}(L)_{16}(H_2O)_4]$ on Au(111) following two different procedures, which are schematized in Fig. 10. In both cases, a PDMS stamp exhibiting 5-μm wide protrusions separated by 3-μm wide gaps was used. In the "direct-printing method", 5-μm wide ML stripes of Mn_{12} complexes were

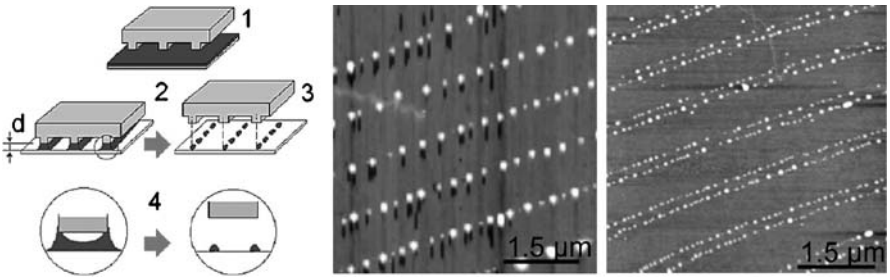

Fig. 9 Stamp-assisted wetting/dewetting method (*left*). AFM images of Mn_{12} complexes printed on oxidized silicon using a dilute solution (*center*) and a very dilute solution (*right*) (modified from [102])

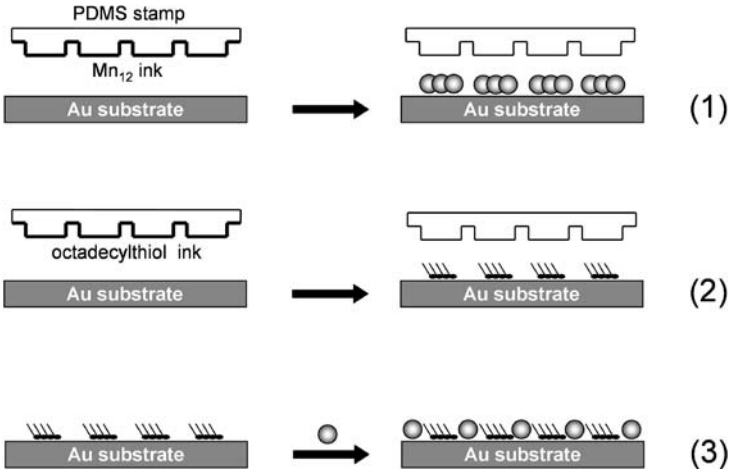

Fig. 10 μCP of Mn_{12} SMMs on gold by direct printing (**1**) and back filling (**2**,**3**)

created on the Au(111) surface by simply inking the stamp in a dilute Mn_{12} solution (1). The effective patterning in the regions defined by the stamp protrusions has been confirmed by ToF-SIMS imaging applied for the first time to the investigation of SMMs adsorbates. In the "back filling" approach, the substrate was initially pre-patterned with octadecylthiol (2) and subsequently soaked in a dilute solution of the cluster (3). Thanks to the different width of protrusions and gaps it was possible to superimpose profile sections extracted from AFM images of the same sample taken at stages (2) and (3). This procedure, also known as "molecular ruler", allowed one to directly measure the thickness of the Mn_{12} adsorbate confined in the bare gold regions, which was found to be consistent with a single layer of molecules [103]. Because of the characteristics of the μCP technique, these stripes are scalable and different architectures can be created starting from a different stamp.

Other deposition methods, commonly used for simple molecular systems, can in principle be transferred to SMMs, including thermal evaporation, sputtering, electron-beam evaporation and so on. However, the thermolability of Mn_{12} molecules often requires the adjustment of deposition techniques. For instance, Dunbar and coworkers have prepared thin films of Mn_{12}-*acetate* using PLD [106] and MAPLE [107]. The MAPLE technique allows milder evaporation conditions, because the clusters are solubilized in a relatively volatile solvent matrix, which is frozen before irradiation. The laser energy is then mostly absorbed by the solvent and the solute molecules can be transferred to the vapor phase without structural damage. When a suitable substrate is placed in the path of the evaporated clusters, a continuous film is deposited. The authors invoke an improved quality of the MAPLE films with respect to those produced by PLD, whose structural and magnetic properties clearly suggest remarkable fragmentation of the clusters.

We conclude this section by highlighting procedures that enable organization of Mn_{12} aggregates into bidimensional domains at the surface of polymeric thin films. Quite simply, a dispersion of Mn_{12} complexes in PC is prepared and cast into a thin film which is subsequently exposed to solvent vapors. With this technique, randomly arranged Mn_{12} aggregates become accessible at the polymer–air interface and can be addressed by AFM and MFM [66]. The position of the clusters can be controlled by molding the dispersion with a structured master, such as a recorded DVD. When the polymer replica is treated with solvent vapors, the polymer softening leads to accumulation of Mn_{12} molecules at the positions of the original protrusions. The resulting magnetic pattern faithfully reproduces the topographic features of the master and can be read using MFM [67]. Notice, however, that the possibility to observe a MFM magnetic signal from a paramagnetic sample, like the Mn_{12} clusters, at RT is still debated. In fact, the force gradient is expected to be extremely weak, as the stray magnetic field of the tip is the only source of magnetic polarization.

4 Concluding Remarks

SMMs are a class of magnetic molecules that exhibit borderline behavior between classical and quantum physics and offer the possibility of storing magnetic information at the molecular level. The incorporation of SMMs into new, multifunctional materials is thus expected to become a very fruitful research area in the near future. We have illustrated selected examples of Mn_{12}-containing materials in which the SMM complex not only carries its unique magnetic properties, but also leads to structural reinforcement or enhanced electrical conductivity of a polymeric network. In this area, the importance of controlled structural alteration and molecular design cannot be overemphasized.

Beside bulk materials, new devices containing individual SMMs as active units are being conceived as well. The simplest consists of a single molecule deposited on a substrate and investigated by a scanning probe technique. Along this line, strategies that allow a controlled deposition of Mn_{12} clusters on Au(111) or on the technologically relevant Si(100) surface are already available and represent a viable route toward high-density molecular devices for data storage and spin electronics. Many important issues, however, remain to be addressed. For instance, the influence of the surface on the magnetic properties of deposited molecules has not been fully ascertained yet. In addition, reliable techniques to prepare arrays of iso-oriented SMMs are still lacking. Finally, after carbon nanotubes, organic molecules or simple metal-organic complexes it is conceivable that SMM will soon be contacted to metallic leads and the first SMM-containing devices will be investigated. The

unique physical behavior of SMMs, combined with the accessibility of multiple charge states, are expected to lead to exotic transport properties. Work in this area is only at a very early stage.

Acknowledgements The financial support of Italian MIUR, through FISR, FIRB, and PRIN projects, and of the EU through Human Potential Program RTN-QUEMOLNA (FP6-CT-2003-504880) and NE "MAGMANET" (FP6-NMP3-CT-2005-515767) is gratefully acknowledged.

References

1. Kahn O (1993) Molecular Magnetism. Wiley, Weinheim
2. For a detailed reference see the entire special issue on Molecule-Based Magnets (2000) MRS Bull 25, N. 11
3. Blundell SJ, Pratt FL (2004) J Phys Condens Matter 16:R771
4. Manriquez JM, Yee GT, McLean RS, Epstein AJ, Miller JS (1991) Science 252:1415
5. Ferlay S, Mallah T, Ouahès R, Veillet P, Verdaguer M (1995) Nature 378:701
6. Caneschi A, Gatteschi D, Sessoli R, Barra AL, Brunel LC, Guillot M (1991) J Am Chem Soc 113:5873
7. Sessoli R, Gatteschi D, Caneschi A, Novak MA (1993) Nature 365:141
8. Caneschi A, Gatteschi D, Sangregorio C, Sessoli R, Sorace L, Cornia A, Novak MA, Paulsen C, Wernsdorfer W (1999) J Magn Magn Mater 200:182
9. Gatteschi D, Sessoli R, Cornia A (2003) Magnetism from the molecular to the nanoscale. In: Meyer TJ, McCleverty JA (eds) Comprehensive Coordination Chemistry II—From Biology to Nanotechnology, vol 7. Elsevier/Pergamon, Amsterdam
10. Coronado E, Galán-Mascarós JR, Gómez-García CJ, Laukhin V (2000) Nature 408:447
11. Bolink HJ, Coronado E, Forment-Aliaga A, Gómez-García CJ (2005) Adv Mater 17:1018
12. Kim G-H, Kim T-S (2004) Phys Rev Lett 92:137203
13. Leuenberger MN, Loss D (2001) Nature 410:789
14. Gatteschi D, Sessoli R, Cornia A (2000) Chem Commun 725
15. Christou G (2005) Polyhedron 24:2065
16. Aromi G, Aubin SMJ, Bolcar MA, Christou G, Eppley HJ, Folting K, Hendrickson DN, Huffman JC, Squire RC, Tsai H-L, Wang S, Wemple MW (1998) Polyhedron 17:3005
17. Brechin EK (2005) Chem Commun 5141
18. Lehn JM (1995) Supramolecular Chemistry—Concepts and Perspectives. Wiley, Weinheim
19. Tasiopoulos AJ, Vinslava A, Wernsdorfer W, Abboud KA, Christou G (2004) Angew Chem Int Ed 43:2117
20. Winpenny REP (2002) J Chem Soc, Dalton Trans 1
21. Lis T (1980) Acta Crystallogr B Struct Sci 36:2042
22. Weinland RF, Fischer G (1921) Z Anorg Allg Chem 120:161
23. Cornia A, Fabretti AC, Sessoli R, Sorace L, Gatteschi D, Barra AL, Daiguebonne C, Roisnel T (2002) Acta Crystallogr C Cryst Struct Commun 58: m371
24. Cornia A, Sessoli R, Sorace L, Gatteschi D, Barra AL, Daiguebonne C (2002) Phys Rev Lett 89:257201
25. Takahashi S, Edwards RS, North JM, Hill S, Dalal NS (2004) Phys Rev B 70:094429
26. Eppley HJ, Tsai H-L, de Vries N, Folting K, Christou G, Hendrickson DN (1995) J Am Chem Soc 117:301

27. Sessoli R, Tsai H-L, Schake AR, Wang S, Vincent JB, Folting K, Gatteschi D, Christou G, Hendrickson DN (1993) J Am Chem Soc 115:1804
28. Bian G-Q, Kuroda-Sowa T, Konaka H, Hatano M, Maekawa M, Munakata M, Miyasaka H, Yamashita M (2004) Inorg Chem 43:4790
29. Wei Y-G, Zhang S-W, Shao M-C, Tang Y-Q (1997) Polyhedron 16:1471
30. Soler M, Artus P, Folting K, Huffman JC, Hendrickson DN, Christou G (2001) Inorg Chem 40:4902
31. Chakov NE, Abboud KA, Zakharov LN, Rheingold AL, Hendrickson DN, Christou G (2003) Polyhedron 22:1759
32. Chakov NE, Wernsdorfer W, Abboud KA, Hendrickson DN, Christou G (2003) Dalton Trans 2243
33. Kuroda-Sowa T, Handa T, Kotera T, Maekawa M, Munakata M, Miyasaka H, Yamashita M (2004) Chem Lett 33:540
34. Artus P, Boskovic C, Yoo J, Streib WE, Brunel L-C, Hendrickson DN, Christou G (2001) Inorg Chem 40:4199
35. Kuroda-Sowa T, Fukuda S, Miyoshi S, Maekawa M, Munakata M, Miyasaka H, Yamashita M (2002) Chem Lett 31:682
36. Boskovic C, Pink M, Huffman JC, Hendrickson DN, Christou G (2001) J Am Chem Soc 123:9914
37. Brockman JT, Abboud KA, Hendrickson DN, Christou G (2003) Polyhedron 22:1765
38. Pacchioni M, Cornia A, Fabretti AC, Zobbi L, Bonacchi D, Caneschi A, Chastanet G, Gatteschi D, Sessoli R (2004) Chem Commun 2604
39. Aubin SMJ, Sun Z, Pardi L, Krzystek J, Folting K, Brunel L-C, Rheingold AL, Christou G, Hendrickson DN (1999) Inorg Chem 38:5329
40. Kuroda-Sowa T, Nakano M, Christou G, Hendrickson DN (2001) Polyhedron 20:1529
41. Soler M, Chandra SK, Ruiz D, Davidson ER, Hendrickson DN, Christou G (2000) Chem Commun 2417
42. Soler M, Chandra SK, Ruiz D, Huffman JC, Hendrickson DN, Christou G (2001) Polyhedron 20:1279
43. Takeda K, Awaga K (1997) Phys Rev B 56:14560
44. Kuroda-Sowa T, Lam M, Rheingold AL, Frommen C, Reiff WM, Nakano M, Yoo J, Maniero AL, Brunel L-C, Christou G, Hendrickson DN (2001) Inorg Chem 40:6469
45. Coronado E, Forment-Aliaga A, Gaita-Ariño A, Giménez-Saiz C, Romero FM, Wernsdorfer W (2004) Angew Chem Int Ed 43:6152
46. Friedman JR, Sarachik MP, Tejada J, Ziolo R (1996) Phys Rev Lett 76:3830
47. Thomas L, Lionti F, Ballou R, Gatteschi D, Sessoli R, Barbara B (1996) Nature 383:145
48. McInnes EJL, Pidcock E, Oganesyan VS, Cheesman MR, Powell AK, Thomson AJ (2002) J Am Chem Soc 124:9219
49. Cheesman MR, Oganesyan VS, Sessoli R, Gatteschi D, Thomson AJ (1997) Chem Commun 1677
50. Domingo N, Williamson BE, Gómez-Segura J, Gerbier P, Ruiz-Molina D, Amabilino DB, Veciana J, Tejada J (2004) Phys Rev B 69:052405
51. Robinson RA, Brown PJ, Argyriou DN, Hendrickson DN, Aubin SMJ (2000) J Phys Condens Matter 12:2805
52. Barra A-L, Gatteschi D, Sessoli R, Abbati GL, Cornia A, Fabretti AC, Uytterhoeven MG (1997) Angew Chem Int Ed Engl 36:2329
53. Villain J, Hartmann-Boutron F, Sessoli R, Rettori A (1994) Europhys Lett 27:159
54. Gatteschi D, Sessoli R (2003) Angew Chem Int Ed 42:268
55. Chakov NE, Soler M, Wernsdorfer W, Abboud KA, Christou G (2005) Inorg Chem 44:5304

56. Soler M, Wernsdorfer W, Abboud KA, Huffman JC, Davidson ER, Hendrickson DN, Christou G (2003) J Am Chem Soc 125:3576
57. Coronado E, Feliz M, Forment-Aliaga A, Gómez-García CJ, Llusar R, Romero FM (2001) Inorg Chem 40:6084
58. Forment-Aliaga A, Coronado E, Feliz M, Gaita-Ariño A, Llusar R, Romero FM (2003) Inorg Chem 42:8019
59. Coradin T, Larionova J, Smith AA, Rogez G, Clerac R, Guérin C, Blondin G, Winpenny REP, Sanchez C, Mallah T (2002) Adv Mater 14:896
60. Willemin S, Arrachart G, Lecren L, Larionova J, Coradin T, Clerac R, Mallah T, Guérin C, Sanchez C (2003) New J Chem 27:1533
61. Clemente-León M, Coronado E, Forment-Aliaga A, Amorós P, Ramírez-Castellanos J, González-Calbet JM (2003) J Mater Chem 13:3089
62. Clemente-León M, Coronado E, Forment-Aliaga A, Martínez-Agudo JM, Amorós P (2003) Polyhedron 22:2395
63. Schubert U, Hüsing N (2005) Synthesis of Inorganic Materials. Wiley, Weinheim
64. Gómez-Romero P, Sanchez C (eds) (2004) Functional Hybrid Materials. Wiley, Weinheim
65. Willemin S, Donnadieu B, Lecren L, Henner B, Clérac R, Guérin C, Meyer A, Pokrovskii AV, Larionova J (2004) New J Chem 28:919
66. Ruiz-Molina D, Mas-Torrent M, Gómez J, Balana AI, Domingo N, Tejada J, Martínez MT, Rovira C, Veciana J (2003) Adv Mater 15:42
67. Cavallini M, Gomez-Segura J, Ruiz-Molina D, Massi M, Albonetti C, Rovira C, Veciana J, Biscarini F (2005) Angew Chem Int Ed 44:888
68. Seminario JM (2005) Nat Mater 4:111
69. Joachim C, Gimzewski JK, Aviram A (2000) Nature 408:541
70. Aviram A, Ratner MA (1974) Chem Phys Lett 29:277
71. Aviram A, Joachim C, Pomerantz M (1988) Chem Phys Lett 146:490
72. Datta S, Tian W, Hong S, Reifenberger R, Henderson JI, Kubiak CP (1997) Phys Rev Lett 79:2530
73. Szuchmacher Blum A, Kushmerick JG, Long DP, Patterson CH, Yang JC, Henderson JC, Yao Y, Tour JM, Shashidhar R, Ratna BR (2005) Nat Mater 4:167
74. Chen J, Reed MA, Rawlett AM, Tour JM (1999) Science 286:1550
75. Holmlin RE, Haag R, Chabinyc ML, Ismagilov RF, Cohen AE, Terfort A, Rampi MA, Whitesides GM (2001) J Am Chem Soc 123:5075
76. Tans SJ, Verschueren ARM, Dekker C (1998) Nature 393:49
77. Jarillo-Herrero P, Sapmaz S, Dekker C, Kouwenhoven LP, van der Zant HSJ (2004) Nature 429:389
78. Reed MA, Zhou C, Muller CJ, Burgin TP, Tour JM (1997) Science 278:252
79. Kervennic YV, van der Zant HSJ, Morpurgo AF, Gurevich L, Kouwenhoven LP (2002) Appl Phys Lett 80:321
80. Park H, Park J, Lim AKL, Anderson EH, Alivisatos AP, McEuen PL (2000) Nature 407:57
81. Liang W, Shores MP, Bockrath M, Long JR, Park H (2002) Nature 417:725
82. Park J, Pasupathy AN, Goldsmith JI, Chang C, Yaish Y, Petta JR, Rinkoski M, Sethna JP, Abruña HD, McEuen PL, Ralph DC (2002) Nature 417:722
83. Clemente-León M, Soyer H, Coronado E, Mingotaud C, Gómez-García CJ, Delhaès P (1998) Angew Chem Int Ed 37:2842
84. Clemente-León M, Coronado E, Forment-Aliaga A, Romero FM (2003) CR Chimie 6:683
85. Bigelow WC, Pickett DL, Zisman WA (1946) J Colloid Interface Sci 1:513

86. Sagiv J (1980) J Am Chem Soc 102:92
87. Allara DL, Nuzzo RG (1985) Langmuir 1:45
88. Ulman A (1996) Chem Rev 96:1533
89. Cornia A, Fabretti AC, Pacchioni M, Zobbi L, Bonacchi D, Caneschi A, Gatteschi D, Biagi R, Del Pennino U, De Renzi V, Gurevich L, van der Zant HSJ (2003) Angew Chem Int Ed 42:1645
90. Zobbi L, Mannini M, Pacchioni M, Chastanet G, Bonacchi D, Zanardi C, Biagi R, Del Pennino U, Gatteschi D, Cornia A, Sessoli R (2005) Chem Commun 1640
91. Lavrich DJ, Wetterer SM, Bernasek SL, Scoles G (1998) J Phys Chem B 102:3456
92. Phark S, Khim ZG, Kim BJ, Suh BJ, Yoon S, Kim J, Lim JM, Do Y (2004) Jpn J Appl Phys 43:8273
93. Condorelli GG, Motta A, Fragalà IL, Giannazzo F, Raineri V, Caneschi A, Gatteschi D (2004) Angew Chem Int Ed 43:4081
94. Fleury B, Catala L, Huc V, David C, Zhong WZ, Jegou P, Baraton L, Palacin S, Albouy P-A, Mallah T (2005) Chem Commun 2020
95. Gerbier P, Ruiz-Molina D, Domingo N, Amabilino DB, Vidal-Gancedo J, Tejada J, Hendrickson DN, Veciana J (2003) Monatsh Chem 134:265
96. Nait Abdi A, Bucher JP, Rabu P, Toulemonde O, Drillon M, Gerbier P (2004) J Appl Phys 95:7345
97. Nait Abdi A, Bucher JP, Gerbier P, Rabu P, Drillon M (2005) Adv Mater 17:1612
98. Steckel JS, Persky NS, Martinez CR, Barnes CL, Fry EA, Kulkarni J, Burgess JD, Pacheco RB, Stoll SL (2004) Nano Lett 4:399
99. Coronado E, Forment-Aliaga A, Romero FM, Corradini V, Biagi R, De Renzi V, Gambardella A, Del Pennino U (2005) Inorg Chem 44:7693
100. Smith RK, Lewis PA, Weiss PS (2004) Prog Surf Sci 75:1
101. Kim K, Seo DM, Means J, Meenakshi V, Teizer W, Zhao H, Dunbar KR (2004) Appl Phys Lett 85:3872
102. Cavallini M, Biscarini F, Gomez-Segura J, Ruiz D, Veciana J (2003) Nano Lett 3:1527
103. Mannini M, Bonacchi D, Zobbi L, Piras FM, Speets EA, Caneschi A, Cornia A, Magnani A, Ravoo BJ, Reinhoudt DN, Sessoli R, Gatteschi D (2005) Nano Lett 5:1435
104. Bain CD, Troughton EB, Tao Y-T, Evall J, Whitesides GM, Nuzzo RG (1989) J Am Chem Soc 111:321
105. Hidber PC, Helbig W, Kim E, Whitesides GM (1996) Langmuir 12:1375
106. Means J, Meenakshi V, Srivastava RVA, Teizer W, Kolomenskii AA, Schuessler HA, Zhao H, Dunbar KR (2004) J Magn Magn Mater 284:215
107. Meenakshi V, Teizer W, Naugle DG, Zhao H, Dunbar KR (2004) Solid State Commun 132:471

Struct Bond (2006) 122: 163–206
DOI 10.1007/430_030

Published online: 24 March 2006

Single-Chain Magnets: Theoretical Approach and Experimental Systems

Claude Coulon[1] · Hitoshi Miyasaka[2,3] · Rodolphe Clérac[1] (✉)

[1]Centre de Recherche Paul Pascal, CNRS UPR-8641, 115 av. Albert Schweitzer, 33600 Pessac, France
coulon@crpp-bordeaux.cnrs.fr, clerac@crpp-bordeaux.cnrs.fr

[2]Department of Chemistry, Graduate School of Science, Tohoku University, Aramaki-Aza-Aoba, Aoba-ku, 980-8578 Sendai, Japan
miyasaka@agnus.chem.tohoku.ac.jp

[3]CREST, Japan Science and Technology Agency, 4-1-8 Honcho, Kawaguchi, 332-0012 Saitama, Japan

Abstract Recently, a new class of nano-magnets has been discovered and called single-chain magnets (SCMs) by analogy to the single-molecule magnets (SMMs). These materials are composed of magnetically isolated chains that can be individually magnetized. As

purely one-dimensional systems are known to have a long-range order only at $T = 0$ K, these SCM materials remains in their paramagnetic state at any finite temperature. Nevertheless, the combination of a large uni-axial anisotropy and large magnetic interactions between the high-spin magnetic units of the chain promotes long relaxation times and the system can behave as a magnet. Although the presently available materials possess long relaxation times only below about 10 K, the limitations to produce SCMs compatible with industrial applications seem less severe than for SMMs. This is one of the reasons explaining why the chemistry and the physics on SCMs have quickly become a very active field. In the first part of this review, we have summarized the last developments on the theoretical understanding of the SCM behavior. In these systems, the key analysis of the magnetic properties is the comparison between static susceptibility and dynamic data that leaves no arbitrary parameter and allows an unambiguous identification of a SCM. The second part of this review is devoted to the experimental SCM systems reported so far. In particular, selected examples are presented to illustrate how it is possible to characterize experimentally a material with SCM properties.

Keywords Magnetic properties · Low dimensional systems · Magnets · Single-chain magnets

Abbreviations

SCM	single-chain magnet
SMM	single-molecule magnet
EPR	electron paramagnetic resonance spectroscopy
DFT	density functional theory
1D	one dimensional
NMR	nuclear magnetic resonance
μSR	muon spin rotation

1 Introduction

The synthesis of new magnets, i.e. of magnetic systems being able to keep a magnetization (M) in the absence of an applied magnetic field (H)[1], is a major issue for many industrial applications. The commonly used magnets are systems exhibiting three-dimensional ferromagnetic or ferrimagnetic order; but the perpetual quest to reduce the size of the magnetic unit being able to store information has led to the tailoring of these materials into small grains [1, 2]. Below a critical size, these grains become single magnetic domains and exhibit field hysteresis loops when they possess a sig-

[1] In some papers, materials that display a three-dimensional order with a spontaneous magnetization (e.g. ferromagnet, ferrimagnets…) are qualified as "true" or "classical" magnets while single-molecule and single-chain magnet properties have been often described as a magnet-like behavior. In this review, we have decided to use a general definition of a magnet that includes all the systems exhibiting M vs. H hysteresis loops with a bistability at zero field.

nificant uni-axial magnetic anisotropy. Nevertheless, this approach has its own limit. Indeed, reducing the size of the particles, the magnetic anisotropy is itself decreased until it becomes comparable to the thermal energy. The thermal fluctuations then randomly reverse moments carried by the particles and the relaxation time of the magnetization becomes fast. The system thus displays a superparamagnetic behavior and its potential applications as a magnet are lost. Therefore, miniaturization of the elementary memory unit is stopped by what is called the superparamagnetic limit [3, 4]. In this context, the discovery of single-molecule magnets (SMM) [5–7] has been viewed as an important step in the miniaturization process of future memory devices. In this case, the relaxation of the magnetization is understood at the molecular level. A macroscopic material is an assembly of non-interacting SMMs and is therefore in a paramagnetic state. Very long relaxation times are, however, observed at low temperature and this type of material is indeed considered to be a magnet. SMMs have been intensively studied in the last 15 years and it is now well established that the observed slow magnetization relaxation results from the combined effect of high molecular spin ground state and large uniaxial anisotropy (promoting an easy axis). As for magnetic nano-particles, evaluation of parameters immediately shows that it will be very hard to produce SMMs with a long enough relaxation time at room temperature for potential applications in information storage. More recently, a new class of nano-magnets has been discovered and called single-chain magnets (SCMs) by analogy to the SMMs [8]. The idea is to produce a material composed of magnetically isolated chains that can be individually magnetized. It is already well established that independently of the spin dimensionality, n ($n = 1$, Ising; $n = 2$, XY; $n = 3$, Heisenberg), one-dimensional magnetic systems with short-range interactions do not experience long-range order at a finite temperature. Nevertheless, the whole material can remain in a paramagnetic state like SMMs, and also display long relaxation times of the magnetization promoted by the combination of a large uni-axial anisotropy and large magnetic interactions between the high-spin magnetic units of the chain. This type of one-dimensional system can thus behave as a magnet. Although the presently available materials only show long relaxation times at low temperature, the limitations to produce samples compatible with industrial applications seem less severe than for SMMs. This is one of the reasons that explains why the synthesis and characterization of SCMs have quickly become a very active field. In this review, we will successively present the latest developments in the theoretical understanding of SCM behavior, selected examples to illustrate how it is experimentally possible to characterize a material with SCM properties and an exhaustive list of the systems labeled SCM.

2
Theoretical Approach on SCMs

As mentioned in the Introduction, single-chain-magnet materials are composed of magnetically isolated chains for which a finite magnetization can be frozen in the absence of an applied magnetic field. The relaxation of the magnetization becomes so slow at low temperature that these systems can then be considered to be real magnets. As this situation is metastable, the main theoretical challenge is to understand the slow dynamics of return to an equilibrium state. However, the description of the thermodynamic state is also a key point in the analysis of SCM properties. In fact, we will demonstrate that an accurate understanding of SCM behavior is achieved only when both dynamic and thermodynamic data are consistently described. Thus, the two first parts of this section will deal successively with the thermodynamic description of magnetic chains and then with the theory of the magnetic relaxation. Both parts will be essentially devoted to the infinite chain of ferromagnetically coupled spins that gives the simplest approach for SCMs. In the third part, we will show how these theoretical models should be adapted to discuss the simplest real SCM systems studied so far. In particular, the mechanism for individual spin-flips, the description of non-regular chains in terms of effective spins and the role of the defects always present in real materials will be discussed.

2.1
Thermodynamic Description of a Magnetic Chain

As single-chain magnet materials are composed of magnetically isolated chains, the magnetic measurements obtained for these systems essentially reveal the intrinsic behavior of a single chain, i.e. of a one-dimensional system. 1D models have been extensively discussed and studied over the last few decades as they are more tractable than the same models developed at higher dimensions (for a review, see for example [9]). Moreover, many kinds of quasi-one dimensional systems have been experimentally synthesized and their properties have been successfully compared to the theory (for a review, see for example [10]). For both these theoretical and experimental reasons, 1D systems and their experimental properties are well known. One of the main conclusions demonstrated for 1D systems with only short-range interactions (like a magnetic exchange usually restricted to the first neighbors) is that long-range magnetic order can not be obtained at a finite temperature. However, their low temperature behavior is singular as strong short-range order is present until a critical point is finally reached at $T = 0$ K. Thus, the description of the low temperature magnetic response of a chain is strongly influenced by magnetic correlations and thus the simple mean-field approximation fails to describe these systems at low temperature. Fortunately,

specific methods are available to obtain exact results for 1D magnetic systems and in particular for the zero-field magnetic susceptibility [11]. We will first summarize here the main results of these models, focusing the discussion on ferromagnetic chains. For simplicity, we will consider systems with only first neighbor interactions and a single orientation of the magnetic easy axis.

2.1.1 The Classical-Spin Heisenberg Chain

Analytical results are essentially obtained when the spins are treated in the classical approximation to avoid any heavy quantum mechanical problems. In this approximation, relevant when the spin is large enough (typically larger than 2), the spin operators can be replaced by classical vectors. A simple example to illustrate this approach is the classical-spin Heisenberg chain described by the following Hamiltonian[2]:

$$H = -2J \sum_{-\infty}^{+\infty} \vec{S}_i \vec{S}_{i+1} = -2JS^2 \sum_{-\infty}^{+\infty} \vec{u}_i \vec{u}_{i+1} \,, \tag{1}$$

where $\vec{u}_i$ is a unit vector [12]. With ferromagnetic interactions ($J > 0$), the zero-field susceptibility, χ, presents a T^{-2} divergence at low temperature [12]. This result can be readily obtained using a relationship valid for any classical model:

$$\frac{\chi T}{C} = \sum_{n=-\infty}^{n=+\infty} < \vec{u}_i \vec{u}_{i+n} > \,, \tag{2}$$

with $< \vec{u}_i \vec{u}_{i+n} >= \Gamma^n$ and $\Gamma =< \vec{u}_i \vec{u}_{i+1} >$ being the nearest neighbors correlation function (<> means average on the chain). It should be noted that C is the Curie constant ($C = g^2 \mu_B^2 S(S+1)/(3k_B)$) normalized per site, g is the gyromagnetic factor, μ_B is the Bohr magneton, S is the spin value and k_B is the Boltzmann constant. Then, Eq. 2 can be simplified as:

$$\frac{\chi T}{C} = \sum_{n=-\infty}^{n=+\infty} \Gamma^n = \frac{1+\Gamma}{1-\Gamma} \,. \tag{3}$$

For the classical Heisenberg model and using the notations of Eq. 1, the correlation function Γ is given by:

$$\Gamma = \coth(2\beta JS^2) - (2\beta JS^2)^{-1} \,, \tag{4}$$

[2] By convention $J > 0$ corresponds to ferromagnetic interactions. Note that a factor 2 has been introduced to remain consistent with our previous publications, but this factor is not always present in other publications.

where $\beta = 1/(k_B T)$. As the temperature goes to 0, the correlation function becomes close to 1 and, in this limit, Eq. 3 can be simplified to:

$$\frac{\chi T}{C} \approx 4\beta J S^2 \,. \tag{5}$$

Equation 5 demonstrates the T^{-2} divergence of the susceptibility and the occurrence of a critical point at $T = 0$ K. Finally, it should be mentioned that the magnetic correlation length, ξ, can also be introduced in an equivalent form of the Eq. 5:

$$\frac{\chi T}{C} \approx 2\frac{\xi}{a} \,, \tag{6}$$

with a being the cell parameter of the chain. In this limit, χT directly measures the magnetic correlation length that diverges as $1/T$ for the classical Heisenberg model.

2.1.2 The Ising Chain

An exact solution has also been obtained for the Ising chain model, for which the spins are assumed to be aligned along a given z axis. In this limit, the spins possess an infinite uni-axial magnetic anisotropy with an easy z axis. The corresponding Hamiltonian reads[3]

$$H = -2J \sum_{-\infty}^{+\infty} S_{i,z} S_{i+1,z} = -2JS^2 \sum_{-\infty}^{+\infty} \sigma_i \sigma_{i+1} \,, \tag{7a}$$

where $\sigma_i = \pm 1$. Note that this Hamiltonian is often written in a more compact form in Physics papers:

$$H = -J_I \sum_i \sigma_i \sigma_{i+1} \,. \tag{7b}$$

This form is obviously equivalent to Eq. 7a with $J_I = 2JS^2$. The parameter J_I, proportional to the exchange between neighboring atoms, measures directly the characteristic energy in the chain.

The Ising model is also a classical model and Eqs. 2, 3 and 6 are still valid when $\vec{u}_i$ is replaced by σ_i. Equation 3 gives the parallel susceptibility (when the magnetic field is applied along the z axis) with the Curie constant per spin $C = g^2 \mu_B^2 S^2 / k_B$. The main difference with the classical Heisenberg model is the expression of the correlation function Γ [14]:

$$\Gamma = \tanh(2\beta J S^2) \,. \tag{8}$$

[3] The Hamiltonian given by Eq. 7a is equivalent to an $S = 1/2$ Ising model after rescaling the exchange and the individual magnetic moment. A $(2S + 1)$ state Ising model has also been considered [13]. Both models differ by the expression of the Curie constant but the magnetic susceptibility follows in both cases an exponential low temperature dependence.

Therefore, at low temperature and in the ferromagnetic case, the correlation function is obtained by $\Gamma \approx 1 - 2\exp(4\beta JS^2)$ and the parallel magnetic susceptibility ($\chi_{//}$) of the uniform Ising chain diverges exponentially as:

$$\frac{\chi_{//}T}{C} \approx \exp(4\beta JS^2)\,. \tag{9}$$

As deduced from Eq. 6, the correlation length increases also exponentially at low temperature. Note that the perpendicular susceptibility of the Ising chain has also been calculated [15] and stays constant at low temperature remaining much smaller than the parallel susceptibility. The above Eqs. 5 and 9 show that the Heisenberg and the Ising models possess completely different low temperature behaviors. This result comes from the different nature of the magnetic excitations. They are gapless in the Heisenberg case, while the low energy excited states of the 1D Ising model consist of large oriented domains separated by sharp domain walls as illustrated by Fig. 1.

Following Eq. 7, the energy necessary to create one of these domains is $\Delta_\xi = 4|J|S^2$. The correlation length can thus be obtained by writing that this energy is balanced by the entropy gained when creating a defect on a chain segment of 2ξ size:

$$\Delta_\xi = k_B T \ln\left(\frac{2\xi}{a}\right)\,. \tag{10}$$

This relation is equivalent to Eq. 9, as the correlation length is still given by Eq. 6. It is also important to notice that the magnitude of the correlation length between the Heisenberg and the Ising models is dramatically different. For a given value of $J/k_B T$, Eqs. 5 and 9 lead to a much larger value of ξ in the Ising case. We will see in the next section the importance of this remark in discussing the slow relaxation of the magnetization.

Using theoretical methods specifically adapted to 1D problems, like the matrix transfer method, the field dependence of the magnetization can also be determined [16, 17]. In particular, a compact expression is obtained for the infinite Ising chain:

$$m = \frac{\sinh(\mu\beta H)}{\sqrt{\sinh^2(\mu\beta H) + \exp(-8\beta JS^2)}}\,, \tag{11}$$

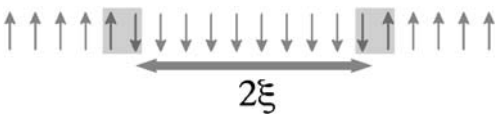

Fig. 1 Schematic view of a magnetic Ising chain in zero applied magnetic field with large oriented domains of average length 2ξ separated by sharp domain walls

where m is the normalized magnetization per site: $m = M/M_{sat}$ (where M_{sat} is the magnetization at saturation) and μ is the site magnetic moment. Then increasing the ferromagnetic interaction along the chain, the saturation of the magnetization with the applied field will be increasingly quicker at low temperature even if the system is still in the paramagnetic phase.

2.1.3 The Anisotropic Heisenberg Chain

Although the Heisenberg and Ising models have been intensively used in theoretical works, the description of real materials often requires more complicated Hamiltonians. For example when single-ion anisotropy is relevant, a finite magnetic anisotropy has to be considered. In this case, the corresponding Hamiltonian can be written:

$$H = -2J \sum_{-\infty}^{+\infty} \vec{S}_i \vec{S}_{i+1} + D \sum_{-\infty}^{+\infty} \vec{S}_{iz}^2 \,. \tag{12a}$$

As seen previously, unit vectors can be introduced in Eq. 12a:

$$H = -2JS^2 \sum_{-\infty}^{+\infty} \vec{u}_i \vec{u}_{i+1} + DS^2 \sum_{-\infty}^{+\infty} \vec{u}_{iz}^2 \,. \tag{12b}$$

The magnetic properties deduced from this model have been described in [18]. When $\boldsymbol{z}$ is an easy axis (i.e. when D is negative following Eq. 12), the correlation length diverges exponentially at low temperature. In fact, the nature of the low temperature magnetic excitations is the same as for the Ising model, i.e. large oriented domains separated by domain walls. The shape and the energy of these domain walls have been calculated by B. Barbara (in the papers by B. Barbara, our J and D parameters are noted W and K, respectively [19]). As long as $|D/J|$ is larger than 4/3, sharp domain walls (with a thickness equal to a single unit cell) are present with a creation energy still given by $\Delta_\xi = 4|J|S^2$. For smaller anisotropies ($|D/J| < 4/3$), the width of a domain wall is larger than a unit cell and its energy Δ_ξ is a function of D and J. A simple expression, $\Delta_\xi \approx 4S^2\sqrt{|JD|}$, is obtained in the limit of a small anisotropy (i.e. when $|D| \ll |J|$). As long as D is negative, the domain wall is still a localized topological defect and the argument given above for the Ising model leading to Eq. 10 still applies. At low temperature, when the correlation length is much larger than the width of the domain wall, one obtains:

$$\frac{\chi T}{C} \approx \exp(\beta \Delta_\xi) \,, \tag{13}$$

where Δ_ξ is the energy of the domain wall. Equation 13 is therefore the generalization of Eq. 9. As expected, both equations give an identical result for large anisotropy ($|D/J| \gg 4/3$). For any negative value of the magnetic anisotropy,

a plot of $\ln(\chi T)$ versus $1/T$ gives a straight line at low temperature with a slope directly related to the creation energy of the domain walls.

2.2 Relaxation of the Magnetization

The simplest descriptions of a magnetic chain in terms of non-equilibrium states rely on stochastic models (for a review, see for example [20]). Back in the 1960s, the time-dependent statistics of an Ising chain were described in the pioneering work of R.J. Glauber [21]. The interacting spins are represented by stochastic functions of time, $\sigma_i(t)$, in contact with a large thermal bath which induces spontaneous spin-flips. Glauber's model assumes only single-spin flips where the transition probability per unit time that the i^{th} spin flips from σ_i to $-\sigma_i$, $W_i(\sigma_i)$, depends on the neighboring spins as:

$$W_i(\sigma_i) = \frac{1}{2\tau_0}\left(1 - \frac{\gamma}{2}\sigma_i\left(\sigma_{i-1} + \sigma_{i+1}\right)\right) , \tag{14}$$

where τ_0 is the characteristic time which describes the flip of a given spin in the absence of interaction and $\gamma = \tanh(4\beta JS^2)$, following the notations of Eq. 7. It is worth noting that the time τ_0 is a priori temperature dependent even if in this model τ_0 is considered to be a simple adjustable parameter [22]. As discussed in the following, the expression of the transition probability given by Eq. 14 is not the only possible choice. The unique requirement is that the equilibrium state is a solution of the dynamic equations at infinite time. This condition implies a detailed balance relation [21, 23, 24] also verified for generalized versions of Eq. 14. However, Glauber's assumption remains the simplest choice allowing an exact resolution of the 1D case and consistent conclusions with experimental results. When introduced in a master equation, Eq. 14 implies (with <> meaning average on the chain):

$$\tau_0 \frac{\mathrm{d} < \sigma_i >}{\mathrm{d}t} + < \sigma_i > = < \tanh(\beta E_i) > . \tag{15a}$$

E_i is the local field (in energy units) seen by the spin σ_i which is given by:

$$E_i = 2JS^2(\sigma_{i-1} + \sigma_{i+1}) . \tag{15b}$$

Then, the dynamic equation can be simplified to:

$$\tau_0 \frac{\mathrm{d} < \sigma_i >}{\mathrm{d}t} + < \sigma_i > (1 - \gamma) = 0 . \tag{16}$$

This equation implies that the magnetization relaxes exponentially, i.e. with a single characteristic time (τ):

$$\tau = \frac{\tau_0}{1 - \tanh(4\beta JS^2)} . \tag{17}$$

In other words, Eq. 16 is the familiar Debye equation which also leads to a linear response of a chain to an ac magnetic field of frequency ν:

$$\chi(\omega) = \frac{\chi_{\mathrm{dc}}}{1 + i\omega\tau}\,, \tag{18}$$

with χ_{dc} being the static susceptibility and $\omega = 2\pi\nu$.

At low temperature and in the ferromagnetic case, Eq. 17 can be approximated by:

$$\tau = \frac{\tau_0}{2}\exp(8\beta JS^2)\,. \tag{19}$$

Indeed, the Glauber model predicts a divergence of the relaxation time as:

$$\tau = 2\tau_0\left(\frac{\xi}{a}\right)^2\,. \tag{20}$$

Equation 20 shows that magnetic correlations imply an enhancement of the relaxation time which is nothing but the "critical slowing down" expected near any critical point. A singular situation occurs in one dimension as the critical point is located at $T = 0$ K. In this case, the enhancement factor, τ/τ_0, is proportional to ξ^2, i.e. the dynamic exponent, z, deduced from the Glauber model is thus $z = 2$[4]. It is interesting to mention that the above expression of the relaxation time can be deduced with very simple arguments (omitting numerical arguments) [23]. Considering the Ising model, the low temperature equilibrium state can be described as large domains of size ξ separated by narrow domain walls. From Eq. 15b, the local field E_i is equal to $4JS^2$ inside a magnetic domain and thus much larger than $k_{\mathrm{B}}T$ at low temperature. The consequence is a very small probability of spin-flip inside the domain. On the other hand, the local field vanishes for a spin of the domain wall and thus this spin can flip with the characteristic time τ_0. The dominant mechanism for the decay of the magnetization at zero field is the random motion of the domain walls behaving like free particles along the chain. One step of this dynamic occurs every τ_0 and according to the diffusion theory [23], the wall moves statistically during $(\xi/a)^2$ steps to cover the distance ξ. Therefore, the characteristic time for this event to occur scales as predicted by Eq. 20.

As we have seen before, several models (like the anisotropic Heisenberg model when D is negative) also predict domain walls at low temperature. For this class of models, the above argument can be applied and Eq. 20 is also valid even if the definition of τ_0 may need to be generalized in the case of broad domain walls. This equation shows that large τ values are essentially obtained when the correlation length increases exponentially at low temperature and therefore explains why the anisotropy is an essential ingredient in order to obtain single-chain magnet behavior.

Models for which n simultaneous spin flips have also been considered [25]. By analogy with the Glauber model, the transition probability for the n-flip

[4] Generally, the dynamic critical exponent z is defined by $\tau \propto \xi^z$.

model is:

$$W_{i,n}(\sigma_i) = \frac{1}{2\tau_{0n}}\left(1 - \frac{\gamma}{2}(\sigma_{i-1}\sigma_i + \sigma_{i+n-1}\sigma_{i+n})\right) . \quad (21)$$

The individual time τ_{0n} is expected to be temperature dependent and a function of n. The parameter γ has the same meaning as for the Glauber model.

The essential result is that the critical behavior (i.e. the dependence upon ξ) is independent of n [25]:

$$\tau_n \propto \tau_{0n}\left(\frac{\xi}{a}\right)^2 . \quad (22)$$

Nevertheless, several competing channels (for different n values) must be considered to describe the relaxation of the magnetization, but the expression of the different times τ_{0n} must be first clarified. In the next paragraph, we will come back to this particular point.

2.3 Towards Real Systems

In the following sections, we will see that even the simplest presently known SCM system can not be considered as a regular ferromagnetic Ising chain. Therefore, some improvements of the previous models are essential to describe experimental magnetic properties.

2.3.1 The Characteristic Time τ_0

As already mentioned, the individual time τ_0 is considered to be an adjustable parameter in the Glauber theory. The same remark can be made for models considering n spin-flip processes. To compare with experimental results, the temperature dependence of this characteristic time should, however, be considered. This discussion has been made for magnetic chains described by the anisotropic Heisenberg model (Eq. 12) and in the large anisotropy limit ($|D/J| > 4/3$) which corresponds to narrow domain walls [26]. As seen in the previous paragraph, τ_0 describes the dynamics of a spin inside a domain wall, where the local field vanishes. Then, the problem is reduced to the flip of a single spin (from $+z$ to $-z$). During this flip, Eq. 12b shows that the spin experiences an energy barrier $\Delta_A = DS^2$. Thus, τ_0 follows an Arrhenius law, i.e. the temperature dependence of τ_0 is given by:

$$\tau_0(T) = \tau_i \exp(\Delta_A/k_B T) , \quad (23)$$

where the pre-factor τ_i describes the intrinsic dynamics of the spin in contact with the thermal bath, in the absence of an energy barrier.

It should be noted that this argument can be generalized for an n spin-flip process. Considering the simultaneous flip of two spins, each of them experiences an energy barrier $\Delta_A = |D|S^2$. The probability to observe this double flip is the square of the probability for a single flip. In other words, the activation energy of the Arrhenius law becomes $2|D|S^2$.

This approach can be easily generalized to the n spin-flip process and therefore the temperature dependence of τ_{0n} is obtained by:

$$\tau_{0n}(T) = \tau_{in} \exp(n|D|S^2/k_B T) \,. \tag{24}$$

At low temperature, the influence of n on τ_{0n} is dominated by the exponential term. Hence, it is interesting to note that Eq. 22 implies that the n spin-flip process is slower than the single spin-flip for an infinite chain.

2.3.2 Non-Regular Chains, the Effective Spin Limit

The theoretical descriptions detailed in the two previous paragraphs have been developed for a regular ferromagnetic chain (i.e. presenting only one exchange interaction J and a single local easy axis along the chain). Unfortunately, as we will see in Sect. 3, chemistry has not succeeded yet in designing this type of simple system exhibiting slow relaxation of the magnetization. Therefore, these theoretical approaches must be generalized to non-regular chains (presenting several exchange interactions J_i) such as those described in Sect. 3.2 that present a structure composed of an assembly of trimers interacting along the chain through a ferromagnetic interaction.

Thermodynamic properties of non-regular chains have been described in reference [27]. In that case, several correlation functions Γ_i should be introduced. Taking the simple example of a chain of spin S with an alternation of J_1 and J_2 magnetic exchanges (i.e. a chain of dimers with J_1 and J_2 being the intra-dimer and inter-dimer interactions, respectively), the corresponding Ising Hamiltonian reads:

$$H = -2J_1S^2 \sum_{-\infty}^{+\infty} \sigma_i s_i - 2J_2S^2 \sum_{-\infty}^{+\infty} s_i \sigma_{i+1} \,, \tag{25}$$

where σ_i and s_i are equal to ± 1. Thus, $\chi T/C$ can still be deduced from the generalization of Eq. 2 ($\vec{u}_i$ being replaced by σ_i or s_i):

$$\frac{\chi T}{C} = \frac{1 + \Gamma_1 + \Gamma_2 + \Gamma_1\Gamma_2}{1 - \Gamma_1\Gamma_2} \,. \tag{26}$$

In the low temperature limit and for J_1 and J_2 positive, the correlation functions are given by $\Gamma_i \approx 1 - 2\exp(-4\beta J_i S^2)$. Thus, Eq. 26 can be approximated

to:

$$\frac{\chi T}{C} \approx \frac{2}{\exp(-4\beta J_1 S^2) + \exp(-4\beta J_2 S^2)} . \tag{27a}$$

When, $0 < J_2 \ll J_1$, an equivalent expression is:

$$\frac{\chi T}{C} \approx 2\exp(4\beta J_2 S^2) . \tag{27b}$$

It is interesting to note the analogy between this last expression and Eq. 9 that highlights the notion of *effective spin*. When $J_1 \gg J_2$, the only populated states at low temperature correspond to $s_i = \sigma_i$. Therefore, the first term of the Hamiltonian (Eq. 21) remains constant and can be omitted. The Hamiltonian becomes:

$$H_{\text{eff}} = -2J_2 S^2 \sum_{-\infty}^{+\infty} \sigma_i \sigma_{i+1} = -2J_{\text{eff}} S_{\text{eff}}^2 \sum_{-\infty}^{+\infty} \sigma_i \sigma_{i+1} , \tag{28}$$

with $S_{\text{eff}} = 2S$ and $J_{\text{eff}} = J_2/4$. This result demonstrates that a dimer unit composed of two S spins strongly coupled by J_1 can be considered as an *effective spin* of size $2S$. Equation 27b can be rewritten as:

$$\frac{\chi T}{C_{\text{eff}}} \approx \exp\left(4\beta J_{\text{eff}} S_{\text{eff}}^2\right) , \tag{29}$$

which gives the expected result for a regular chain of these effective spins (S_{eff}) coupled by J_{eff}[5]. The magnetic correlations and therefore the magnetic susceptibility are thus only controlled by the weakest interaction.

The relaxation of the dimerized chain can also be described by a stochastic approach. Assuming single spin-flips and an alternation of exchange interactions J_1 and J_2 along the chain, one obtains [27, 28]:

$$\tau_1 \propto \tau_{01} \left(\frac{\xi}{a}\right)^{1+|J_1/J_2|} , \tag{30}$$

where it was assumed $|J_1| \geq |J_2|$. Hence, independently of the signs of the exchange interactions, a non-universal dynamic critical exponent z is found. At low temperature and in the ferromagnetic case ($J_1 \gg J_2 > 0$) where the magnetic susceptibility is given by Eq. 27b, the above expression is equivalent to:

$$\tau_1 \propto \tau_{01} \exp(4\beta J_1 S^2 + 4\beta J_2 S^2) . \tag{31}$$

As expected, this expression is equivalent to Eq. 19 when $J_1 = J_2$. It implies that the characteristic time for single spin-flips becomes dramatically long as soon as one of the exchange constants is large. In particular, this is the case if the spins are strongly coupled inside dimers with the J_1 interaction while

[5] Note that the effective Curie constant per site, C_{eff}, is equal to $2C$: quite generally C is proportional to S^2, which brings a factor of 4 from $S_{\text{eff}} = 2S$, but the number of sites becomes divided by 2 and the final multiplicative factor is thus only 2. This remark can be generalized for an effective spin $S_{\text{eff}} = nS$ and the corresponding Curie constant per site will be $C_{\text{eff}} = nC$.

the inter-dimer J_2 interaction is much smaller. However, the competition with double spin-flips (where the two spins of a dimer flip together) should be also considered. For this process, the starting Hamiltonian is given by Eq. 28 and we can apply the result obtained for regular chains, i.e.:

$$\tau_2 \propto \tau_{02} \exp\left(8\beta J_{\text{eff}} S_{\text{eff}}^2\right) \propto \tau_{02} \exp\left(8\beta J_2 S^2\right) . \tag{32}$$

Therefore, two channels of magnetization relaxation are in competition. In order to compare them, the temperature dependence of the two individual times τ_{01} and τ_{02} should be introduced. Considering Eq. 24 (i.e. assuming that both spins in the dimer experience the same energy barrier), one readily obtains the activation energy for τ_1 and τ_2:

$$\Delta_{\tau_1} = 4\left(J_1 + J_2\right) S^2 + |D|S^2 \qquad \text{for single spin-flips} \tag{33a}$$

$$\Delta_{\tau_2} = 8J_2 S^2 + 2|D|S^2 \qquad \text{for double spin-flips} \tag{33b}$$

When J_1 becomes very large, the double spin-flips process becomes the fastest pathway of relaxation. In this limit, the description in terms of effective spin units becomes also relevant for the dynamics and Eq. 33b can be identified to:

$$\Delta_{\tau_2} = 8J_{\text{eff}} S_{\text{eff}}^2 + |D_{\text{eff}}| S_{\text{eff}}^2 . \tag{33c}$$

This argument can be generalized to chains with more complex magnetic units as soon as intra-unit interactions are much stronger that the coupling between units along the chain. In this case, the global flip of the unit effective spin becomes the dominant process for the relaxation of the magnetization. When these units are coupled by a unique ferromagnetic interaction along the chain, the problem is then reduced to the description of a regular ferromagnetic chain as we will see on an experimental system in Sect. 3.2.

2.3.3 Ferrimagnetic Chains

Although the previous sections were essentially devoted to ferromagnetic chains, some of the given arguments can be extended to the ferrimagnetic case. Considering an alternation of two kinds of spins, S_1 and S_2, and an antiferromagnetic exchange interaction, J, the corresponding Hamiltonian in the Ising limit (using the same notations as for Eq. 25) reads:

$$H = -2JS_1S_2 \sum_{-\infty}^{\infty} \left(\sigma_i s_i + s_i \sigma_{i+1}\right) . \tag{34}$$

At low temperature, the chain magnetic structure also consists of large oriented domains separated by domain walls. Their creation energy is now $4|J|S_1S_2$ in the case of a large Ising-like anisotropy (i.e. for narrow domain walls). Whatever is the anisotropy value, we expect an activated behavior of $\ln(\chi T)$ versus $1/T$ with a gap Δ_ξ giving the creation energy of these domain

walls. This means that Eq. 13 is still valid. A detailed theory for the relaxation of the magnetization in the ferrimagnetic case is still missing. However, the physical arguments given in Sect. 2.2 suggest that Eq. 20 can also be used in the ferrimagnetic case.

2.3.4 Finite-Size Effects

As the magnetic correlation length becomes very large at low temperature, even the presence of a very small number of defects on the chain can have a drastic effect. This is particularly true in the Ising case (or for the anisotropic Heisenberg model) where an exponential increase of the correlation length is predicted (vide supra). To understand this phenomenon, we will specifically consider the Ising model assuming the presence of non-magnetic defects breaking the chain into finite magnetic segments. Two different kinds of models have been developed based on a "mono-disperse" and "poly-disperse" description of the chain length.

2.3.4.1 Finite-Size Effects in the "Monodisperse Approximation"

As a first approach, all the chain segments can be considered to possess the exact same length. Within this "mono-disperse" description and considering an open uniform chain of n sites, the magnetic susceptibility per site can be calculated (with the notations of Eq. 7) [29]:

$$\frac{\chi_n T}{C} = \exp\left(4\beta JS^2\right)\left(1 - \frac{2\Gamma(1-\Gamma^n)}{n(1-\Gamma^2)}\right) . \tag{35a}$$

In the ferromagnetic case ($J > 0$), the low temperature expression of Γ can be used ($\Gamma \approx 1 - 2\exp(-4\beta JS^2)$) which implies (for $n \gg 1$):

$$\frac{\chi_n T}{C} = \exp\left(4\beta JS^2\right)\left(1 - \frac{1-\exp(-2n\exp(-4\beta JS^2))}{2n\exp(-4\beta JS^2)}\right) . \tag{35b}$$

This expression leads to a crossover of $\chi_n T/C$ when $2n\exp(-4\beta JS^2) \approx 1$, i.e. for $n \approx \xi/a$, between the exponential regime expected for the infinite chain and a new regime at lower temperature where $\chi_n T/C \approx n$. Below the crossover temperature, all the spins are parallel within a segment which can be seen as an effective spin of size nS. The response of these segments is then a Curie law with the Curie constant per site equal to nC.

A small number of defects can also have a drastic effect on dynamics at low temperature, when the correlation length becomes very large. The problem of finite size scaling has been discussed by J.H. Luscombe et al. in the frame of the single-spin-flip Glauber model [30]. For an open chain of size $L = na$ (with

a being the cell parameter of the chain), the relaxation time becomes:

$$\tau = \tau_\infty f(L/\xi) \tag{36}$$

where ξ and τ_∞ are the correlation length and the relaxation time (given by Eq. 20) for the infinite chain. The function f can be obtained numerically as shown by J.H. Luscombe et al. [30]. When ξ becomes much larger than L, $f(x) \approx x/2$ and the low temperature relaxation time is:

$$\tau = \frac{\tau_0 L}{2a} \exp(4\beta JS^2) \,. \tag{37}$$

As for the magnetic susceptibility, a crossover is expected for $L \approx \xi$. Below the temperature of this crossover, magnetic correlations still give a contribution to the relaxation time but the corresponding enhancement factor is now proportional to ξ (while it was in ξ^2 in the high temperature regime, Eq. 20). Following this model, the magnetization still relaxes exponentially in this finite-size regime.

As for the infinite chain, a simple physical argument supports this result [27]. In this low temperature regime, spin-flips are expected to occur essentially at the ends of the finite segment with a probability proportional to $\exp(-4\beta JS^2)$. Moreover, the probability for the domain wall to reach the other side of the chain segment instead of being destroyed is $1/(N-1) \approx 1/N$. Then, $1/\tau$ is proportional to the joint probability for the creation and propagation of a domain wall [31], in agreement with Eq. 37. As for the high temperature regime, Eq. 37 may be presented in a more general form valid for any Ising-like model:

$$\tau = \frac{\tau_0 \xi L}{a^2} \,. \tag{38}$$

Finally, n spin flip processes can also be considered. In the case of short chains, a collective reversal of the magnetization has also been discussed [31]. In this latter case, the interaction between magnetic units plays no role and the result is simply, for a segment of n magnetic sites:

$$\tau = \tau_{0n} \,. \tag{39}$$

Note, however, that this collective reversal can be ignored in the Ising limit (when $|D| \gg J$). In fact, the activation energy deduced from Eq. 39 ($n|D|S^2$) is always larger in this limit than the one resulting from Eq. 38 ($4JS^2 + |D|S^2$), even for small values of n.

2.3.4.2 Finite-Size Effects in the "Poly-Disperse Approximation"

The ideal image of perfectly mono-disperse segments is probably far from reality even if for most of the systems, this approach might be enough to describe the observed magnetic properties. Nevertheless, when this is not

the case, "poly-dispersity" on the segment size can be introduced. In this frame, two new adjustable parameters must be considered: (i) the concentration of defects and (ii) the statistics to distribute these defects along the chain. Two types of spatial defect distributions have been described in the literature respectively called *annealed* and *quenched* limits [32]. True thermal equilibrium is assumed in the *annealed* case, while defects are randomly distributed in the *quenched* limit. Discussing SCM systems, we expect that the existing defects are created during the synthesis and therefore randomly distributed along the chains without the possibility of annealing. Hence, the *quenched* limit has been adopted to describe SCMs. Nevertheless, there are still two approaches to describe the introduction of defects, called respectively *site* and *bond* models where either non-magnetic sites (bearing no spin) or non-magnetic bonds (with $J = 0$) are considered [32]. Introducing the probability c of finding a defect (respectively a diamagnetic site or a non-magnetic bond), both models give an average value of the site number per segment[6], $< n >$, equal to $2/c$. Moreover, the average magnetic susceptibility per site, $< \chi >$, can be calculated from:

$$< \chi > = \frac{1}{N} \sum_{n=1}^{\infty} n < \nu(n) > \chi_n \,, \tag{40}$$

where χ_n is the susceptibility per site (N being the total number of sites for the system) for an open chain of size n and $< \nu(n) >$ the average number of open chains of size n. For regular chains, and when the concentration of defects is small, both the site and bond models give [32, 33]:

$$\frac{< \chi > T}{C} = \frac{1 + (1 - c)\Gamma}{1 - (1 - c)\Gamma} \,. \tag{41}$$

For ferromagnetic interactions, an approximate expression can be deduced at low temperature:

$$\frac{< \chi > T}{C} \approx \frac{2}{c + 2\exp(-4\beta JS^2)} \,. \tag{42}$$

As for the mono-disperse case, a crossover is predicted, when $< n > \exp(-4\beta JS^2) \approx 1$. Below the crossover, $< \chi > T/C \approx 2/c = < n >$. Figure 2 compares the prediction of the mono-disperse and poly-disperse models, for $n = 100$ and $< n > = 2/c = 100$, respectively. As very similar $< \chi > T/C$ vs. $2\beta JS^2$ plots are found, it is clear that the magnetic susceptibility cannot be used to discriminate between the two descriptions.

[6] As shown in [32], the average number of size n segment, $< \nu(n) >$, can be estimated in the thermodynamic limit: $< \nu(n) > = N(1 - p)^2 p^n$ and $< \nu(n) > = N(1 - b)^2 b^{n-1}$ for the site and bond model respectively (p and b are respectively the probability of finding a diamagnetic site or a missing bond on the chain of N sites). Introducing the probability of finding a defect, i.e. $c = 1 - p$ or $c = 1 - b$ to describe respectively the site and bond problems, one obtains the probability that a site belongs to a chain of size N. When c is small and n in the thermodynamic limit, $p(n) = nc^2(1 - c)^{n-1}$ and $< n > = \sum_{n=1}^{\infty} np(n) \approx \frac{2}{c}$ in both cases.

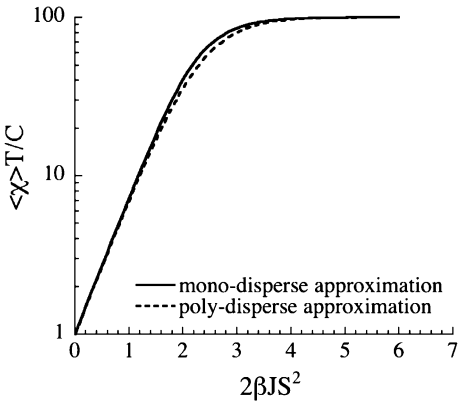

Fig. 2 $< \chi > T/C$ vs. $2\beta JS^2$ plots for the mono-disperse and poly-disperse models taking $n = 100$ and $< n > = 2/c = 100$, respectively

The effect of disorder on the relaxation has also been discussed using a poly-disperse model [34]. In particular, the relaxation of the magnetization has been studied for the *bond* model, i.e. when diamagnetic bonds are introduced with a probability *c*. This poly-disperse description preserves the existence of the crossover described by J.H. Luscombe et al. The essential difference is the time dependence of the relaxation below the crossover temperature. Except at very short or very long times, the decay of the magnetization, $m(t)$, is now given by Eq. 43 (using the notations of Eqs. 36 and 37, where L is now the average chain length):

$$\ln m(t) = -\, t/\tau_\infty - 2\sqrt{t/\tau}\,. \tag{43}$$

Below the crossover temperature, the square root term becomes dominant and the relaxation of the magnetization is no longer exponential. In contrast with the magnetic susceptibility, the mono-disperse and poly-disperse models predict qualitatively different dynamic behaviors. However, the dominant characteristic time τ is still given by Eqs. 37 or 38.

2.4 Concluding Theoretical Remarks

To conclude on this theoretical part dedicated to the SCM behavior, the most important points are summarized in the following paragraph.

For infinite chains, an activated correlation length, ξ, is predicted at low temperature for the Ising model (see Sect. 2.1.2) but also for any anisotropic model which favors an easy axis (like the anisotropic Heisenberg model, see Sect. 2.1.3). All these models are usually classified as "Ising-like". This particular temperature dependence of the correlation length is the result of the low temperature magnetic ground state: large magnetic oriented domains

of average size 2ξ separated by domain walls (Fig. 1). The consequence is a linear variation of $\ln(\chi T)$ vs. $1/T$ which can be probed experimentally. The corresponding slope, Δ_ξ, gives the creation energy for a domain wall along the chain independently of the domain wall structure which depends on the anisotropy value. Taking the example of the anisotropic Heisenberg model, we have shown that a threshold between narrow and broad domain wall regimes occurs for $\Delta_A = 4J_I/3$ (where J_I and Δ_A are introduced in Eqs. 7b and 23). More generally, these two situations are expected for $\Delta_A \gg J_I$ and $\Delta_A \ll J_I$, respectively. In the first case, $\Delta_\xi = 2J_I$ (or $\Delta_\xi = 4JS^2$ using the notations of Eq. 7a), i.e. the structure and the formation energy of the domain walls are identical to the Ising model. To emphasize this point, the regime where narrow domain walls are obtained is sometimes qualified as the "Ising limit". In the latter case ($\Delta_A \ll J_I$), a more complex expression of Δ_ξ is predicted which depends on both the exchange and anisotropy energies.

For an infinite chain, the relaxation time (τ) of the magnetization is activated with the corresponding energy gap (Δ_τ) expressed as a function of Δ_A and Δ_ξ. The difference between Δ_A and the total activation energy of τ describes the effect of the magnetic correlations. For the infinite chain, the expression of Δ_τ is:

$$\Delta_\tau = \Delta_A + 2\Delta_\xi \,. \tag{44}$$

As this expression only relies on the temperature dependence of the magnetic correlations, Eq. 44 is valid for any Ising-like chain independently of the domain wall structure. More specifically, in the case of narrow domain walls and for single-ion anisotropy this expression becomes (using the notations of Eqs. 7a and 23):

$$\Delta_\tau = |D|S^2 + 8JS^2 \,. \tag{45}$$

At lower temperature, when defects become relevant, we expect a saturation of the correlation length and therefore of the χT product (Fig. 2). Similarly, the general expression of Δ_τ becomes:

$$\Delta_\tau = \Delta_A + \Delta_\xi \,. \tag{46}$$

For narrow domain walls and for single-ion anisotropy, Eq. 46 is:

$$\Delta_\tau = |D|S^2 + 4JS^2 \,. \tag{47}$$

The above expressions show that the key analysis of a single-chain magnet system is the comparison between susceptibility and relaxation data. In fact, the observation of an activated relaxation time is not characteristic of SCM behavior (a similar behavior is obtained for other systems like SMMs) and a discussion based only on the dynamic data remains highly ambiguous. The situation is different if the thermodynamic and dynamic properties are compared as Δ_ξ can be deduced from susceptibility data and then considered to

discuss the relaxation time and to estimate Δ_A. Independently, this energy can be determined (i) from the study of isolated magnetic units composing the chain; or (ii) from direct measurements on a single crystal of the chain compound, i.e. from the field dependence of the magnetization when a magnetic field is applied perpendicular to the easy axis. A detailed comparison of these data leaves no arbitrary parameter and allows an unambiguous analysis of single-chain magnet materials.

3
Experimental SCM Systems

3.1
First Evidence of Slow Relaxation in a 1D System

Surprisingly, the first evidence of slow relaxation in a one-dimensional compound was reported only in 2001 by the group of D. Gatteschi [35]. Far from the prototype 1D topology imagined by Glauber, this compound is composed of "ferrimagnetic" chains: $Co^{II}(hfac)_2(NITPhOMe)$ (hfac = hexafluoroacetylacetonate, NITPhOMe = 4′-methoxy-phenyl-4,4,5,5-tetramethylimidazoline-1-oxyl-3-oxide), where $Co(hfac)_2$ and NITPhOMe radical moieties are alternately arranged in a helical chain (Fig. 3a) [35, 36]. In an octahedral coordination sphere, Co^{II} metal ions can be considered as an effective $S = 1/2$ spin with highly anisotropic g values. The strong uniaxial anisotropy of the Co^{II} ions has been studied in $Co^{II}(hfac)_2(NITPhOMe)$ by single crystal susceptibility experiments [35] and also on related complexes: $Co^{II}(hfac)_2(NITPhOMe)_2$ by EPR spectroscopy and susceptibility measurements on single crystals [37]. Therefore, the antiferromagnetic alternating arrangement of Co^{II} and NITPhOMe radical ($S = 1/2$ and $g \approx 2$) leads to a non-compensation of the magnetic moments, i.e. a "ferrimagnetic" chain.

The exchange interaction between Co^{II} and the NITPhOMe radical has been estimated by several models [35, 37, 40] with the more reliable value being around $2JS_1S_2/k_B = -90$ K [38, 39] (using Eq. 34). The helical arrangement of the cobalt local anisotropy tensors leads to a complex magnetic behavior involving step features in the field dependence of the magnetization (Fig. 3b) [35, 40]. This particular behavior has been qualitatively modeled by Vindigni et al. and attributed theoretically to the proximity of a disorder point [41]. In the vicinity of this point, they also conclude there is a vanishing of the correlation length while the energy gap of the relaxation time remains finite. In other words, they argue that the Eq. 20 is no longer valid in this special case. Nevertheless, independently of this complicated structural arrangement, the correlation length of the system exponentially increases above 25 K as seen on the $\ln(\chi T)$ vs. T^{-1} plot (Fig. 3c) with an energy gap of

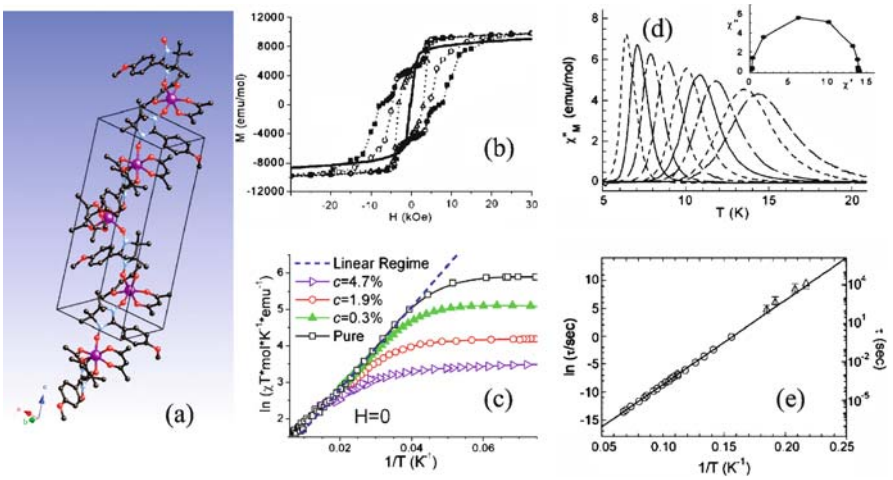

Fig. 3 **a** View of the helical chain in $Co^{II}(hfac)_2(NITPhOMe)$ (Co: in *purple*, C: in *black*, N: in *blue*, O: in *red*) adapted from [36]. For the sake of clarity, the hydrogen and fluorine atoms have been omitted. **b** Hysteresis loops recorded on a single crystal applying the field in the a^*b plane (*solid line*) at 2 K and along the chain axis at 2.0 K (■), 3.5 K (○) and 4.5 K (△). Reprinted with permission from [40]. Copyright 2002, EDP Science. **c** $\ln(\chi T)$ vs. $1/T$ scaling plot, the *dashed line* evidences the linear behavior observable between 55 and 25 K. All data were taken in zero dc field and at an ac field frequency of 27 Hz on iso-oriented crystals along the *c* axis. Measurements were taken for different concentrations of the Zn^{II} dopant: (□) represent the undoped sample, (▲) C = 0.3%, (○) C = 1.9%, (△) C = 4.7%. Reprinted with permission from [38]. Copyright 2005, APS. **d** Temperature dependence of the imaginary component of the ac susceptibility measured in zero static field and with an ac field oscillating parallel to the *c* axis for frequencies ranging from 0.18 Hz to 95 kHz. *Inset*: Cole–Cole plot measured at 10 K. Reprinted with permission from [40]. Copyright 2002, EDP Science. **e** $\ln(\tau)$ vs. $1/T$ plot. The *solid line* represents the fit to the Arrhenius law. Reprinted with permission from [40]. Copyright 2002, EDP Science

$\Delta_\xi/k_B = 117$ K [38]. As explained in the theoretical section of this paper, these results highlight the presence of uni-axial anisotropy in this one-dimensional compound. At low temperature, slow relaxation of the magnetization is observed as seen by the hysteresis loops displayed in Fig. 3b and by the ac measurements shown in Fig. 3d [35, 40]. The characteristic time of relaxation has been studied using different techniques: ac susceptibility [35, 40], μ-SQUID magnetometer [42], ^{1}H nuclear magnetic resonance (NMR) [43, 44] and muon spin rotation (μSR) [44]. This relaxation time follows an Arrhenius law with a gap $\Delta_\tau/k_B = 153 \pm 2$ K and a pre-exponential factor of $3(\pm 2) \times 10^{-11}$ s [35, 40]. Moreover, no crossover is observed in the temperature range experimentally available. It is worth noting that NMR and μSR measurements have demonstrated the existence of a second relaxation time faster than the one observed on the ac susceptibility and on the magnetization decay. The

two modes have been tentatively assigned to the magnetization relaxation of the two different sub-lattices composed of Co^{II} and radical spins [43, 44]. As the energy gap of the relaxation time is smaller than $2\Delta_\xi$, the dynamic measurements are clearly made in the regime where the finite-size effects (see Sect. 2.3.3) are relevant even in the pristine $Co^{II}(hfac)_2$(NITPhOMe) material. This result is further supported by the fact that the relaxation time has been measured in the temperature domain where the $\ln(\chi T)$ vs. $1/T$ plot is saturated (Fig. 3c). Controlled introduction of further defects has been done by doping the system by diamagnetic Zn^{II} metal ions [38, 39, 45]. Detailed static (Fig. 3c) and dynamic properties of the doped materials have been investigated and understood invoking a collective relaxation mode of the magnetic segments [31]. Despite the complexity of this system, we may still try to use the general arguments given in Sect. 2.4. As relaxation data are taken in the low temperature regime, the activation energy Δ_A should be deduced from Eq. 38, $\Delta_A/k_B = (\Delta_\tau - \Delta_\xi)/k_B \approx 36$ K. Therefore, as $2|J|S_1S_2 > \Delta_A$, the system seems to be far from the Ising limit and large domain walls are then expected. This conclusion is also in agreement with the occurrence of collective spin reversal which cannot exist in the Ising limit (see Sect. 2.3.3.1).

3.2 Simple Ferromagnetic-Like SCMs

3.2.1 $[Mn_2(saltmen)_2Ni(pao)_2(L)_2](A)_2$ SCM Compounds

In 2002, a new 1D compound $[Mn_2(saltmen)_2Ni(pao)_2(py)_2](ClO_4)_2$ (saltmen^{2-} = *N*,*N*′–(1,1,2,2-tetramethylethylene) bis(salicylideneiminate), pao$^-$ = pyridine-2-aldoximate, py = pyridine) [8] was synthesized and can be considered to be an isolated chain of ferromagnetically coupled anisotropic $S = 3$ units. Packing diagrams of this compound are given in Fig. 4a–c to highlight the parallel arrangement of the chain and also their good magnetic isolation (without $\pi - \pi$ stacking or hydrogen bonding...). Moreover, the asymmetric unit contains only one Mn^{III} moiety leading by symmetry to an easy axis of magnetization along the chain direction. Fitting of the susceptibility above 30 K was achieved using a Heisenberg model considering a one-dimensional arrangement of $[Mn^{III} \cdots Ni^{II} \cdots Mn^{III}]$ trimer with $Ni^{II} \cdots Mn^{III}$ antiferromagnetic interaction ($J/k_B = -21$ K) connected through weak ferromagnetic interactions between the trimers (treated in the frame of a mean field approximation, $J'/k_B = +0.7$ K) [8]. Therefore, at low temperature, this compound can be described as an assembly of isolated chains of ferromagnetic coupled $S = 3$ $[Mn^{III} \cdots Ni^{II} \cdots Mn^{III}]$ units. As shown by oriented single-crystal measurements, the susceptibility becomes very anisotropic below 60 K [8]. Above 6 K (Fig. 4d), the exponential increase of the $\ln(\chi T)$ vs. $1/T$ plot further confirms the one-dimensional nature of

the system and its Ising-like magnetic anisotropy [26]. The deduced energy gap is $\Delta_\xi/k_B = 28$ K in good agreement with the inter-trimer interaction obtained at high temperature ($J'/k_B \approx +0.77$ K). Below 5 K, the $\ln(\chi T)$ vs. $1/T$ plot shows a saturation as expected in the presence of finite-size effects when $\xi \gg L$ (Fig. 4d). The fit of the data (solid line, Fig. 4d) using the generalization of Eq. 35a for weakly interacting segments (inset of Fig. 4h) leads to a chain length of about 110 units or $L \approx 140$ nm [26].

At low temperatures, slow relaxation of the magnetization is detected as shown on Figs. 4e and 4f. When the magnetic field is applied in the easy direction, large field hysteresis loops of the magnetization are observed with a coercive field reaching up to 2.75 T below 0.4 K [46]. Applying the magnetic field perpendicular to the easy axis (Fig. 4g), the magnetization follows linear field dependence at low fields before saturation at higher fields as expected in the presence of a uni-axial anisotropy. An anisotropy field of 11.0 T is deduced from these data which gives $D/k_B = -2.5$ K for the $[Mn^{III}\cdots Ni^{II}\cdots Mn^{III}]$ units and therefore $\Delta_A = 23$ K [26]. It is interesting to note that the magnetic properties of the isolated $[Mn^{III}\cdots Ni^{II}\cdots Mn^{III}]$ unit has been also studied on two related compounds: $[Mn_2(5\text{-Rsaltmen})_2Ni(pao)_2(phen)](ClO_4)_2$ (where R is Cl or Br and phen is the 1,10-phenanthroline) [47]. These $S = 3$ complexes display SMM behavior and a D value ($D/k_B = -2.3$ to -2.4 K) close to the estimation made for the tri-nuclear units of the chain compound.

The magnetization relaxation time of $[Mn_2(saltmen)_2Ni(pao)_2(py)_2](ClO_4)_2$ has been studied using combined ac (temperature and frequency dependences of the ac susceptibility) and dc (time relaxation of the magnetization, inset Fig. 4h) measurements [8, 26]. The resulting temperature dependence of the relaxation time, displayed in Fig. 4h, exhibits a crossover at 2.7 K between two activated regimes. Above and below 2.7 K, the energy gaps are $\Delta_{\tau 1}/k_B \approx 74$ K ($\tau_0 = 3.5 \times 10^{-11}$ s) and $\Delta_{\tau 2}/k_B \approx 55$ K ($\tau_0 = 2.5 \times 10^{-8}$ s), respectively [26]. This crossover has been attributed to the effects of the chain finite-size as already observed on the susceptibility measurements (Fig. 4d). The experimental energy gaps are in very good agreement with theoretical ones ($\Delta_{\tau 1}/k_B \approx 79$ K and $\Delta_{\tau 2}/k_B \approx 51$ K) deduced from the energy parameters of the system ($\Delta_A/k_B \approx 23$ K and $\Delta_\xi/k_B = 28$ K) and Eqs. 44 and 46. The effects of poly-dispersity and weak inter-segment or inter-chain interactions have been invoked to explain the difference of crossover temperature observed on the susceptibility (5 K) and the relaxation time (2.7 K) [26].

In the past 5 years, a rational synthetic approach has been developed to obtain SMM and SCM systems [48]. This research project has led to a complete family of SCM compounds related to the original SCM compound described above: $[Mn_2(saltmen)_2Ni(pao)_2(L)_2](A)_2$ ($A^- = ClO_4^-$ with L = 4-picoline, 4-*t*-butylpyridine, or *N*-methylimidazole; and L = pyridine with $A^- = BF_4^-$, PF_6^- or ReO_4^-) [46]. The magnetic properties of these compounds have been studied in details highlighting a similar SCM behavior of these heterometallic chains independently of their inter-chain environments.

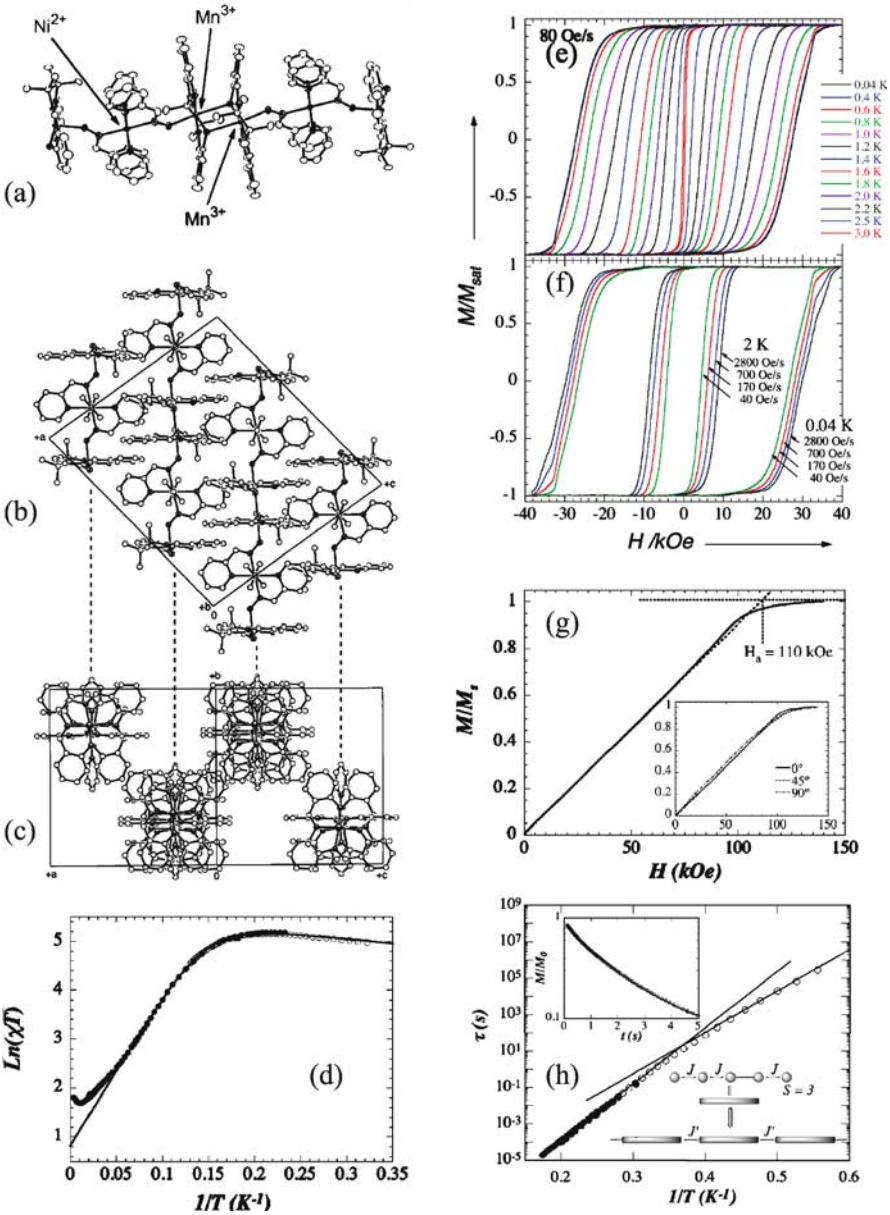
Ni2+
Mn3+
Mn3+
(a)
(b)
(c)
(d)
Ln(χT)
1/T (K-1)
(e)
80 Oe/s
0.04 K
0.4 K
0.6 K
0.8 K
1.0 K
1.2 K
1.4 K
1.6 K
1.8 K
2.0 K
2.2 K
2.5 K
3.0 K
(f)
M/Msat
2 K
2800 Oe/s
700 Oe/s
170 Oe/s
40 Oe/s
0.04 K
2800 Oe/s
700 Oe/s
170 Oe/s
40 Oe/s
H /kOe
(g)
M/Mt
Ha = 110 kOe
0°
45°
90°
H (kOe)
(h)
τ (s)
M/M0
t (s)
J
J
J
S = 3
J'
J'
1/T (K-1)

◀ **Fig. 4** Views of $[Mn_2(saltmen)_2Ni(pao)_2(py)_2](ClO_4)_2$ showing **a** the hetero-metallic chain **b** the projection in the *ac* plane and **c** the projection along the chain axis. Hydrogen atoms and perchlorate ions located between chains are omitted for clarity. Reprinted with permission from [8]. Copyright 2002 American Chemical Society. **d** Semi-log plot of χT vs. $1/T$. Reprinted with permission from [26]. Copyright 2004 American Physical Society. **e** M vs. H plots at different temperatures and **f** at 2 K and 0.04 K at different field sweep rates measured on a single crystal in the easy direction. Reprinted with permission from [46]. Copyright 2003 American Chemical Society. **g** M vs. H plots when the magnetic field is applied perpendicular to the easy axis at 1.5 K. *Inset:* Similar measurements than the main figure at three angles in the plane normal to the easy axis. The main figure is at $\theta = 0°$. Reprinted with permission from [26]. Copyright 2004 American Physical Society. **h** Semi-log plot of τ vs. $1/T$. The *full and open dots* were obtained from ac and dc measurements, respectively. *Inset:* Relaxation of the magnetization at 3 K and schematic view of the magnetic interactions. Reprinted with permission from [26]. Copyright 2004 American Physical Society

3.2.2 The $(NEt_4)[Mn_2(5\text{-}MeOsalen)_2Fe(CN)_6]$ System

In 2005, a new cyano-based single-chain magnet system: $(NEt_4)[Mn_2(5\text{-}MeOsalen)_2Fe(CN)_6]$ [where 5-MeOsalen^{2-} is *N*,*N*′–ethylethylene bis(salicylideneiminate)] has been reported illustrating a step-by-step strategy to design SCMs by coupling ferromagnetically SMMs in one-dimension [49]. Although many examples of architectures built from Mn^{III}/salen building blocks and hexacyanometalate are known to date [50–59], $(NEt_4)[Mn_2(5\text{-}MeOsalen)_2Fe(CN)_6]$ constitutes the first example of SCM behavior in this family of materials.

This compound was synthesized arranging the trinuclear $[Mn^{III}(SB) - NC - Fe^{III} - CN - Mn^{III}(SB)]$ motif into a one-dimensional assembly (Fig. 5a) well separated by $[NEt_4]^+$ counter-cations. Down to 10 K, the susceptibility was fitted to a Heisenberg model considering a one-dimensional arrangement of $[Mn^{III}\cdots Fe^{III}\cdots Mn^{III}]$ trimer with $Fe^{III}\cdots Mn^{III}$ ferromagnetic interaction ($J/k_B = +6.5$ K) connected through weak ferromagnetic interactions between the trimers (treated in the frame of a mean field approximation, $J'/k_B = +0.07$ K). Considering that $J \gg J'$, this 1D system can be viewed at low temperature as a chain of ferromagnetically coupled $S = 9/2$ units. To probe the magnetic characteristics of the constitutive $S = 9/2$ trinuclear unit, the magnetic properties of the trimer complex: $(NEt_4)[Mn_2(salmen)_2(MeOH)_2Fe(CN)_6]$ [where salmen^{2-} is *N*,*N*′–(methylethylethylene) bis(salicylideneiminate)] [54] has been reinvestigated demonstrating its SMM behavior and estimating its uni-axial anisotropy ($D/k_B = -1.3$ K) [49]. As expected for a 1D system with Ising-like anisotropy, the $\ln(\chi T)$ vs. $1/T$ plot for the chain compound increases exponentially at low temperatures (Fig. 5b). The obtained energy gap ($\Delta_\xi/k_B = 6.1$ K) confirms the magnitude of the inter-trimer interaction ($J'/k_B \approx +0.08$ K). Below 1.4 K, the saturation of $\ln(\chi T)$ reveals the

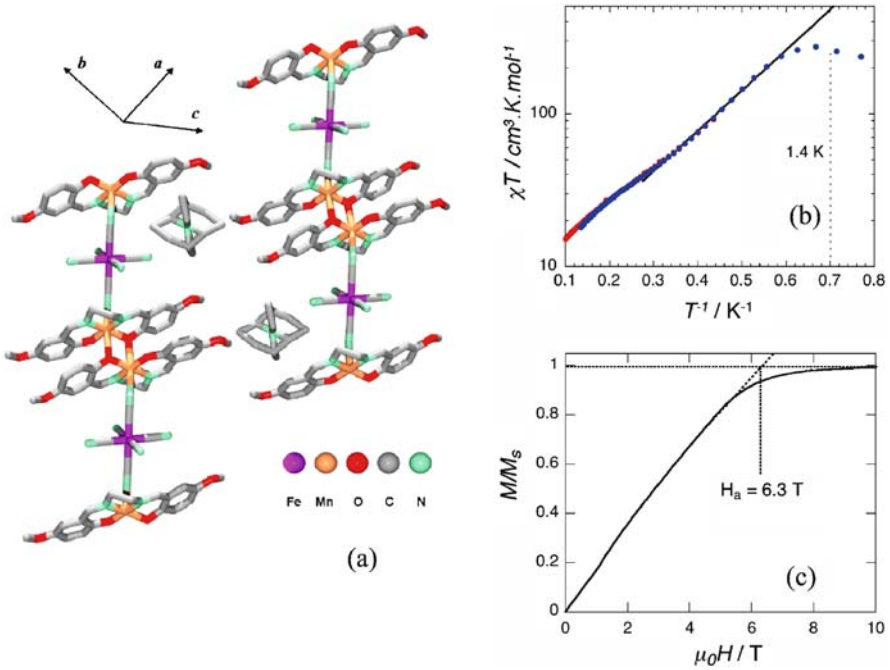

Fig. 5 **a** View of the crystal structure of $(NEt_4)[Mn_2(5-MeOsalen)_2Fe(CN)_6]$ showing the hetero-metallic chain. **b** Semi-log plot of χT vs. $1/T$ (where χ is the zero-field susceptibility). *Red and blue dots* have been obtained with ac (0.1 Hz, 0.3 mT of ac field modulation) and dc (numerical derivative of M vs. H plots around zero dc field) techniques, respectively. **c** Field dependence of the normalized magnetization (M/M_s) as a function of a magnetic field applied perpendicular to the chain direction (in the hard plane), measured on a single crystal at 1.5 K. Reprinted with permission from [49]. Copyright 2005 American Chemical Society

presence of finite-size effects expected when $\xi \gg L$ (Fig. 5b) with a chain length of about 40 units or $L \approx 55$ nm [49]. Applying the magnetic field in the easy direction, large field hysteresis loops of the magnetization have been observed below 1.4 K in agreement with the presence of magnetization slow relaxation (the coercive field reaching 0.36 T at 0.04 K with a field sweep rate of 0.14 T/s). The magnetization measured at 1.5 K when the magnetic field is applied perpendicularly to the easy axis (Fig. 5c), is almost isotropic and confirms the presence of a uni-axial anisotropy. In this hard plane, the magnetization increases linearly with the magnetic field before saturation around 6.3 T. This field corresponds to $D/k_B = -0.94$ K for the $[Mn^{III}\cdots Fe^{III}\cdots Mn^{III}]$ units and therefore to $\Delta_A = 19$ K. It is interesting to note that the magnitude of the uni-axial single-ion anisotropy parameter is in agreement with the value deduced for the isolated trimer complex: $(NEt_4)[Mn_2(salmen)_2(MeOH)_2Fe(CN)_6]$.

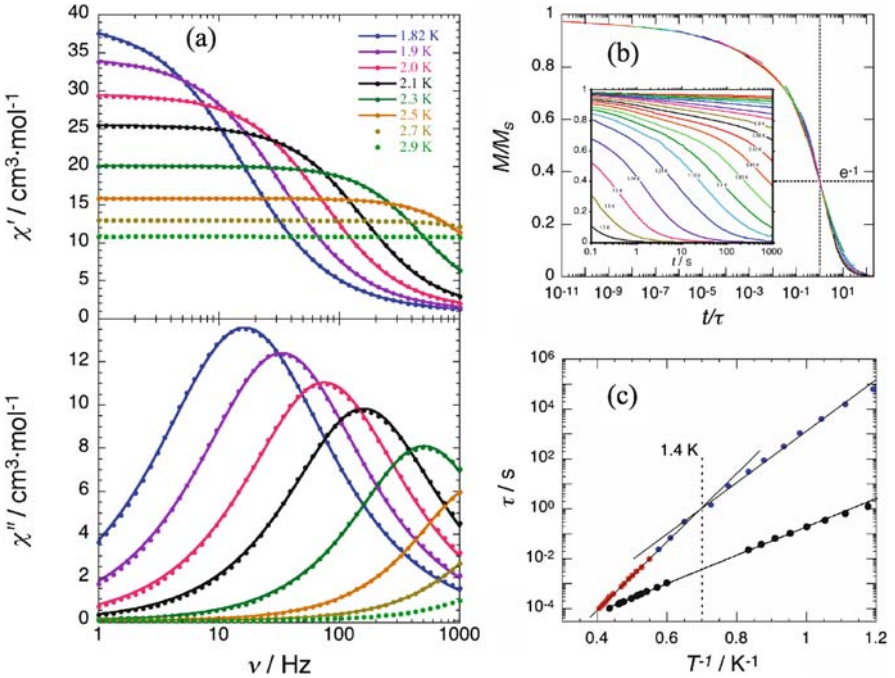

Fig. 6 **a** Frequency dependence of the real (χ') and imaginary (χ'') parts of the ac susceptibility for $(NEt_4)[Mn_2(5-MeOsalen)_2Fe(CN)_6]$ measured between 1.82 and 2.9 K. The *solid lines* are the best fits obtained with the generalized Debye model. All data have been well simulated with small α values of less than 0.06. **b** Single-crystal relaxation measurements: scaling plot of M/M_s vs. t/τ. *Inset:* Single-crystal relaxation measurements plotted as M/M_s vs. t curves. **c** Relaxation time (τ) versus $1/T$ plot for $(NEt_4)[Mn_2(salmen)_2(MeOH)_2Fe(CN)_6]$ (*black dots*) and $(NEt_4)[Mn_2(5-MeOsalen)_2Fe(CN)_6]$ deduced from ac (*red dots*) and dc (*blue dots*) measurements. Reprinted with permission from [49]. Copyright 2005 American Chemical Society

As for the previous example described in Sect. 3.2.1, the relaxation of the magnetization has been studied using combined ac (Fig. 6a) and dc (Fig. 6b) measurements. In order to extract the relaxation time of the system (τ), the obtained frequency dependence of the in-phase χ' and out-of-phase χ'' susceptibilities and furthermore the Cole–Cole plots (χ'' vs. χ' plot) were fitted simultaneously to a generalized Debye model (solid lines in Figs. 6a and 6b). The fact that the found α parameters of this model are less than 0.06, indicates that the system is close to a pure Debye model with hence a single relaxation time. This indication is confirmed by the quasi-exponential decay of the magnetization observed between 1.8 and 0.8 K (Fig. 6b).

Combining these two techniques, an experimental relaxation time of the magnetization has been obtained (Fig. 6c). It is first very interesting to note on Fig. 6c that the thermal variations of the relaxation time observed for the

chain compound and for the tri-nuclear complex composing the chain are completely different and attest that the exchange coupling between the SMM trimers dramatically influences the relaxation of the magnetization. Interestingly, two activated regimes (with the following characteristics: $\Delta_{\tau 1}/k_B \approx 31$ K/$\tau_0 = 3.7 \times 10^{-10}$ s and $\Delta_{\tau 2}/k_B \approx 25$ K/$\tau_0 = 3 \times 10^{-8}$ s) have been identified with a crossover temperature of about 1.4 K in perfect agreement with the saturation the $\ln(\chi T)$ vs. $1/T$ plot (Fig. 5b) and the presence of finite-size chain effects. In both regimes, the energy parameters of the system $\Delta_A/k_B \approx 19$ K and $\Delta_\xi/k_B \approx 6.1$ K used in the Eqs. 44 and 46 ($\Delta_{\tau 1}/k_B = 31.2$ K and $\Delta_{\tau 2}/k_B = 25.1$ K are obtained) reproduce very well the experimental energy gaps of the relaxation time.

Chronologically $(NEt_4)[Mn_2(5\text{-MeOsalen})_2Fe(CN)_6]$ is the second example of a system that exhibits a SCM behavior with the two relaxation regimes: (i) above the crossover temperature, the chain can be considered as infinite ($\xi \ll L$) and introducing a finite anisotropy, the observed relaxation can be understood in the frame of Glauber's theory; (ii) while below the crossover temperature, the chains must be viewed as finite objects ($\xi \geq L$) and finite-size effects become relevant to describe the relaxation. To date, the two families of materials reviewed in Sect. 3 seems to be the simplest systems known to study single-chain magnet behavior. Three important advantages can be mentioned: (i) each chain is structurally and magnetically well isolated by the counter anions and bulky ligands, which precludes a magnetic order; (ii) the local easy axes of the chain repeating units are all parallel to the unique chain orientation; and (iii) the magnetic anisotropy can be easily modeled by a single-ion term while staying larger than the intra-chain interaction ($\Delta_A > 4J_I/3$ or $\Delta_A > 2\Delta_\xi/3$). In this regard, these chains, composed of ferromagnetically coupled anisotropic units, are the archetype that we had of a Glauber Ising-type chain and hence supplies us with simple experimental systems to model the magnetic dynamics in one-dimension.

3.3 Other Known SCM Systems

Since 2001, only a few examples of material exhibiting single-chain magnet behavior have been reported. In addition to chains of ferromagnetically coupled Ising spins (Sects. 3.2, 3.3.1.2 and 3.3.1.3), different types of system have been identified that lead to SCM properties: helical ferromagnetic chains (Sect. 3.3.1.1), double "zig-zag" ferromagnetic chains (Sect. 3.3.1.4), ferrimagnetic chains (Sects. 3.1 and 3.3.2) and canted-antiferromagnetic chains (Sect. 3.3.4). It is worth noting that in most of these systems the anisotropy has been introduced using Co^{II} or Mn^{III} metal ions known to possess a large uni-axial anisotropy. Recently, two original approaches have been employed to introduce anisotropy into one-dimensional systems using the easy-plane

magnetic anisotropy of Fe^{II} ions and the large uni-axial anisotropy of rare-earth metal ions. The compounds obtained with these ingredients will be presented in Sects. 3.3.2.2 and 3.3.3, respectively. In most cases, magnetic properties of the claimed SCM materials have been analyzed only from the dynamic side studying the relaxation time of the magnetization. As explained in the theoretical part of this review, this monolithic view (without a detailed study of the static data) does not clearly answer the question: "Is the observed slow relaxation of the magnetization derived from SCM behavior?". Nevertheless, we would like to review here a hopefully exhaustive list of the compounds that have been labeled SCM materials in the past 3 years.

3.3.1
Chains of Ferromagnetically Coupled Units

3.3.1.1
A One-Dimensional Helical Arrangement of Ferromagnetic Coupled Co^{II} Metal Ions

In 2003, Gao et al. reported on a helical Co^{II} chain, [Co(2,2′-bithiazoline)$(N_3)_2$], which displays slow relaxation of the magnetization [60]. This compound possesses a structure composed of chains of Co^{II} metal ions bridged by two azide ligands in the *end-on* coordination mode (Fig. 7a). Three independent Co sites with three different octahedron environments are present leading to a helical arrangement of the Co metal ions along the chain direction (Fig. 7b). The magnetic susceptibility was fitted considering a Heisenberg $S = 3/2$ chain model. The interactions between Co^{II} were found to be ferromagnetic and estimated at $2J/k_B = +17.8$ K (using the notation of Eq. 1). Slow relaxation of the magnetization is observed on the field dependence of the magnetization at 1.85 K that exhibits a small hysteresis effect with a coercive field of about 1000 Oe. Moreover, step features are observed at 17, 26 and 46 kOe and have been attributed to the presence of different anisotropy axes on the three Co^{II} sites. The relaxation time of the system was studied using ac susceptibility measurements above 1.8 K. As shown on Fig. 7c, strong frequency dependences of both ac susceptibility components are observed. The relaxation mode was found to be very broad and was fitted with a generalized Debye model considering α values between 0.65 and 0.7. The relaxation time extracted from the ac data (Fig. 7d) follows an Arrhenius law with $\Delta_\tau/k_B = 94$ K and $\tau_0 = 3.4 \times 10^{-12}$ s.

Using the description of a SCM made in the first part of this review, the creation energy of a domain wall should be in this system about 80 K (Δ_ξ) from the ferromagnetic interactions mentioned above ($2J/k_B = +17.8$ K using Eq. 7a notation). As $\Delta_\tau < 2\Delta_\xi$, the system should be in the finite-size chain regime with $\Delta_A/k_B \approx (\Delta_\tau - \Delta_\xi)/k_B \approx 14$ K. This quick analysis suggests that this compound is not in the Ising limit and large domain walls are probably relevant.

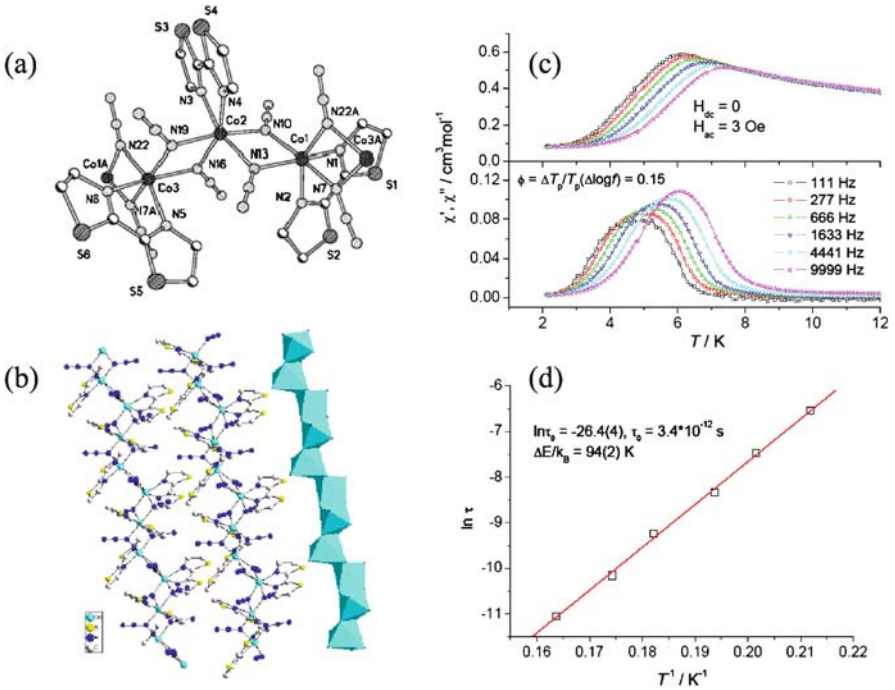

Fig. 7 (**a**) Molecular structure of [Co(2,2′-bithiazoline)$(N_3)_2$]. (**b**) Helical chains along the *a* axis and the octahedrons of Co(II) ions. (**c**) Temperature dependence of the real (*top*) and imaginary (*bottom*) components of the ac susceptibility in zero applied static field with an oscillating field of 3 Oe at a frequency of 111–9999 Hz. The *lines* are guides. (**d**) Arrhenius plot using τ vs. T^{-1} data extracted from the ac susceptibility measurements. The *red line* is a fit to the Arrhenius equation. Reprinted with permission from [60]. Copyright 2003 American Chemical Society

3.3.1.2 A Supramolecular SCM built from Ferromagnetic Coupled Mn^{III} Metal Ions

Another example of magnetization slow relaxation in a one-dimensional arrangement has been reported by Shaikh et al. [61]. The compound of formula: Mn_2^{II}(bispicen)$_2(\mu_3$-Cl)$_2Mn^{III}(Cl_4Cat)_2Mn^{III}(Cl_4Cat)_2(H_2O)_2$ (where bispicen is *N*,*N*′-bis(2-pyridylmethyl)-1,2-ethanediamine and Cl_4Cat is tetrachlorocatecholate dianion) exhibits a two-dimensional network of Mn^{II} and Mn^{III} (Fig. 8a). Because of dimerization of the Mn^{II} metal ions and the intradimer antiferromagnetic interaction, the compound has been described as a chain of ferromagnetically coupled Mn^{III} (Fig. 8a).

As suggested by the authors, the ferromagnetic interaction (of about + 1.4 K) would be mediated between Mn^{III} through strong hydrogen-bonding interactions. The analysis of the magnetic properties has been done only on

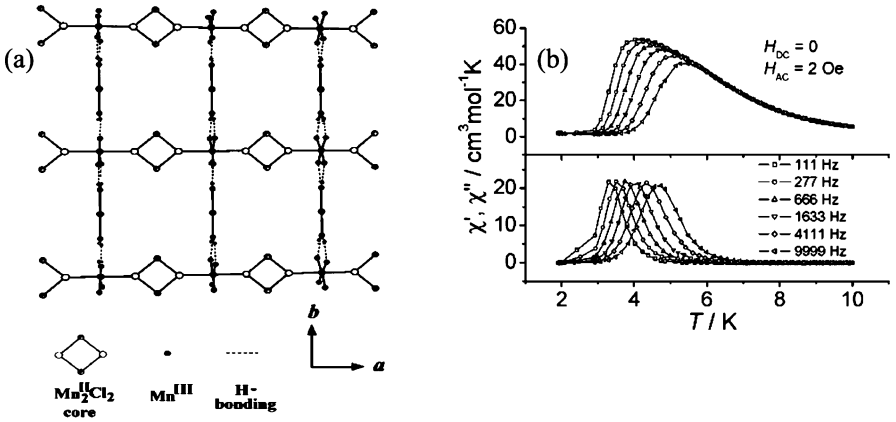

Fig. 8 **a** Skeletal representation of $Mn^{II}_2(bispicen)_2(\mu_3 - Cl)_2Mn^{III}(Cl_4Cat)_2Mn^{III}(Cl_4Cat)_2(H_2O)_2$ in the *ab* plane. **b** Temperature dependence of the real and imaginary component of the ac susceptibility in zero applied static field with an oscillating field 2 Oe in a frequency of 111–9999 Hz. The *solid lines* are guides. Reprinted with permission from [60]. Copyright 2004 American Chemical Society

the dynamics studying the relaxation time by ac susceptibility that follows an Arrhenius law with an energy gap of 50.5(5) K (and $\tau_0 = 3.4 \times 10^{-10}$ s) (Fig. 8b).

3.3.1.3 A Supramolecular SCM built from Ferromagnetic Coupled Mn_7 Complexes

In a recent paper of G. Christou et al. [62], two mixed-valence Mn^{III}/Mn^{IV} materials: $[Mn_7O_8(O_2SePh)_8(O_2Me)(H_2O)]$ and $[Mn_7O_8(O_2SePh)_9(H_2O)]$ exhibiting a supramolecular one-dimensional arrangement have been described as SCMs. Both compounds possess a unique $[Mn_7O_8]^{9+}$ core comprising three Mn^{III} and four Mn^{IV} metal ions bridged by $[PhSeO_2]^-$ groups. These heptanuclear complexes are arranged in a chain motif through weak Se...O inter-cluster interactions as seen in Fig. 9a.

Combined dc and ac magnetic measurements have been used to determine an $S = 2$ ground state of the Mn_7 units. Between 1.8 and 4 K, frequency dependence (up to 997 Hz) of the ac susceptibility is observed for both compounds. This indication of magnetization slow relaxation has been confirmed by the detection of hysteresis loops on the M vs. H plot below 4 K. The analysis of these data leads to the conclusion that intra-chain and inter-chain magnetic interactions were of ferromagnetic and antiferromagnetic nature, respectively. Moreover the dc susceptibility below 10 K was fitted to the Curie–Weiss law ($\theta = -2$ K) to argue that antiferromagnetic interactions were much weaker than the intra-chain ferromagnetic ones. Unfortunately, the magnitude of these interactions was not determined due to low-lying

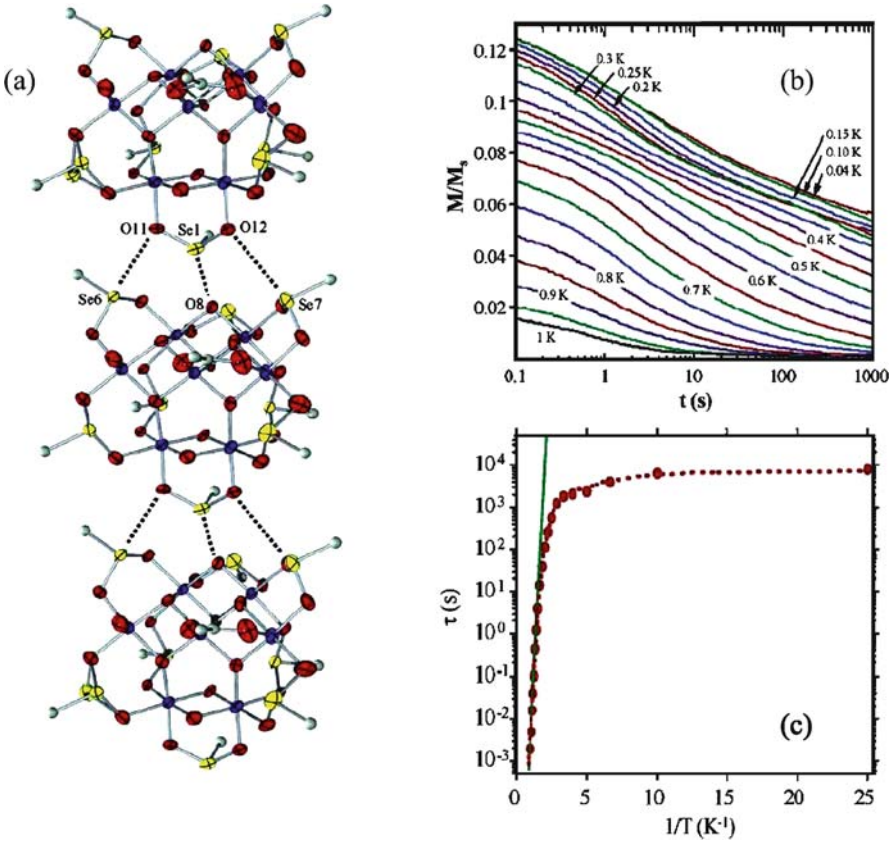

Fig. 9 **a** ORTEP representation in PovRay format at the 50% probability level of the packing of complex $[Mn_7O_8(O_2SePh)_8(O_2Me)(H_2O)]$ along the *a* axis of the crystal. For clarity, the hydrogen atoms have been omitted and only the *ipso* C atoms of the phenyl groups are shown. **b** M/M_s vs. t decay plots for a single crystal of $[Mn_7O_8(O_2SePh)_8(O_2Me)(H_2O)]$ at the indicated temperatures. **c** Arrhenius plot using the resulting relaxation lifetime τ vs. $1/T$ data. The *green line* is a fit of the thermally activated region to the Arrhenius equation. Reprinted with permission from [62]. Copyright 2004 American Chemical Society

excited states of the Mn_7 complexes. Direct time relaxation of the magnetization has been measured below 1 K using a μ-SQUID technique (Fig. 9b) in order to determine the characteristic relaxation time of the systems. As shown for $[Mn_7O_8(O_2SePh)_8(O_2Me)(H_2O)]$ in Fig. 9c, τ follows an Arrhenius law ($\Delta_\tau/k_B = 14.2$ K and $\tau_0 = 1.9 \times 10^{-9}$ s) between 1 and 0.5 K before a progressive saturation (at $\approx 10^4$ s). This temperature independence of the relaxation time has been attributed to quantum tunneling of the magnetization through the anisotropy barrier. It is worth noting that this effect has not yet been observed in any other material reported to be a SCM.

3.3.1.4 Cyanide-Bridged Heterometallic Double and bis-Double Zig-Zag Chains

The use of versatile building-blocks such as $[Fe^{III}L1(CN)_4]^-$ and $[Fe^{III}L2(CN)_3]^-$ [where L1 is 2,2′-bipyridine (bpy) or 1,10-phenanthroline (phen) and L2 is tris(pyrazolyl)hydriborate (Tp)] together with Co^{II} or Cu^{II} metal ions has led to two types of one-dimensional architecture (Fig. 10a–c) in materials that were reported to be single-chain magnets. The first type of chain is made of shared-corner squares (also called a double zigzag chain) as illustrated in Fig. 10a by $[Fe(bpy)(CN)_4]_2Co(H_2O)_2 \cdot 4H_2O$ [63, 64]. Restricting ourselves to the materials relevant for this review, a few other related systems have been reported: $[Fe(phen)(CN)_4]_2Co(H_2O)_2 \cdot 4H_2O$ [63, 64], $[Fe(bpy)(CN)_4]_2Cu(H_2O)_2 \cdot 4H_2O$ [65] and $[Fe(Tp)(CN)_3]_2Cu(CH_3OH) \cdot 2CH_3OH$ [66]. In all these compounds, the intra-chain coupling $Fe^{III}...M^{II}$ (M: Co and Cu) has been found to be ferromagnetic based on dc susceptibility measurements [63–66], fitting procedures [66] and DFT calculations [64, 65].

For $[Fe(L1)(CN)_4]_2Co(H_2O)_2 \cdot 4H_2O$ compounds, large hysteresis loops are observed below 7 K together with the apparition of a frequency dependent ac signal in a zero dc magnetic field (Fig. 10d–e). The relaxation time deduced from ac data for $[Fe(bpy)(CN)_4]_2Co(H_2O)_2 \cdot 4H_2O$ follows an activated behavior with $\Delta_\tau/k_B = 142$ K and $\tau_0 = 9.4 \times 10^{-12}$ s [64]. The absence of a transition signature in heat capacity measurements and the presence of slow relaxation are indications that have been used by the authors to qualify these compounds as single-chain magnets[7]. The same type of magnetic behavior has been observed for $[Fe(Tp)(CN)_3]_2Cu(CH_3OH) \cdot 2CH_3OH$ (τ follows an Arrhenius law with $\Delta_\tau/k_B = 112.3$ K and $\tau_0 = 2.8 \times 10^{-13}$ s) [66] and $[Fe(bpy)(CN)_4]_2Cu(H_2O)_2 \cdot 4H_2O$ [65]. The second type of one-dimensional arrangement can be viewed as a fusion of two shared-corner square chains (also called a bis-double zigzag chain) as illustrated in Fig. 10b–c [65, 67]. As for the previous one-dimensional architecture, Fe^{III}/Co^{II} and Fe^{III}/Cu^{II} systems have been reported to exhibit slow relaxation of the magnetization: $[Fe(bpy)(CN)_4]_2Co(H_2O) \cdot MeCN \cdot 0.5H_2O$ [67], $[Fe(phen)(CN)_4]_2Cu \cdot H_2O$ [65] and $[Fe(bpy)(CN)_4]_2Cu \cdot 2H_2O$ [65]. In these materials, the one-dimensional objects possess intra-ferromagnetic interactions (in agreement with the double zigzag chain described above) and are coupled together through space by weak antiferromagnetic interactions (of the order of -0.1 K). At low temperature, this type of magnetic topology leads to a metamagnetic-like behavior as seen on the M vs. H plot displayed in Fig. 10f. A maximum of susceptibility is observed at 7.5 K, 5.2 K 5.5 K for $[Fe(bpy)(CN)_4]_2Co(H_2O) \cdot MeCN \cdot 0.5H_2O$ [67], $[Fe(phen)(CN)_4]_2Cu \cdot H_2O$ [65] and $[Fe(bpy)(CN)_4]_2Cu \cdot 2H_2O$ [65], respectively. Below these

[7] See [63]; measurements of the 2nd harmonic non-linear susceptibility for $[Fe(phen)(CN)_4]_2 \cdot Co(H_2O)_2 \cdot 4H_2O$ was taken as a evidence for a ferromagnetic ordering at 8.1 K. The authors suggest the possibility of a coexistence between a ferromagnetic ordering and a glassy relaxation behavior.

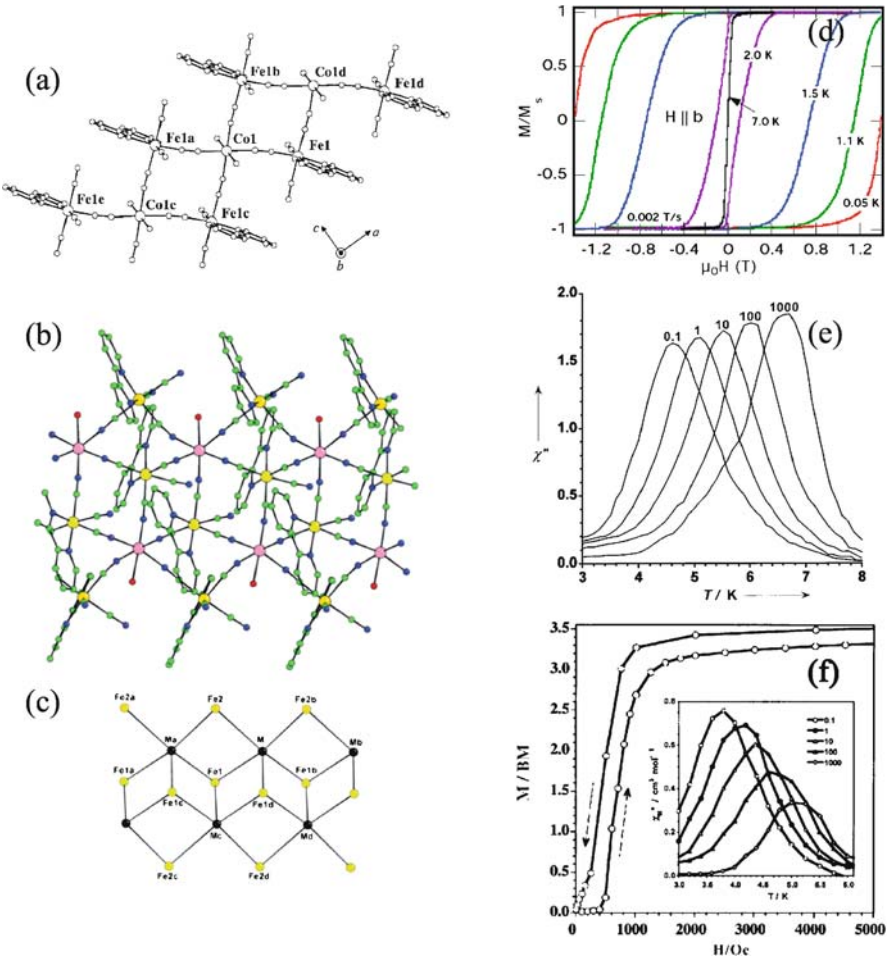

Fig. 10 **a** View of a fragment of the double zigzag chain: $[Fe(bpy)(CN)_4]_2Co(H_2O)_2 \cdot 4H_2O$ running parallel to the *a* axis. Uncoordinated water molecules have been omitted for clarity. Reprinted with permission from [64]. Copyright 2004 Wiley. **b** A view of the structure of $[Fe(bpy)(CN)_4]_2Co(H_2O) \cdot MeCN \cdot 0.5H_2O$ along the *b* axis. The metals are *yellow* (Fe) and *pink* (Co) [67]—Reproduced by permission of The Royal Society of Chemistry. **c** Schematic view of the metallic frame of $[Fe(bpy)(CN)_4]_2Co(H_2O) \cdot MeCN \cdot 0.5H_2O$ [67]—Reproduced by permission of The Royal Society of Chemistry. **d** Hysteresis loops as a function of the temperature at $0.002T/s$ for a single crystal of $[Fe(bpy)(CN)_4]_2Co(H_2O)_2 \cdot 4H_2O$ in its easy direction. Reprinted with permission from [64]. Copyright 2004 Wiley. **e** Temperature dependence of the out-of-phase (χ'') component of the ac susceptibility on a single crystal of $[Fe(bpy)(CN)_4]_2Co(H_2O)_2 \cdot 4H_2O$ in zero applied static field and with the oscillating field (1 Oe) applied along the *b* axis at different frequencies. Reprinted with permission from [64]. Copyright 2004, Wiley. **f** Magnetization vs. H plot at 2 K for $[Fe(bpy)(CN)_4]_2Co(H_2O) \cdot MeCN \cdot 0.5H_2O$. *Inset:* χ''_{ac} susceptibility (1 G oscillating field, 0.1–1000 Hz, 800 G applied dc field) [67]—Reproduced by permission of The Royal Society of Chemistry

temperatures, the susceptibility becomes strongly field dependent as expected for antiferromagnetic or metamagnetic orders. Nevertheless, when applying only a small dc field (800–1000 Oe), a frequency dependent ac signal appears which, for the authors, rules out the possibility of three-dimensional order (inset Fig. 10f)[8]. The relaxation time of this mode has been studied for $[Fe(bpy)(CN)_4]_2Co(H_2O)\cdot MeCN\cdot 0.5H_2O$ [67] and $[Fe(bpy)(CN)_4]_2Cu\cdot 2H_2O$ [65] for which the ac signal is observed above 1.8 K. In both cases, τ follows an Arrhenius law with $\Delta_\tau/k_B = 152\,K/\tau_0 = 1.5\times10^{-17}$ s and $\Delta_\tau/k_B = 50.3\,K/\tau_0 = 4\times10^{-13}$ s, respectively. These compounds have been classified as metamagnetic-like systems that display "single-chain magnet behavior under low applied magnetic fields" [65].

Nevertheless, an interesting question concerning the magnetic anisotropy remains open after the description of these cyanide-bridged heterometallic double and bis-double zig-zag chains. While in the Fe^{III}/Co^{II} systems, the magnetic anisotropy is clearly coming from the Co^{II} metal ions, its origin remains unclear in the Fe^{III}/Cu^{II} systems and will probably require further investigations.

3.3.2
Chains with a Ferrimagnetic Arrangement

We have described in Sect. 3.1 the first evidence of a single-chain magnet behavior in a chain of antiferromagnetically coupled Co^{II} and NITPhOMe radical. This system, $Co^{II}(hfac)_2(NITPhOMe)$ [35], is thus also the first example of single-chain magnet behavior in a "ferrimagnetic chain". Since this pioneering work, only two new examples of a chain with a ferrimagnetic arrangement have been described in the literature.

3.3.2.1
Co^{II}–Cu^{II} Bimetallic Single-Chain Magnet

In 2004, E. Pardo et al. reported on a $Co^{II}-Cu^{II}$ bimetallic single-chain magnet: $[CoCu(2,4,6\text{-tmpa})_2(H_2O)_2]\cdot 4H_2O$ (2,4,6-tmpa: *N*-2,4,6-trimethylphenyloxamate) [68]. This compound consists of neutral ribbon-like oxamato-bridged $Co^{II}Cu^{II}$ chains where the bis(oxamato)copper(II) unit acts as a bis-bi-dentate donor ligand through the *cis* carbonyl oxygen atoms towards *trans* diaquacobalt(II) units (Fig. 11a). The phenyl ring of the tmpa ligands affords an effective shielding between neighboring chains running along the *c* axis (Fig. 11b). Dc susceptibility measurements at high temperature have been performed and a preliminary analysis of the data leads to an estimation of the antiferromagnetic coupling ($2J/k_B$ using Eq. 7a notation) between Co^{II}

[8] Note that for $[Fe(bpy)(CN)_4]_2Co(H_2O)\cdot MeCN\cdot 0.5H_2O$, heat capacity measurements have been performed and don't show any λ-peak [67].

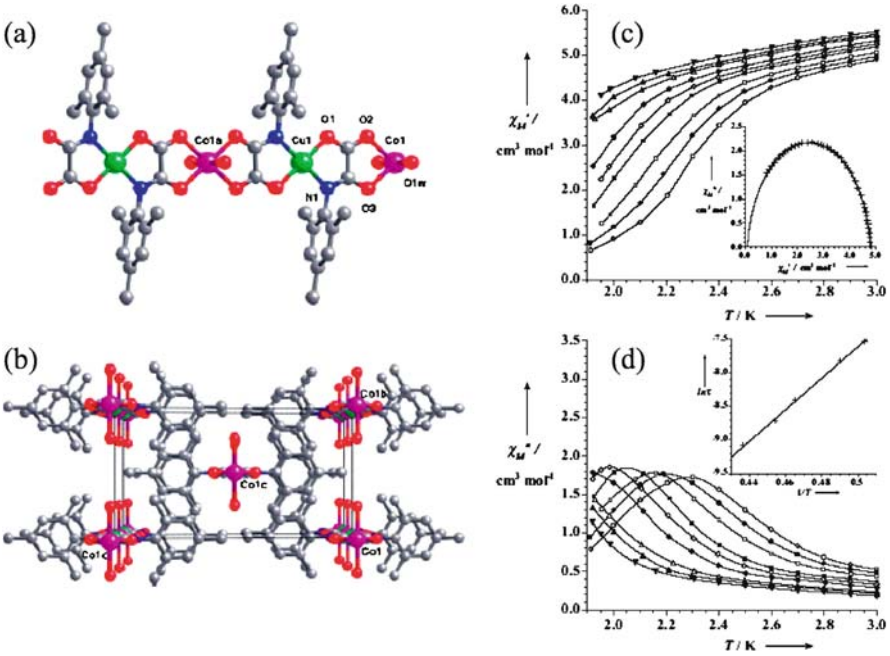

Fig. 11 **a** View of a fragment of the bimetallic chain of $[CoCu(2,4,6\text{-tmpa})_2(H_2O)_2]\cdot 4H_2O$ [68]. **b** Perspective drawing of the crystal packing of $[CoCu(2,4,6\text{-tmpa})_2(H_2O)_2]\cdot 4H_2O$ along the *c* axis [68]. Temperature dependence of the real **c** and imaginary **d** component of the ac susceptibility in zero applied static field with an oscillating field 1 Oe at different frequencies of the oscillating field (▼) 50, (▲) 75, (△) 100, (⧫) 200, (◇) 300, (■) 400, (□) 700, (●) 1000, (○) 1400 Hz. The *solid lines* are guides. *Inset* of **c**: Cole–Cole plot at 2.0 K. *Inset* of **d**: Arrhenius plot ($\ln\tau$ vs. $1/T$). Reprinted with permission from [68]. Copyright 2004 Wiley

and Cu^{II} of about – 38 K. $[CoCu(2,4,6-tmpa)_2(H_2O)_2]\cdot 4H_2O$ exhibits in-phase and out-of-phase ac susceptibility signals at low temperature which are frequency dependent (Figs. 11c and 11d). A Cole–Cole plot (inset Fig. 11c) at 2.0 K has been fitted to a generalized Debye model with an α value of 0.05 indicating the presence of a single relaxation process. The characteristic relaxation time (τ) of this mode has been extracted from the ac data and is shown as an $\ln\tau$ vs. $1/T$ plot (inset Fig. 11d) to emphasize its activated behavior ($\Delta_\tau/k_B = 23.5$ K and $\tau_0 = 4\times10^{-9}$ s).

3.3.2.2 Fe^{II}–Fe^{III} Mixed Valence Single-Chain Magnet Induced by a Twisted Arrangement of Easy-Plane Magnetic Anisotropy

T. Kajiwara et al. reported in 2005 on a quite original 1D system, $[Fe^{II}(ClO_4)_2\{Fe^{III}(bpca)_2\}](ClO_4)$, that displays a single-chain magnet behavior induced

by a ferrimagnetic arrangement of Fe^{II} and Fe^{III} metal ions and the easy-plane anisotropy of the Fe^{II} sites [69]. This group has developed a synthetic method for the preparation of homo- and hetero-metallic chain systems using $[M(bpca)_2]$ and $[M'(bpca)_2]^+$ building units [70–74] (with M: Mn^{II}, Fe^{II}, Ni^{II}; M′: Cr^{III}, Fe^{III}, Co^{III} and Hbpca: bis(2-pyridylcarbonyl)amine). Among this series of material, $[Fe^{II}(ClO_4)_2\{Fe^{III}(bpca)_2\}](ClO_4)$ is an alternating chain of Fe^{II} and Fe^{III} metal ions connected through the bpca ligand (Fig. 12a) [69]. The Fe^{II} ions (orange atoms of Fig. 12a) have an axial-elongated geometry with four equatorial carbonyl oxygen atoms and two axial ClO_4^- oxygen atoms. While the Fe^{III} ions can be considered as isotropic, the distorted geometries of the two Fe^{II} sites leads to an easy-plane (or hard axis) anisotropy. The important aspect is that the two easy-planes are orthogonally oriented alternately along a chain (Fig. 12a). The dc suscepti-

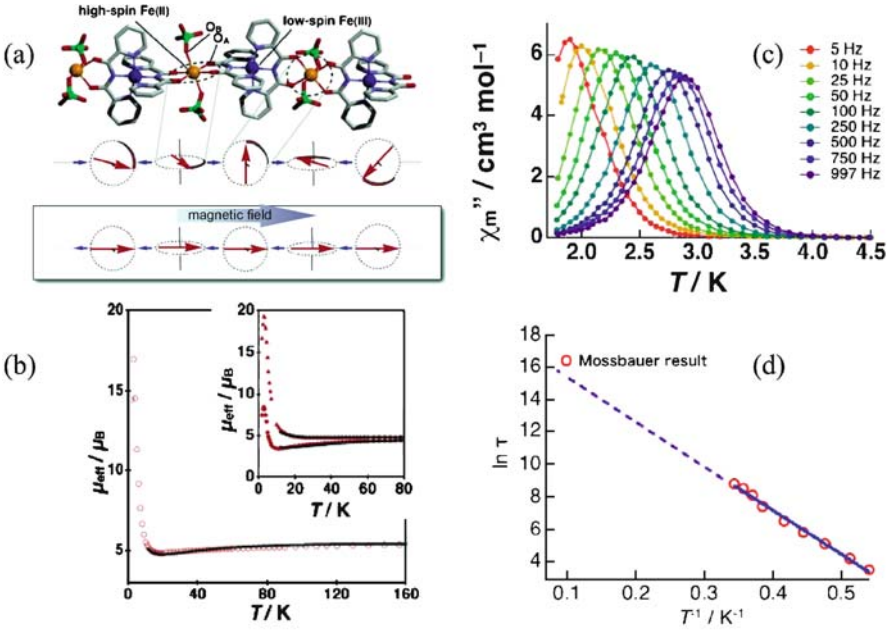

Fig. 12 **a** Crystal structure and spin arrangement of high-spin Fe^{II} and low-spin Fe^{III} alternating in $[Fe^{II}(ClO_4)_2\{Fe^{III}(bpca)_2\}](ClO_4)$. Each atom is depicted as follows: Fe^{III} *blue*, Fe^{II} *orange*, Cl *green*, O *red*, N *pale blue*, and C *gray*. **b** Temperature dependence of μ_{eff} (O) for the powder sample. *Inset* Magnetic measurements on an oriented single crystal of $[Fe^{II}(ClO_4)_2\{Fe^{III}(bpca)_2\}](ClO_4)$ in the dc field applied along (▲) and perpendicular (●) to the chain. The *solid lines* are theoretical curves. **c** Out-of-phase (χ_m'') ac magnetic susceptibility versus temperature in a 3.0 Oe ac field oscillating at the indicated frequencies and with a zero dc field. *Solid lines* are a guide for the eyes. **d** Arrhenius plot for $[Fe^{II}(ClO_4)_2\{Fe^{III}(bpca)_2\}](ClO_4)$. Reprinted with permission from [69]. Copyright 2005 American Chemical Society

bility of $[Fe^{II}(ClO_4)_2\{Fe^{III}(bpca)_2\}](ClO_4)$ has been measured on both polycrystalline and single-crystal samples. These data have been fitted based on an anisotropic Heisenberg alternating $S = 2$, $S = 1/2$ chain model (Fig. 12b) allowing an estimation of the intra-chain interactions: $J/k_B = -10$ K and of the Fe^{II} anisotropy: $D/k_B = +14.9$ K (using the notation of Eqs. 34 and 12a). Single-crystal measurements show the presence of an easy axis along the chain (a–c axis) that has been rationalized on the basis of the Fe^{II}/Fe^{III} antiferromagnetic coupling and the orthogonal orientation of the two easy-plane anisotropic Fe^{II}.

Slow relaxation of the magnetization is observed as shown by the frequency dependence of the ac susceptibility (Fig. 12c). Fitting of the Cole–Cole plot using a generalized Debye model leads to small α values ranging from 0.09 to 0.13 indicating that the relaxation possesses a characteristic time with a narrow distribution. This relaxation time was deduced from the ac susceptibility together with Mössbauer data (with a time scale of 10^{-7} s) and plotted in a $-\ln\tau$ vs. $1/T$ diagram (Fig. 12d) to highlight its activated behavior ($\Delta_\tau/k_B = 27$ K and $\tau_0 = 1.6 \times 10^{-8}$ s). Even if a theoretical treatment of the relaxation in such ferrimagnetic SCMs is not yet available, the authors comment that the obtained Δ_τ gap is quite small in comparison to the energy barrier of Glauber's approach suggesting that the easy-plane anisotropy plays a key role in the relaxation process.

3.3.3 Rare-Earth Based Single-Chain Magnet

The group of J.P. Costes was the first to report on the use of rare-earth ions as the anisotropic source to design single-chain magnet systems [75]. Slow relaxation of the magnetization was observed in a Cu^{II}/Tb^{III} heterometallic complex unfortunately not structurally characterized but formulated $(LCu)_2Tb(NO_3)$ on the basis of elemental analysis (with H_3L: 2-hydroxy-*N*-{2-[2-hydroxyethyl-amino]ethyl}benzamide). Frequency dependence of the ac susceptibility was observed below 5 K (for frequencies ranging from 1 to 1000 Hz). From these data, the relaxation time of the magnetization was extracted and found to follow an activated behavior with $\Delta_\tau/k_B = 28.5$ K and $\tau_0 = 3.8 \times 10^{-8}$ s. Without further analysis of the magnetic properties, this feature was attributed to a SCM behavior.

More recently, D. Gatteschi et al. have reported on a dysprosium-nitronyl nitroxide 1D compound with interesting dynamic properties [76]. Their work illustrates nicely how presently coordination chemistry can modulate a known system [Dy(hfac)$_3$NITEt] [77–80] (with hfac: hexafluoroacetylacetonate and NITEt: 4′-ethyl-4,4,5,5-tetramethylimidazoline-1-oxyl-3-oxide) to achieve fine control of the physical properties. [Dy(hfac)$_3$ NITEt] is composed of alternating chains of Dy(hfac)$_3$ units and NITEt radicals. This compound displays a transition to a three-dimensional mag-

netic order at 4.3 K induced by the through space inter-chain couplings. Gatteschi's idea was then to functionalize the radical moieties in order to minimize these inter-chain interactions and thus to avoid the magnetic order for the benefit of a single-chain magnet behavior. The NITEt radical was replaced by the bulky NITPhOPh derivative (NITPhOPh: 4′-phenoxy-benzyl-4,4,5,5-tetramethylimidazoline-1-oxyl-3-oxide) leading to the [Dy(hfac)$_3$NITPhOPh] compound and increasing the inter-chain distances in all the different directions (Fig. 13a). As shown by the dc susceptibility measurements, this engineering strategy was successful as no magnetic order was observed above 1.8 K. Moreover, the activated behavior of the χT product (shown in Fig. 13b) highlights the magnetic one-dimensional nature of the compound together with its Ising-like anisotropy. The corresponding slope, Δ_ξ, is not quoted by the authors but can be estimated from Fig. 13b at about 20 K. It is also worth noting that the

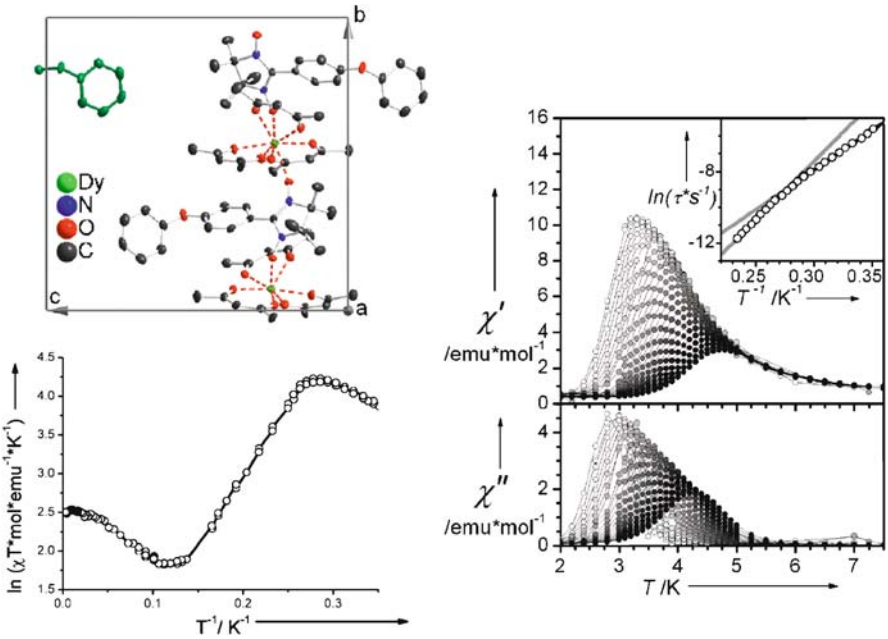

Fig. 13 **a** View of the crystal structure of the [Dy(hfac)$_3$NITPhOPh] chain compound along the *a* axis, showing the chain structure together with the unit cell. The aromatic tail of the radical of an adjacent chain is also shown, in *green*. Ellipsoids are drawn at 50% confidence and fluorine and hydrogen atoms were omitted for clarity [76]. **b** Semi-log plot of χT vs. $1/T$ (where χ is the zero-field susceptibility) [76]. **c** Temperature dependence of the real (*top*) and imaginary (*bottom*) components of the ac magnetic susceptibility measured in zero applied field in the frequency range 25 Hz–20 kHz. The *inset* shows the obtained Arrhenius plot and the crossover. Reprinted with permission from [76]. Copyright 2005 Wiley

$\ln(\chi T)$ vs. $1/T$ plot has a maximum around 2.7 K, which might be indicative of finite-size effects ($\xi \gg L$) as observed in $Co^{II}(hfac)_2(NITPhOMe)$ (Fig. 3c), $[Mn_2(saltmen)_2Ni(pao)_2(L)_2](A)_2$ (Fig. 4d) or in $(NEt_4)[Mn_2(5\text{-}MeOsalen)_2Fe(CN)_6]$ (Fig. 5b).

Dc measurements made in zero-field cooled and field cooled modes at 100 Oe are different below 2.6 K indicating the presence of a slowing down of the magnetization relaxation. As expected from this result, a small hysteresis loop is observed on the M vs. H data at 1.9 K. The dynamics of the system were studied using ac susceptibility measurements and is shown in Fig. 13c. Both in-phase and out-of-phase susceptibilities are frequency dependent. Cole–Cole diagrams have been fitted to a generalized Debye model with an α value of 0.16 indicating a narrow distribution of relaxation time. The average relaxation time is given as a $\ln(\tau)$ vs. $1/T$ plot (Inset Fig. 13c). Two different activated regimes are observed above and below 2.7 K with $\Delta_{\tau 1}/k_B \approx 69$ K and $\Delta_{\tau 2}/k_B \approx 42$ K, respectively. As suggested by the $\ln(\chi T)$ vs. $1/T$ plot (Fig. 13b), this crossover has been attributed to the finite-size of the chains. The difference between the two gaps of the relaxation time is estimated at 27 K, which would be equal to Δ_ξ following Eqs. 44 and 46. It is interesting to note that this value is slightly higher but coherent with the experimental Δ_ξ deduced from Fig. 13b. However, the description of this system may be more complicated as the authors invoke comparable values of nearest-neighbor ferromagnetic and next nearest-neighbor antiferromagnetic interactions along the chain. Indeed, this special interaction topology leads to the presence of a disorder point where two types of short-range orders are in competition. Nevertheless, the whole set of data reported by the authors shows unambiguously the single-chain magnet behavior of their compound and demonstrates the success of their synthetic strategy.

3.3.4 A Canted Antiferromagnetic Chain

In 2005, J.-G. Mao and K.R. Dunbar et al. reported on an antiferromagnetically coupled Co^{II} chain exhibiting single-chain magnet behavior [81]. Hydrothermal synthesis of 4-Me – C_6H_4 – $CH_2N(CH_2PO_3H_2)_2$ (noted H_4L in the following) and cobalt(II) acetate lead to a one-dimensional compound: $Co(H_2L)(H_2O)$. Pseudo-octahedral Co^{II} sites are linked by phosphonate oxygen atoms to form a zig-zag chain. Using an Ising chain model of Co(II) spins [82], the dc susceptibility of $Co(H_2L)(H_2O)$ was fitted allowing an estimation of the inter-Co^{II} interaction $J/k_B = -15.1$ K (using the notation of Eq. 7a). Frequency-scan and temperature-scan measurements of the ac susceptibility reveal the presence of slow relaxation of the magnetization. The relaxation time extracted from these data follows an Arrhenius law with $\Delta_\tau/k_B \approx 27–29$ K and $\tau_0 \approx 8.4–34 \times 10^{-10}$ s. According to the authors, the

presence of slow relaxation in $Co(H_2L)(H_2O)$ is induced by canting of the Co^{II} spins along the chain.

4 Concluding Remarks

We hope to have shown in this review that the subject of single-chain magnets is an appealing new trend of research that is currently emerging in the field of molecule-based magnetic materials. The motivation of the community on this topic can be explained essentially by their potential technological applications and the theoretical questions that can be raised by these systems. Indeed, a remarkable opportunity has been opened by the discovery of SCM properties to synthesize new nano-magnets interesting for future industrial applications. Although the presently available systems do not exhibit a frozen magnetization near ambient temperature, the synthesis of more efficient systems seems possible by a further increase of the magnetic exchange and anisotropy energies. This quest is certainly a major challenge for chemists in this field. On the other hand, the understanding of SCM properties involves very specific one-dimensional theories. Although it is still necessary to fill the gap between the existing models and the real materials, basic arguments deduced from the theory have been clearly confirmed by recent experimental results. A typical example is the pioneering work of R.J. Glauber that has received a spectacular validation with the study of the first SCM systems described in this review. This breakthrough is encouraging physicists to adapt and to generalize the existing theoretical models in order to establish a more realistic description of the experimental properties. Among the problems that researchers are currently working on, a few important ones should be highlighted as a conclusion of this review. At this stage of the subject, it appears that the known models describing simple regular ferromagnetic chains are not adapted for all the experimental systems. Hence, new models deriving from the available ones should be tailored to discuss more complicated arrangements, as for example ferrimagnetic chains. On the other hand, it is certainly important to synthesize new materials with very simple chain structure to analyze in detail their magnetic properties. For example, a simple regular chain of ferromagnetically coupled anisotropic spins (with iso-oriented local anisotropy tensors) is still missing. The role of small inter-chain couplings is another important point that should be considered as these interactions become relevant as soon as the intra-chain correlation length becomes very large. In fact, the occurrence of a 3D magnetic order can always compete with SCM behavior. On this topic, new experimental systems (as for example described by D. Gatteschi et al. [76] and in Sect. 3.3.3) with a fine tune of the inter-chain interactions would be very helpful to probe the frontier between these two extreme magnetic behaviors. Finally, defects along the chains could become rapidly

a major issue in this domain. Although finite-size effects have already been emphasized, more efforts are certainly needed to discover potential specific behaviors of finite chains. A recent example is given by the work of L. Bogani et al. [39] showing that a specific field dependence of the magnetization does exist for finite ferrimagnetic chains. Moreover, we have recently discovered that a slow relaxation of the dc magnetization can be observed with finite-size antiferromagnetic chains due to the presence of segments with an odd number of spin units. The time dependence of this relaxation has also been shown to be in agreement with the poly-disperse description [83]. The motivation for these problems is still reinforced by the fact that future application of SCMs will necessarily involve finite chains as defects are always present in real systems.

Acknowledgements The authors gratefully acknowledge E. Bonet (LLN, Grenoble, France), F. Nallet (CRPP, Pessac, France), S.S.P. Parkin (IBM, Almaden Research Center, San Jose, USA), A. Vindigni (ETH, Zurich, Switzerland) and W. Wernsdorfer (LLN, Grenoble, France) for their fruitful collaboration and the hours of helpful and passionate discussions. The authors also thank our students and post-docs at TMU and CRPP for their everyday hard work but also for their curiosity, enthusiasm and ability on this project, which have emphasized our motivation and creativity. This work was supported by PRESTO and CREST projects, Japan Science and Technology Agency, Grant-in-Aid from the Ministry of Education, Culture, Sports, Science, and Technology (Japan), the CNRS, the University of Bordeaux 1 and the Conseil Régional d'Aquitaine.

References

1. Kodoma RH (1999) J Magn Magn Mater 200:259
2. Thompson DA, Best JS (2000) IBM J Res Dev 44:311
3. Weller D, Moser A (1999) IEEE Trans Magn 35:4423
4. Skumryev V, Stoyanov S, Zhang Y, Hadjipanayis G, Givord D, Nogués J (2003) Nature 423:850
5. Christou G, Gatteschi D, Hendrickson DN, Sessoli R (2000) MRS Bull 25:66
6. Gatteschi D, Sessoli R (2003) Angew Chem Int Ed 42:268
7. Ritter SK (2004) Chem Eng News 82:29
8. Clérac R, Miyasaka H, Yamashita M, Coulon C (2002) J Am Chem Soc 124:12837
9. Thompson CJ (1972) In: Domb C, Green MS (eds) Phase Transitions and Critical Phenomena, vol 1. Academic Press, London
10. Delhaès P, Drillon M (eds) (1987) Organic and inorganic low-dimensional crystalline materials, vol 168. NATO ASI Series B:Physics. Plenum Press, New York
11. Georges R, Borras-Almenar JJ, Coronado E, Curely J, Drillon M (2001) In: Miller JS, Drillon M (eds) Magnetism: Molecules to Materials. Wiley, New York, p 1
12. Fisher ME (1964) Am J Phys 32:343
13. Suzuki M, Tsujiyama B, Katsura S (1967) J Math Phys 8:124
14. Ising E (1925) Z Phys 31:253
15. Fisher ME (1963) J Math Phys 4:124
16. Steiner M, Villain J, Windsor CG (1976) Adv Phys 25:87
17. Boersma F, de Jonge WJM, Kopinga K (1981) Phys Rev B 23:186

18. Loveluck JM, Lovesey SW, Aubry S (1975) J Phys C: Solid State Phys 8:3841
19. Barbara B (1973) J Physique 34:1039 (1994) J Magn Magn Mat 129:79
20. Kawasaki K (1972) In: Domb C, Green MS (eds) Phase Transitions and Critical Phenomena, vol 2. Academic Press, London, p 443
21. Glauber RJ (1963) J Math Phys 4:294
22. Suzuki M, Kubo R (1968) J Phys Soc Japan 24:51
23. Cordery R, Sarker S, Tobochnik J (1981) Phys Rev B 24:5402
24. Haake F, Thol K (1980) Z Phys B Condens Matt 40:219
25. Felderhof BU, Suzuki M (1971) Physica 56:43
26. Coulon C, Clérac R, Lecren L, Wernsdorfer W, Miyasaka H (2004) Phys Rev B 69:132408
27. Luscombe JH (1987) Phys Rev B 36:501
28. Droz M, Kamphorst Leal da Silva J, Malaspinas A (1986) Phys Lett 115:448
29. Imry Y, Montano PA, Hone D (1975) Phys Rev B 12:253
30. Luscombe JH, Luban M, Reynolds JP (1996) Phys Rev E 53:5852
31. Vindigni A, Rettori A, Bogani L, Caneschi A, Gatteschi D, Sessoli R, Novak MA (2005) Appl Phys Lett 87:073102
32. Wortis M (1974) Phys Rev B 10:4665
33. Matsubara F, Yoshimura K, Katsura S (1973) Can J Phys 51:1053
34. Dhar D, Barma M (1980) J Statist Phys 22:259
35. Caneschi A, Gatteschi D, Lalioti N, Sangregorio C, Sessoli R, Venturi G, Vindigni A, Rettori A, Pini MG, Novak MA (2001) Angew Chem Int Ed 40:1760
36. Caneschi A, Gatteschi D, Lalioti N, Sangregorio C, Sessoli R (2000) J Chem Soc Dalton Trans 3907
37. Caneschi A, Gatteschi D, Lalioti N, Sessoli R, Sorace L, Tangoulis V, Vindigni A (2002) Chem Eur J 8:286
38. Bogani L, Sessoli R, Pini MG, Rettori A, Novak MA, Rosa P, Massi M, Fedi ME, Giuntini L, Caneschi A, Gatteschi D (2005) Phys Rev B 72:064406
39. Bogani L, Caneschi A, Fedi ME, Gatteschi D, Massi M, Novak MA, Pini MG, Rettori A, Sessoli R, Vindigni A (2004) Phys Rev Lett 92:207204-1
40. Caneschi A, Gatteschi D, Lalioti N, Sangregorio C, Sessoli R, Venturi G, Vindigni A, Rettori A, Pini MG, Novak MA (2002) Europhys Lett 58:771
41. Vindigni A, Regnault N, Jolicoeur Th (2004) Phys Rev B 70:134423
42. Roland L, Simonet V, Wernsdorfer W, Bogani L, Sessoli R (2004) J Mag Mag Mater 272–276:1079
43. Lascialfari A, Micotti E, Aldrovandi S, Caneschi A, Gatteschi D (2003) J Appl Phys 93:8749
44. Micotti E, Lascialfari A, Rigamonti A, Aldrovandi S, Caneschi A, Gatteschi D, Bogani L (2004) J Mag Mag Mater 272–276:1087
45. Vindigni A, Bogani L, Gatteschi D, Sessoli R, Rettori A, Novak MA (2004) J Mag Mag Mater 272–276:297
46. Miyasaka H, Clérac R, Mizushima K, Sugiura K, Yamashita M, Wernsdorfer W, Coulon C (2003) Inorg Chem 42:8203
47. Miyasaka H, Nezu T, Sugimoto K, Sugiura K, Yamashita M, Clérac R (2005) Chem Eur J 11:1592
48. Miyasaka H, Clérac R (2005) Bull Chem Soc Jpn 78:1725
49. Ferbinteanu M, Miyasaka H, Wernsdorfer W, Nakata K, Sugiura K, Yamashita M, Coulon C, Clérac R (2005) J Am Chem Soc 127:3090
50. Choi HJ, Sokol JJ, Long JR (2004) Inorg Chem 43:1606

51. Miyasaka H, Matsumoto N, Okawa H, Re N, Gallo E, Floriani C (1995) Angew Chem Int Ed 34:1446
52. Miyasaka H, Matsumoto N, Okawa H, Re N, Gallo E, Floriani C (1996) J Am Chem Soc 118:981
53. Miyasaka H, Matsumoto N, Re N, Gallo E, Floriani C (1997) Inorg Chem 36:670
54. Miyasaka H, Ieda H, Matsumoto N, Re N, Crescenzi R, Floriani C (1998) Inorg Chem 37:25
55. Miyasaka H, Okawa H, Miyazaki A, Enoki T (1998) J Chem Soc Dalton Trans 3991
56. Miyasaka H, Okawa H, Miyazaki A, Enoki T (1998) Inorg Chem 37:4878
57. Miyasaka H, Ieda H, Matsumoto N, Sugiura K, Yamashita M (2003) Inorg Chem 42:3509
58. Clemente-León M, Coronado E, Galán-Mascarós JR, Gómez-García CJ, Woike T, Clemente-Juan JM (2001) Inorg Chem 40:87
59. Przychodzén P, Lewinski K, Balanda M, Pelka R, Rams M, Wasiutynski T, Guyard-Duhayon C, Sieklucka B (2004) Inorg Chem 43:2967
60. Liu T, Fu D, Gao S, Zhang Y, Sun H, Su G, Liu Y (2003) J Am Chem Soc 125:13976
61. Shaikh N, Panja A, Goswami S, Banerjee P, Vojtisek P, Zhang Y-Z, Su G, Gao S (2004) Inorg Chem 43:849
62. Chakov NE, Wernsdorfer W, Abboud KA, Christou G (2004) Inorg Chem 43:5919
63. Chang F, Gao S, Sun HL, Hou YL, Su G (2002) Proceeding of the ICSM 2002 Conference (June 29–July 5th 2002), Fudan University, Shanghai, China, p 182
64. Lescouëzec R, Vaissermann J, Ruiz-Pérez C, Lloret F, Carrasco R, Julve M, Verdaguer M, Dromzee Y, Gatteschi D, Wernsdorfer W (2003) Angew Chem Int Ed 42:1483
65. Toma LM, Delgado FS, Ruiz-Pérez C, Carrasco R, Cano J, Lloret F, Julve M (2004) Dalton Trans 2836
66. Wang S, Zuo JL, Gao S, Song Y, Zhou HC, Zhang YZ, You XZ (2004) J Am Chem Soc 126:8900
67. Toma LM, Lescouëzec R, Lloret F, Julve M, Vaissermann J, Verdaguer M (2003) Chem Commun 1850
68. Pardo E, Ruiz-Garcia R, Lloret F, Faus J, Julve M, Journaux Y, Delgado F, Ruiz-Perez C (2004) Adv Mater 16:1597
69. Kajiwara T, Nakano M, Kaneko Y, Takaishi S, Ito T, Yamashita M, Igashira-Kamiyama A, Nojiri H, Ono Y, Kojima N (2005) J Am Chem Soc 127:10150
70. Kamiyama A, Noguchi T, Kajiwara T, Ito T (2000) Angew Chem Int Ed 39:3130
71. Kamiyama A, Noguchi T, Kajiwara T, Ito T (2002) Inorg Chem 41:507
72. Kamiyama A, Noguchi T, Kajiwara T, Ito T (2003) Cryst Eng Commun 5:231
73. Kajiwara T, Sensui R, Noguchi T, Kamiyama A, Ito T (2002) Inorg Chim Acta 337:299
74. Kajiwara T, Ito T (1999) Mol Cryst Liq Cryst 335:73
75. Costes JP, Clemente-Juan JM, Dahan F, Milon J (2004) Inorg Chem 43:8200
76. Bogani L, Sangregorio C, Sessoli R, Gatteschi D (2005) Angew Chem Int Ed 44:5817
77. Benelli C, Caneschi A, Gatteschi D, Sessoli R (1992) Adv Mater 4:504
78. Benelli C, Caneschi A, Gatteschi D, Sessoli R (1993) Inorg Chem 32:4797
79. Benelli C, Caneschi A, Gatteschi D, Sessoli R (1993) J Appl Phys 73:5333
80. Benelli C, Caneschi A, Gatteschi D, Pardi L, Rey P (1990) Inorg Chem 29:4223
81. Sun Z-M, Prosvirin AV, Zhao H-H, Mao J-G, Dunbar KR (2005) J Appl Phys 97:10B305
82. Coronado E, Drillon M, Nugteren PR, de Jongh LJ, Beltran D (1988) J Am Chem Soc 110:3907
83. Lecren L, Roubeau O, Coulon C, Li Y-G, Le Goff X, Wernsdorfer W, Miyasaka H, Clérac R (2005) J Am Chem Soc 127:17353

Struct Bond (2006) 122: 207–250
DOI 10.1007/430_033

Published online: 29 April 2006

General Theory of Superexchange in Molecules

Jacques Curély[1] (✉) · Bernard Barbara[2]

[1]Centre de Physique Moléculaire Optique et Hertzienne (C.P.M.O.H.), Université Bordeaux 1, 351 Cours de la Libération, 33405 Talence Cedex, France
j.curely@cpmoh.u-bordeaux1.fr

[2]Laboratoire L. Néel, CNRS, B.P. 166, 38042 Grenoble Cedex 09, France

Abstract After recalling the basic physical backgrounds, we examine the concept of *magnetic orbital*, which is very useful for treating the mechanism of *superexchange*. Then we recall the general broad lines of the first historical model proposed by Anderson. In a second step, we develop a new general treatment for superexchange, in the case of the centrosymmetrical model AXB. A and B are $3d^1$ metal cations characterized by σ-type

bonds on both sides of the diamagnetic bridge X without the presence of a π-type orbital (with here A = B or A $\neq$ B). The cationic orbitals are of the *d*-type, whereas that of diamagnetic ligand is of the *s*- or *p*-type. This treatment allows one to retrieve the expression of exchange energy *J vs* key molecular integrals, as respectively proposed by several authors such as Anderson, on the one hand, Hay, Thibeault and Hoffmann, on the other one, and, finally, Kahn and Briat. This *toy model* may be easily generalized to $3d^n$ ions (with $n > 1$) with or without transfer between both cations, with A = B or A $\neq$ B. Under these conditions we show that this general treatment allows one to calculate superexchange interactions in any type of molecule.

Keywords Superexchange · Magnetic orbital · Anderson model · Hay–Thibeault–Hoffmann model · Kahn–Briat model

1 Introduction

The concept of exchange coupling within and between atoms and molecules has been long to emerge, and its development was marked by many errors and obscurities. One may consider that this concept took place in 1895 when P. Curie reported in his thesis entitled "Magnetic properties of compounds at various temperatures", that magnetic systems could be classified into three distinct groups: diamagnetics, paramagnetics and ferromagnetics, where exchange couplings will appear later as crucial [1]. In 1905 Langevin gave a good interpretation of Curie's results on diamagnetism and paramagnetism [2, 3]. The most important point was the link between a microscopic variable (the magnetic moment per atom in presence of an external magnetic field) and a macroscopic one (the magnetization derived from experiment). In order to understand the existence of ferromagnetism below a characteristic temperature (the Curie temperature), Langevin suggested that a possible mechanism could be a co-operative phenomenon between atomic moments. In 1906 Weiss exploited this fruitful idea and introduced the notion of "molecular field", acting on these moments and proportional to the net magnetization [4–6]. An interesting idea then emerged when considering a possible electrostatic origin of this field [7, 8]. However (i) the field magnitude rapidly appeared as "physically" unrealistic and (ii) various attempts to quantify the Weiss theory failed [7–9].

The first convincing mechanism for the exchange interaction came with the formal development of quantum mechanics which gave an important impetus to the microscopic understanding of magnetism. Notably the introduction of the concept of electron spin in 1925 allowed the identification of the fundamental origin of magnetism. Finally the recognition by Heisenberg [10] and Dirac [11] that Pauli's exclusion principle (1925) implies that the wave function of a many-electron system must be antisymmetrical under coordinate–spin permutations has played an important role. Then, the ap-

plication of Hund's rules for the coupling of spins in atoms [12, 13] has immediately followed [14].

In this context, the notion of "exchange energy" resulting from electrostatic interactions between the electrons shared by two atoms i and j, with spins $\boldsymbol{s}_i$ and $\boldsymbol{s}_j$, was successfully represented by the "Heisenberg–Dirac" Hamiltonian, $J\boldsymbol{s}_i \cdot \boldsymbol{s}_j$ (where J is the "exchange constant"). These formal developments naturally led to the first coherent microscopic theory of ferromagnetism. Clearly the lowest state of a ferromagnet is characterized by a parallel alignment of spins. Discussing the sign of exchange energy, Néel [15] first introduced the concept of antiferromagnetism, a state in which two sublattices of spins in a crystal may align themselves antiparallel. Two years later the idea of "superexchange" first appeared when Kramers [16] tried to understand early adiabatic demagnetization measurements, which indicated that small exchange couplings existed even between ions separated by one or several diamagnetic groups. Finally, to these central themes of the microscopic theory of magnetism in insulators and semiconductors, one may add the basic ideas of the crystal field theory introduced by Van Vleck [17].

It was necessary to wait for the end of the 1950s to have a good understanding of superexchange interactions when Anderson first proposed a theory of coupling between identical ions characterized by a $3d^n$ electronic configuration, without orbital degeneracy ($n = 1$) [18, 19], later generalized to $n > 1$. In this case the exchange Hamiltonian is of the Heisenberg–Dirac type $J\boldsymbol{s}_1 \cdot \boldsymbol{s}_2$. Anderson's publication has been the starting point for generalizations, notably with the introduction of orbital degeneracy [20–23]. A recent generalization of the Anderson model has been derived by one of us for identical $3d^1$ ions A appearing in the symmetrical entity AXA, where X is a diamagnetic ligand. The exchange energy J of each bond A–X has been expressed *vs* fundamental molecular integrals characterizing each of the σ-type bonds created between the diamagnetic ligand and the magnetic ion A [24].

In this review, we consider the most general case of *two different magnetic* $3d^1$ *ions A and B characterized by* σ*-type bonds on both sides of the diamagnetic bridge X without the presence of a* π*-type overlap*. The cationic orbitals are of d-type whereas that of the diamagnetic ligand is of s- or p-type. The paper is ordered as follows. After a first section devoted to physical background, we will detail the key points of the Anderson model of superexchange as well the limits of this model and the Goodenough–Kanamori rules (Sect. 2). In Sect. 3 we shall consider the most general case of *two different magnetic* $3d^1$ *ions*. As for the entity AXA the exchange energy J of each bond A–X (or X–B) is expressed *vs* fundamental molecular integrals characterizing each of the σ-type bonds created between the diamagnetic ligand and the magnetic ion A or B. This *toy model* may be easily generalized to $3d^n$ ions (with $n > 1$). Under these conditions we show that this general treatment allows one to calculate superexchange interactions in any type of molecule. Doing so the exchange energy J of any bond is evaluated *vs* the key molecular integrals

characterizing this bond as well as the other bonds of the molecule. This aspect may reveal itself as being of high interest for biopolymers or molecules showing magnetic tunnelling, photomagnetism.

2
Physical Background

In this section we discuss the main difficulties which arise when describing the basic coupling of two electronic spins. This fundamental operation which is a purely quantum mechanism is of high interest whatever the nature of the considered exchange i.e., for *direct exchange* or *superexchange*. Here, for clarity and simplicity, we shall precisely define the problem of *direct exchange* only and see that the required theoretical adaptations of Anderson's model for *superexchange* use the same basic principles involved in the formal description of *direct exchange*. This will allow one to introduce in an easy way the main "technical" differences which will necessarily appear.

2.1
The Hamiltonian Symmetries and Pauli's Exclusion Principle

Let us consider a system containing N electrons, each one being labelled by the current index i ($i = 1, \ldots, N$). Each electron is characterized by its position $\boldsymbol{r}_i$ (with respect to the atom to which it belongs) and its spin $\boldsymbol{s}_i$. If we set $\boldsymbol{u}_i = (\boldsymbol{r}_i, \boldsymbol{s}_i)$, the corresponding Hamiltonian may be written:

$$H(\boldsymbol{u}_1, \boldsymbol{u}_2, \ldots, \boldsymbol{u}_i, \boldsymbol{u}_j, \ldots, \boldsymbol{u}_N) = \sum_{i=1}^{N}(T_i + V_i) + \sum_{i \neq j} U_{i,j} \tag{1}$$

where T_i is the kinetic energy of each particle i, V_i the corresponding potential energy and $U_{i,j}$ the interaction potential between two different electrons i and j i.e.,

$$T_i = -\frac{\hbar^2}{2m}\nabla_i^2, \quad V_i = V(\boldsymbol{r}_i), \quad U_{i,j} = U(\boldsymbol{r}_i, \boldsymbol{r}_j)\,. \tag{2}$$

H is even with respect to the interchange of any particle index (double symmetry group for each pair). As a result of group theory we immediately derive that the corresponding eigenstates are either even or odd:

$$\Psi(\boldsymbol{u}_1, \boldsymbol{u}_2, \ldots, \boldsymbol{u}_i, \ldots, \boldsymbol{u}_j, \ldots, \boldsymbol{u}_N) = \pm\Psi(\boldsymbol{u}_1, \boldsymbol{u}_2, \ldots, \boldsymbol{u}_j, \ldots, \boldsymbol{u}_i, \ldots, \boldsymbol{u}_N)\,, \tag{3}$$

so that many types of solutions combining all the pair behaviours (symmetry or antisymmetry) are possible. However Pauli's exclusion principle states that the eigenstates which are relevant when dealing with electrons (i.e., fermions

characterized by half-integer spins) must be strictly odd with respect to the interchange of any two particle indices:

$$\Psi(\boldsymbol{u}_1, \boldsymbol{u}_2, \ldots, \boldsymbol{u}_i, \ldots, \boldsymbol{u}_j, \ldots, \boldsymbol{u}_N) = -\Psi(\boldsymbol{u}_1, \boldsymbol{u}_2, \ldots, \boldsymbol{u}_j, \ldots, \boldsymbol{u}_i, \ldots, \boldsymbol{u}_N)\,, \quad (4)$$

bringing a considerable restriction to the available solution domain.

2.2 Formal Coupling of Two Electrons Initially Isolated and Their Binding to a Single Atom

Let us consider the formal case of two electrons labelled 1 and 2, respectively, initially isolated and which may couple their spin. We suppose that there is no spin-orbit coupling. As a consequence, the orbital and spin parts of the collective wave function describing the system of coupled electrons are disconnected i.e.,

$$\Psi(\boldsymbol{u}_1, \boldsymbol{u}_2) = \Phi(\boldsymbol{r}_1, \boldsymbol{r}_2)\chi(\boldsymbol{s}_1, \boldsymbol{s}_2)\,. \quad (5)$$

The Hamiltonian given by Eq. 1 (in which $V_1 = V_2 = 0$) only determines the orbital contribution:

$$H\Phi(\boldsymbol{r}_1, \boldsymbol{r}_2) = E\Phi(\boldsymbol{r}_1, \boldsymbol{r}_2)\,. \quad (6)$$

Pauli's exclusion principle imposes that either $\Phi(\boldsymbol{r}_1, \boldsymbol{r}_2)$ or $\chi(\boldsymbol{s}_1, \boldsymbol{s}_2)$ must be odd (the other one remaining even) with respect to the interchange of indices 1 and 2. If the Coulomb repulsion $U(\boldsymbol{r}_1, \boldsymbol{r}_2) = e^2/4\pi\varepsilon_0|\boldsymbol{r}_1 - \boldsymbol{r}_2|$ between both electrons is small, this contribution to the Hamiltonian H may be considered as a perturbation. Let $\Phi_a(\boldsymbol{r})$ (respectively, $\Phi_b(\boldsymbol{r})$) be the eigenstate of the Hamiltonian $H_1 = T_1 = \boldsymbol{p}_1^2/2m$ (respectively, $H_2 = T_2 = \boldsymbol{p}_2^2/2m$) characterized by the eigenvalue E_a (respectively, E_b). In this framework, this approximation allows us to solve the well-known secular equation $\det(H - E\mathbf{1}) = 0$ (where $\mathbf{1}$ is the identity matrix and $H = T_1 + T_2 + U(\boldsymbol{r}_1, \boldsymbol{r}_2)$). In the subspace spanned by the spatially symmetrical and antisymmetrical wave functions $\Phi_S(\boldsymbol{r}_1, \boldsymbol{r}_2)$ and $\Phi_A(\boldsymbol{r}_1, \boldsymbol{r}_2)$ containing functions $\Phi_a(\boldsymbol{r}_1)$ and $\Phi_b(\boldsymbol{r}_2)$, we have:

$$\Phi_S(\boldsymbol{r}_1, \boldsymbol{r}_2) = \frac{1}{\sqrt{2}}(\Phi_a(\boldsymbol{r}_1)\Phi_b(\boldsymbol{r}_2) + \Phi_a(\boldsymbol{r}_2)\Phi_b(\boldsymbol{r}_1))$$
$$\Phi_A(\boldsymbol{r}_1, \boldsymbol{r}_2) = \frac{1}{\sqrt{2}}(\Phi_a(\boldsymbol{r}_1)\Phi_b(\boldsymbol{r}_2) - \Phi_a(\boldsymbol{r}_2)\Phi_b(\boldsymbol{r}_1))\,. \quad (7)$$

Note that these functions are orthogonal by construction i.e., $\langle\Phi_S(\boldsymbol{r}_1, \boldsymbol{r}_2)|\Phi_A(\boldsymbol{r}_1, \boldsymbol{r}_2)\rangle = 0$, and are the eigenstates of the permutation operator P of both particles:

$$P\Phi_S(\boldsymbol{r}_1, \boldsymbol{r}_2) = +\Phi_S(\boldsymbol{r}_1, \boldsymbol{r}_2), \quad P\Phi_A(\boldsymbol{r}_1, \boldsymbol{r}_2) = -\Phi_A(\boldsymbol{r}_1, \boldsymbol{r}_2)\,. \quad (8)$$

Let us now consider the spin part. As the spin states $|\boldsymbol{s}_1\rangle$ and $|\boldsymbol{s}_2\rangle$ are disconnected, the collective spin states $\chi(\boldsymbol{s}_1, \boldsymbol{s}_2) = |\boldsymbol{s}_1, \boldsymbol{s}_2\rangle$ may be written as direct

products $|s_1\rangle \otimes |s_2\rangle$. If one arbitrarily defines a z-direction in each spin space i.e., an axis of quantization, we have:

$$\chi(s_1, s_2) = |s_1, s_2\rangle = |s_1\rangle \otimes |s_2\rangle = \left|s_1^z\right\rangle \otimes \left|s_2^z\right\rangle = \left|s_1^z, s_2^z\right\rangle = \begin{cases} |\uparrow\uparrow\rangle \\ |\uparrow\downarrow\rangle \\ |\downarrow\uparrow\rangle \\ |\downarrow\downarrow\rangle \end{cases} \tag{9}$$

Even and odd linear combinations of these spin states may be built up. As there is no spin-orbit coupling, the full rotation group operates in each spin space with the representation $\mathcal{D}_{1/2}$ for a spin 1/2 associated with each electron. We have:

$$\mathcal{D}_{1/2} \otimes \mathcal{D}_{1/2} = \mathcal{D}_0 \oplus \mathcal{D}_1 \,, \tag{10}$$

where $\oplus$ is the direct sum symbol. It means that, if we introduce the total spin operators:

$$S = s_1 + s_2, \quad S^u = s_1^u + s_2^u, \quad u = x, \, y \text{ or } z \tag{11}$$

we may define a new basis $|S, S^z\rangle$ in a 4×4 dimensional space from the starting basis as $|s_1, s_2\rangle$ with $S = 0$ ($S^z = 0$, *singlet* state) and $S = 1$ ($S^z = 0, \pm 1$, *triplet* state):

$$\begin{aligned} &|0,0\rangle = \frac{1}{\sqrt{2}}(|\uparrow\downarrow\rangle - |\downarrow\uparrow\rangle), \qquad S = 0 \text{ (singlet state)} \\ &\left.\begin{aligned} &|1,1\rangle = |\uparrow\uparrow\rangle \,, \\ &|1,0\rangle = \tfrac{1}{\sqrt{2}}(|\uparrow\downarrow\rangle + |\uparrow\downarrow\rangle), \\ &|1,-1\rangle = |\downarrow\downarrow\rangle \end{aligned}\right\} \quad S = 1 \text{ (triplet state)} \end{aligned} \tag{12}$$

The triplet states $|1, S^z\rangle$ are even with respect to the interchange of indices 1 and 2, while the singlet state $|0,0\rangle$ is odd. Consequently, because of Pauli's exclusion principle, we have the following symmetries:

$$\begin{aligned} &S = 1 \quad \chi(s_1, s_2) = |s_1, s_2\rangle \quad \text{even}, \qquad \Phi(r_1, r_2) = \Phi_{\mathrm{A}}(r_1, r_2) \quad \text{odd} \\ &S = 0 \quad \chi(s_1, s_2) = |s_1, s_2\rangle \quad \text{odd}, \qquad \Phi(r_1, r_2) = \Phi_{\mathrm{S}}(r_1, r_2) \quad \text{even} \,. \end{aligned} \tag{13}$$

From a physical point of view, a singlet state ($S = 0$) *will be a non-magnetic state* (*i.e., a purely diamagnetic state*) *whereas the triplet state* ($S = 1$) *will be a magnetic one.*

Now we wish to express the Hamiltonian H given by Eq. 1 *vs* spin operators, exclusively. As H commutes with the permutation operator P, its representation in the subspace spanned by the basis functions $\Phi_{\mathrm{S}}(r_1, r_2)$ and $\Phi_{\mathrm{A}}(r_1, r_2)$ is diagonal:

$$H = \begin{pmatrix} E_a + E_b + u + j & 0 \\ 0 & E_a + E_b + u - j \end{pmatrix} \tag{14}$$

where E_a and E_b are the eigenvalues associated with the eigenstates $\Phi_a(\boldsymbol{r}_1)$ and $\Phi_b(\boldsymbol{r}_2)$ appearing in $\Phi_S(\boldsymbol{r}_1, \boldsymbol{r}_2)$ and $\Phi_A(\boldsymbol{r}_1, \boldsymbol{r}_2)$ given by Eq. 7; similarly u and j are defined as:

$$u = \int \mathrm{d}\boldsymbol{r}_1 \, \mathrm{d}\boldsymbol{r}_2 |\Phi_a(\boldsymbol{r}_1)|^2 U(\boldsymbol{r}_1, \boldsymbol{r}_2) |\Phi_b(\boldsymbol{r}_2)|^2$$

$$j = \int \mathrm{d}\boldsymbol{r}_1 \, \mathrm{d}\boldsymbol{r}_2 \Phi_a^*(\boldsymbol{r}_1) \Phi_b^*(\boldsymbol{r}_2) U(\boldsymbol{r}_1, \boldsymbol{r}_2) \Phi_b(\boldsymbol{r}_1) \Phi_a(\boldsymbol{r}_2) \tag{15}$$

u is the Hartree term (or direct term) whereas j is the Fock term (or exchange term). j is nothing but the electrostatic energy of the charge distribution $-e\Phi_a^*(\boldsymbol{r})\Phi_b(\boldsymbol{r})$ and is positive definite. As a consequence, if we examine Eq. 7 where the spatially symmetrical and antisymmetrical wave functions are defined, we derive that the *function* $\Phi_A(\boldsymbol{r}_1, \boldsymbol{r}_2)$ *corresponds to the state of lowest energy*. Owing to Pauli's exclusion principle, it is associated with *the triplet spin state* ($S = 1$, *cf* Eq. 12) characterized by a symmetrical spin function. Under these conditions, the singlet state ($S = 0$ and antisymmetrical spin wave function, *cf* Eq. 12) is associated with a spatially symmetrical wave function $\Phi_S(\boldsymbol{r}_1, \boldsymbol{r}_2)$ and characterizes the state of highest energy. At this step the physical interpretation is easy: the Coulomb repulsion between both electrons favours the state with a parallel spin alignment (see comments below about Hund's rule). The energy

$$J = E_{S,0} - E_{T,0} = 2j \,, \tag{16}$$

where $E_{S,0}$ and $E_{T,0}$ are the energies associated with the low-lying singlet and triplet states, is called "exchange energy". It characterizes the process of *direct exchange* between two electronic spins. As noted by Herring [25], it is possible to give a physical picture for describing this quantity. If we consider both electrons at the time origin $t = 0$ and in the initial state $\Phi_a(\boldsymbol{r}_1)\Phi_b(\boldsymbol{r}_2)$, the potential $U(\boldsymbol{r}_1, \boldsymbol{r}_2)$ achieves a connection with the permuted state $\Phi_a(\boldsymbol{r}_2)\Phi_b(\boldsymbol{r}_1)$ by the bias of the matrix element j. Over a small time range Δt, the probability amplitude of the permuted state increases as $j\Delta t$ ($j > 0$). In other words j measures the initial ratio with which two tagged electrons, placed one in each state, may be exchanged between these states.

It is straightforwardly shown that the spectrum and the eigenvalues of the effective spin Hamiltonian (expressed in $\hbar$ units)

$$H_{\mathrm{eff}} = E_0 \mathbf{1} - J\boldsymbol{s}_1 \cdot \boldsymbol{s}_2, \quad E_0 = E_a + E_b + u - \frac{j}{2} \tag{17}$$

coincide with those of H defined by Eq. 1, restricted to the two electrons 1 and 2, with $V_1 = V_2 = 0$, the spin operator of which is given by the set of Pauli's matrices $\boldsymbol{\sigma}_1$ and $\boldsymbol{\sigma}_2$ (with $\boldsymbol{s}_i = \hbar\boldsymbol{\sigma}_i/2$, $i = 1, 2$). $\mathbf{1}$ is the 4×4 identity matrix. The quantity $-J\boldsymbol{s}_1 \cdot \boldsymbol{s}_2$ is called *exchange Hamiltonian*. Then, if we express the

projector operators P_T and P_S on the triplet and singlet states, respectively, we have for spins 1/2 (in $\hbar$ unit):

$$P_T = \frac{3}{4}\mathbf{1} + \boldsymbol{s}_1 \cdot \boldsymbol{s}_2, \quad P_S = \frac{1}{4}\mathbf{1} - \boldsymbol{s}_1 \cdot \boldsymbol{s}_2 \tag{18}$$

so that:

$$H_{\text{eff}} = E_0\mathbf{1} - \frac{j}{2}(P_T - 3P_S) \tag{19}$$

corresponds to the electronic Hamiltonian expressed in terms of the singlet and triplet states.

Now, this study may be simply extended to the case of a single atom with two-valency electrons, simply by adding the Coulomb potential $U(\boldsymbol{r})$. This effective potential describes the global interaction of the nucleus and the internal electronic shells with the two-valency electrons, belonging to the external shell. If the Coulomb repulsion between these electrons may be neglected, a treatment similar to the previous case of the two isolated electrons may be set on: this is the well-known *Hartree–Fock approximation*. We immediately derive that the atom with two-valency electrons has a ground state which is a triplet, thus satisfying Hund's rule. The effective Hamiltonian is given by Eq. 17 where E_a and E_b must be renormalized due to the presence of the extra term $U(\boldsymbol{r})$ in H_1 and H_2.

2.3 What are the Formal Difficulties and the Usual Approximations Encountered when Describing an Atomic or a Molecular System?

The first fundamental point concerns the nature of the Hamiltonian used when describing any quantum system composed of interacting spins. We have previously seen that the spin–spin exchange coupling between two electrons initially isolated has a strictly orbital origin [26]. Furthermore the exchange coupling has appeared as a consequence of the interplay between Pauli's exclusion principle and various energy terms. Thus, any term T_1, T_2, V_1, V_2 and/or U_{12}, ... may contribute to the exchange coupling between two electrons, through the energy difference of the singlet and triplet states, $E_{S,0} - E_{T,0}$ (see Fig. 1 where the excited states are also reported, the ground state being the triplet). The use of the spin–spin Hamiltonian $-J\boldsymbol{s}_i \cdot \boldsymbol{s}_j$, with here $J = E_{S,0} - E_{T,0}$, is submitted to the two conditions: (i) $J \ll \Delta$ and (ii) $k_B T \ll \Delta$ where T is the absolute temperature, k_B the Boltzmann's constant and $\Delta = E_{S,1} - E_{S,0}$ is the difference between the ground state and the first excited state energies in the singlet spectrum.

At this step we must mention that the energy level spectrum described in Fig. 1 corresponds to a case often encountered in molecular systems. In

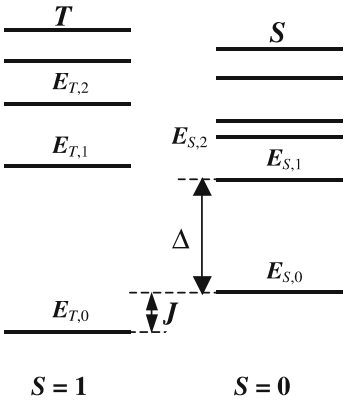

Fig. 1 Description of a commonly encountered molecular energy level spectrum; the singlet ($S = 0$) and triplet ($S = 1$) spectra have been artificially separated

addition the following spin Hamiltonian

$$H = E_0\mathbf{1} + J\boldsymbol{s}_1 \cdot \boldsymbol{s}_2, \quad J = -(E_{\mathrm{S},0} - E_{\mathrm{T},0}) \tag{20}$$

may be conventionally employed ($J > 0$ corresponds to an antiferromagnetic arrangement, with $E_{\mathrm{T},0} > E_{\mathrm{S},0}$, whereas $J < 0$ corresponds to a ferromagnetic one, with $E_{\mathrm{T},0} < E_{\mathrm{S},0}$). Slight modifications in the crystal structure (for instance due to the static or dynamical Jahn–Teller effect [27, 28]) or in the molecular arrangement (crystallized or solvated state) should have strong effects on exchange couplings and, correlatively, on the ground state spin of the molecule.

Finally we must examine the property of additivity of the exchange Hamiltonian. Let us consider, for instance, four interacting electrons and let us specifically examine the exchange coupling between electrons 1 and 2. The effect of electrons 3 and 4 is treated through the effective (mean) potentials $\delta V(\boldsymbol{r}_1)$ and $\delta V(\boldsymbol{r}_2)$ "seen" by electrons 1 and 2 (*Hartree–Fock approximation*). Under these conditions the general Hamiltonian for electrons 1 and 2 may be written:

$$H(\boldsymbol{r}_1, \boldsymbol{r}_2) + \delta H(\boldsymbol{r}_1, \boldsymbol{r}_2) = \sum_{i=1}^{2}(T_i + V_i) + \frac{e^2}{4\pi\varepsilon_0 r_{12}} + \delta V(\boldsymbol{r}_1) + \delta V(\boldsymbol{r}_2) \tag{21}$$

where T_i and V_i are given by Eq. 2 and $r_{12} = |\boldsymbol{r}_1 - \boldsymbol{r}_2|$. The energies of the even and odd low-lying solutions allow one to define the effective exchange constant J_{12} between spins $\boldsymbol{s}_1$ and $\boldsymbol{s}_2$. Through $\delta H(\boldsymbol{r}_1, \boldsymbol{r}_2) = \delta V(\boldsymbol{r}_1) + \delta V(\boldsymbol{r}_2)$, J_{12} depends on the mean distribution (orbital functions) of electrons 3 and 4, which depends itself on the relative orientation of spins $\boldsymbol{s}_3$ and $\boldsymbol{s}_4$:

$$J_{12} = J_{12}(\boldsymbol{s}_3 \cdot \boldsymbol{s}_4)\,. \tag{22}$$

Hence the exchange Hamiltonian may be written as:

$$H_{ex}(\boldsymbol{s}_1, \boldsymbol{s}_2) = -J_{12}(\boldsymbol{s}_3 \cdot \boldsymbol{s}_4)\boldsymbol{s}_1 \cdot \boldsymbol{s}_2 \,. \tag{23}$$

Of course this argument holds for the six distinct electron pairs and, in the present Hartree–Fock approach, the general Hamiltonian will be:

$$H_{ex}(\boldsymbol{s}_1, \boldsymbol{s}_2, \boldsymbol{s}_3, \boldsymbol{s}_4) = \sum_i \sum_{j \neq i} H_{ex}(\boldsymbol{s}_i, \boldsymbol{s}_j) \,. \tag{24}$$

This simple form of the exchange Hamiltonian will be severely complicated by the introduction of spin–orbit couplings [29]. Some questions resulting from the presence of this kind of coupling will be examined in the next subsection.

In the general case where more than two spins interact, several contributions to the Hamiltonian may co-exist and compete. As a consequence, it would be necessary to introduce higher-order couplings involving all the mechanisms describing the totality of spin interactions. In this respect a special review has been achieved by Herring [25]. However, due to the specific treatment of higher-order couplings, this aspect will not be evoked in the present article in spite of the fact that the importance of these couplings has been pointed out since the beginning of the 1960s. More particularly we shall see that the general model proposed in this article for superexchange and involving fundamental molecular integrals allows one to avoid this difficulty.

The second fundamental point concerns the nature of wave functions that must be employed when dealing with molecules. In 1927 Heitler and London [30–35] gave the first treatment for atoms coupling to form molecules by considering the particular case of the dihydrogen molecule. They assumed spatial wave functions of the same form, as those given by Eq. 7. But, the important mass difference between electrons and nuclei allowed them to fix the nuclei positions $\boldsymbol{R}_a$ and $\boldsymbol{R}_b$. As a consequence, the Hamiltonian describing the motion of the two electrons in the field of the two nuclei may be decomposed into two hydrogenoid contributions and a potential interaction describing the Coulomb repulsion between electrons (respectively, between protons) and the attraction with the other proton. This is the well-known *Born–Oppenheimer approximation* [36]. *It will be always used when treating quantum atomic or molecular systems*. Under these conditions the Hamiltonian may be written:

$$H = H_{1a}(\boldsymbol{r}_1) + H_{2b}(\boldsymbol{r}_2) + U_{int}(\boldsymbol{r}_1, \boldsymbol{r}_2) \tag{25}$$

with:

$$H_{1a}(\boldsymbol{r}_1) = \frac{\boldsymbol{p}_1^2}{2m} - \frac{e^2}{4\pi\varepsilon_0 r_{1a}}, \quad H_{2b}(\boldsymbol{r}_2) = \frac{\boldsymbol{p}_2^2}{2m} - \frac{e^2}{4\pi\varepsilon_0 r_{2b}}$$
$$U_{int}(\boldsymbol{r}_1, \boldsymbol{r}_2) = \frac{e^2}{4\pi\varepsilon_0}\left(\frac{1}{R_{ab}} + \frac{1}{r_{12}} - \frac{1}{r_{2a}} - \frac{1}{r_{1b}}\right) \tag{26}$$

where the various distances r_{1a}, r_{1b}, r_{2a}, r_{2b}, r_{12} and R_{ab} are defined in Fig. 2.

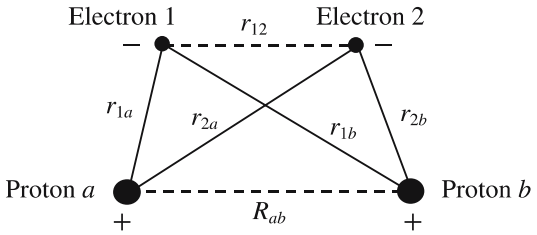

Fig. 2 Description of the distances between protons and electrons in the molecule H_2; the *dashed lines* correspond to repulsive interactions

Let $\Phi_a(\boldsymbol{r}_1) = \Phi(\boldsymbol{r}_{1a})$ and $\Phi_b(\boldsymbol{r}_2) = \Phi(\boldsymbol{r}_{2b})$ be the eigenstates of Hamiltonians $H_{1a}(\boldsymbol{r}_1)$ and $H_{2b}(\boldsymbol{r}_2)$, respectively; the corresponding ground state is characterized by the energy E_0^*. The approximation consisting in *the choice of free-atom wave function for each atom of the molecule* is called *Heitler–London approximation*. Oppositely to the case of the formal coupling of two electrons where the orbitals are orthogonal by definition, the orbitals $\Phi_a(\boldsymbol{r}_1) = \Phi(\boldsymbol{r}_{1a})$ and $\Phi_b(\boldsymbol{r}_2) = \Phi(\boldsymbol{r}_{2b})$ are not orthogonal and allow one to construct the spatially symmetrical and antisymmetrical wave functions of the two electrons of the molecule:

$$\Phi_{\mathrm{S}}(\boldsymbol{r}_1, \boldsymbol{r}_2) = \frac{1}{\sqrt{2(1+\mathrm{S}^2)}} \left(\Phi_a(\boldsymbol{r}_1)\Phi_b(\boldsymbol{r}_2) + \Phi_a(\boldsymbol{r}_2)\Phi_b(\boldsymbol{r}_1)\right)$$
$$\Phi_{\mathrm{A}}(\boldsymbol{r}_1, \boldsymbol{r}_2) = \frac{1}{\sqrt{2(1-\mathrm{S}^2)}} \left(\Phi_a(\boldsymbol{r}_1)\Phi_b(\boldsymbol{r}_2) - \Phi_a(\boldsymbol{r}_2)\Phi_b(\boldsymbol{r}_1)\right) . \tag{27}$$

They are eigenfunctions of the permutation operator (see Eq. 8) and are orthogonal. They have been normalized by introducing the overlap integral S:

$$\mathrm{S} = \int \mathrm{d}\boldsymbol{r}\Phi_a^*(\boldsymbol{r})\Phi_b(\boldsymbol{r}) . \tag{28}$$

The terms of Hartree u (direct term) and Fock j (exchange term) may be defined as in Eq. 15 where $U(\boldsymbol{r}_1, \boldsymbol{r}_2)$ is here $U_{\mathrm{int}}(\boldsymbol{r}_1, \boldsymbol{r}_2)$ given by Eq. 26.

In addition the spatial wave functions $\Phi_{\mathrm{S}}(\boldsymbol{r}_1, \boldsymbol{r}_2)$ and $\Phi_{\mathrm{A}}(\boldsymbol{r}_1, \boldsymbol{r}_2)$ must be multiplied by the spin wave function of the adequate symmetry, as imposed by Pauli's exclusion principle (see Eq. 13). Achieving the same reasoning as for the formal coupling of two electrons, it is easy to derive:

$$J = E_{\mathrm{S},0} - E_{\mathrm{T},0} = -2\frac{u\mathrm{S}^2 - j}{1-\mathrm{S}^4} . \tag{29}$$

The associated effective Hamiltonian expressed in terms of spin operators is:

$$H_{\mathrm{eff}} = E_0\mathbf{1} - J\boldsymbol{s}_1 \cdot \boldsymbol{s}_2, \quad E_0 = 2E_0^* + \frac{u - j\mathrm{S}^2}{1-\mathrm{S}^4} - \frac{J}{4} . \tag{30}$$

Ignoring the first two terms in E_0, we find that the eigenvalues of H_{eff} are $-J/4$ (triplet state) and $3J/4$ (singlet state) in $\hbar$ unit, thus reproducing the electronic spectrum. When the separation between hydrogen atoms is large enough, the overlap S is small, and we have:

$$J \approx 2(j - uS^2)\,. \tag{31}$$

As for a single atom, j is an electrostatic energy and is positive definite, as u. Thus, J appears as the difference of two positive quantities and may be: (i) positive, $E_{S,0} > E_{T,0}$ and the ground state is characterized by a ferromagnetic spin arrangement with a spatially antisymmetrical wave function $\Phi_A(\boldsymbol{r}_1, \boldsymbol{r}_2)$; (ii) negative, $E_{S,0} < E_{T,0}$ and the ground state is characterized by an antiferromagnetic spin arrangement with a spatially symmetrical wave function $\Phi_S(\boldsymbol{r}_1, \boldsymbol{r}_2)$.

A calculation shows that, for realistic values of the separation distance R_{ab} between the two protons, case (ii) prevails (antiferromagnetic arrangement). However, for large values R_{ab}, case (i) now prevails (ferromagnetic arrangement). Sugiura [37] has given an exact evaluation of the difference $E_{S,0} - E_{T,0}$ for the case where $\Phi_a(\boldsymbol{r}_1)$ and $\Phi_b(\boldsymbol{r}_2)$ are hydrogenic 1s eigenfunctions:

$$J = E_{S,0} - E_{T,0} \approx \left[-\frac{56}{45} + \frac{4}{15}\gamma + \frac{4}{15}\ln\left(\frac{R}{a_H}\right)\right]\left(\frac{R}{a_H}\right)^3 \exp\left(-2\frac{R}{a_H}\right)\,, \tag{32}$$

where $\gamma = 0.577$ is the Euler's constant and a_H is the radius of hydrogen atom (Bohr radius). Thus, for reasonable values of R, $J < 0$ (antiferromagnetic arrangement) but $J > 0$ (ferromagnetic arrangement) at very large R values because of the logarithm. Unfortunately the latter result contradicts a theorem established by Courant ([38, 39], Chap. VI, Sect. 6; 25) that states that the ground state eigenfunction of a semi-bounded Sturm–Liouville differential operator, acting in a space of any dimension, must be free from nodes. *In the H_2 problem, this means that, for any R, the ground state must be a singlet* (the triplet being characterized by a spatially antisymmetrical wave function). This problem simply comes from the fact that, using atomic orbitals in the *Heitler–London approximation*, electron–electron correlations are not very well accounted for. The presence of a second atom induces a polarization in the atomic orbitals and increases the probability of finding the electrons between the two protons. In addition, the two electrons do not exchange themselves on the axis joining the two protons because both electrons try to avoid each other to minimise the Coulomb repulsion.

Nevertheless this method has been successfully used by Van Vleck when establishing the nature of the effective Hamiltonian for a magnetic insulator [40]. In that case, the electrons involved in the magnetic properties are localized on each atom. In other words, an *assumption of localization* is made for each free-atom wave function: its magnitude decreases exponentially when any electron is removed to a large distance from the center $\boldsymbol{R}_{i(m)}$ of

its own atom $i(m)$ so that it may be written as $C \exp\left(-\sum_m \alpha_{i(m)} \left|\boldsymbol{r}_m - \boldsymbol{R}_{i(m)}\right|\right)$, where C is an algebraic factor and $\alpha_{i(m)}$ is the decay constant of the atomic wave function. Due to the fact that the electrons belonging to different atoms are weakly correlated, the overlaps between atomic orbitals are weak and the Heitler–London approximation is plainly justified. The main credit of Van Vleck's work [40] was to point out that *the exchange energy J characterizing the direct exchange between the involved electrons is determined by the coordinate functions and the symmetries of the problem*. When giving below the general model for superexchange, we shall see that a similar physical situation occurs with the coupling of the electrons belonging to the magnetic ion and the diamagnetic ligand, respectively.

All the problems evoked in this subsection have been thoroughly and recently examined by Silvi et al. for the topological analysis of the electron localization function [41] and by Bocă and Linert [42] for the dihydrogen molecule and the related molecular cation and anion.

2.4 The Problem of Spin-orbit Coupling and its Consequences

In the absence of interactions, electrons are described by the Dirac equation (1928), which rules out the quantum relativistic motion of an electron in static electric and magnetic fields $\boldsymbol{E} = -\nabla U$ and $\boldsymbol{B} = \mathbf{curl}\, \boldsymbol{A}$ (where U and $\boldsymbol{A}$ are the scalar and vectorial potentials, respectively) [43–45]. As the electrons involved in a solid structure are characterized by a small velocity with respect to the light celerity c ($v/c \sim 10^{-2}$) a $1/c$-expansion of the Dirac equation may be achieved. More details are given in a paper published by one of us [46]. At the zeroth order, the Pauli equation (1927), in which the electronic spin contribution appears, is retrieved then conferring to this last one a relativistic origin. At first order the spin-orbit interaction arises and is described by the following Hamiltonian H^e_{so}:

$$H^e_{\mathrm{so}} = -\frac{\mu_{\mathrm{B}}}{2mc^2}\boldsymbol{\sigma} \cdot (\boldsymbol{E} \times (\boldsymbol{p} - q\boldsymbol{A}))\,, \tag{33}$$

where $\mu_{\mathrm{B}} = -e\hbar/2m$ is the Bohr magneton. This Hamiltonian H^e_{so} may be rewritten under the form (for a vanishing field $\boldsymbol{B}$ i.e., for $\boldsymbol{A} = \boldsymbol{0}$):

$$H^e_{\mathrm{so}} = \lambda^e(r)\boldsymbol{\ell} \cdot \boldsymbol{s}, \quad \lambda^e(r) = \frac{1}{2m^2c^2r}\frac{\mathrm{d}V(r)}{\mathrm{d}r}, \quad \boldsymbol{\ell} = \boldsymbol{r} \times \boldsymbol{p}, \quad \boldsymbol{s} = \frac{\hbar}{2}\boldsymbol{\sigma}\,. \tag{34}$$

For an atom composed of N electrons, the spin-orbit Hamiltonian is simply:

$$H_{\mathrm{so}} = \sum_{i=1}^{N} \lambda^e(r_i)\boldsymbol{\ell}_i \cdot \boldsymbol{s}_i, \quad \lambda^e(r_i) = \frac{1}{2m^2c^2r_i}\frac{\mathrm{d}V(r_i)}{\mathrm{d}r_i}\,. \tag{35}$$

If we define the total orbital momentum $\boldsymbol{L} = \sum_{i=1}^{N} \boldsymbol{\ell}_i$ and the total spin momentum $\boldsymbol{S} = \sum_{i=1}^{N} \boldsymbol{s}_i$, $\boldsymbol{L}$ and $\boldsymbol{S}$ are no more constants of motion, separately,

due to the fact that the spin momentum of each electron is coupled to its orbital momentum. However, the total momentum $\boldsymbol{\mathcal{J}} = \boldsymbol{L} + \boldsymbol{S}$ becomes the new constant of motion as well as its projection $M_J = M_L + M_S$ along the z-axis of quantization. In addition, owing to the Wigner–Eckart theorem which states that, inside each multiplicity $\mathcal{J}$, all the vectorial operators have identical matrix elements *via* a multiplicative constant, Eq. 34 may be replaced by:

$$H_{so} = \lambda \boldsymbol{L} \cdot \boldsymbol{S} \,. \tag{36}$$

Under these conditions, if we consider the coupling relation $\boldsymbol{\mathcal{J}} = \boldsymbol{L} + \boldsymbol{S}$, the orbital momentum $\boldsymbol{L}$ acts in a space $\mathcal{E}_L$ (with $\dim\mathcal{E}_L = 2L + 1$) and the spin momentum $\boldsymbol{S}$ in a space $\mathcal{E}_S$ (with $\dim\mathcal{E}_S = 2S + 1$). Consequently, the total momentum $\boldsymbol{\mathcal{J}}$ acts in the tensorial product space $\mathcal{E}_J = \mathcal{E}_L \otimes \mathcal{E}_S$ (with $\dim\mathcal{E}_J = (2L + 1) \times (2S + 1)$). A basis of this new space is given by $|LM_LSM_S\rangle = |LM_L\rangle \otimes |SM_S\rangle$. Then important consequences appear.

(i) The spin-orbit coupling splits $(2\mathcal{J} + 1)$ times each initial multiplet characterized by the set $\{LM_LSM_S\}$. As just seen, the spaces $\mathcal{E}_L$ (which is linked to the crystallographic group space) and $\mathcal{E}_S$ (spin space) are coupled so that *a relation of the type $\Phi(\boldsymbol{r}_i)\chi(\boldsymbol{s}_i)$ given by Eq. 5 is no longer valid ($\Phi(\boldsymbol{r}_i)$ and $\chi(\boldsymbol{s}_i)$ being eigenfunctions of the crystallographic and spin spaces, respectively).*

(ii) *Hund's rules* [12, 13] may be derived. These rules try to explain how Coulomb repulsion and Pauli's exclusion principle must be considered simultaneously. This aspect has been thoroughly examined in a recent paper [46]. *Hund's rules are exclusively valid for ground state configurations* and we must have: $S = S_{max}$, $L = L_{max}$ (for $S = S_{max}$) *compatible with the exclusion principle; the eigenvalue of the total orbital momentum $\boldsymbol{\mathcal{J}} = \boldsymbol{L} + \boldsymbol{S}$ is $\mathcal{J} = |L - S|$ if the shell is at most half-filled ($\boldsymbol{L}$ and $\boldsymbol{S}$ are antiparallel) and $\mathcal{J} = L + S$ if the shell is more than half-filled ($\boldsymbol{L}$ and $\boldsymbol{S}$ are parallel).*

(iii) When the spin-orbit contribution remains small, a perturbation theory may be used. For instance, this is the case of 3*d* transition ions (for which the mean value of orbital momentum in the ground state $|0\rangle$ is null due to time reversal symmetry). In a first step, if one examines the case of a single ion, one may use an effective Hamiltonian H_{eff} acting on the spin states of the subspace $|0\rangle$. At second order, the corresponding eingenvalue E_{eff} is:

$$E_{eff} = \langle 0| \left(H_Z + H_{so}\right) |0\rangle \,, \quad H_Z = -\left(g_L \boldsymbol{L} + g_S \boldsymbol{S}\right)\mu_B \boldsymbol{B} \,, \tag{37}$$

where H_{so} is defined by Eq. 36, g_L and g_S are Landé factors, respectively, associated with the orbital and spin momenta and are given by $g_L = 1$ and $g_S = 2$. Expanding E_{eff} at second order in perturbation theory, this allows one to introduce the tensor of anisotropy Λ and the correspond-

ing Hamiltonian. As a consequence the Landé factor becomes anisotropic and is described by the g-tensor: $g_{ij} = g_S\delta_{ij} - g_L\lambda\Lambda_{ij}$, where δ_{ij} is the Kronecker symbol. When two magnetic ions characterized by spins $\boldsymbol{S}_1$ and $\boldsymbol{S}_2$, respectively, are involved, a similar treatment may be achieved but, now, an exchange interaction J between both ions must be added [47]. It leads to the Dzialoshinski–Moriya contribution [48–50] characterized by the following Hamiltonian H_{DM} [46–50]:

$$H_{\mathrm{DM}} = \boldsymbol{D}\cdot(\boldsymbol{S}_1 \times \boldsymbol{S}_2)\,, \tag{38}$$

where $\boldsymbol{D}$ is called the Dzialoshinski–Moriya vector.

(iv) Taking into account all the previous remarks, a general Hamiltonian may finally be written between two magnetic centres A and B as:

$$H = -J\boldsymbol{S}_{\mathrm{A}}\cdot\boldsymbol{S}_{\mathrm{B}} + \boldsymbol{S}_{\mathrm{A}}(\Lambda)\boldsymbol{S}_{\mathrm{B}} + \boldsymbol{D}\cdot(\boldsymbol{S}_{\mathrm{A}}\times\boldsymbol{S}_{\mathrm{B}}) + \ldots \tag{39}$$

the ellipses representing the possible contribution of higher-order couplings. *This Hamiltonian is a purely phenomenological one.* J appears as the difference between the first low-lying energy levels with $S = 0$ and $S = 1$ (cf. Eq. 16 and Fig. 1); the tensor Λ and the vector $\boldsymbol{D}$ have just been defined above. These two latter contributions come from the presence of spin-orbit coupling whereas higher-order couplings (omitted here for clarity) have a completely different origin. In other words, the first term in Eq. 39 leads to a singlet–triplet splitting; the second term splits the triplet state and the third one couples the singlet and triplet states. As for the spin-orbit coupling, it shows itself a domain of validity (for more details see [46]). In conclusion, *the phenomenological Hamiltonian* given by Eq. 1 *shows eigenvalues which correspond to the experimental low-lying states but does not provide any information on the microscopic mechanisms really involved so that it has no predictive character*. Consequently, it becomes necessary to built up a new microscopic Hamiltonian.

2.5 The Concept of Magnetic Orbital [51, 52]

Let us consider the simplest case of an A–B bimetallic system in which A and B are metal ions surrounded by their ligands, with a common ligand between A and B. In addition the ground states of A and B are both characterized by one unpaired electron. As a consequence, the interaction between the two single-ion doublet states gives rise to molecular singlet and triplet states and the singlet-triplet energy gap, J, is a physical observable and not a simple phenomenological parameter. Due to the *non-predictive character of the phenomenological Hamiltonian* (*cf* Eq. 39), it becomes necessary to use a *microscopic Hamiltonian* taking into account the kinetic

energy of the unpaired electrons T_i on A and B, the electron-cores potential energies V_i and the electrostatic interaction between the electrons of the system:

$$H_{\text{micro}} = \sum_{i=1}^{n}(T_i + V_i) + \sum_{i=1}^{n}\sum_{i<j}\frac{e^2}{4\pi\varepsilon_0 r_{ij}} + H_{\text{so}}\,, \tag{40}$$

where $r_{ij} = |\boldsymbol{r}_i - \boldsymbol{r}_j|$ is an interelectronic distance and H_{so} is the spin-orbit coupling Hamiltonian. In this article, we shall take $H_{\text{so}} = 0$. Of course, the microscopic Hamiltonian seems less easy to handle than the phenomenological one given by Eq. 1. However, the idea of comparing the eigenvalues of H_{micro} and H_{phen} may be maintained owing to justified approximations. In other words, each orbital model employed for finding the eigenvalues of H_{micro} must be precisely characterized by the nature of the chosen approximations.

Without interactions the wave functions describing A and B are simply:

$$\Phi_{\pm}(\boldsymbol{r}_1, \boldsymbol{r}_2) = \frac{1}{\sqrt{2}}\left[\Phi_{\text{A}}(\boldsymbol{r}_1)\Phi_{\text{B}}(\boldsymbol{r}_2) \pm \Phi_{\text{A}}(\boldsymbol{r}_2)\Phi_{\text{B}}(\boldsymbol{r}_1)\right], \tag{41}$$

where + holds for the singlet and – for the triplet. If the interaction between A and B is no longer zero but remains weak enough, the Heitler–London [30] function $\Phi_{\pm}(\boldsymbol{r}_1, \boldsymbol{r}_2)$ given by Eq. 41 is a good first-order approximation to describe the two low-lying states thermally populated. Note that the overlap $S = \langle\Phi_{\text{A}}(\boldsymbol{r}_1)|\Phi_{\text{B}}(\boldsymbol{r}_1)\rangle$ must appear in the normalization coefficient. The semi-localized orbitals Φ_{A} and Φ_{B}, which will describe the magnetic properties of A–B, are called *magnetic orbitals*. They are, in principle, non-orthogonal and the overlap S plays a key role in the description of the interaction between A and B. These non-orthogonal magnetic orbitals (NMO) have been named *natural* by Girerd et al. [53]. For most authors, the magnetic orbitals may be rigorously orthogonal by construction (OMO) [54]. In the case on which we focus, non-orthogonal magnetic orbitals (NMO) will be denoted Φ_{A} and Φ_{B} whereas orthogonal magnetic orbitals will be Φ'_{A} and Φ'_{B}.

Φ_{A} and Φ_{B} are chosen as the highest occupied molecular orbitals for the A (or B) fragment. Thus, Φ_{A} and Φ_{B} are nothing but the eigenfunctions of one-electron local Hamiltonians [55, 56]. By definition, they are centred on each metal ion and partially delocalized towards the surrounding ligands.

When Φ_{A} and Φ_{B} are orthogonalized through a Löwdin procedure [57]:

$$\begin{pmatrix}\Phi'_{\text{A}}\\ \Phi'_{\text{B}}\end{pmatrix} = \begin{pmatrix}1 & S\\ S & 1\end{pmatrix}^{-\frac{1}{2}}\begin{pmatrix}\Phi_{\text{A}}\\ \Phi_{\text{B}}\end{pmatrix}. \tag{42}$$

Φ'_{A} is still localized on centre A, with a residual contribution on centre B, outside the bridging region common to A and B, and increasing with the overlap [53]. Φ'_{A} and Φ'_{B} may be derived by another process. We

start from the two-highest singly occupied molecular orbitals φ_+ and φ_- for the low-lying triplet state of A–B. When A = B, Φ'_A and Φ'_B are given by [54]:

$$\Phi'_A = \frac{1}{\sqrt{2}}(\varphi_+ + \varphi_-)\,, \quad \Phi'_B = \frac{1}{\sqrt{2}}(\varphi_+ - \varphi_-)\,. \tag{43}$$

They are equivalent to the Wannier functions used by Anderson for periodic lattices (see below) [54]. Under these conditions, OMO's derived by Eqs. 42 and 43 are not strictly equivalent, simply due to the fact that the one-electron Hamiltonian of A–B is not the sum of the local Hamiltonians for A and B, considered separately. However, both types of OMO's show the same defect of localization. In addition, from a practical point of view, the OMO approach leads to much simpler calculations, as shown by Anderson [54], whereas the NMO approach is closer to the real mechanism involved in the nature of interaction and will favour the use of more realistic molecular integrals. From now and for clarity, magnetic orbitals will be written without the prime (′) notation.

3 Anderson Model for Superexchange

According to Anderson [54] *superexchange acquired its name because of the relatively large distances over which the exchange effect often was found to act between ions, radicals or molecules*. In other words (i) the *direct overlap* of the wave functions associated with the two magnetic centres separated by a non-magnetic bridge (or ligand) is quasi negligible [58]; (ii) the ligand wave function is slightly modified by the presence of the magnetic ions and (iii) the corresponding modification confers a magnetic character which is at the origin of the exchange interactions between the two ions. Under these conditions, Anderson [59] has considered the simplest modification: the transfer of one of the ionic ligand electron into the external shell of the magnetic ion. For instance, in the well-known case of 3*d* shells, this transfer could only take place into a partially empty *d* orbital. This transfer has been illustrated by measurements of the hyperfine interaction of the ligand nuclear spin in the presence of the "magnetic" ion. Indeed these results demonstrated graphically that the ligand wave function is partially magnetic, with the expected degree [60–63]. The electronic transfer of the spin up (down) of the diamagnetic ligand to the empty left (right) *d* orbital being ballistic, it conserves the spin, thus leading to an antiferromagnetic coupling. The diagram of Fig. 3 gives an illustration of the process leading to superexchange.

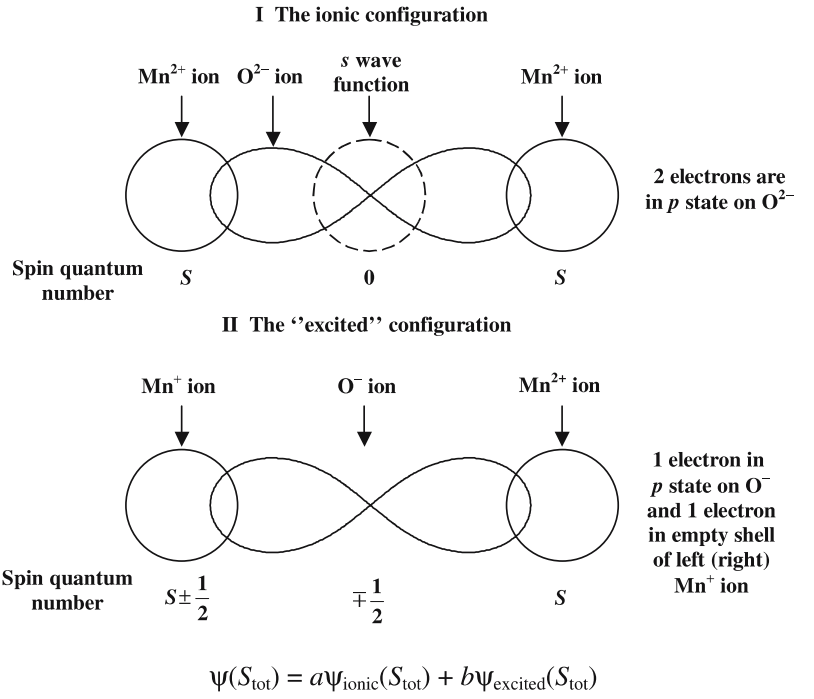

$$\psi(S_{\text{tot}}) = a\psi_{\text{ionic}}(S_{\text{tot}}) + b\psi_{\text{excited}}(S_{\text{tot}})$$

Fig. 3 "Ground" and "excited" configurations in the original superexchange process for the sequence Mn – O – Mn appearing in the crystallized compound MnO (from [54])

3.1 Description of Anderson Model

Of course, for treating analytically superexchange, the choice of wave functions is fundamental and finally conditions the important aspect of overlap. The main problem concerns the interaction of an electron with the rest of the lattice. This aspect is taken into account through the ligand field theory. As experimentally shown by the comparative NMR study of dilute and concentrated versions of a same compound, the electronic transfer from ligands is weak enough so that their wave functions are not strongly disturbed. Thus, one can consider that the wave function characterizing each magnetic ion is well-defined and is not drastically modified by its surrounding.

As a consequence, Anderson chose two levels of sophistication for treating the electrons belonging to the magnetic ions and the ligand, respectively. The first level consists in treating the extra electrons in terms of the simple one-electron Hartree–Fock functions while the second is treating them as excitations of a many-body system. Thus, Anderson considers the extra electrons in the periodic potential of the nuclei and the "core" electrons as

weak excitations of the "magnetic" electron system. It is important to note that core electrons (including those of the involved ligand) contribute to the self-consistent field and the "magnetic electrons" wave functions must be orthogonalized to all the cores. It interesting to remark that true spin polarization of the cores is considered as a minor effect, in contrast to the situation of the free (or "*s*") electrons in the Zener–Ruderman–Kittel exchange via free electrons in metals.

Under these conditions, the Coulomb interaction between the electrons involved in the collective wave function is introduced by the bias of the Hartree–Fock mean-field approximation. As previously seen in the introduction, an assumption concerning the starting magnetic configuration is required: Anderson chose a ferromagnetic configuration. This aspect could have been questionable but Kondo showed that there is no pernicious effect [64]. Then the secular problem may be solved self-consistently. The ligand field wave function $\varphi_i(\boldsymbol{r})$ is assumed to be a solution of the Hartree–Fock equations:

$$-\frac{\hbar^2}{2m}\nabla^2\varphi_i(\boldsymbol{r}) + \left[\left(V(\boldsymbol{r}) + \sum_j \frac{e^2}{4\pi\varepsilon_0}\int \mathrm{d}\boldsymbol{r}'\frac{|\varphi_j(\boldsymbol{r}')|^2}{|\boldsymbol{r}-\boldsymbol{r}'|}\right)\varphi_i(\boldsymbol{r}) - \frac{e^2}{4\pi\varepsilon_0}\sum_j\left(\int \mathrm{d}\boldsymbol{r}'\frac{\varphi_j^*(\boldsymbol{r}')\varphi_i(\boldsymbol{r}')}{|\boldsymbol{r}-\boldsymbol{r}'|}\right)\varphi_j(\boldsymbol{r})\right] = \varepsilon_i\varphi_i(\boldsymbol{r})\,. \tag{44}$$

Note that the integrals are also spin sums and the *j* sums may extend over all occupied functions including *i*. At this step, due to the experimental reasons previously evoked, we may recall that one can neglect the relative arrangement of the "magnetic" electrons. In this purpose Anderson has adopted the Wigner–Seitz scheme of removing the "magnetic" electron charge from the cell in which it finds itself (this scheme must be understood as a "trick" to find usable wave functions). Then the equation for the ligand field wave function may be simply rewritten artificially as:

$$-\frac{\hbar^2}{2m}\nabla^2\varphi_{\boldsymbol{k}}(\boldsymbol{r}) + V(\boldsymbol{r})\varphi_{\boldsymbol{k}}(\boldsymbol{r}) + \frac{e^2}{4\pi\varepsilon_0}\left(\sum_{\boldsymbol{k}'}\int \mathrm{d}\boldsymbol{r}'\frac{|\varphi_{\boldsymbol{k}'}(\boldsymbol{r}')|^2}{|\boldsymbol{r}-\boldsymbol{r}'|}\right)_{\substack{\boldsymbol{r}\text{ and }\boldsymbol{r}'\text{ not in}\\ \text{the same cell}}}\varphi_{\boldsymbol{k}}(\boldsymbol{r}) + \frac{e^2}{4\pi\varepsilon_0}\sum_j\left(\int \mathrm{d}\boldsymbol{r}'\frac{|\varphi_j(\boldsymbol{r}')|^2}{|\boldsymbol{r}-\boldsymbol{r}'|}\varphi_{\boldsymbol{k}}(\boldsymbol{r}) - \int \mathrm{d}\boldsymbol{r}'\frac{\varphi_j^*(\boldsymbol{r}')\varphi_{\boldsymbol{k}}(\boldsymbol{r}')}{|\boldsymbol{r}-\boldsymbol{r}'|}\varphi_j(\boldsymbol{r})\right)_{\substack{\text{ligands}\\ \text{and cores}}} = \varepsilon(\boldsymbol{k})\varphi_{\boldsymbol{k}}(\boldsymbol{r})\,. \tag{45}$$

Since Eq. 45 has the periodicity of the lattice, its solutions are Bloch waves $\varphi_{\boldsymbol{k}}$ with wave vectors $\boldsymbol{k}$. The most important properties of these functions are deducible from the quantity $\varepsilon(\boldsymbol{k})$. It contains both the crystal field effects

and the kinetic energy. To each d band labelled m, non-degenerate and well separated with respect to the other bands, corresponds a particular energy spectrum $\varepsilon_m(\boldsymbol{k})$. Since $\varepsilon_m(\boldsymbol{k})$ is periodic, it may be expanded in a Fourier series:

$$\varepsilon_m(\boldsymbol{k}) = a_m + \sum_{\boldsymbol{\tau}} b_m(\boldsymbol{\tau}) \exp(-\mathrm{i}\boldsymbol{k}\cdot\boldsymbol{\tau}) , \tag{46}$$

where the $\boldsymbol{\tau}$'s are fundamental translations of the lattice.

Now the final Bloch solutions of Eq. 45 may be unitary transformed to a new orthonormal set composed of Wannier functions:

$$\varphi_m(\boldsymbol{r}-\boldsymbol{n}) = \frac{1}{\sqrt{N}} \sum_{\boldsymbol{k}} \varphi_{\boldsymbol{k}}^m(\boldsymbol{r}) \exp(\mathrm{i}\boldsymbol{k}\cdot\boldsymbol{n}) , \tag{47}$$

where N is the number of lattice sites involved. Thus, the effect of the self-consistent field on the localized functions φ_m is obtained by applying Eqs. 46 and 47 in the following Schrödinger equation:

$$H_{\mathrm{sc}}\varphi_m(\boldsymbol{r}-\boldsymbol{n}) = a_m\varphi_m(\boldsymbol{r}-\boldsymbol{n}) + \sum_{\boldsymbol{\tau}} b_m(\boldsymbol{\tau})\varphi_m(\boldsymbol{r}-(\boldsymbol{n}+\boldsymbol{\tau})) . \tag{48}$$

a_m represents the crystal field parameter, this crystal field separating the different d levels m. $b_m(\boldsymbol{\tau})$ appears as a transfer integral representing the effect of the kinetic energy (responsible of the electron motion through the lattice). A more rigorous discussion [65] has allowed us to take into account other d bands m' and Eq. 48 may be simply generalized as:

$$H_{\mathrm{sc}}\varphi_m(\boldsymbol{r}-\boldsymbol{n}) = a_m\varphi_m(\boldsymbol{r}-\boldsymbol{n}) + \sum_{m',\boldsymbol{\tau}} b_{mm'}(\boldsymbol{\tau})\varphi_{m'}(\boldsymbol{r}-(\boldsymbol{n}+\boldsymbol{\tau})) , \tag{49}$$

where now the transfer integral $b_{mm'}(\boldsymbol{\tau})$ is:

$$b_{mm'}(\boldsymbol{\tau}) = \int \mathrm{d}\boldsymbol{r}\varphi_m^*(\boldsymbol{r}-\boldsymbol{n})(T+V)\varphi_{m'}(\boldsymbol{r}-(\boldsymbol{n}+\boldsymbol{\tau})) . \tag{50}$$

m and m' thus label the corresponding orbitals, each one containing one electron. Anderson has designated this contribution to exchange coupling as *kinetic exchange*, simply due to the fact that, during the formation of the weak chemical bond characterized by an antiferromagnetic effect, there is a gain in kinetic energy.

Interactions between *magnetic* electrons on the same ion core interact very strongly and may show three forms:

(i) Two electrons belonging to the same ion may repel each other with an average Coulombic energy called U which does not depend on their relative orbital or spin functions (for d electrons $U \approx 10$ eV [18, 19]). U is nothing but the energy which keeps the electrons localized. In other words, each electron stays on its own core exactly and the difference between the first excited state and the ground one is precisely U.

(ii) When the unpaired electrons are in orthogonal orbitals the spins are coupled parallel and the contribution to the exchange coupling is given by:

$$J_{mm'}(\text{potential}) = \int \mathrm{d}\boldsymbol{r}\,\mathrm{d}\boldsymbol{r}'\varphi_m^*(\boldsymbol{r}-\boldsymbol{n})\varphi_{m'}^*(\boldsymbol{r}-\boldsymbol{n})\frac{e^2}{4\pi\varepsilon_0|\boldsymbol{r}-\boldsymbol{r}'|}\varphi_{m'}(\boldsymbol{r}'-\boldsymbol{n})\varphi_m(\boldsymbol{r}'-\boldsymbol{n})\,. \tag{51}$$

It is *attractive* because two electrons described by similar wave functions tend to avoid each other through the *Fermi hole*, which occurs when spins are parallel, this hole being less repulsive when electrons are closer to each other. Anderson has designated this contribution as *potential exchange*. In the next subsection we shall give physical comments concerning the labels *kinetic* and *potential exchanges*.

(iii) Small differences in the repulsive energies may also occur due to the relative orientations of the orbitals involved i.e.,

$$\int \mathrm{d}\boldsymbol{r}\,\mathrm{d}\boldsymbol{r}'|\varphi_{m_1}(\boldsymbol{r}-\boldsymbol{n})|^2\frac{e^2}{|\boldsymbol{r}-\boldsymbol{r}'|}|\varphi_{m_2}(\boldsymbol{r}'-\boldsymbol{n})|^2 \neq \int \mathrm{d}\boldsymbol{r}\,\mathrm{d}\boldsymbol{r}'|\varphi_{m_3}(\boldsymbol{r})|^2\frac{e^2}{|\boldsymbol{r}-\boldsymbol{r}'|}|\varphi_{m_4}(\boldsymbol{r}')|^2\,. \tag{52}$$

These differences are the well-known Slater integrals, which determine how the orbital moments orient themselves for a free ion. In a real crystal, there will always exist a competition between the crystal field parameters (described by the $a_{m'}s$) and integrals like those appearing in Eq. 52 which will condition the ionic state.

Thus, superexchange occurs because the best Hartree–Fock orbitals are not the Wannier functions of Eq. 47 when some of the spins are antiparallel to others. As Anderson noted [54], when two neighbouring spins are parallel, their orbitals must, of course, be orthogonal; when they are antiparallel, their spin functions are automatically orthogonal and the orbitals may overlap each other. The gain of energy has been calculated by Anderson [18, 19] and Kondo [64], owing to perturbation theory. For two antiparallel neighbours at a distance $\boldsymbol{\tau}$ we have from Eq. 49:

$$\begin{aligned}\varphi_m(\boldsymbol{r}-\boldsymbol{n}) &\to \varphi_m(\boldsymbol{r}-\boldsymbol{n}) + \sum_{m'}\frac{b_{mm'}(\boldsymbol{\tau})}{U}\varphi_{m'}(\boldsymbol{r}-\boldsymbol{n}-\boldsymbol{\tau})\\ \varphi_{m'}(\boldsymbol{r}-\boldsymbol{n}-\boldsymbol{\tau}) &\to \varphi_{m'}(\boldsymbol{r}-\boldsymbol{n}-\boldsymbol{\tau}) + \sum_{m}\frac{b_{mm'}(\boldsymbol{\tau})}{U}\varphi_m(\boldsymbol{r}-\boldsymbol{n})\,,\end{aligned} \tag{53}$$

where $U > 0$ is the Coulomb repulsion energy so that, for a single pair of spins:

$$\Delta E(\text{parallel/antiparallel}) = -\frac{2b_{mm'}(\boldsymbol{\tau})^2}{U}\,. \tag{54}$$

The effect is always antiferromagnetic and depends on the presence of half-filled orbitals on the two involved ions, with non-vanishing $b_{mm'}$'s. Finally,

Kondo [64] and Anderson [18, 19] have separately shown that, in spite of the fact that superexchange differs from true usual exchange, it is equivalent to an $\boldsymbol{s}_1 \cdot \boldsymbol{s}_2$ coupling:

$$\Delta H = \sum_{\substack{m,m',\\ \boldsymbol{n},\boldsymbol{\tau}}} \frac{b_{mm'}(\boldsymbol{\tau})^2}{U} \left(-\frac{1}{2}\mathbf{1} + 2\boldsymbol{s}_{\boldsymbol{n}}^{m}.\boldsymbol{s}_{\boldsymbol{n}+\boldsymbol{\tau}}^{m'} \right) , \tag{55}$$

so that the "kinetic" contribution to the exchange integral is:

$$J_{mm'}(\text{kinetic}) = -\frac{2b_{mm'}(\boldsymbol{\tau})^2}{U} , \tag{56}$$

and is characterized by a negative sign. It means that the energies of parallel spins (ferromagnetic arrangement) are not affected but those of antiparallel spins (antiferromagnetic arrangement) are lowered. This is opposite to the true exchange effect where antiparallel spins are not affected. The total exchange is finally $J = J_{mm'}(\text{potential}) + J_{mm'}(\text{kinetic})$, the conventional writing of exchange Hamiltonian being $-2J\boldsymbol{S}_{\text{A}}.\boldsymbol{S}_{\text{B}}$.

3.2
Physical Comments and Improvements of the Model

We have just seen that Anderson has suggested that the ferromagnetic part be called *potential exchange* and the antiferromagnetic one *kinetic exchange* [18, 19]. These terms are only partially adequate. The first one takes into account the Coulombic potential energy, which plays a major role in this mechanism but ignores the fact that the extension of the Fermi hole is governed by the smoothness of the wave functions, which find their origin in the kinetic energy term. For the second label, despite the contribution to the energy lowering which results from a partial electron delocalization, it must be recalled that this comes in fact from the non-vanishing term $b_{mm'}(\boldsymbol{\tau})$ which contains both kinetic and potential contributions.

These remarks allow one to point out the fundamental complexity of the exchange problem. Indeed we deal with tiny (or at least very small) energy terms, generally accessible through a chain of perturbation process. In addition, since any modification of the wave functions simultaneously affects most of contributions to the Hamiltonian, it is not possible to strictly separate them via a variational process and to specifically attribute to one of them any energy lowering. Finally, it must be emphasized that $b_{mm'}(\boldsymbol{\tau})$ contains the Coulomb electron–electron interactions as well as the one-electron energy terms, since the self-consistent Hamiltonian involves the two-particle energy through the effective mean-field interaction potential.

After the publication of Anderson's initial model [59], experimental works [66] have pointed out that superexchange could also lead to purely

ferromagnetic spin arrangements between magnetic centres. A first improvement to Anderson's model has consisted in considering the true polarization effects [18, 19]. In addition, the perturbation expansion has been examined at higher orders, in particular the case of a delocalized orbital containing the unpaired electron and overlapping with an empty orbital on a second metal ion. Intra-atomic coupling of the electrons in the orthogonal metal orbitals leads to a ferromagnetic spin arrangement. This contribution to the exchange integral is:

$$J'_{mm'}(\text{potential}) = \left(\frac{b_{mm'}(\boldsymbol{\tau})}{U}\right)^2 J(\text{intra-atomic})\,. \tag{57}$$

Calculations have given $|J_{mm'}(\text{kinetic})| \gg J'_{mm'}(\text{potential})$ so that, when both kinetic and potential exchanges co-exist, the kinetic contribution is usually the largest one and the resultant exchange coupling is antiferromagnetic. Ferromagnetic interactions have been considered as resulting from the operation of Hund's rules where the unpaired electrons are delocalized into orthogonal orbitals on a common bridging ligand. Only the exchange pathways involving overlaps between non-orthogonal orbitals give rise to antiferromagnetism.

It early appeared that qualitative rules allowing the prediction of the nature of the interaction between two magnetic centres A and B should be proposed according to the symmetry of the AXB entity. From Anderson's first paper [59], it was suggested that superexchange between ions with *d* shells half filled or more might be antiferromagnetic, with less ferromagnetic. However experimental contradictions have rapidly appeared (for instance, with compounds containing Cr^{3+} ions which are almost uniformly antiferromagnetic, with a *d* shell less than half full [66]). A first step proposed by Anderson has involved the orientation of magnetic orbitals in the entity AXB. *Anderson's rules suggest that there is a stronger interaction between two spins with a ligand directly between them in 180° position than at right angles with respect to the ligand ion.*

However a considerably more satisfactory system of semi-empirical rules has been developed in the second part of the 1950s by Goodenough [67, 68] and most clearly stated by Kanamori [69]. These rules take into account the occupation of the various *d* levels as recommended by ligand field theory. They are related to Anderson's prescription about the sign of superexchange energy. Finally, *the angular relationship to the intermediate ligand ion does not play a major role.* Under these conditions the Goodenough–Kanamori rules are [54]:

(i) *When the two ions have lobes of magnetic orbitals pointing toward each other in such a way that the orbitals would have a reasonably large overlap integral, the exchange is antiferromagnetic. There are several subcases:*
   1. *When the lobes are d_{z^2}-type orbitals in the octahedral case, particularly in the "180° position" in which these lobes point directly toward a ligand and each other, one obtains a large superexchange energy.*

2. *When d_{xy} orbitals are in the 180° position to each other, so that they interact via $p\pi$ orbitals on the ligand, one again obtains antiferromagnetic superexchange.*
3. *In a 90° ligand situation, when one ion has a d_{z^2} occupied and the other a d_{xy}, the $p\pi$ for one is the $p\sigma$ for the other and one expects a strong overlap and thus antiferromagnetic exchange.*

(ii) *When the orbitals are arranged in such a way that they are expected to be in contact but to have no overlap integral – most notably a d_{z^2} and a d_{xy} in* 180° *position where the overlap is zero by symmetry – the rule gives ferromagnetic interaction* (*not as strong as the antiferromagnetic one in absolute value*).

These two rules have explained almost the complete gamut of spin arrangements encountered in a wide variety of compounds. At this step we may make the following comments. (i) Antiferromagnetic superexchange effect can only arise between two orbitals having a finite transfer integral b connecting them and the exchange energy is proportional to b^2 (cf. Eq. 56). In other words, the two orbitals must have the same symmetry in the region of overlap. (ii) If the orbitals do not have the same symmetry so that $b = 0$ (orthogonality by symmetry), one can expect a ferromagnetic exchange. Important applications have been achieved for verifying these rules [70] as well as numerous regularities suggested by theory [54].

4
A New General Treatment for the Superexchange Mechanism

In this part we develop a general formalism for the AXB centrosymmetrical model system, where A and B are two magnetic centres with one unpaired electron each, and X is a closed-shell diamagnetic bridge (or ligand). A first approach has been previously given by Georges [71]. Under these conditions, let us start with the two-particle Hamiltonian for the fragment AX of the entity AXB:

$$H_{AX} = T_1 + V_1 + T_2 + V_2 + \frac{e^2}{4\pi\varepsilon_0 r_{12}}, \quad r_{12} = |\boldsymbol{r}_1 - \boldsymbol{r}_2| \,. \tag{58}$$

The potentials $V_1 = V(\boldsymbol{r}_1)$ and $V_2 = V(\boldsymbol{r}_2)$ include all the nucleus and extra electron contributions to the Coulomb field acting on electrons 1 and 2. In other words, we operate in the framework of the *Hartree–Fock approximation* i.e., the action of extra electrons over electrons 1 and 2 is taken into account through a *mean-field approximation*. A similar Hamiltonian H_{XB} may be written for the fragment XB (with $H_{AX} = H_{XB}$ when A = B). In this article we shall exclusively consider the fragment AX of the entity AXB. Thus, all the physical quantities globally labelled Q_{XB} and derived from the Hamiltonian H_{XB} will

be simply transposed from the corresponding ones Q_{AX} by interchanging B and A. They will be here omitted for clarity.

4.1 Basic Assumptions

The potential operator $V(\boldsymbol{r})$ commutes with any symmetry operator $\mathcal{O}$. $\mathcal{O}$ forms a double group $\mathcal{G}$ with the identity operation **1**. Thus, as we deal with a two-electron problem on both sides of ligand X, separately, the two low-lying states of each of the bonds A–X and X–B are a spin singlet and a spin triplet of respective irreducible representations (irreps) ${}^1\Gamma_g$ and ${}^3\Gamma_u$. They are close enough in energy to both be populated at room temperature. In Fig. 4 we have reported the general shape of $V(\boldsymbol{r})$ as well as the energy diagram for the AXB model. The three atomic orbitals involved are Φ_A and Φ_B centred on A and B, respectively, and Φ_X centred on the bridge X (the corresponding states are $|A\rangle$, $|B\rangle$ and $|X\rangle$). Φ_A, Φ_B and Φ_X are assumed to be real and are considered as starting (non-disturbed) wave functions i.e., free atomic wave functions, which give a spatial description of each of the states $|A\rangle$, $|B\rangle$ or $|X\rangle$. *For instance, Φ_A and Φ_B are cationic d-orbitals and Φ_X is an anionic (s or p) orbital.*

We have the following conventions based on the symmetry problem, notably on the fact that A and B are far apart and without interaction:

(i) the states are normalized but not orthogonal (except $|A\rangle$ and $|B\rangle$):

$$\langle A|A\rangle = 1, \quad \langle B|B\rangle = 1, \quad \langle X|X\rangle = 1, \quad \langle A|B\rangle = \langle B|A\rangle = 0\,. \tag{59}$$

The fact that $|A\rangle$ and $|B\rangle$ are orthogonal (i.e., without overlap) simply means that there is no π bond between A and B (but this could be taken into account in the present model). As noted after Eq. 58, only two unpaired electrons belonging respectively to cations A and B participate in the creation of a bond on each side of the central ligand X, the other electrons being considered as passive. This is the *active-electron approximation*, which is plainly justified from an experimental point of view. In-

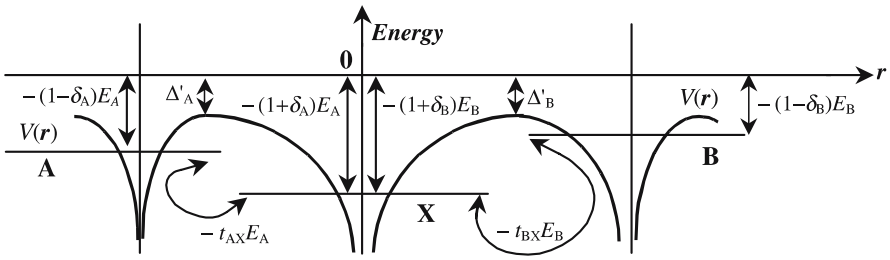

Fig. 4 Energy diagram for the periodic AXB model in the general case of different magnetic centres (A ≠ B) on both sides of ligand X

deed, for numerous compounds (for instance, for oxo- or fluoro-bridged compounds), the highest-occupied molecular orbitals of the bridging ligands that interact with the metal ions are low in energy compared to the cationic *d* orbitals. In addition they are well separated from other metal or ligand occupied orbitals.

(ii) the overlap between A and X on the one hand, X and B on the other one, may be defined as follows:

$$\langle \mathrm{A}|\mathrm{X}\rangle = \mathbf{s}_\mathrm{A}, \quad \langle \mathrm{X}|\mathrm{B}\rangle = \mathbf{s}_\mathrm{B}, \quad \mathbf{s}_\mathrm{A} > 0, \quad \mathbf{s}_\mathrm{B} > 0\,, \tag{60}$$

in the particular case where A = B, then $\mathbf{s}_\mathrm{A} = \mathbf{s}_\mathrm{B} = \mathbf{s} > 0$.

(iii) both magnetic centres A and B have a cationic energy level higher than the anionic one, as is generally the case for transition metal compounds; the energy difference between A and X levels (respectively, X and B levels) is $2\delta_\mathrm{A}E_\mathrm{A}$, with $E_\mathrm{A} > 0$ (respectively, $2\delta_\mathrm{B}E_\mathrm{B}$, with $E_\mathrm{B} > 0$), so that we have for the fragment AX:

$$\begin{aligned}
&\langle \mathrm{A}|\,(T_1 + V_1)\,|\mathrm{A}\rangle = -\,(1-\delta_\mathrm{A})E_\mathrm{A}, \quad \langle \mathrm{B}|\,(T_1 + V_1)\,|\mathrm{B}\rangle = -\,(1-\delta_\mathrm{AB})E_\mathrm{B},\\
&\langle \mathrm{X}|\,(T_1 + V_1)\,|\mathrm{X}\rangle = -\,(1+\delta_\mathrm{A})E_\mathrm{A}, \quad E_\mathrm{A} > 0, \quad E_\mathrm{B} > 0, \quad \mathrm{A} \neq \mathrm{B},\\
&\langle \mathrm{A}|\,(T_1 + V_1)\,|\mathrm{A}\rangle = \langle \mathrm{B}|\,(T_1 + V_1)\,|\mathrm{B}\rangle = -\,(1-\delta)E,\\
&\langle \mathrm{X}|\,(T_1 + V_1)\,|\mathrm{X}\rangle = -\,(1+\delta)E, \quad E > 0, \quad \mathrm{A} = \mathrm{B}\,.
\end{aligned} \tag{61}$$

As previously noted, similar expressions may be written for the fragment XB. δ_A for the fragment AX (respectively, δ_B for the fragment XB) is lower than unity but not necessarily small; $\delta_i > 0$ (with i = A or B) is a very usual case and $\delta_i < 0$ corresponds to the particular case of dihydrogen molecule (with A = X = B). A similar remark may be given for δ_AB, which is defined by analogy with respect to δ_A and characterizes the link between fragments AX and XB. In Fig. 4 it is also reported that, due to the stabilization of the entity AXB during the creation of the bonds A–X and X–B, we must have automatically $-\,(1+\delta_\mathrm{A})E_\mathrm{A} = -\,(1+\delta_\mathrm{B})E_\mathrm{B}$. When A = B, the two magnetic ions show the same energy level; the system becomes degenerate and $\delta_\mathrm{A} = \delta_\mathrm{AB} = \delta_\mathrm{B}$.

(iv) The transfer integrals between $|\mathrm{A}\rangle$ and $|\mathrm{X}\rangle$ on the one hand, $|\mathrm{X}\rangle$ and $|\mathrm{B}\rangle$ on the other one, are given by:

$$\begin{aligned}
&\langle \mathrm{A}|\,(T_1 + V_1)\,|\mathrm{X}\rangle = -\,t_\mathrm{AX}E_\mathrm{A}, \quad \langle \mathrm{X}|\,(T_1 + V_1)\,|\mathrm{B}\rangle = -\,t_\mathrm{XB}E_\mathrm{B}, \quad \mathrm{A} \neq \mathrm{B},\\
&\langle \mathrm{A}|\,(T_1 + V_1)\,|\mathrm{B}\rangle = 0
\end{aligned} \tag{62}$$

for the fragment AX. When A = B we have $t_\mathrm{AX} = t_\mathrm{XB}$ but when A ≠ B we have automatically $t_\mathrm{AX} \neq t_\mathrm{XB}$. The last equation which states that there is no transfer between A and B but exclusively between A and X or X and B is a consequence of condition (i). However, as previously noted, the case $\langle \mathrm{A}|(T_1 + V_1)|\mathrm{B}\rangle \neq 0$ could be introduced in a more general model, without difficulty, notably by the bias of a π orbital between A and B.

(v) s_A, t_{AX} and t_{XB} are small compared to unity and t_{AX} or t_{XB} is mainly related to the potential interaction between the anion and the cation so that:

$$-t_{AX}E_A \approx -s_A\Delta'_A < -s_A(1-\delta_A)E_A\,, \tag{63}$$

where Δ'_A is defined in Fig. 4. A similar relation may be written for the fragment XB, with Δ'_B defined in Fig. 4.

4.2 Construction of the Intermediate Cationic States

Without direct overlap and transfer between A and B, any exchange interaction between electrons belonging to the magnetic centres A and B must automatically occur through the anionic intermediate bridge X. In a first step we diagonalize the one-particle Hamiltonian $T_i + V_i$ ($i = 1, 2$) in the reduced basis $\{|A\rangle, |X\rangle\}$ for the fragment AX (respectively, $T_i + V_i$ ($i = 3, 4$) in the reduced basis $\{|X\rangle, |B\rangle\}$ for the fragment XB, separately). The goal of such an operation is to obtain the new cationic (antibonding) normalized eigenstates $|\mathcal{A}\rangle$ and $|\mathcal{B}\rangle$ such as:

$$|\mathcal{A}\rangle = (1-\alpha_A)\,|A\rangle + \beta_A\,|X\rangle\,, \quad |\mathcal{B}\rangle = \beta_B\,|X\rangle + (1-\alpha_B)\,|B\rangle\,, \tag{64}$$

where α_i and β_i (with i = A or B) are real numbers. As we deal with a weak chemical bond between A and X or X and B, β_i must remain small. Then, using condition (i) of the previous subsection i.e., the normalization condition $\langle A|A\rangle = \langle B|B\rangle = 1$, as well as condition (ii), the new normalization condition $\langle\mathcal{A}|\mathcal{A}\rangle = \langle\mathcal{B}|\mathcal{B}\rangle = 1$ leads to the following equation:

$$\begin{aligned}&(1-\alpha_A)^2 + 2\beta_A(1-\alpha_A)s_A + \beta_A^2 - 1 = 0\,,\\ &(1-\alpha_B)^2 + 2\beta_B(1-\alpha_B)s_B + \beta_B^2 - 1 = 0\,,\end{aligned} \tag{65}$$

characterized by the solutions $1-\alpha_i = -\beta_i s_i \pm \sqrt{1-\beta_i^2+(\beta_i s_i)^2}$ (with i = A or B). If we define the new direct overlap $S = \langle\mathcal{A}|\mathcal{B}\rangle = \langle\mathcal{B}|\mathcal{A}\rangle$ we derive:

$$\begin{aligned}&S = \beta_B(1-\alpha_A)s_A + \beta_A(1-\alpha_B)s_B + \beta_A\beta_B > 0\,, \quad A \neq B\,,\\ &S = 2\beta(1-\alpha)s + \beta^2 > 0\,, \quad A = B\,.\end{aligned} \tag{66}$$

Setting:

$$S_A = 2\beta_A(1-\alpha_A)s_A + \beta_A^2 > 0\,, \quad S_B = 2\beta_B(1-\alpha_B)s_B + \beta_B^2 > 0\,, \tag{67}$$

where S_A and S_B are functionals of the various overlaps corresponding to the bonds A–X and X–B, respectively, we have:

$$S = \frac{1}{2}\left(\frac{\beta_B}{\beta_A}S_A + \frac{\beta_A}{\beta_B}S_B\right) \tag{68}$$

and by reporting Eq. 67 in Eq. 65 we have:

$$1-\alpha_A = \pm\sqrt{1-S_A}\,, \quad 1-\alpha_B = \pm\sqrt{1-S_B}\,, \quad A \neq B\,,$$
$$1-\alpha = \pm\sqrt{1-S}\,, \quad A = B\,. \tag{69}$$

From now, the sign + will be conventionally adopted. The new energy is:

$$\mathcal{E}_A = \langle\mathcal{A}|\,(T_1+V_1)\,|\mathcal{A}\rangle\,, \quad \mathcal{E}_{AB} = \langle\mathcal{B}|\,(T_1+V_1)\,|\mathcal{B}\rangle\,, \quad A \neq B\,,$$
$$\mathcal{E} = \mathcal{E}_A = \mathcal{E}_{AB} = \langle\mathcal{A}|\,(T_1+V_1)\,|\mathcal{A}\rangle\,, \quad A = B\,. \tag{70}$$

Thus, if $A \neq B$ (general case), the system is non-degenerate ($\mathcal{E}_A \neq \mathcal{E}_B$) but, if $A = B$, we deal with a degenerate state ($\mathcal{E} = \mathcal{E}_A = \mathcal{E}_B$). Introducing the definition of $|\mathcal{A}\rangle$ and $|\mathcal{B}\rangle$ given by Eq. 64 we may write:

$$\mathcal{E}_A = -\left[(1-\alpha_A)^2(1-\delta_A) + \beta_A^2(1+\delta_A)\right]E_A - 2\beta_A(1-\alpha_A)t_{AX}E_A\,,$$
$$\mathcal{E}_{AB} = -\left[(1-\alpha_B)^2(1-\delta_{AB})E_B + \beta_B^2(1+\delta_A)E_A\right] - 2\beta_B(1-\alpha_B)t_{XB}E_B\,,$$
$$A \neq B\,,$$
$$\mathcal{E} = \mathcal{E}_A = \mathcal{E}_{AB} = -\left[(1-\alpha)^2(1-\delta) + \beta^2(1+\delta)\right]E - 2\beta(1-\alpha)tE\,, \quad A = B\,. \tag{71}$$

The undetermined parameter β_i (with i = A or B) may now be chosen so that $\mathcal{E}_i$ is minimum i.e., owing to Eq. 71, the equation $\partial\mathcal{E}_i/\partial\beta_i = 0$ gives after few calculations:

$$\beta_A = \pm(1-\alpha_A) = \pm\sqrt{1-S_A}\,, \quad \beta_B = \pm(1-\alpha_B) = \pm\sqrt{1-S_B}\,, \tag{72}$$

where S_A and S_B are given by Eq. 67. Thus, β_i and $1-\alpha_i$ (with i = A or B) may show the same sign or opposite signs: if $\beta_i > 0$ (respectively, $\beta_i < 0$) the state $|\mathcal{A}\rangle$ or $|\mathcal{B}\rangle$ will be represented by a spatially symmetrical wave function (respectively, spatially antisymmetrical). In addition, as β_i is small, $1-\alpha_i$ is small too and α_i is close to unity. Then, using the particular value of β_i given by Eq. 72, the ground state energy is:

$$\mathcal{E}_A = -2(1-S_A)(1\pm t_{AX})E_A\,,$$
$$\mathcal{E}_{AB} = -(1-S_B)[(1-\delta_{AB})E_B + (1+\delta_A)E_A \pm 2t_{XB}E_B]\,, \quad A \neq B\,,$$
$$\mathcal{E} = \mathcal{E}_A = \mathcal{E}_{AB} = -2(1-S)(1\pm t)\mathcal{E}_A\,, \quad A = B\,, \tag{73}$$

with $t = t_{AX} = t_{XB}$. We finally define the transfer integral $\mathcal{T}_{AB}$ as:

$$\mathcal{T}_{AB} = \langle\mathcal{A}|\,(T_1+V_1)\,|\mathcal{B}\rangle = \langle\mathcal{B}|\,(T_1+V_1)\,|\mathcal{A}\rangle\,. \tag{74}$$

Proceeding as for S and $\mathcal{E}$ we derive:

$$\mathcal{T}_{AB} = -\beta_B(1-\alpha_A)t_{AX}E_A - \beta_A(1-\alpha_B)t_{XB}E_B - \beta_A\beta_B(1+\delta_A)E_A\,, \quad A \neq B\,,$$
$$\mathcal{T} = -2\beta(1-\alpha)tE - \beta^2(1+\delta)E\,, \quad A = B\,, \tag{75}$$

with $t = t_{AX} = t_{XB}$ and $\mathcal{T} = \mathcal{T}_{AB} = \mathcal{T}_{BA}$ whereas $\mathcal{T}_{AB} \neq \mathcal{T}_{BA}$ if $A \neq B$. Then, using the particular value of β_i (with $i = A$ or B) given by Eq. 72 we have:

$$\begin{aligned}
\mathcal{T}_{AB} &= -\sqrt{1 - S_A}\sqrt{1 - S_B}\,[(1 + \delta_A)E_A \pm t_{AX}E_A \pm t_{XB}E_B]\,, \quad A \neq B\,,\\
\mathcal{T} &= -(1 - S)(1 + \delta \pm 2t)E\,, \quad A = B\,,
\end{aligned} \tag{76}$$

where the sign + holds for $\beta_i > 0$ and – for $\beta_i < 0$. As $E_i > 0$, $1 - S_i > 0$, $1 + \delta_i > 0$ whatever the sign of δ_i, $E_A \approx E_B$ and $|t| \ll 1$, $\mathcal{T}_{AB}$ (if $A \neq B$) or $\mathcal{T}$ (if $A = B$) is *negative*. Thus, before constructing the collective states, it is clear that S_A, $\mathcal{E}_A$ *and* $\mathcal{T}_{AB}$ (*respectively,* S_B, $\mathcal{E}_B$ *and* $\mathcal{T}_{BA}$) *appear as the basic parameters of the bond A–X (respectively, X–B) and finally characterize the collective states of AXB.*

4.3
Construction of the Collective States

The cationic states $|\mathcal{A}\rangle$ and $|\mathcal{B}\rangle$ may now give rise to four cationic spin–orbital states: $|\mathcal{A}, +\rangle$, $|\mathcal{A}, -\rangle$, $|\mathcal{B}, +\rangle$ and $|\mathcal{B}, -\rangle$ from which we may construct, in a first step, four molecular states adapted to the $\mathcal{G}$ symmetry group molecular orbitals. Notably, owing to their behaviour under the interchange of $|\mathcal{A}\rangle$ and $|\mathcal{B}\rangle$, we may call them "gerade" (unchanged) or "ungerade" (sign change). Thus we may write:

$$\begin{aligned}
|g, \sigma\rangle &= \frac{1}{\sqrt{2(1 + S)}}\,(|\mathcal{A}, \sigma\rangle + |\mathcal{B}, \sigma\rangle)\,,\\
|u, \sigma\rangle &= \frac{1}{\sqrt{2(1 - S)}}\,(|\mathcal{A}, \sigma\rangle - |\mathcal{B}, \sigma\rangle)\,, \quad \sigma = \pm\,,
\end{aligned} \tag{77}$$

for the "gerade" and "ungerade" states, respectively labelled g and u. The coefficients $[2(1 \pm S)]^{-1/2}$ are self-evident normalizing factors and $\sigma = \pm$ recalls the nature of the corresponding spin state ("up" or "down"). At this step, due to the orthogonality conditions $\langle \mathcal{X}, \sigma | \mathcal{X}, \sigma' \rangle = \delta_{\sigma\sigma'}$ (with $\mathcal{X} = \mathcal{A}$ or $\mathcal{B}$) and $\langle \mathcal{A}, \sigma | \mathcal{B}, \sigma' \rangle, = S\delta_{\sigma\sigma'}$, we must have $\langle X, \sigma | X, \sigma' \rangle = \delta_{\sigma\sigma'}$, with $X = g$ or u. Then it is easily shown that the related energies are:

$$\begin{aligned}
\mathcal{E}_{Ag} &= \frac{\mathcal{E}_A + 2\mathcal{T}_{AB} + \mathcal{E}_{AB}}{2(1 + S)}\,, \quad \mathcal{E}_{Au} = \frac{\mathcal{E}_A - 2\mathcal{T}_{AB} + \mathcal{E}_{AB}}{2(1 - S)}\,, \quad A \neq B\,,\\
\mathcal{E}_g &= \frac{\mathcal{E} + \mathcal{T}}{1 + S}\,, \quad \mathcal{E}_u = \frac{\mathcal{E} - \mathcal{T}}{1 - S}\,, \quad A = B\,,
\end{aligned} \tag{78}$$

where $\mathcal{E}$ and $\mathcal{T}$ are given by Eqs. 73 and 76, respectively, and the difference of energy between the "gerade" and "ungerade" states is:

$$\mathcal{E}_{\mathrm{A}g} - \mathcal{E}_{\mathrm{A}u} = \frac{2\mathcal{T}_{\mathrm{AB}} - \mathrm{S}(\mathcal{E}_{\mathrm{A}} + \mathcal{E}_{\mathrm{AB}})}{1 - \mathrm{S}^2}, \quad \mathrm{A} \neq \mathrm{B},$$

$$\mathcal{E}_g - \mathcal{E}_u = 2\frac{\mathcal{T} - \mathrm{S}\mathcal{E}}{1 - \mathrm{S}^2}, \quad \mathrm{A} = \mathrm{B}, \tag{79}$$

i.e., as β_i, s_i (with i = A or B), t_{AX} and t_{XB} (A ≠ B), $t = t_{\mathrm{AX}} = t_{\mathrm{XB}}$ (A = B) and S are small:

$$\mathcal{E}_{\mathrm{A}g} - \mathcal{E}_{\mathrm{A}u} \approx -2\beta_{\mathrm{A}}\beta_{\mathrm{B}}(1 + \delta_{\mathrm{A}})E_{\mathrm{A}}, \quad \mathrm{A} \neq \mathrm{B},$$

$$\mathcal{E}_g - \mathcal{E}_u \approx -2\beta^2(1 + \delta)E, \quad \mathrm{A} = \mathrm{B}. \tag{80}$$

Thus, $\mathcal{E}_{\mathrm{A}g} - \mathcal{E}_{\mathrm{A}u}$ is independent of the sign of $\beta_{\mathrm{A}}\beta_{\mathrm{B}}$, as expected, remains very small, as β_{A} or β_{B} is small, and negative.

With two electrons and four available spin orbitals, 2^4 determinantal collective states may be then built. However, Pauli's exclusion principle coupled to the notion of particle indiscernibility contributes to reduce this number to 6. Let us label $|X_{S,S^z}\rangle$ the collective states: $X = U$ (ungerade) or $X = G$ (gerade) refers to the symmetry of the orbital part with respect to the interchange of $|\mathcal{A}\rangle$ and $|\mathcal{B}\rangle$; S and S^z describe the total spin configuration. We shall denote $|\mathcal{P}, \sigma; \mathcal{P}', \sigma'\rangle$ the Slater determinant:

$$\left|\mathcal{P}, \sigma; \mathcal{P}', \sigma'\right\rangle = \frac{1}{\sqrt{2}} \begin{vmatrix} |P(r_1)\sigma(s_1)\rangle & |P'(r_1)\sigma'(s_1)\rangle \\ |P(r_2)\sigma(s_2)\rangle & |P'(r_2)\sigma'(s_2)\rangle \end{vmatrix}. \tag{81}$$

It is then easy to understand that a combination of a g-type orbital and a u-type one allows one to obtain a U-type collective state, whereas combining two g- or two u-orbitals gives rise to a G-type orbital. As a consequence we may build the six following collective states:

$$\begin{aligned}
\left|U_{1,1}\right\rangle &= \left|u, +; g, +\right\rangle, \\
\left|U_{1,0}\right\rangle &= \frac{1}{\sqrt{2}}\left(\left|u, +; g, -\right\rangle + \left|u, -; g, +\right\rangle\right), \\
\left|U_{1,-1}\right\rangle &= \left|u, -; g, -\right\rangle, \\
\left|U_{0,0}\right\rangle &= \frac{1}{\sqrt{2}}\left(\left|u, +; g, -\right\rangle - \left|u, -; g, +\right\rangle\right), \\
\left|G^g_{0,0}\right\rangle &= \left|g, +; g, -\right\rangle, \\
\left|G^u_{0,0}\right\rangle &= |u, +; u, -\rangle.
\end{aligned} \tag{82}$$

It is very easily checked that these functions are orthogonal by construction. Their spin characters may be simply verified by applying to each of the previous collective states the convenient total spin operator. Then, introducing the expressions previously obtained for the molecular spin-orbital states (cf.

Eqs. 77 and 81), we derive:

$$
\begin{aligned}
\left|U_{1,1}\right\rangle &= \frac{1}{\sqrt{1-S^2}}\,|\mathcal{A},+;\mathcal{B},+\rangle\ ,\\
\left|U_{1,0}\right\rangle &= \frac{1}{\sqrt{2(1-S^2)}}\,\left(|\mathcal{A},-;\mathcal{B},+\rangle + |\mathcal{A},+;\mathcal{B},-\rangle\right)\ ,\\
\left|U_{1,-1}\right\rangle &= \frac{1}{\sqrt{1-S^2}}\,|\mathcal{A},-;\mathcal{B},-\rangle\ ,\\
\left|U_{0,0}\right\rangle &= \frac{1}{\sqrt{2(1-S^2)}}\,\left(|\mathcal{A},+;\mathcal{A},-\rangle - |\mathcal{B},+;\mathcal{B},-\rangle\right)\ ,\\
\left|G^{g}_{0,0}\right\rangle &= \frac{1}{2(1+S)}\,\big(|\mathcal{A},+;\mathcal{A},-\rangle + |\mathcal{A},+;\mathcal{B},-\rangle\\
&\qquad + |\mathcal{B},+;\mathcal{A},-\rangle + |\mathcal{B},+;\mathcal{B},-\rangle\big)\ ,\\
\left|G^{u}_{0,0}\right\rangle &= \frac{1}{2(1-S)}\,\big(|\mathcal{A},+;\mathcal{A},-\rangle - |\mathcal{A},+;\mathcal{B},-\rangle\\
&\qquad - |\mathcal{B},+;\mathcal{A},-\rangle + |\mathcal{B},+;\mathcal{B},-\rangle\big)\ .
\end{aligned}
\tag{83}
$$

Concerning these latter states, it is useful to notice that they may be also expressed by means of the polar and non-polar normalized (but non strictly orthogonal) states $|G^{\mathrm{p}}_{0,0}\rangle$ and $|G^{\mathrm{np}}_{0,0}\rangle$, respectively:

$$
\begin{aligned}
\left|G^{g}_{0,0}\right\rangle &= \frac{\sqrt{1+S^2}}{\sqrt{2}(1+S)}\,\left(\left|G^{\mathrm{p}}_{0,0}\right\rangle + \left|G^{\mathrm{np}}_{0,0}\right\rangle\right)\ ,\\
\left|G^{u}_{0,0}\right\rangle &= \frac{\sqrt{1+S^2}}{\sqrt{2}(1-S)}\,\left(\left|G^{\mathrm{p}}_{0,0}\right\rangle - \left|G^{\mathrm{np}}_{0,0}\right\rangle\right)
\end{aligned}
\tag{84}
$$

with:

$$
\begin{aligned}
\left|G^{\mathrm{p}}_{0,0}\right\rangle &= \frac{1}{\sqrt{2(1+S^2)}}\,\left(|\mathcal{A},+;\mathcal{A},-\rangle + |\mathcal{B},+;\mathcal{B},-\rangle\right)\ ,\\
\left|G^{\mathrm{np}}_{0,0}\right\rangle &= \frac{1}{\sqrt{2(1+S^2)}}\,\left(|\mathcal{A},+;\mathcal{B},-\rangle + |\mathcal{B},+;\mathcal{A},-\rangle\right)\ .
\end{aligned}
\tag{85}
$$

4.4 Hamiltonian Matrix and Energy Spectrum

The last step consists in evaluating the elements of the Hamiltonian matrix in the new basis $\{|G^{g}_{0,0}\rangle\,,\ |G^{u}_{0,0}\rangle\,,\ |U_{0,0}\rangle\,,\ |U_{1,1}\rangle\,,\ |U_{1,0}\rangle\,,\ |U_{1,-1}\rangle\}$. The non-vanishing terms are those ones existing between states belonging to the same irreducible representation (irrep) of the orbital ($\mathcal{G}$) and spin ($\mathcal{R}$) symmetry groups. As a consequence one may expect: (i) diagonal and off-diagonal terms between $|G^{g}_{0,0}\rangle$ and $|G^{u}_{0,0}\rangle$; (ii) only diagonal terms for the states $|U_{S,S^z}\rangle$ with $S=0$ ($S^z=0$) and $S=1$ ($S^z=0,\ \pm 1$); (iii) finally all the diagonal terms of the states $|U_{1,S^z}\rangle$ are equal because we deal with the irrep $\mathcal{D}_1\otimes{}^3\Gamma_u$. Under these

conditions, the Hamiltonian matrix is:

$$H = \begin{pmatrix} E_0^{Gg} & K & 0 & 0 & 0 & 0 \\ K & E_0^{Gu} & 0 & 0 & 0 & 0 \\ 0 & 0 & E_0^U & 0 & 0 & 0 \\ 0 & 0 & 0 & E_1^U & 0 & 0 \\ 0 & 0 & 0 & 0 & E_1^U & 0 \\ 0 & 0 & 0 & 0 & 0 & E_1^U \end{pmatrix}, \tag{86}$$

with:

$$\begin{aligned} E_0^{Gg} &= \left\langle G_{0,0}^g \middle| H \middle| G_{0,0}^g \right\rangle, \quad K = \left\langle G_{0,0}^g \middle| H \middle| G_{0,0}^u \right\rangle = \left\langle G_{0,0}^u \middle| H \middle| G_{0,0}^g \right\rangle, \\ E_0^{Gu} &= \left\langle G_{0,0}^u \middle| H \middle| G_{0,0}^u \right\rangle, \quad E_0^U = \left\langle U_{0,0} \middle| H \middle| U_{0,0} \right\rangle, \\ E_1^U &= \left\langle U_{1,1} \middle| H \middle| U_{1,1} \right\rangle = \left\langle U_{1,0} \middle| H \middle| U_{1,0} \right\rangle = \left\langle U_{1,-1} \middle| H \middle| U_{1,-1} \right\rangle. \end{aligned} \tag{87}$$

At this step we introduce the following quantities:

$$\begin{aligned} U_{\mathrm{A}} &= \langle \mathcal{A}| \langle \mathcal{A}| U_{1,2} |\mathcal{A}\rangle |\mathcal{A}\rangle, \quad U_{\mathrm{AB}} = \langle \mathcal{B}| \langle \mathcal{B}| U_{1,2} |\mathcal{B}\rangle |\mathcal{B}\rangle, \\ C_{\mathrm{A}} &= \langle \mathcal{A}| \langle \mathcal{B}| U_{1,2} |\mathcal{B}\rangle |\mathcal{A}\rangle, \\ \gamma_{1\mathrm{A}} &= \langle \mathcal{A}| \langle \mathcal{B}| U_{1,2} |\mathcal{A}\rangle |\mathcal{B}\rangle = \langle \mathcal{A}| \langle \mathcal{A}| U_{1,2} |\mathcal{B}\rangle |\mathcal{B}\rangle, \\ \gamma_{2\mathrm{A}} &= \langle \mathcal{A}| \langle \mathcal{A}| U_{1,2} |\mathcal{A}\rangle |\mathcal{B}\rangle, \quad \gamma_{2\mathrm{AB}} = \langle \mathcal{A}| \langle \mathcal{B}| U_{1,2} |\mathcal{B}\rangle |\mathcal{B}\rangle, \end{aligned} \tag{88}$$

with:

$$\langle \mathrm{W}| \langle \mathrm{X}| U_{1,2} |\mathrm{Y}\rangle |\mathrm{Z}\rangle = \int \mathrm{d}\boldsymbol{r}_1 \, \mathrm{d}\boldsymbol{r}_2 \Phi_{\mathrm{W}}^*(\boldsymbol{r}_1) \Phi_{\mathrm{X}}^*(\boldsymbol{r}_2) \frac{e^2}{4\pi\varepsilon_0 r_{12}} \Phi_{\mathrm{Y}}(\boldsymbol{r}_2) \Phi_{\mathrm{Z}}(\boldsymbol{r}_1), \tag{89}$$

where $r_{12} = |\boldsymbol{r}_1 - \boldsymbol{r}_2|$. The physical meaning of parameters U_{A}, U_{AB},C_{A}, $\gamma_{1\mathrm{A}}$, $\gamma_{2\mathrm{A}}$ and $\gamma_{2\mathrm{AB}}$ is simply the following one: (i) U_i (with i = A or B) and U_{AB} represent the Coulomb energy for an electron pair occupying the same site (they are both in A or in B); when A = B then $U = U_{\mathrm{A}} = U_{\mathrm{AB}}$; (ii) C_{A} is the Coulomb energy for two electrons occupying different sites (1 in A and 2 in B or vice versa); when A = B then $C = C_{\mathrm{A}}$; (iii) $\gamma_{1\mathrm{A}}$ is the Coulomb self-energy of the exchange charge distribution $-e\Phi_{\mathrm{A}}(\boldsymbol{r})\Phi_{\mathrm{B}}(\boldsymbol{r})$ and is thus referred to as the exchange integral; (iv) $\gamma_{2\mathrm{A}}$ (respectively, $\gamma_{2\mathrm{AB}}$) appears as the Coulomb energy between the exchange charge distribution and an electron charge localized on site A (respectively, site B); when A = B then $\gamma_2 = \gamma_{2\mathrm{A}} = \gamma_{2\mathrm{AB}}$. In other words $\gamma_{2\mathrm{A}}$ or $\gamma_{2\mathrm{AB}}$ is a transfer integral between two cationic orbitals, resulting from the effective Coulombic potential created by the charge of another electron involved in the secular problem.

Under these conditions, the matrix elements given by Eq. 87 may be easily calculated:

$$E_0^{Gg} = 2\mathcal{E}_{\mathrm{A}g} + \frac{U_\mathrm{A} + U_\mathrm{AB} + 2C_\mathrm{A} + 4\gamma_{1\mathrm{A}} + 4\gamma_{2\mathrm{A}} + 4\gamma_{2\mathrm{AB}}}{4(1+\mathrm{S})^2}\,,$$
$$E_0^{Gu} = 2\mathcal{E}_{\mathrm{A}u} + \frac{U_\mathrm{A} + U_\mathrm{AB} + 2C_\mathrm{A} + 4\gamma_{1\mathrm{A}} - 4\gamma_{2\mathrm{A}} - 4\gamma_{2\mathrm{AB}}}{4(1-\mathrm{S})^2}\,, \quad \mathrm{A} \neq \mathrm{B}\,, \tag{90a}$$
$$E_0^{Gg} = 2\mathcal{E}_g + \frac{U + C + 2\gamma_1 + 4\gamma_2}{2(1+\mathrm{S})^2}\,,$$
$$E_0^{Gu} = 2\mathcal{E}_u + \frac{U + C + 2\gamma_1 - 4\gamma_2}{2(1-\mathrm{S})^2}\,, \quad \mathrm{A} = \mathrm{B}\,, \tag{90b}$$

$$K = \frac{U_\mathrm{A} + U_\mathrm{AB} - 2C_\mathrm{A}}{4(1-\mathrm{S}^2)}\,, \quad \mathrm{A} \neq \mathrm{B}\,, \tag{91a}$$
$$K = \frac{U - C}{2(1-\mathrm{S}^2)}\,, \quad \mathrm{A} = \mathrm{B} \tag{91b}$$

$$E_0^U = 2(\mathcal{E}_{\mathrm{A}g} + \mathcal{E}_{\mathrm{A}u}) + \frac{U_\mathrm{A} + U_\mathrm{AB} - 2\gamma_{1\mathrm{A}}}{2(1-\mathrm{S}^2)}\,,$$
$$E_1^U = 2(\mathcal{E}_{\mathrm{A}g} + \mathcal{E}_{\mathrm{A}u}) + \frac{C_\mathrm{A} - \gamma_{1\mathrm{A}}}{1-\mathrm{S}^2}\,, \quad \mathrm{A} \neq \mathrm{B}\,, \tag{92a}$$
$$E_0^U = 2(\mathcal{E}_g + \mathcal{E}_u) + \frac{U - \gamma_1}{1-\mathrm{S}^2}\,, \quad E_1^U = 2(\mathcal{E}_g + \mathcal{E}_u) + \frac{C - \gamma_1}{1-\mathrm{S}^2}\,, \quad \mathrm{A} = \mathrm{B}\,, \tag{92b}$$

where $\mathcal{E}_{\mathrm{A}g}$ and $\mathcal{E}_{\mathrm{A}u}$ (respectively $\mathcal{E}_g$ and $\mathcal{E}_u$ if A = B) are given by Eq. 78 and U_A, U_AB, C_A, $\gamma_{1\mathrm{A}}$, $\gamma_{2\mathrm{A}}$ and $\gamma_{2\mathrm{AB}}$ (respectively, U, C, γ_1 and γ_2 if A = B) by Eq. 88. In addition, by diagonalizing the upper 2×2 matrix in Eq. 86, we have the following eigenvalues:

$$E_{0,0}^{\pm} = \frac{1}{2}\left(E_0^{Gg} + E_0^{Gu} \pm \sqrt{(E_0^{Gg} - E_0^{Gu})^2 + 4K^2}\right)\,, \tag{93}$$

as well as the diagonal energy terms E^p and E^np for $|G_{0,0}^\mathrm{p}\rangle$ and $|G_{0,0}^\mathrm{np}\rangle$, respectively:

$$E^\mathrm{p} = \frac{2(\mathcal{E}_\mathrm{A} + \mathcal{E}_\mathrm{AB} + 2\mathrm{S}\mathcal{T}_\mathrm{AB}) + U_\mathrm{A} + U_\mathrm{AB} + 2\gamma_{1\mathrm{A}}}{2(1+\mathrm{S}^2)}\,,$$
$$E^\mathrm{np} = \frac{2(\mathcal{E}_\mathrm{A} + \mathcal{E}_\mathrm{AB} + 2\mathrm{S}\mathcal{T}_\mathrm{AB}) + 2C_\mathrm{A} + 2\gamma_{1\mathrm{A}}}{2(1+\mathrm{S}^2)}\,, \quad \mathrm{A} \neq \mathrm{B}\,, \tag{94a}$$
$$E^\mathrm{p} = \frac{2(\mathcal{E} + \mathrm{S}\mathcal{T}) + U + \gamma_1}{1+\mathrm{S}^2}\,, \quad E^\mathrm{np} = \frac{2(\mathcal{E} + \mathrm{S}\mathcal{T}) + C + \gamma_1}{1+\mathrm{S}^2}\,, \quad \mathrm{A} = \mathrm{B}\,. \tag{94b}$$

From the definitions of γ_2, C, γ_1 and U given by Eq. 88 (if A = B), we may deduce the following classification:

$$\gamma_2 \ll C \approx \gamma_1 \ll U\,, \tag{95}$$

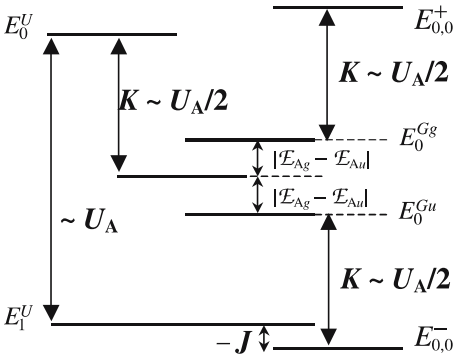

Fig. 5 Description of the energy level scheme for the AXB centrosymmetrical model system (A ≠ B); the difference $|\mathcal{E}_{Ag} - \mathcal{E}_{Au}|$ has been artificially zoomed for clarity

the "physical" values ranging from tenths of eV to a few eV. The resulting energy level scheme is reported in Fig. 5 and it will be the basis of the physical discussion in next subsection. Most of considerations will concern the classification of the Coulombic terms with respect to the difference $|\mathcal{E}_{Ag} - \mathcal{E}_{Au}|$ and the relative positions of the levels characterized by the energies E_1^U and $E_{0,0}^-$, their difference giving rise to the expression of J.

5
Comparison with Previous Models and Illustrations

5.1
Return to Hund's First Rule

Let us briefly show that the previous formalism is suitable to establish the Hund's first rule. Here, the orbitals describing the states $|\mathcal{A}\rangle$ and $|\mathcal{B}\rangle$ belong to the same ion, atom or molecule (with here A = X = B). *Since they are solutions of the same secular problem, they exhibit vanishing common overlap and transfer integrals*. Thus, the eigenvalues of the upper 2×2 matrix appearing in the Hamiltonian and given by Eq. 93 may be written:

$$E_{0,0}^+ \approx 2\mathcal{E} + U + \gamma_1 + \frac{4\gamma_2^2}{U - C}, \quad E_{0,0}^- \approx 2\mathcal{E} + C + \gamma_1 - \frac{4\gamma_2^2}{U - C}, \tag{96}$$

where $\mathcal{E} = \mathcal{E}_A = \mathcal{E}_B = \mathcal{E}_{AB}$ (as A = B) is given by Eqs. 70, 71 and 73 and which must be compared to E_0^U and E_1^U (given by Eq. 92), respectively close to $2\mathcal{E} + U - \gamma_1$ and $2\mathcal{E} + C - \gamma_1$. In addition, for an atom, $\gamma_2 = 0$ and, for a molecule or a polyatomic ion, $\gamma_2 \neq 0$.

Clearly, owing to the previous discussion concerning the order of magnitude of the Coulombic terms, the ground level corresponds to the triplet state

and appears to be stabilized by about $2\gamma_1$ ($\sim$ eV for intra-atomic exchange) with respect to the first excited level. A similar argument may prevail whenever some orbital degeneracy occurs. The ferromagnetic interaction based on the Coulomb exchange integral γ_1 is often called Heisenberg exchange.

The Pauli exclusion principle states that two electrons cannot occupy the same spatial position, when showing the same spin, since due to its antisymmetry property, the corresponding wave function then vanishes. This function must vary smoothly, as required for avoiding too large kinetic energy. Thus, it keeps weak values when two electrons characterized by parallel spins are not enough separated. This result also concerns the probability density. As a result a hole appears in the up (down) spin electron distribution in the vicinity of one of them (Fermi hole). As a consequence, the larger distance thus maintained between similar spin electrons explains their lower Coulomb energy, as compared to antiparallel spin electrons.

5.2
Molecular Orbital Model

In that case, the Coulomb interaction is assumed to play a secondary role. Then, the scheme of energy levels appearing in Fig. 5 becomes that one given in Fig. 6. Clearly, the ground state is one of the singlets $|g,+;g,-\rangle$ or $|u,+;u,-\rangle$ owing to the relative stability of the orbital states $|g,\sigma\rangle$ and $|u,\sigma\rangle$ (G-type collective state). The first excited state is the triplet $|U_{1,S^z}\rangle$, with $S^z = 0, \pm 1$.

This approach is relevant when the overlap between orbitals belonging to neighbouring sites is large (for instance in C – C covalent bonds). In case of orbital degeneracy, two low-lying states $|g,\sigma\rangle$ or $|u,\sigma\rangle$ are available for the electron pair which may then form a singlet or a triplet. Of course, the Hund's first rule tells us that the triplet is more stable, as often encountered.

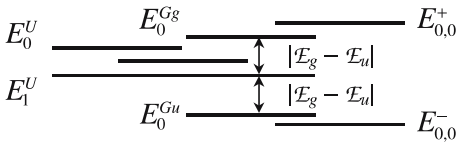

Fig. 6 Description of the energy level scheme for the AXB centrosymmetrical model system (with A = B for simplicity) when Coulomb interactions are negligible (molecular orbital model)

5.3
Comparison with the Anderson Model [54]

The Anderson model of the isotropic exchange has been proposed for extended systems like oxides and fluorides. In a first step, Anderson builds up

the molecular orbitals of the A–B system in a triplet state (with A = B). Then, he determines the orthogonal magnetic orbitals (OMO), as defined in Eq. 43. These functions are the Wannier functions (the symmetry group being the crystal translation group). From the ground state (with one unpaired electron per magnetic orbital), it appears a singlet state and a triplet one. One singlet state arises from the excited configurations and may couple with the low-lying singlet state, thus allowing its stabilization. We have seen that the total exchange constant is such as: $J = J_{mm'}$(potential) + $J_{mm'}$(kinetic), where $J_{mm'}$(potential) and $J_{mm'}$(kinetic) are given by Eqs. 51 and 56. The link between the transfer integral $b_{mm'}(\boldsymbol{\tau})$ defined by Eq. 50 and our model is:

$$b_{mm'}(\boldsymbol{\tau}) = \gamma_2 + \mathcal{T} \,, \tag{97}$$

where $\mathcal{T} = \mathcal{T}_{AB}$ and $\gamma_2 = \gamma_{2A}$ are given by Eqs. 74 and 88. In addition, the Coulomb energy U appearing in Anderson model corresponds to the quantity $U - C$ in our model. Taking into account the conventional writing of the exchange Hamiltonian ($H_{ex} = -2J\boldsymbol{S}_A \cdot \boldsymbol{S}_B$) we may write:

$$J_{And} = \gamma_1 - \frac{2(\gamma_2 + \mathcal{T})^2}{U - C} \,. \tag{98}$$

From the eigenvalues of the upper 2×2 matrix in the Hamiltonian given by Eq. 93, we obtain the lowest eigenvalue:

$$E^-_{0,0} \approx 2\mathcal{E} + C + \gamma_1 - \frac{4(\gamma_2 + \mathcal{T})^2}{U - C} \,. \tag{99}$$

We must now compare this value to E^U_1 written in the vanishing-S limit i.e.:

$$E^U_1 \approx 2\mathcal{E} + C - \gamma_1 \approx 2\mathcal{E} \quad \text{as} \quad C \sim \gamma_1 \,. \tag{100}$$

From the conventional writing of the exchange Hamiltonian we have now $-2J = E^U_1 - E^-_{0,0}$ i.e.,

$$J_{And} = \gamma_1 - \frac{2(\gamma_2 + \mathcal{T})^2}{U - C} = J \,, \tag{101}$$

where J is derived from our model.

5.4
Comparison with Hay–Thibeault–Hoffmann (HTH) Model [72]

In spite of the fact that the method of calculation is somewhat different, the HTH model is very close to the Anderson one. This model may be seen as the reduction of the homo-(poly)nuclear Anderson model to the homo-(bi)nuclear case (A = B). The HTH model also focuses on the two-singly occupied magnetic orbitals in the triplet state φ_+ and φ_- (cf. Eq. 43), with the energies ε_+ and ε_-. These authors introduce orthogonal magnetic orbitals

(OMO) and find J (with, as in Anderson model, $H_{ex} = -2J\boldsymbol{S}_A \cdot \boldsymbol{S}_B$):

$$J_{HTH} = K_{ab} - \frac{(\varepsilon_+ - \varepsilon_-)^2}{2(J_{aa} - J_{ab})}, \tag{102}$$

where we have the following correspondence with our model $K_{ab} = \gamma_1$, $J_{aa} - J_{ab} = U - C$, K_{ab} being the exchange integral, and, J_{aa} and J_{ab}, the one- and two-centre Coulomb repulsion integrals. Let us make the following comments about Eq. 102: (i) the ground state will be a triplet for the degenerate case $\varepsilon_+ = \varepsilon_-$ ($J = K_{ab}$, with $K_{ab} > 0$); (ii) the triplet state is destabilized with respect to the singlet state if $\varepsilon_+ \neq \varepsilon_-$; (iii) the difference $|E_{T,0} - E_{S,0}|$ can become vanishingly small for certain values of the integrals and energies which describe the exchange coupling process, but in some cases the paramagnetic centres remain exchange coupled; (iv) for certain values of the integrals and energies, the singlet state may become the ground state [73].

The HTH model derives from our general framework by: (i) taking into account the polar state, (ii) neglecting the overlap integral S. This situation is thus formally analogous to that one which prevails in the establishment of the Hund's first rule. The last correspondence with our model concerns the quantity $\varepsilon_+ - \varepsilon_-$: we have $\varepsilon_+ - \varepsilon_- = 2(\gamma_2 + \mathcal{T})$, where $\mathcal{T}$ does not a priori vanish between orbitals which are no longer distinct eigenfunctions of the same one-particle effective Hamiltonian. As a consequence, we have, with the same conventional writing of the exchange Hamiltonian as Anderson's one:

$$J_{HTH} = J_{And} = J, \tag{103}$$

where J is derived from our model. Thus, the exchange coupling shows a ferromagnetic contribution (basically Coulombic) and an antiferromagnetic one (mixing orbital and Coulomb processes).

Here the important novelty is that the antiferromagnetic contribution appears even in the case of vanishing overlap. It is related to the possibility of virtual excitation of an electron from one site to another one, without simultaneous reverse motion of the other electron (formation of a polar state). It results from an elementary perturbation theory that such an admixture necessarily pushes down the lowest non-disturbed energy level. In the present framework, since only two orbitals are involved in the mechanism, such polar states are possible only with antiparallel spins. As a consequence, this admixture favours the singlet state.

When orthogonality occurs because the orbitals involved in the mechanism are solutions of the same one-particle Hamiltonian, $\mathcal{T}$ may vanish. In practice, this situation is not often encountered: (i) the intervening orbitals are primarily considered in their own idealized environments and are solutions of *distinct* Hamiltonians; (ii) the effects of the surrounding extra atoms (potential energy contribution, symmetry lowering) introduced when synthetizing the molecule are generally neglected. However, even if $\mathcal{T}$ vanishes, γ_2 remains and favours an antiferromagnetic coupling.

5.5
Comparison with Kahn–Briat (KB) Model [74]

Kahn and Briat have investigated many molecular systems involving metal cations linked by various organic bridges. The situation is at the opposite of that one which supports the molecular orbital model. The overlap and transfer integrals are small now and the Coulomb integrals must no longer be ignored.

Kahn and Briat start from the observation that, in this limit, the states $|G^g_{0,0}\rangle$ and $|G^u_{0,0}\rangle$ are nearly degenerate. Thus, the strong off-diagonal term K in the upper 2×2 matrix associated with the Hamiltonian (cf. Eq. 96) strongly mixes them, then giving the eigenstates $|G^{\pm}_{0,0}\rangle \sim |G^g_{0,0}\rangle \pm |G^u_{0,0}\rangle$, which appear to be respectively very close to the polar and non-polar states $|G^{\rm p}_{0,0}\rangle$ and $|G^{\rm np}_{0,0}\rangle$ (cf. Eq. 94 in the vanishing-S limit). Kahn and Briat exclude the polar state due to its very high energy. As a consequence, the low-lying states are the non-polar triplet and singlet states i.e., $|U_{1,S^z}\rangle$ (with $S^z = 0, \pm 1$) and $|G^{\rm np}_{0,0}\rangle$. Using the conventional writing of Eq. 39 for the exchange part, also adopted in the KB model, we may immediately derive the difference $-J = E^U_1 - E^-_{0,0}$ (up to second order in S and $\mathcal{T}$), with E^U_1 and $E^-_{0,0}$, respectively, given by Eqs. 92 and 93:

$$J = 2(\gamma_1 - C\mathrm{S}^2) + 4\mathrm{S}(\mathcal{T} - \mathrm{S}\mathcal{E}) - 4\,\frac{[\gamma_2 + \mathcal{T} - \mathrm{S}(C+\gamma_1)]^2}{U-C} + \ldots \tag{104}$$

After a convenient translation with the KB notation [51–53, 74], it is easy to show that Eq. 104 exactly coincides with the result obtained by these authors. The first contribution finds its origin in the electron-electron Coulomb interaction U_{12}. Since γ_1 and C have been shown to be of the same order of magnitude, γ_1 dominates $C\mathrm{S}^2$. The Coulomb contribution remains positive and favours a ferromagnetic coupling. In the second term, the quantity $\mathcal{T} - \mathrm{S}\mathcal{E}$ is proportional to the quantity $\mathcal{E}_g - \mathcal{E}_u$ defined by Eq. 79. It emphasizes the key role of the overlap in the stabilization of the singlet state. As it is negative (cf. Eq. 80), this term added to the third one describes the antiferromagnetic contribution. Following Kahn and Briat we define:

$$J_{\uparrow\uparrow} = 2(\gamma_1 - C\mathrm{S}^2)\,,\; J_{\uparrow\downarrow} = 4\mathrm{S}(\mathcal{T} - \mathrm{S}\mathcal{E}) - 4\,\frac{[\gamma_2 + \mathcal{T} - \mathrm{S}(C+\gamma_1)]^2}{U-C} + \ldots\,, \tag{105}$$

so that:

$$J = J_{\uparrow\uparrow} + J_{\uparrow\downarrow}\,. \tag{106}$$

The ferromagnetic contribution $J_{\uparrow\uparrow}$ dominated by γ_1 is actually a *misadventure* of the Hund's first rule (Fermi hole), while the antiferromagnetic one $J_{\uparrow\downarrow}$ is mainly associated with the prohibition for the electrons to occupy the same orbital with the same spin. Both are demonstrations of Pauli's exclusion principle. The first term of $J_{\uparrow\downarrow}$ vanishes with the overlap, while the second

one remains a residual contribution. Thus, in case of orbital orthogonality, we asymptotically deal with the ferromagnetic contribution only.

This has been an important axis of research to elaborate high-spin molecular ferromagnets [75–86, 91–102]. In this respect, a strategy has been proposed to favour ferromagnetic interactions between nearest magnetic centres, based on the concept of orthogonality of the magnetic orbitals [26, 75–77]. It may be summarized as follows. The starting point concerns an A–B pair, with n_A unpaired electrons on A occupying the a_μ magnetic orbitals, and n_B unpaired electrons on B occupying the b_ν magnetic orbitals. a_μ (respectively, b_ν) transforms as Γ_μ^a (respectively, Γ_ν^b), the irreducible representation (irrep) of the point symmetry group characterizing the A–B pair. The magnetic orbitals are orthogonal if $\Gamma_\mu^a \neq \Gamma_\nu^b$ for any couple (μ,ν). As a consequence, the ground state has the highest spin multiplicity $(n_A + n_B)/2$. Because of the orthogonality of the magnetic orbitals a_μ and b_ν, it is not possible to form low-energy molecular orbitals, delocalized on the whole A–B pair, for which the "magnetic" electrons would pair. Under these conditions, Hund's rule holds and one obtains a parallel spin arrangement for the lowest energy state. This strategy has been successfully tested on the copper(II)-orthosemiquinone entity, a copper(II)-vanadyl(II) complex and a Cr(III)Ni(II)$_3$ tetranuclear species [75].

5.6 Other Models Illustrating the Charge Transfer Process

Models for organic ferromagnets with unpaired electrons in non-bonded orbitals have been proposed by Mataga and Ovchinnikov [78, 79]. A model using π electrons in a mixed (...DADADA...) stack has been proposed by McConnell [87] and extended by Breslow [88], in the context of charge transfer complexes. It is characterized by the introduction of excited (anomalously polarized) configurations in the Hamiltonian basis, similarly to the polar states introduced in our model. From that point of view, they do not basically differ from that scheme based on the energy lowering term $4(\gamma_2 + \mathcal{T})^2/(U - C)$ involving the transfer integral.

In the Anderson model (see Fig. 7, case (*a*)), the excited configuration is assumed to be a singlet whereas the ground starting configuration is a triplet, thus contributing to antiferromagnetism. Conversely, McConnell has pointed out that molecules showing a triplet ground state might be used to construct organic ferromagnets [87]. In this respect, McConnell considers an ionic molecular crystal D^+A^- characterized by an alternation of species D^+ and A^-, and formed with: (i) a donor molecule D whose neutral ground state is a triplet and a singlet state acceptor molecule A (case (*b*1)), (ii) a donor molecule D characterized by a neutral singlet ground state and an acceptor A showing a neutral triplet ground state (case (*b*2)). In both cases a charge transfer mechanism is involved, thus leading to a charge-transferred diradi-

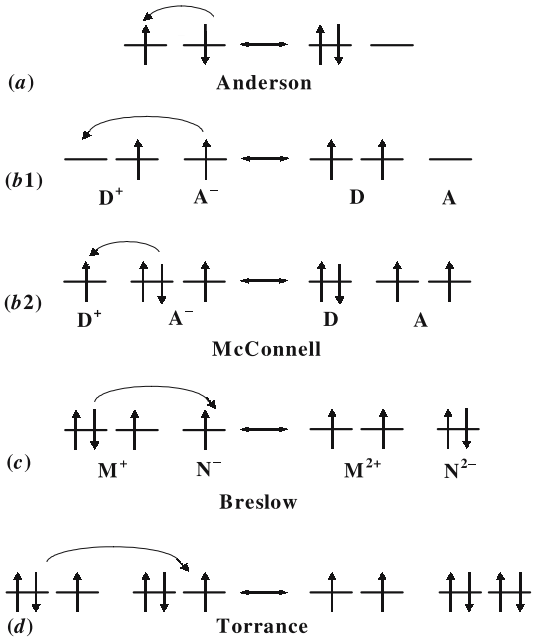

Fig. 7 Various examples of charge transfer models proposed by McConnell [87], Breslow [88] and Torrance et al. [89] for explaining ferromagnetic molecular ground states

cal characterized by a triplet ground state, keeping the spins parallel on both species. The charge transfer can go in either direction: the spin on a given A^- is parallel to the spins on both neighbours D^+ so that ferromagnetic domains may appear in the whole crystal. If the charge transfer is not only linear, one can expect 2D or 3D domains. Of course, this model does not work if both D and A show a triplet ground state.

A simple change has been proposed by Breslow [88]: the triplet species is a dication. In Fig. 7 case (*c*) shows a version in which species M has fully donated an electron to species N, making the $M^{+\bullet}/N^{-\bullet}$ pair. But the charge transfer study indicates that there is a contribution of M^{2+}/N^{2-} to the structure. If M^{2+} has a triplet ground state, N^{2-} being a singlet, the charge transfer then leads to a ferromagnetic coupling. This mechanism also works if N^{2-} is the triplet and M^{2+} the singlet.

Later on, Torrance et al. [89] have proposed another model for a segregated stack of radical ions causing a ferromagnetic spin alignment. In this respect, they consider a pair of adjacent radical anions $M_1^{-\bullet}$ and $M_2^{-\bullet}$, each species having an unpaired electron delocalized in a π orbital over an aromatic molecule. The ground state of the two molecule dimer may be written as $M_1^{-\bullet}$ $M_2^{-\bullet}$ and may be either a singlet or a triplet. The excited state is the one induced by

the charge transfer of an electron from one molecule to its neighbour i.e., $M_1^{2-}M_2^0$ or $M_1^0M_2^{2-}$. The effect of the overlap is to mix ground and excited states. When synthetizing the molecule the aim is to make a triplet with the lowest excited state. This occurs via Hund's rule in case of orbital degeneracy: the two unpaired electrons in the dianion must go into different (but degenerate) orbitals, with their spins parallel. In the case of an aromatic molecule, the orbital degeneracy is caused by the high molecular symmetry; in another molecule, it may arise from appropriate non-bonded orbitals (see Fig. 7, case (*d*)).

Part of the difficulties arises from the triplet state molecular engineering [90–102]. As already pointed out incidentally, stabilizing a triplet state generally requires special symmetry properties. These properties are not often met in free molecules due to their own conformation. Electron–phonon coupling itself (Jahn–Teller effect) may be quite efficient in reducing the degeneracy of the available orbitals. In addition, the crystallization process may contribute to reduce it again. Although strict degeneracy or orbital orthogonality is not required, molecular crystals showing ferromagnetic couplings are not numerous [80–86, 91–102].

6 Conclusion

In this article we have developed a general model in order to describe the superexchange mechanism for the centrosymmetrical system AXB, where A and B are magnetics centres and X is a common bridging ligand. We have considered the degenerate case A = B, but also the general one $A \neq B$, where A or B is described by a cationic *d*-orbital and X by a *p* (or *s*) ligand orbital. In addition the orbitals describing the states $|A\rangle$ and $|B\rangle$ do not overlap but the important case of overlap between A and B may be also taken into account. However, in both cases, the overlap between $|A\rangle$ and $|X\rangle$ or $|X\rangle$ and $|B\rangle$ is always considered as weak.

Under these conditions, the general treatment which has been set on has allowed us to construct an energy level spectrum and the corresponding energies have been derived. Notably, from the singlet–triplet splitting of the low-lying states, a closed-form expression of the exchange energy *J* may be expressed vs. key molecular integrals. The restriction of the present model to the most important cases previously published allows one to exactly retrieve the *J* expression respectively derived by Anderson on the one hand, Hay–Thibeault–Hoffmann on the other or finally by Kahn and Briat, thus bringing a strong validation to our model.

Important generalizations may be brought. Notably, spin polarization effects may be introduced for the fragment AXB, as well as the spin-orbit coupling. In particular, as this latter contribution must remain small, the

formalism may be slightly altered by replacing the zeroth-order magnetic orbitals by new magnetic orbitals taking into account the spin-orbit perturbation. However, the most important key point concerns the possible generalization of our formalism to any kind of molecule or polyatomic ion, opening the possibility of exact calculations of exchange couplings in real molecules.

References

1. Curie P (1895) Ann Chim Phys (Paris) 5:289
2. Langevin P (1905) J Phys (Paris) 4:678
3. Langevin P (1905) Ann Chim Phys (Paris) 5:70
4. Weiss P (1906) Comptes Rendus Acad Sci (Paris) 143:1136
5. Weiss P (1907) J Phys (Paris) 6:661
6. Weiss P (1908) Physik Z 9:358
7. Debye P (1925) In: Marx E (ed) Handbuch der Radiologie, vol IV. Akad Verlagsges, Leipzig, p 597
8. Weiss P (1914) Ann Phys (Paris) 1(9):134
9. Rozansky D (1926) Physik Z 27:779
10. Heisenberg W (1926) Z Physik 38:411
11. Dirac PAM (1926) Proc Roy Soc A112:661
12. Hund F (1927) In: Linienspektren und periodisches System der Elemente. Springer, Berlin
13. Hund F (1925) Z Physik 33:855
14. Heisenberg W (1926) Z Physik 39:499
15. Néel L (1932) In: Ph D Thesis, chap VIII. Masson, Paris
16. Kramers HA (1934) Physica 1:182
17. Van Vleck JH (1934) In: The Theory of Electric and Magnetic Susceptibilities, chap XI. Oxford University Press, London and New York
18. Anderson PW (1959) Phys Rev 115:2
19. Anderson PW (1963) Solid State Phys 14:99
20. Kanamori J (1957) Prog Theor Physics 17:197
21. Van Vleck JH (1962) Revista de Matematicas y Fisica Teorica (Tucuma, Argentina) 14:189
22. Lévy PM (1964) Phys Rev 135A:155
23. Lévy PM (1966) Phys Rev 147:311
24. Curély J (2005) Monatshefte für Chemie, 136(6):1013
25. Herring C (1966) In: Rado, Suhl (eds) Magnetism, vol IIB. Wiley, New York, p 1
26. Kahn O (1987) Structure and Bonding 68:89
27. Jahn HA, Teller E (1937) Proc Roy Soc (London) A161:220
28. Bates CA (1978) Phys Rep 35:187
29. Hartmann-Boutron F (1968) J Phys (Paris) 29:212
30. Heitler W, London F (1927) Z Physik 44:455
31. Heitler W (1927) Z Physik 46:47
32. Heitler W (1928) Z Physik 47:835
33. Heitler W (1928) Z Physik 51:805
34. London F (1928) Z Physik 46:455
35. London F (1928) Z Physik 50:24
36. Born M, Oppenheimer JR (1927) Ann Physik 84:457

37. Sugiura Y (1927) Z Physik 45:484
38. Courant R, Hilbert D (1931) In: Methoden der Mathematischen Physik, 2nd ed. Springer, Berlin
39. Courant R, Hilbert D (1953) In: Methods of Mathematical Physics. Wiley, New York
40. Van Vleck JH (1934) Phys Rev 45:405
41. Silvi B, Fourré I, Alikhani ME (2005) Monatshefte für Chemie 136(6):855
42. Bocă R, Linert W (2005) Monatshefte für Chemie 136(6):881
43. Dirac PAM (1928) Proc Roy Soc (London) A117:610
44. Dirac PAM (1930) Proc Roy Soc (London) A126:360
45. Boča R (1999) In: Theoretical Foundations of Molecular Magnetism, chap IV and references therein. Elsevier, Amsterdam
46. Curély J (2005) Monatshefte für Chemie 136(6):987
47. Moriya T (1962) In: Rado, Suhl (eds) Magnetism, vol I. Wiley, New York, p 85
48. Dzialoshinski IE (1957) Sov Phys JETP 6:821
49. Dzialoshinski IE (1957) Sov Phys JETP 6:1259
50. Moriya T (1960) Phys Rev 120:91
51. Kahn O (1985) In: Willet, Gatteschi, Kahn (eds) Magneto-Structural Correlations in Exchange Coupled Systems. NATO ASI Series C: Mathematical and Physical Sciences, vol 140. Reidel, Dordrecht, p 37
52. Kahn O (1993) In: Molecular Magnetism. VCH Publishers, New York
53. Girerd JJ, Journaux Y, Kahn O (1981) Chem Phys Lett 82:534
54. Anderson PW (1963) In: Rado, Suhl (eds) Magnetism, vol I. Wiley, New York, p 25
55. Kahn O, Charlot MF (1980) Nouv J Chim 4:567
56. Charlot MF, Kahn O, Drillon M (1982) Chem Phys 70:177
57. Löwdin PO (1950) J Chem Phys 18:365
58. Shull CG, Strauser WA, Wollan EO (1951) Phys Rev 83:333
59. Anderson PW (1950) Phys Rev 79:350
60. Tinkham M (1956) Proc Roy Soc (London) A236:535
61. Shulman RG, Jaccarino V (1956) Phys Rev 103:1126
62. Jaccarino V, Shulman RG (1957) Phys Rev 107:1196
63. Shulman RG, Jaccarino V (1957) Phys Rev 108:1219
64. Kondo J (1957) Prog Theor Phys 18:541
65. Blount EI (1962) Solid State Phys 13:305
66. Goodenough JB (1960) Phys Rev 117:1442
67. Goodenough JB (1955) Phys Rev 100:564
68. Goodenough JB (1958) J Phys Chem Solids 6:287
69. Kanamori J (1959) J Phys Chem Solids 10:87
70. Wollan EO, Child HR, Koehler WC, Wilkinson MK (1958) Phys Rev 112:1132
71. Georges R (1992) In: Proceedings of Primera Escuela Nacional de Materiales Moleculares, vol II, Peñiscola, Spain
72. Hay PJ, Thibeault JC, Hoffmann R (1975) J Am Chem Soc 97:4884
73. Hatfield WE (1985) In: Willet, Gatteschi, Kahn (eds) Magneto-Structural Correlations in Exchange Coupled Systems. NATO ASI Series C: Mathematical and Physical Sciences, vol 140. Reidel, Dordrecht, p 555
74. Kahn O, Briat B (1976) J Chem Soc Faraday II 72:1968
75. Kahn O, Pei Y, Journaux Y (1989) Mol Cryst Liq Cryst 176:429
76. Kahn O, Galy J, Journaux Y, Jaud J, Morgenstern-Badarau I (1982) J Am Chem Soc 104:2165
77. Journaux Y, Kahn O, Zarembowitch J, Galy J, Jaud J (1983) J Am Chem Soc 105:7585
78. Mataga N (1968) Theor Chim Acta (Berlin) 10:372

79. Ovchinnikov AA (1978) Theor Chim Acta (Berlin) 47:297
80. Bencini A, Benelli C, Caneschi A, Carlin RL, Dei A, Gatteschi D (1985) J Am Chem Soc 107:8128
81. Pei Y, Journaux Y, Kahn O (1988) Inorg Chem 27:399
82. Dixon DA, Miller JS (1989) Mol Cryst Liq Cryst 176:211
83. Miller JS, Epstein AJ (1989) Mol Cryst Liq Cryst 176:347
84. Epstein AJ, Miller JS (1989) Mol Cryst Liq Cryst 176:359
85. Tyutyulkov N, Karabunarliev S, Ivano C (1989) Mol Cryst Liq Cryst 176:139
86. Buchachenko AL (1989) Mol Cryst Liq Cryst 176:307
87. McConnell HM (1967) Proc R A Welch Found Conf Chem Res 11:144
88. Breslow R (1982) Pure Appl Chem 54:927
89. Torrance JB, Oostra A, Nazzal A (1987) Synth Met 19:709
90. Breslow R (1989) Mol Cryst Liq Cryst 176:211
91. Julve M, Verdaguer M, Charlot MF, Kahn O, Claude R (1984) Inorg Chim Acta 82:5
92. Pei Y, Verdaguer M, Kahn O, Sletten J, Renard JP (1986) J Am Chem Soc 108:7428
93. Gadet V, Mallah T, Castro I, Verdaguer M, Veillet P (1992) J Am Chem Soc 114:9213
94. Eyert V, Siberchicot B, Verdaguer M (1997) Phys Rev B56:8959
95. Arrio MA, Scuiller A, Sainctavit P, Cartier dit Moulin C, Mallah T, Verdaguer M (1999) J Amer Chem Soc 121:6414
96. Verdaguer M, Bleuzen A, Marvaud V, Vaissermann J, Seuleiman M, Desplanches C, Scuiller A, Train C, Garde R, Gelly G, Lomenech C, Rosenman I, Veillet P, Cartier dit Moulin C, Villain F (1999) Coord Chem Rev 190:1023
97. Vostrikova KE, Luneau D, Wernsdorfer W, Rey P, Verdaguer M (2000) J Am Chem Soc 122:718
98. Verdaguer M (2001) Polyhedron 20:1115
99. Andrés R, Brissard M, Gruselle M, Train C, Vaissermann J, Malézieux B, Jamet JP, Verdaguer M (2001) Inorg Chem 40:4633
100. Lescouëzec R, Vaissermann J, Lloret F, Julve M, Verdaguer M (2002) Inorg Chem 41:5943
101. Tiron R, Wernsdorfer W, Tuyeras F, Scuiller A, Marvaud V, Verdaguer M (2003) Polyhedron 22:2427
102. Verdaguer M, Girolami G (2005) In: Miller JS, Drillon M (eds) Magnetoscience: molecules to materials, vol V. Wiley (Interscience), New York, p 283

Author Index Volumes 101–122

Author Index Vols. 1–100 see Vol. 100

The volume numbers are printed in italics

Subject Index